Iron precipitation and associated metal loss from simulated process solutions

by

Tasawar Javed

A THESIS SUBMITTED IN PARTIAL FULFILLMENT OF

THE REQUIREMENTS FOR THE DEGREE OF

DOCTOR OF PHILOSOPHY

in

THE FACULTY OF GRADUATE AND POSTDOCTORAL STUDIES

(Materials Engineering)

THE UNIVERSITY OF BRITISH COLUMBIA

(Vancouver)

March 2017

Abstract

Ferric iron precipitation is an important integral step of the hydrometallurgical processes. The precipitation product is often amorphous and leads to a significant amount of valuable metal loss to the residue along with residue disposal issues.

Characterization of the leach residue samples from CESL and Vale medium temperature (150 °C) hydrometallurgical processes revealed that the precipitation of iron in the form of amorphous iron oxide phases results in approximately 2-4 times higher metal loss compared to the crystalline phases.

To address the issue, simulated process solutions were used to study the effect of process parameters and their relative importance on batch precipitation conditions with the aim of obtaining a stable iron oxide phase i.e. hematite, while minimising associated metal loss to the precipitation product. It was found that the factors: initial ferric, H_2SO_4 and seed concentrations play an important role in the iron precipitation step. Mathematical models were developed for the iron precipitation and metal loss to the precipitates using statistical data analysis techniques.

Results from this study show that the presence of low ferric or high acid concentrations and moderate amounts of seed are required to minimize metal loss to the precipitation product with moderate to high levels of iron precipitation. The supersaturation and the nucleation to growth ratios were found to determine the final product quality i.e. the particle size and associated metal loss.

The presence of various anions or cations was also found to play an important role on the iron precipitation rate and product quality/nature. For example, the presence of chloride in the solution accelerated precipitation kinetics. The sulphate salts of the metals such as Mg and Cu increased the extent of precipitation, while aluminum sulphate decreased the extent of precipitation. Presence of the sodium ion in the system accelerated the precipitation kinetics but changed the nature of the product to sodium jarosite. The presence of low levels of arsenic (As:Fe ≤ 0.08) in the system were found to severely retard the precipitation rate. Adsorption of sulphate and incorporation of OH^- into the hematite structure were responsible to produce a poorly crystalline hematite product.

Preface

Financial support of the project was provided by Cominco Engineering Services Limited (CESL), a subsidiary of Teck Corporation, Vale Limited and the Natural Science and Engineering Research Council of Canada (NSERC). Conference travel support was provided by the Canadian Institute of Mining Metallurgy and Petroleum (CIM) on various occasions during the course of the project. Conference papers, journal papers and presentations listed below have been prepared from the data presented in this dissertation. I am the principal contributor to all of these contributions and I was responsible for designing and conducting the experiments as well as collecting and analysing the data and writing the contents. The contributing authors include Dr. Edouard Asselin (my supervisor) who provided excellent guidance through all aspects of the project. The data provided in Chapter 4 of the thesis was prepared with the support from the contributing authors: Abdul Baseer (Ph.D. student at UBC who conducted some HaHC dissolution experiments), Professor Dominic Ryan from the department of Physics at McGill University (who conducted the Mossbauer spectroscopy and interpreted the results) and Dr. Mati Raudsepp from the Earth, Ocean and Atmospheric Science department of the University of British Columbia (who performed the analysis of the X-Ray diffraction data).

Journal Papers

Javed, T., Abdul, B., Ryan, D., Raudsepp, M., Asselin, E., 2016. Amorphous iron phases in medium temperature leach residues and associated metal loss, International Journal of Mineral Processing, 148, 65 – 71.

Javed, T., Asselin, E., 2016. Factors affecting the kinetics of iron precipitation from simulated sulphate – chloride solutions at 150 °C (Part-I). Submitted manuscript (revisions invited).

Javed, T., Asselin, E., 2016. Effect of variables on iron precipitation and metal loss from sulphate-chloride solutions at 150 °C: A statistical approach (Part-II). Submitted manuscript (revisions invited).

Conference Papers

Javed, T., Asselin, E., 2014. Thermal behaviour of medium temperature sulphide concentrate leach residues. In: Asselin, E., Dixon, D.G., Doyle, F.M., Dreisinger, D.B., Jeffrey, M.I., Moats, M.S. (Eds.), Hydrometallurgy 2014. CIM, Montreal, Canada, 1, 113 – 126.

Javed, T. Asselin, E., 2015. Hematite precipitation from sulphate – chloride solutions at 150 °C. Conference of metallurgists 2015, CIM, Montreal, Canada, 1-13.

TABLE OF CONTENTS

LIST OF TABLES

LIST OF FIGURES

List of Symbols

S	Saturation ratio
a	Activity (mol/L)
a^*	Equilibrium activity (mol/L)
r	Radius of solid nuclei (m)
r^*	Critical radius of nuclei (m)
$S_{crit.}$	Critical supersaturation ratio
ΔG^*	Maximum free energy (J/mol)
ΔG^*_{hom}	Maximum free energy for homogeneous nucleation (J/mol)
ΔG^*_{het}	Maximum free energy for heterogeneous nucleation (J/mol)
J	Nucleation rate (nuclei/s.m^3)
A^*	Pre-exponential term or attachment frequency
γ	Interfacial tension (J/m^2)
$\gamma_{met.}$	Interfacial tension for metastable phases (J/m^2)
$\gamma_{st.}$	Interfacial tension for stable phases (J/m^2)
T	Temperature (°C or K)
J_{hom}	Homogeneous nucleation rate (nuclei/s.m^3)
A	Constant in an exponential relationship
B	Constant in an exponential relationship
R^2	coefficient of determination
R_{hyd}	Hydrolysis rate (g/L.hour)
K_{hyd}	Kinetic constant (per hour/hour^{-1})
α	Reaction order

List of Terms

CESL	Cominco engineering services limited
DTA	Differential thermal analysis
EDS	Energy dispersive spectroscopy
EDTA	Ethylenediaminetetraacetic acid
HaHC	Hydroxylamine hydrochloride
ICP-OES	Inductively coupled plasma optical emission spectrometry
IR	Infrared
QXRPD	Quantitative X-ray powder diffraction
SEM	Scanning electron microscopy
SX	Sequential extraction
TEM	Transmission electron microscopy
TGA	Thermal gravimetric analysis
XAFS	X-ray absorption fine structure
XRD	X-ray diffraction

Acknowledgements

I wish to acknowledge the financial support from Cominco Engineering Services Limited (CESL), a subsidiary of Teck Resources, Vale Limited and natural science and engineering research council of Canada (NSERC).

I would like to express my sincere gratitude to Dr. Edouard Asselin (my supervisor and mentor) for his unconditional support, patience and optimistic view during the course of this journey. I alone would have not been able to complete this journey without his thoughtful and constructive inputs, healthy discussions and encouragement.

I would also like to thank my supervisory committee members: Dr. David B. Dreisinger and Dr. Berend Wassink for their great advice and comments. I would like to express my special thanks to Mr. Henry Salomon-De-Friedberg from Teck-CESL for his input on regular basis, his truth seeking scientific attitude and his precious time for lengthy meetings and intellectual discussions. I am also very grateful to Dr. Indje Mihaylov from Vale Limited for his useful suggestions and reviewing the work on several occasions.

I am also thankful to Dr. Dominic Ryan from the department of physics at McGill University for his kind help for the Mössbauer analysis; Dr. Mati Raudsepp and Dr. Elisabetta Pani from the earth, ocean and atmospheric science (EOAS) department at the University of British Columbia for obtaining quantitative X-ray analysis data featured in this work. Dr. Philip Wong from department of chemistry at the University of British Columbia is also gratefully acknowledged for obtaining the Raman spectra presented in this work. I am grateful to John MacIntosh from Teck-CESL for carrying-out the many chemical analyses

presented in this work. I am once again thankful to Dr. Berend Wassink for helping me with the sulphur extraction experiments. I am also thankful to Jacob Kabel for assistance in collecting SEM results, Derrick Horne for TEM and Sally Finora for FTIR.

I wish to thank my colleagues: Abdul Baseer and Tim Ward as well summer student Pablo Zuñiga Sanchez for their help. Finally, I am also thankful to my family members for their support and encouragement.

Dedication

To my family

Chapter 1. Introduction and thesis organisation

Sulphide minerals are commonly processed by smelting and hydrometallurgical methods (Berezowsky and Trytten, 2002). However, the more recent commercial implementation of hydrometallurgical processes (such as Vale's medium temperature Ni-sulphide leaching plant in Newfoundland) (Kerfoot *et al.*, 2002) has contributed to the renewed interest in hydrometallurgical processing of the ore concentrates. Hydrometallurgical processes may have an advantage for the treatment of low grades of complex ores containing high impurities as compared to conventional smelting. Dreisinger (2004, 2006) has discussed the developments in hydrometallurgical processing of copper concentrates while Baba *et al*. (2012) have reviewed the options for treating chalcopyrite, one of the most common copper sulphide minerals. The extent of copper recovery and residue stability contribute to the overall success of the process.

Hydrometallurgical leaching of sulphide ores is commonly carried out in oxidative sulphuric acid solutions. Iron is ubiquitous in the ores, whose leaching leads to the dissolution of Fe(II). Fe(II) can be oxidised to Fe(III), which either remains in the solution or precipitates. The precipitation of Fe(III) as an oxide or hydroxide occurs by thermal ageing of the solution under the process operating conditions such as temperature and pH. Fe(III) precipitation is an important integral step of the process. The first stage of the precipitation is the formation of amorphous precipitates which then transform to more stable crystalline phases (Dutrizac, 1980; Demopoulos, 2009).

Cominco Engineering services limited (CESL) and Vale Ltd. are operating medium temperature (150 °C) leach processes for the processing of sulphide concentrates at the pilot and commercial scales, respectively. Typical copper and/or nickel recoveries from these processes are in the range of 96-99 % (Defreyne *et al*., 2006). The source of metal loss to the residue is not clear. In certain cases ~2 % unreacted metal sulphides are reported in the residue (Defreyne *et al*., 2006). Copper and nickel associated with the iron precipitation product can also serve a source of metal loss to the residue. In this thesis focus will be on the iron precipitation and associated metal loss in a typical CESL process (which is a medium temperature hydrometallurgical process for the leaching of chalcopyrite).

It is preferred that iron from the leaching of sulphide ores be precipitated in the form of hematite because of its superior filtration and washing characteristics, its environmental stability and because it typically does not adsorb (see section 2.3.3 of thesis) as much of the valuable metals (Cu and/or Ni) that these processes are trying to recover (Piret and Melin, 1993). However, in actual practice pure hematite is not produced, rather the residue is a mixture of hematite, goethite, jarosite and other iron oxides/oxyhydroxides. Some of the iron-based solid residues are amorphous/poorly crystalline (such as ferrihydrite: see section 2.5). Amorphous/poorly crystalline iron oxides/oxyhydroxides result in higher valuable metal loss to the residue compared with their counterpart crystalline phases (Sahu and Asselin, 2011). Besides, they pose an environmental threat as their transformation to a more stable phase releases acid and adsorbed metals resulting in contamination of the surrounding environment.

With population increase and industrial advancement, the demand for base metals has increased. According to a survey conducted by industry consulting services group "Brook Hunt" (a Wood Mackenzie Company) (Brook Hunt survey, 2011), global refined copper demand is forecast to increase on average at a compound rate of 3.4 % from 2010 to 2025. The increasing worldwide demand for copper and nickel and the depletion of high grade ores necessitates that the loss of the valuable metals to the residue be kept to a minimum. This can also serve as an economic incentive to the operators to maximize % metal recovery from the leaching processes. Secondly, stringent environment regulations demand the iron to be deported in the form of a stable phase to the residue. Hematite is thermodynamically more stable iron oxide phase (Dutrizac, 1987) and its stability would help to ensure that any of the co-precipitated impurities did not leach from the residue impoundment area. In addition, hematite has a commercial value as it can be used in the cement, pigment, steel and ceramic industries, if impurity levels are reduced to a minimum (Dutrizac, 1987). Since hematite processes encounter higher capital cost because of the requirement of high temperature and oxygen consumption; shorter retention times can partially balance the capital cost. CESL and Vale aim to produce a better quality iron residue under shorter retention times.

The aim of this work is to identify the factors leading to higher valuable metal loss to the leach residues, produced under medium temperature conditions, and then to use simulated solutions to predict key variables to reduce the valuable metal (copper) loss to the residue under CESL pressure oxidation conditions.

Subsequent chapters in the thesis are organised as follows: Chapter 2 provides the literature review which includes: an overview of the treatment practices for metallurgical ores, iron removal options as practiced in the hydrometallurgical industry, CESL and Vale hydrometallurgical processes, the precipitation and transformation of metastable iron oxide phases, the chemistry of hematite precipitation and nucleation theory of crystallization.

Chapter 3 summarises the objectives of this study. Chapter 4 provides the results of the characterization of three residue samples from the CESL and Vale demonstration and pilot plant medium temperature hydrometallurgical processes. A correlation between iron precipitation and associated Cu/Ni loss to the residue is established, in this chapter, with the help of different characterization and chemical extraction techniques. Poorly crystalline phases normally constitute a large proportion of the iron bearing residues. This often leads to difficulties in identification and quantification using routine XRD analysis. A combination of several techniques such as: sequential extraction, quantitative x-ray powder diffraction (QXRPD), scanning electron microscopy (SEM) and Mössbauer spectroscopy were used for the true quantification of these phases. Chapter 5 further extends the characterization and explains thermal behaviour as well as the Raman and Fourier transform infrared (FTIR) spectroscopic results.

Chapter 6 provides an investigation of the hematite precipitation and copper loss to the precipitates in simulated process solutions under typical CESL conditions. The effect of key process parameters such as: ferric concentration, acid levels, seed concentration,

retention time, copper, chloride concentrations and temperature are studied using one variable at a time approach in this chapter.

The important parameters and their ranges identified through the one-variable approach in Chapter 6 were further studied using statistical analysis and modelling in Chapter 7. The importance of each variable was studied against two response variables i.e. % Fe precipitation as hematite and % Cu loss to the precipitates. Mathematical models were developed for the two response variables by fitting the data to quadratic models.

Chapter 8 describes the effect of different factors on precipitation kinetics. The effect of commonly encountered impurities such as: arsenic, aluminum, sodium and magnesium on iron precipitation and kinetics is provided in this chapter. Finally, Chapter 9 provides a summary of the findings from this work and gives a brief summary of the future work required to extend the outcomes of the current findings.

Chapter 2. Literature review

Iron is the second most abundant element in the earth and fourth most abundant element in the earth's crust. It is a common constituent in the ores and concentrates of many valuable metals such as copper, nickel, zinc, cobalt, aluminum and titanium. It is present in the structures of common sulphide minerals such as chalcopyrite ($CuFeS_2$), pentlandite {$(Fe, Ni)_9S_8$} and marmatite {(Fe, Zn)S} as well as in the form of iron containing gangue minerals associated with the ores such as: pyrite (FeS_2) and pyrrhotite ($Fe_{1-x}S$) (Chen and Cabri, 1986).

Chalcopyrite ($CuFeS_2$) is the most abundant copper bearing mineral consisting of approximately 70 % of known copper reserves (Thomas, 2009). It is usually associated with many other minerals in the natural environment such as: pyrite (FeS_2), pyrrhotite (Fe_7S_8), chalcocite (Cu_2S), bornite (Cu_5FeS), galena (PbS), siderite ($FeCO_3$), sphalerite (ZnS) and calcite ($CaCO_3$). Chalcopyrite often contains trace amount of contaminants such as: Mn, Zn, Ni, Co, Sb which partially substitute copper and iron in its structure. Some finely inter-grown minerals of Au, Ag, Al, Pt, V, Cr and In may also be found inside host chalcopyrite (Hershel, 2011). Chalcopyrite is not only the most abundant of the copper sulphide minerals but also one of the most difficult to leach because of its refractory nature and stable structure (face centred tetragonal). Leaching of chalcopyrite successively enriches the mineral in terms of copper i.e. it goes through a transition from chalcopyrite ($CuFeS_2$) to chalcocite (Cu_2S) and covellite (CuS) (Brantley, 2003).

Copper metal production from chalcopyrite is carried out mainly by using two methods i.e. conventional pyrometallurgical and recent hydrometallurgical techniques. Baba *et al*. (2012) have reviewed the various techniques for the processing of chalcopyrite. Conventional pyrometallurgical techniques consist of crushing, grinding, flotation, smelting, converting and refining/electro-refining. The by product from Cu smelting and converting furnaces i.e. slag contains significant amounts of unrecovered copper (1-2 % Cu in smelting slag and 4-8 % in converting slag, before recycling to smelter; the percentages further increase as the matte grade increases) (Davenport *et al*., 2002). The presence of large amounts of copper in the slag necessitates a slag cleaning step. Several options: such as the use of slag cleaning electric furnaces and slow cooling of slag followed by crushing/grinding and flotation are used to recover copper from the slag. The tailings from slag cleaning step still contain about 0.4 to 1.0 % Cu which is lost when slag is discarded. Das *et al*. (1987) used leaching techniques to recover copper from the slag tailings. Although their leaching was successful, yet its success on an industrial scale is a question mark.

Hydrometallurgical methods consist of crushing, leaching (pressure oxidation, atmospheric leaching), solvent extraction and electrowinning. Dreisinger (2004, 2006) has given a detailed discussion about the hydrometallurgical processes for copper concentrates. In the past, commercial success of copper hydrometallurgical processes was restricted to Mt. Gordon's pressure oxidation/ferric leaching (Dreisinger *et al*., 2002) and Oxiana's Sepon process (Baxter *et al*., 2004), both for secondary copper sulphides. However, in recent years hydrometallurgical processing of chalcopyrite concentrates has become a reality. For

example, chalcopyrite was successfully leached at Morenci (Arizona, USA) under conditions similar to those discussed in this thesis (though without the addition of chloride) (Marsden, *et al*., 2007a). The CESL and Vale hydrometallurgical processes have received wide attention because of their unique chloride assisted technology and high metal recoveries. CESL targets to make the process more efficient by maximizing copper recovery from chalcopyrite ore concentrates. A brief description of the hydrometallurgical processes in general and CESL medium temperature hydrometallurgical process, in particular, is given below.

2.1 Hydrometallurgical processes

The hydrometallurgical processes that have been developed so far can be classified into low, medium and high temperature categories (McDonald and Muir, 2007a, 2007b). Low temperature processes require ultrafine (5-15 μm) grinding to enhance leaching kinetics, the use of halides to overcome passivation of the mineral or require the addition of catalysts such as silver or silver-bearing pyrite (*cf*. Galvanox; Nazari, *et al*., 2011). Medium temperature processes employ fine grinding, comparatively higher temperatures, 140-150 °C, and the addition of specific reagents for sulfur dispersion (lignosulphonate or orthophenylinediamine). Medium temperature processes also result in moderate to high conversions of sulphides to elemental sulphur and generate comparatively stable leach residues. The generation of elemental sulfur may, however, represent an environmental

liability if it is not separated from the process residues. High temperature processes are usually operated at temperatures 200 – 230 °C. At higher temperatures leaching kinetics are enhanced but the entire sulphide charge is converted to sulphate, which leads to higher oxygen consumption and higher acid levels (which incorporates a neutralization step) in the output liquid stream (McDonald and Muir, 2007a, 2007b).

The focus of this thesis is on medium temperature leaching. During medium temperature processes, sulphide minerals are oxidized to convert the valuable metals into their acid soluble forms. Equations (2.1) and (2.2) describe the reactions involved during the pressure oxidation of chalcopyrite and pentlandite at 150 °C, respectively. The primary objective of the pressure oxidation is to get maximum metal extraction with minimum sulphur oxidation (Jones *et al*., 2009).

$$4CuFeS_2 + 5O_2 + 4H_2SO_4 \rightarrow 4CuSO_4 + 2Fe_2O_3 + 8S^\circ + 4H_2O \qquad (2.1)$$

$$4(Ni,Fe)_9S_8 + 45/2O_2 + 18H_2SO_4 \rightarrow 18NiSO_4 + 9Fe_2O_3 + 32S^\circ + 18H_2O \qquad (2.2)$$

Chalcopyrite and pentlandite concentrates usually contain significant amounts of pyrrhotite and pyrite as these phases are difficult to separate from the primary ores. Pyrrhotite, if present, is oxidized almost quantitatively to hematite and elemental sulphur, without any sulphate formation. The oxidation of pyrrhotite is shown in Equation (2.3), it is a comparatively fast reaction (for simplicity, the Fe:S in pyrrhotite is considered to be 1) (Jones *et al*., 2009)

$$4FeS + 3O_2 \rightarrow 2Fe_2O_3 + 4S^\circ \qquad (2.3)$$

If pyrite is also present in the concentrates, it will result in more sulphur oxidation to sulphuric acid, Equation (2.4). This will have a negative impact on the economics of the process as the excess acid incorporates neutralization costs (Jones *et al*., 2009; Defreyne *et al*., 2006).

$$4FeS_2 + 15O_2 + 8\mathrm{H_2O} \rightarrow 2Fe_2O_3 + 8\mathrm{H_2SO_4} \qquad (2.4)$$

In addition to sulphide minerals, a certain amount of elemental sulphur is also oxidized to sulphate which further increases the acid levels, for example in the CESL process about 5 – 10 % of the elemental sulphur was found to oxidize during the pressure oxidation step according to the reaction shown in Equation (2.5).

$$S^{\circ} + H_2O + 1.5O_2 \rightarrow H_2SO_4 \qquad (2.5)$$

The adoption of hydrometallurgical processes is favoured when they are located near a mine site and a source of process water and when acid can be used as a by product for heap bioleaching or leaching of oxide ores or for the conversion of an existing plant from the treatment of oxide ores to sulphide ores (McDonald and Muir, 2007a, 2007b). Advantages of the hydrometallurgical processes include: reduced consumption of neutralizing agent (as sulphur is rejected mostly in the form of elemental sulphur rather than sulphate), potentially lower capital costs, the possibility of treating complex ores and arguably easier waste control with attendant benefits to the environment (Cordoba *et al*., 2008).

2.2 CESL and Vale medium temperature hydrometallurgical processes

Cominco Engineering Services Limited (CESL – now a subsidiary of Teck Corporation) and Vale Ltd. have developed hydrometallurgical processes for the extraction of copper and nickel from base metal concentrates. CESL is a medium temperature and pressure (1280 kPa) process that occurs in a mixed sulphate-chloride environment at pH of about 1.5-2.5 with retention time of approximately 60 minutes and temperature of 150 °C. The temperature selection comes from the properties of sulphur. Sulphur exists in two stable crystalline forms i.e. monoclinic (stable up to 95.5 °C) and orthorhombic (stable above 95.5 °C). Monoclinic sulphur melts at 112.8 °C and orthorhombic at 119.3 °C. Between 119.3 and 159 °C sulphur is molten and highly fluid. Above 159 °C it becomes highly viscous (due to breakdown of its S_8 ring structure and formation of sulphenyl diradicals i.e. $\cdot S—S_6—S\cdot$ which attack other S_8 rings and initiate polymerization) (Hackl, 1995). Molten sulphur passivates the chalcopyrite surface and slows down the leaching kinetics. Lignosulfonate or other surfactants are used to avoid passivation/encapsulation of the chalcopyrite by the molten sulphur. Above 190 °C the viscosity of sulphur again decreases due to cleavage of S_8 rings. However, higher temperatures result in increased oxidation of sulphur to sulphuric acid which adversely affects the process economics due to neutralization costs. Figure 2.1 shows that sulphur oxidation increases with temperatures and at 190 °C only formation of sulphate ion occurs. The selection of 150 °C temperature therefore results in a compromise as it achieves reasonably high dissolution kinetics and results in limited sulphur oxidation.

Higher temperatures (above 220 °C, for example) result in faster leaching kinetics but complete sulphur conversion to sulphate.

Shorter retention times (~60 minutes) were selected for the CESL process as it was realized during the pilot plant operations that retention times over 60 minutes result in a minimal increase in the copper extraction, see Figure 2.2. Secondly, longer retention times resulted in more sulphur oxidation, see Figure 2.3.

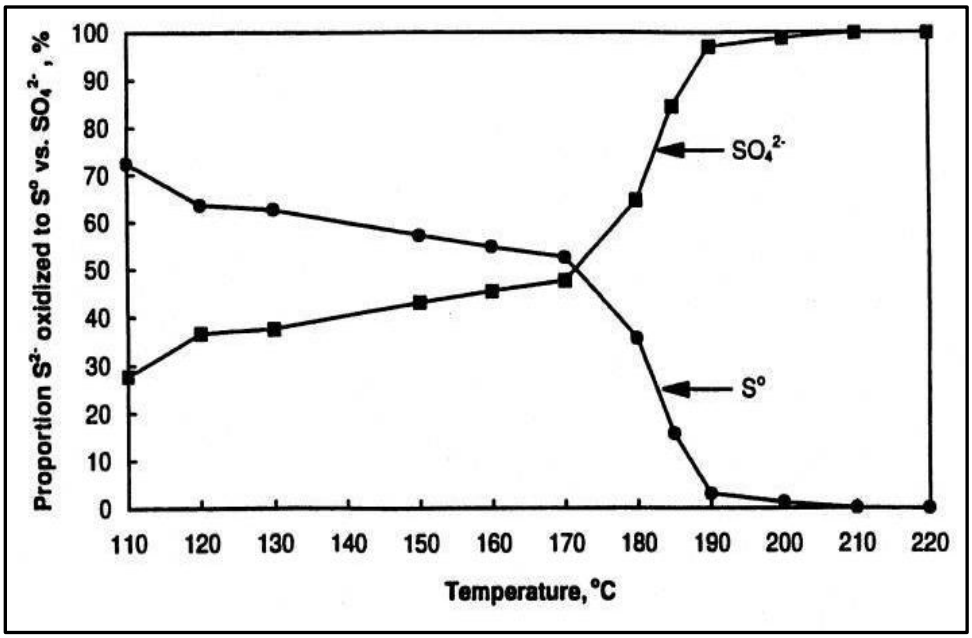

Figure 2.1 Effect of temperature on the relative proportion of sulphur oxidized to S° vs SO_4^{2-} during chalcopyrite leaching (with modification from Hackl, 1995).

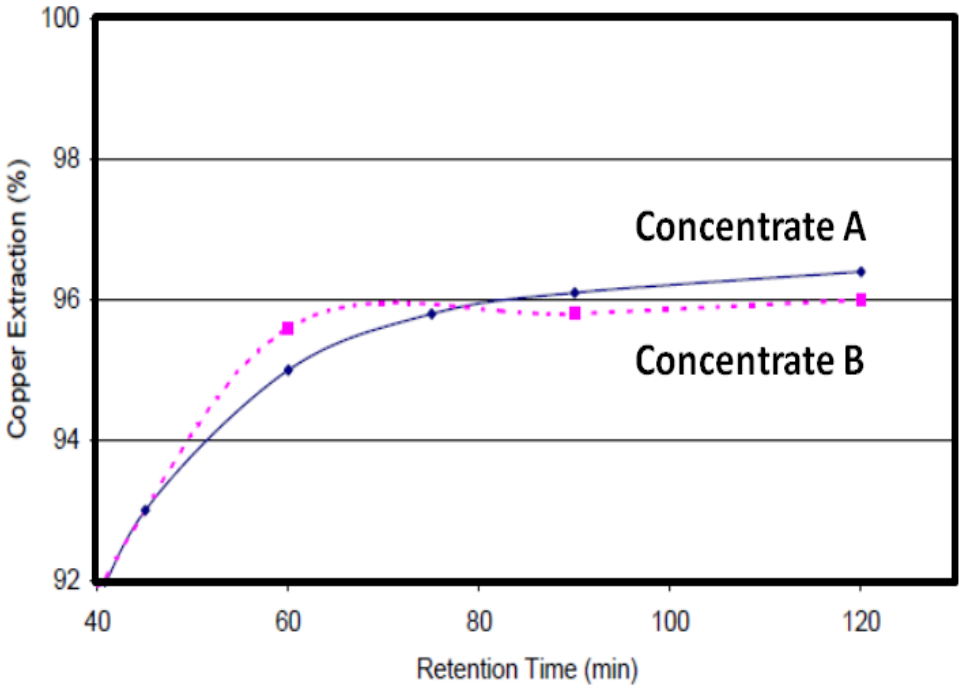

Figure 2.2 Copper extraction results at varying retention times (Barr *et al*., 2005).

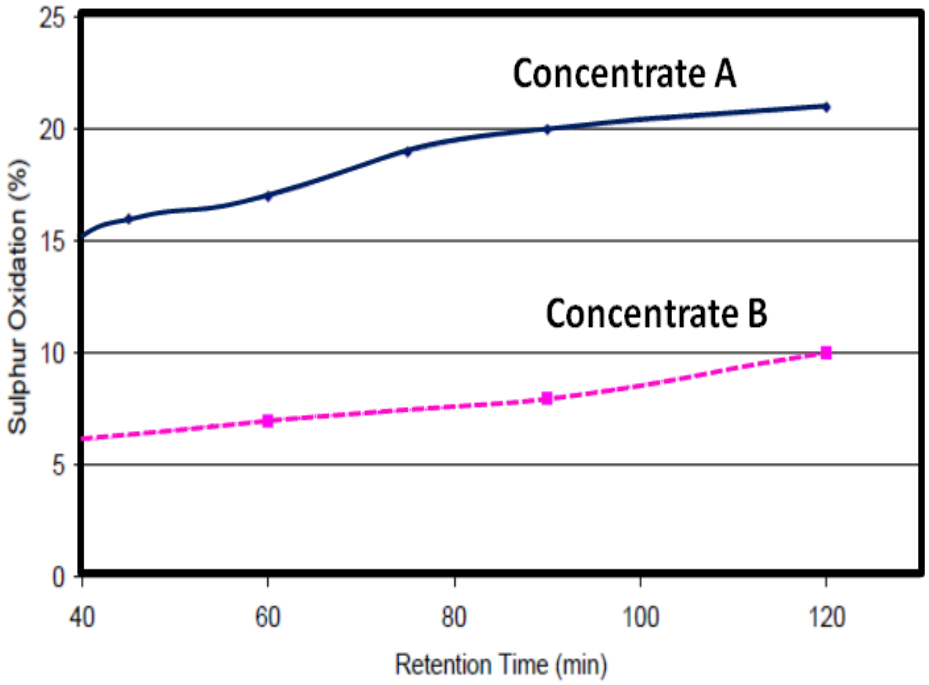

Figure 2.3 Effect of time on sulphur oxidation under autoclave conditions (Barr *et al*., 2005).

The CESL process also utilizes a moderate concentration of chloride (8-12 g/L). It is thought that during leaching of the sulphide minerals, a passive layer of molten sulphur is formed around the un-reacted mineral surface, which decelerates the leaching kinetics. The presence of chloride can break the passive layer or at least can make it porous so that the leaching solution can reach the mineral surface and enhance the leaching kinetics/process efficiency (Defreyne *et al*., 2006; Vignes, 2013). Furthermore, the chloride anion is known to complex with the cuprous ion, which activates the cupric/cuprous couple. The kinetics of mineral oxidation with this couple is thought to be increased (Hirato *et al*., 1987).

Figure 2.4 shows copper extraction results from the CESL test work for different chloride levels in the solution. Significant improvement in the copper extraction was observed when chloride levels in the solution were > 9 g/L (Defreyne and Cabral, 2009).

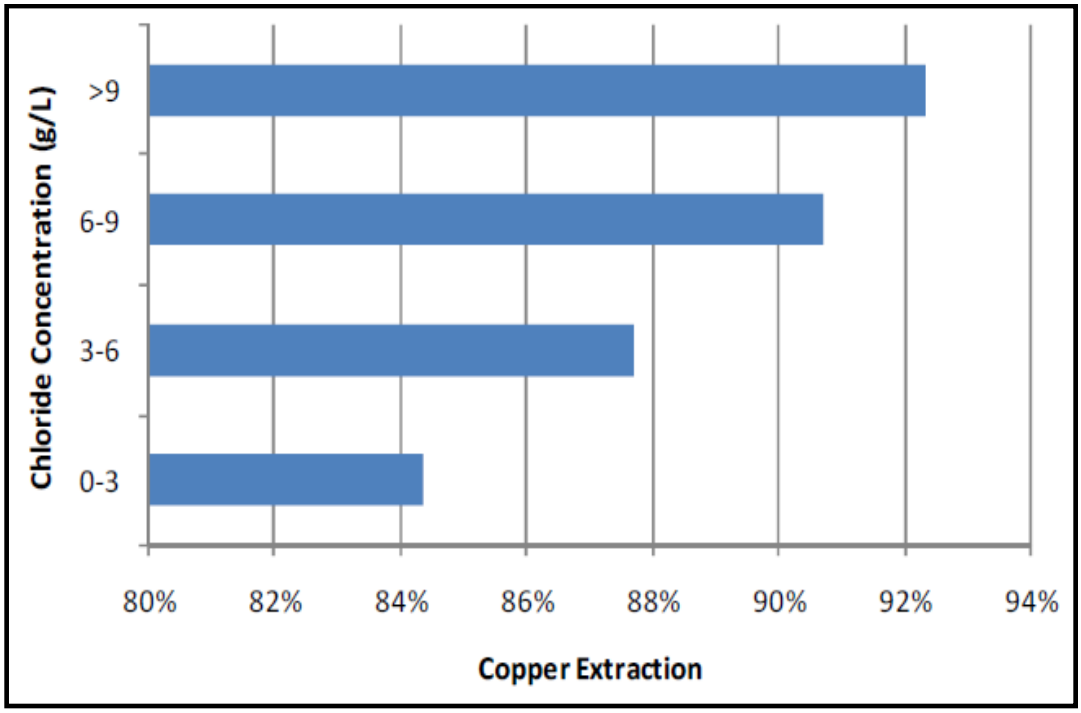

Figure 2.4 Copper extractions at various autoclave chloride levels (Defreyne and Cabral, 2009).

A schematic of the CESL copper process is shown in Figure 2.5. During pressure oxidation of the sulphide minerals, some of the copper is leached into the solution and a portion is converted to basic copper sulphate (antlerite) as shown in Equation (2.6). Basic copper sulphate is then leached in a second step under mild acidic conditions at ambient temperature and pressure, see Equation (2.7). Afterwards, copper is recovered by solvent extraction and electrowinning (Defreyne *et al*., 2006; Defreyne and Cabral, 2009; Mayhew *et al*., 2010).

$$12CuFeS_2 + 15O_2 + 4H_2SO_4 + 4H_2O \rightarrow 4CuSO_4.2Cu(OH)_2 + 2Fe_2O_3 + 24S^\circ \quad (2.6)$$

$$CuSO_4.2Cu(OH)_2 + 2H_2SO_4 \rightarrow 3CuSO_4 + 4H_2O \quad (2.7)$$

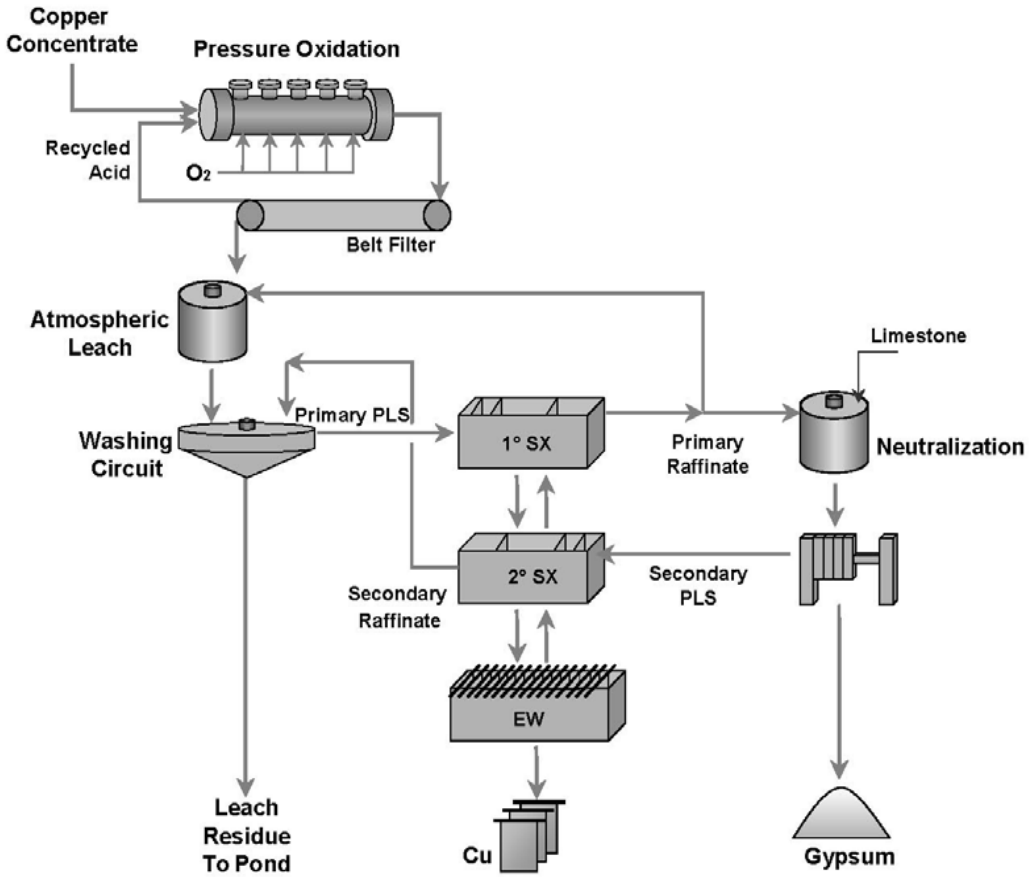

Figure 2.5 Schematic of CESL copper process (Defreyne *et al*., 2006).

CESL started developing its Process in 1992, with the aim of developing a hydrometallurgical process as an economic alternative to conventional smelting. The success of the bench scale tests encouraged the design of a pilot plant facility and by 1994 pilot plant was operational. The pilot plant had a capacity of producing 13 tonnes per annum (tpa) of copper cathode. In 1996; a demonstration plant with a capacity of 730 tpa copper cathodes was constructed. From 1997 to 2010 the demonstration plant was operated for copper concentrates of widely varying grades (Barr *et al*., 2005; Mayhew, *et al*., 2013). After extensive testing at bench, pilot, and demonstration scales further application of the process to Ni, and bulk Cu-Ni concentrates was explored. The success of the bench and pilot scale test work demonstrated that it can also be effectively applied to these concentrates (Jones, 1999; Jones *et al*., 2008).

Vale evaluated several hydrometallurgical processes and, as Inco, patented (Kerfoot *et al.*, 2002) a variant of the CESL process for its own ore bodies. Now, Vale is in the process of commissioning a large “medium temperature” leach facility in Newfoundland and Labrador, Canada. The CESL and Vale processes can efficiently process low grade concentrates with widely varying Fe:Cu and Fe:Ni ratios (Defreyne *et al*., 2006: Defreyne and Cabral, 2009). Typical copper and/or nickel recoveries from medium temperature leach processes are in the range of 96-99 % (Defreyne *et al*., 2006).

An example of two concentrates: A and B from CESL test work is given below. Due to confidentiality, the names of the concentrates are not revealed. Estimated mineralogical results of the concentrates A and B are compared in Table 2-1. It can be noticed that the

two concentrates have different pyrite content. The operating parameters that were used to leach the concentrates in the pressure oxidation step are given Table 2-2.

Table 2-1 Concentrate mineralogy (Barr *et al*., 2005).

Concentrate	Chalcopyrite $CuFeS_2$	Pyrite FeS_2	Bornite Cu_5FeS_4	Chalcocite Cu_2S	Covellite CuS	Magnetite Fe_3O_4	Silicates Si
A	70%	17%	-	-	0.5%	-	11%
B	73%	0.5%	4 %	0.5%	-	10%	12%

Table 2-2 Process operating parameters (Barr *et al*., 2005).

Operating parameters	Concentrate A	Concentrate B
Operating temperature	150 °C	150 °C
Autoclave solids density	16 % (by weight)	18 %
Autoclave retention time	75 min	60 min
Feed chloride tenor	12 g/L	12 g/L
Oxygen overpressure	1000 kPag	1000 kPag
Operating pressure	1380 kPag	1380 kPag

The leach test results are presented in Table 2-3. Overall copper recoveries remained 95.9% and 95.6% for concentrates A and B, respectively. To investigate low copper recoveries, samples from the each autoclave compartment were withdrawn to provide a leaching profile. Analysis of these samples indicated that more than 99 % of the copper, in the form of copper sulphide, was oxidized by the last compartment for each concentrate type. To further investigate lower copper recoveries, the effect of concentrate grind size was studied to determine if a finer size results in an improvement in the % copper extraction. As shown in Table 2-4, the concentrate grind size did not result in a measurable improvement in the copper extraction for concentrate A. Therefore, the concentrate grind size was not the reason for lower copper recoveries. The source of copper loss to the leach residue was not

clear until Sahu and Asselin (2011) characterized different leach residue samples from the CESL pilot and demonstration plants.

Table 2-3 Leaching metallurgical results (Barr *et al*., 2005).

Metallurgical results	Concentrate A	Concentrate B
Copper recovery	95.9 %	95.6 %
Copper in the residue	1.2 %	1.5 %
Concentrate to residue mass loss	16 %	16 %
O_2 ratio, net	0.34	0.21
Sulphur oxidation	20 %	7 %

Table 2-4 Effect of grind size on copper recovery for concentrate A at 75 min retention (Barr *et al*., 2005).

Grind size US mesh	**Copper in residue %**	**Copper extraction %**
5 % + 325	1.19	95.8
5 % + 400	1.20	95.8
5 % + 500	1.18	95.9

These authors demonstrated that copper associated with the iron precipitation product was the major source of copper loss to the residue. It was further noticed that more copper was lost when the iron deported to the leach residue was in the form of amorphous/poor crystalline phases such as ferrihydrite. A comparison of copper loss to ferrihydrite and crystalline phases from their study is provided in Figure 2.6. Figure 2.6 demonstrates that deportment of iron in the form of amorphous phases resulted in 2-4 times more copper loss to the leach residue. This indicates that in certain cases there is an opportunity to reduce the copper loss to the leach residue by controlling the chemistry of iron reported to the leach residue.

From the above discussion it is clear that the control, stabilization and disposal of iron are important aspects in terms of copper loss to the residue. Secondly, stringent environmental regulations and gradual depletion of high grade ores necessitates minimum loss of the valuable metal to the residue. The success of a hydrometallurgical process depends largely on the extent of copper recovery from the ores and economic and sound disposal of iron to the leach residue; for both existing operations and developing technologies. A comparison of the iron removal processes as practiced in the metallurgical industry over the past decades is given below.

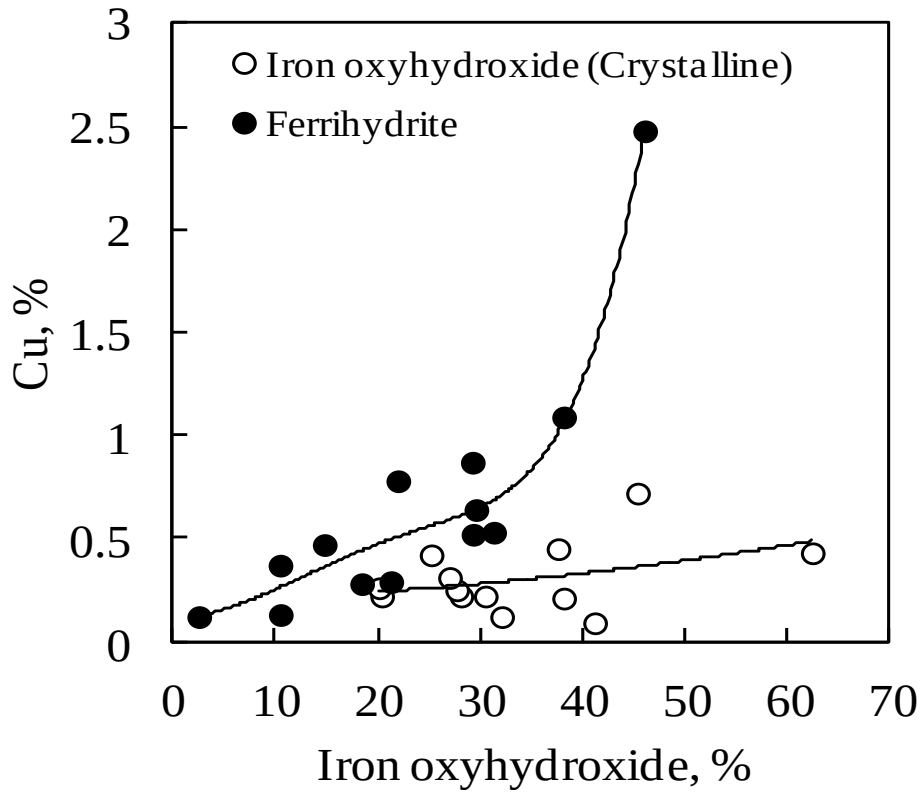

Figure 2.6 Copper association with ferrihydrite (an amorphous/poorly crystalline phase) and crystalline phases (Sahu and Asselin, 2011).

2.3 Iron removal processes

In general, during hydrometallurgical processing of ores, a significant amount of iron dissolves. Downstream processing requires this iron to be removed before the solutions are transferred to the electro winning circuits.

The qualitatively desirable features of iron precipitation product are:

- Good filtration and washing characteristics
- Low cost and compatibility with the remainder of the circuit
- Low incorporation of valuable metals
- Low surface area and adsorption capacity
- Good crystallinity and purity
- Good environmental stability
- Potential marketability for other industries

A simple way to remove iron from the process solutions is to increase the pH as shown in Figure 2.7. Figure 2.7 shows that an increase in the pH results in a decrease in solution ferric concentration i.e. iron is precipitated out of solution. However, the precipitation of iron is not as simple as it may seem. Under atmospheric pressure conditions, pH increase or simple neutralization of the ferric ion rich solutions yields iron precipitates which are difficult to filter and thicken and the precipitates often occlude significant amounts of the processing solution, resulting in the loss of the sought after

metal. Early stage attempts to remove iron from the leach liquors resulted in poorly crystalline and gelatinous precipitates which were difficult to filter (Tainton and Leyson, 1924).

Over the time three iron removal processes were developed to remove iron in a more efficient way from the industrial solutions. These include: the jarosite process, the goethite process and the hematite process (Dutrizac, 1987). These processes have been used for many years for iron control in the zinc industry and in recent years they have been applied for the hydrometallurgical circuits such as those recovering copper and nickel. The consequences of atmospheric condition precipitation can be minimized if iron precipitation is considered during pressure oxidation step.

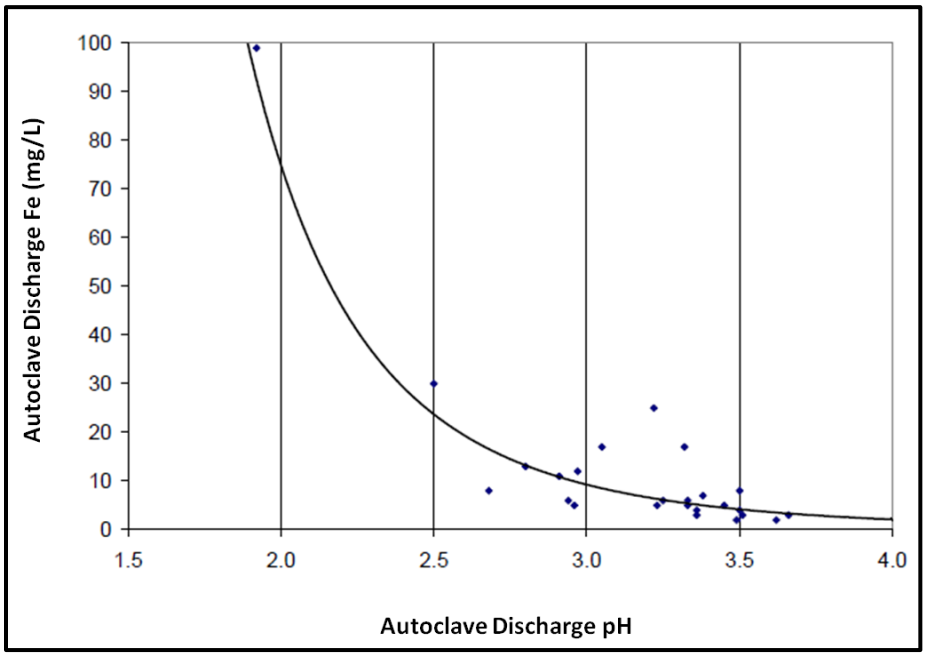

Figure 2.7 Relationship between pH and iron concentration in the autoclave discharge solution (Defreyne *et al.*, 2006).

Iron removal options have been the subject of many publications (Dutrizac, 1980, 1984, 1987, 2009, 2011; Lahtinen and Svens, 2006; Beaulieu *et al*., 2006; Cheng and Demopoulos, 2006). Moreover, four international symposia (1986, 1996, 2006 and 2016) on iron control in hydrometallurgy have been held that reviewed many iron control/precipitation problems and current trends in the industry. A brief overview of iron removal processes is given below.

2.3.1 Jarosite process

The jarosite process was developed in the early 1960s for the precipitation of iron from zinc processing solutions. During leaching of zinc sulphide concentrates high concentrations of iron (15 – 20 g/L Fe(III)) pass into the solution, which must be eliminated before recovery of the valuable metal from the solution. In the jarosite process iron can be readily precipitated as filterable jarosite type compounds $\{MFe_3(SO_4)_2(OH)_6\}$ where M = K^+, Na^+, NH_4^+ etc; Equation (2.8). Temperature is maintained at~95-100 °C, a source of alkali is added and the pH is regulated to 1.1 – 1.5. Addition of jarosite seed can reduce the retention time to a few hours. Jarosite precipitates in a crystalline form and entrains only minor amounts of zinc rich solutions, leaving a final solution containing only 1 – 3 g/L Fe(III).

$$Na_2SO_4 + 3Fe_2(SO_4)_3 + 12H_2O \rightarrow 2NaFe_3(SO_4)_2(OH)_6 + 6H_2SO_4 \qquad (2.8)$$

The jarosite process got wide attention in the zinc industry after its invention as it readily precipitated iron from concentrated acidic solutions and the product was easy to

filter compared to the gelatinous ferric hydroxide. However, jarosite is less inert to environmental degradation, as it slowly converts to more stable iron oxides and hydroxides and releases acid that can contaminate tailings pond effluents and water life. Low iron content, high residue volume, and the ability to incorporate divalent cations such as Pb, Ag, and Cu. in its structure limit the use of this technology.

2.3.2 Goethite process

The goethite process was also developed in the 1960s by the Vieille-Montagne (V-M) company. Goethite precipitation requires low initial iron concentration (< 2 g/L Fe (III)). As most of the processing solutions contain higher iron concentrations (5 – 20 g/L Fe (III)), therefore to take advantage of the goethite process ferric iron concentration should be reduced to the desired levels. V-M devised a technique to precipitate iron as goethite in their zinc process. In this technique ferric iron is reduced to ferrous by the addition of concentrate, Equation (2.9), and in a second step iron is re-oxidized to precipitate as goethite at temperature ~80 – 90 °C and pH of 2 – 3.5 (Dutrizac, 1987).

$$Fe_2(SO_4)_3 + ZnS \rightarrow ZnSO_4 + 2FeSO_4 + S^{\circ} \quad (2.9)$$

The reactions (oxidation, hydrolysis, neutralization of excess acid with calcine) involved in the goethite precipitation are given below:

$$2FeSO_4 + 1/2O_2 + H_2SO_4 \rightarrow Fe_2(SO_4)_3 + H_2O \quad (2.10)$$

$$Fe_2(SO_4)_3 + 4H_2O \rightarrow 2FeOOH + 3H_2SO_4 \quad (2.11)$$

$$H_2SO_4 + ZnO\ (calcine) \rightarrow ZnSO_4 + H_2O \quad (2.12)$$

In another process developed by Electrolytic Zinc of Australia, the concentrated ferric solution is rapidly diluted, instead of reducing to ferrous state, along with addition of neutralizing agent in a heated precipitation tank so that the ferric concentration remains low to favour goethite precipitation. This process is also called "paragoethite process". Goethite residues have higher iron content compared to jarosite, lower volume and they are relatively more environmentally stable than jarosite residues (Allan *et al*., 1973; Dutrizac, 1987).

2.3.3 Hematite process

The hematite process used at the Akita Zinc company of Japan is the oldest and best known hematite process operated since 1973. In the Akita hematite process Fe (III) is reduced to Fe (II) with SO_2 or H_2S at 95 – 100 °C. The reduction reaction is described in Equation (2.13) (Cheng and Demopoulos, 2006).

$$2Fe^{3+} + SO_2 + 2H_2O \rightarrow 2Fe^{2+} + {SO_4}^{2-} + 4H^+ \quad (2.13)$$

Ferrous iron allows raising pH without iron precipitation and eases solution purification (removal of other impurities). Afterwards, iron is precipitated as hematite at 180 – 200 °C and 18 atmosphere oxygen pressure for 3 hours of retention, Equations (2.14) and (2.15).

$$2FeSO_4 + 1/2O_2 + H_2SO_4 \rightarrow Fe_2(SO_4)_3 + H_2O \quad (2.14)$$

$$Fe_2(SO_4)_3 + 3H_2O \rightarrow Fe_2O_3 + 3H_2SO_4 \quad (2.15)$$

Several advantages of the hematite process include: high iron content of the residue, low volume, good filtration and washing properties, good environmental stability, low adsorption capacity and potential marketability to the steel, cement and ceramics industry. However, this technology encounters higher capital costs.

A schematic of the three iron control processes is shown in Figure 2.8. The major features of the three iron removal processes are summarized in Table 2-5. Figure 2.9 compares the % zinc extraction with each method. Figure 2.9 shows that hematite precipitation process results in maximum metal extraction.

Because of the several advantages of the hematite process there is growing interest for the adoption of this technology. Recently several patents have been filed for the precipitation of hematite under atmospheric (Lahtinen *et al*., 2007; Aguilar, *et al*., 2013) and elevated temperature (Rodriguez and Wedderburn, 2007) conditions. However, the commercial success of these processes is not well documented.

CESL and Vale hydrometallurgical processes aim to remove iron from pressure oxidation step in the form of hematite. However, ideal hematite is not always produced in their processes. Instead iron is precipitated as a mixture of hematite, jarosite, goethite and/or other iron oxides/oxyhydroxides with varying crystallinity, such as ferrihydrite (Jambor and Dutrizac, 1998; Claassen *et al*., 2002; Loan *et al*., 2002, 2006) and schwertmannite (Bigham *et al*., 1996). The aim of the current work is to maximize the

proportion of hematite and minimize the valuable metal loss to the iron precipitation product within the window of CESL and Vale medium temperature operating conditions.

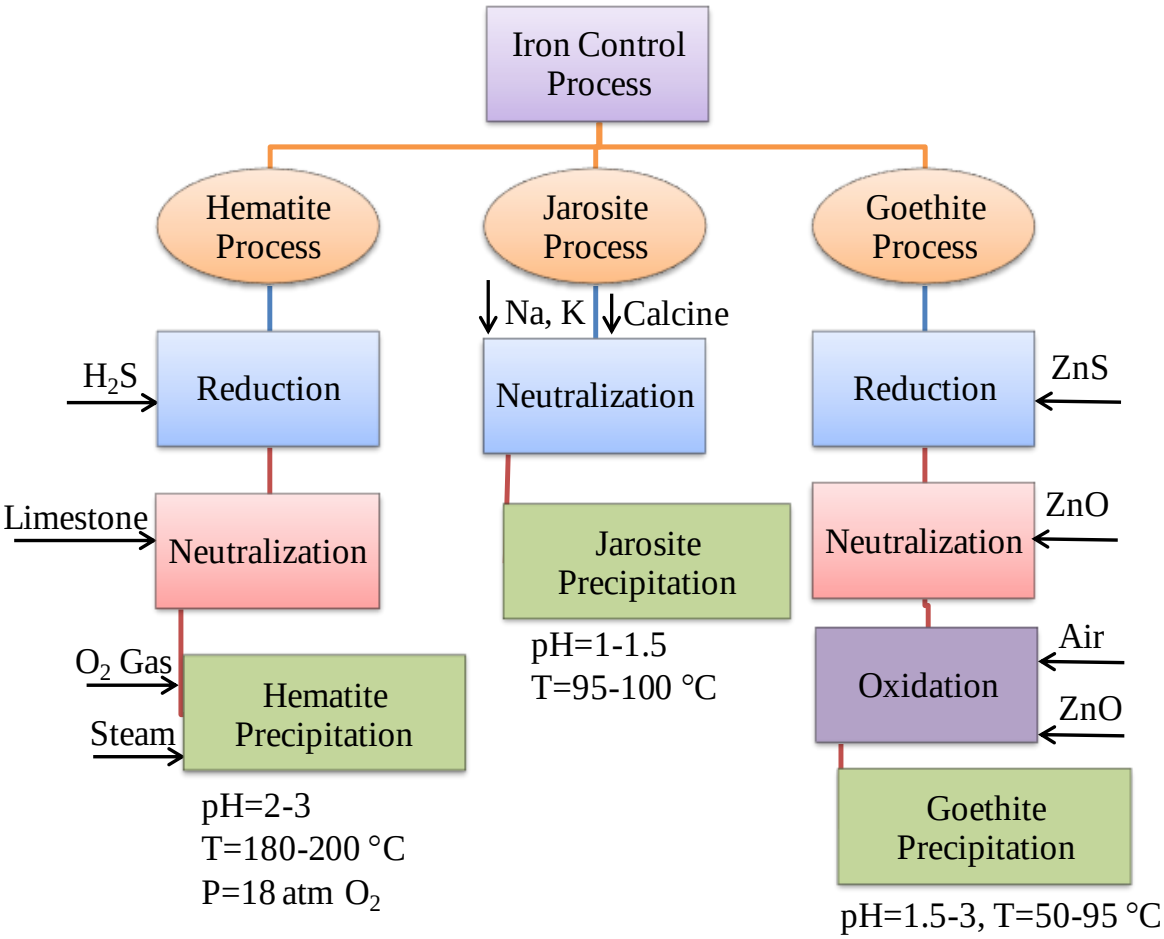

Figure 2.8 Schematic of various iron removal processes used in zinc industry (Beaulieu *et al.*, 2006; Dutrizac, 1987).

Table 2-5 Comparison of the major features of the three main iron precipitation methods (Lahtinen and Svens, 2006; Onozaki *et al*., 1986; Dutrizac, 1980; Pelino *et al*., 1996).

Process	Hematite	Goethite	Jarosite
Formula	α-Fe_2O_3	α-FeOOH	$MFe_3(SO_4)_2(OH)_6$ M=Na, K, NH_4
Yield %			
Cu	98.2	90	90
Zn	98.2	96	96
Residue composition %			
Fe theoretical	69.9	62.9	30-35
Fe actual	50-60	40-45	25-30
Zn	0.5-1	5-10	4-6
S	2-3	2.5-5	10-12
Zn loss t/t	0.002	0.025	0.025
Moisture content %	10	50	50

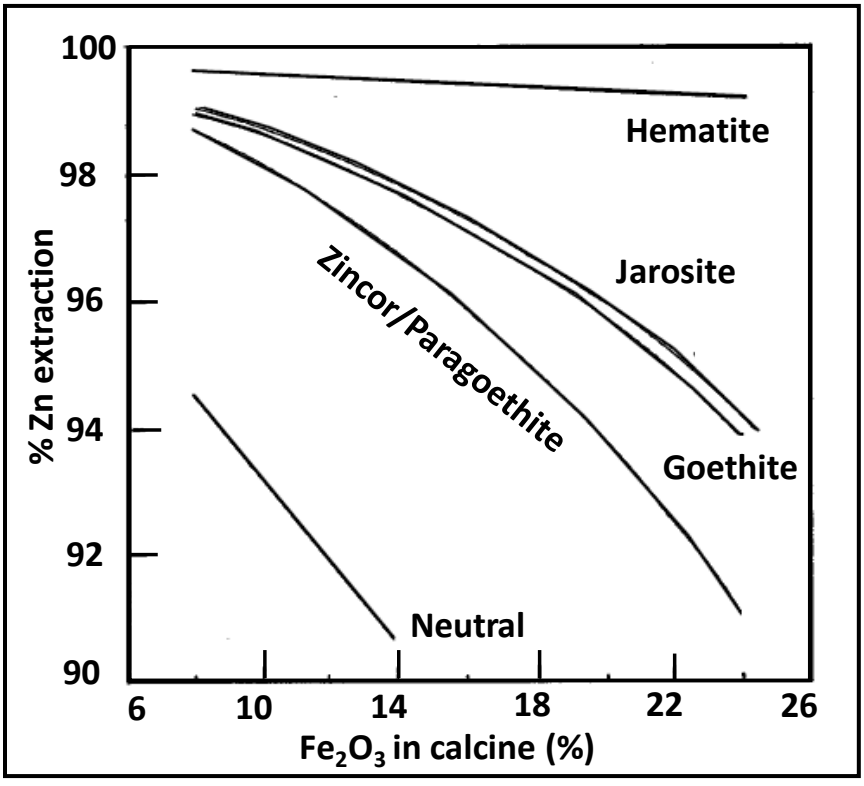

Figure 2.9 The effect of iron content of the calcine or Zn-Ferrite (expressed as Fe_2O_3) on zinc extraction for different iron removal processes (Van Niekerk and Begley, 1991).

2.4 Environmental aspects and residue disposal

Large amounts of iron precipitates are being generated by hydrometallurgical processes. These may contain various impurities such as: Pb, As, Cd, SO_4^{2-} etc. The presence of these impurities requires that the residue must be disposed-off in sealed ponds. These ponds occupy a large area of land and can be a source of airborne dust. Environmental legislation being implemented today is increasingly stringent and the use of well managed and nearby disposal sites are considered to be good options for storage. Polymer linings, in combination with soil and clay layers, are used in the pond structure to minimize the possibility of contamination of the soil and surrounding environment (Lahtinen and Svens, 2006).

Several residues produced throughout the history have been characterized as toxic by environmental legislators. For example, jarosite produced by Canadian Electrolytic Zinc (CEZinc) in Valleyfield, Canada was characterized as toxic waste by the Quebec ministry of environment. Similarly the goethite residue from the Vieille-Montagne process was also found to be leachable by the toxicity characteristics leach procedure (TCLP) (Rosato and Agnew, 1996). Stringent environmental regulation and storage problems as discussed above have compelled the hydrometallurgical industry either to fix the residue stability or to produce “waste free” and stable residues.

In the past, several efforts have been made to improve the stability of the residues. For example, David and Mathe (1983) decomposed jarosite by 1 hour roasting at 1000 °C

and subsequently leached the alkali sulphate with water to leave a pigment grade Fe_2O_3, Equations (2.16) and (2.17).

$$KFe_3(SO_4)_2(OH)_6 \rightarrow KFe(SO_4)_2 + Fe_2O_3 + 3H_2O \quad (2.16)$$

$$2KFe(SO_4)_2 + 3H_2O \rightarrow K_2SO_4 + Fe_2O_3 + 3H_2SO_4 \quad (2.17)$$

Technologies developed at Shell Ltd. have also used roasting to convert jarosite to hematite but the product still contained As, Pb and SO_4^{2-}. Martin and Feltz (1984) used low temperature (560 °C) roasting to produce hematite, but a large quantity of the ferric sulphate was produced and the hematite produced was also impure. In other attempts, reductive smelting of the jaroste using DC electric arc furnaces to produce stable iron rich slag (Hanusch, 1984), and in situ aqueous decomposition of the jarosite or goethite residues have also been considered. Outokumpu "half – conversion process" is an example of in situ decomposition. In this process jarosite is mechanically mixed with a ferrite containing residue, the mixture in then heated in an autoclave to 220 – 250 °C where the jarosite is converted to hematite and the liberated acid leaches ferrite, Equation (2.18)

$$3ZnO.Fe_2O_3 + 2NaFe_3(SO_4)_2(OH)_6 \rightarrow 3ZnSO_4 + Na_2SO_4 + 6Fe_2O_3 + 6H_2O \quad (2.18)$$

Hematite produced in this process contained Pb and sulphate which limited its potential use. CESL and Vale's interest also lies in the production of a stable iron residue with minimum impurity levels.

2.5 Precipitation of metastable phases

The composition and the physical nature of the iron precipitation product depend upon kinetic and equilibrium relationship of the precipitation reaction. Temperature and pH are the two most important parameters which define the nature of the precipitates. Babacan (1971) studied the nature of different iron phases formed during the hydrolysis of 0.5 M ferric sulphate solution. Figure 2.10 represents the relationship between, pH, temperature and the main equilibrium phases as determined by Babacan (1971).

Figure 2.10 shows that iron concentration in the solution is directly related to pH i.e. at lower pH values the equilibrium solubility of Fe (III) is higher and it decreases with an increase in solution pH. Therefore, at higher pH values excess iron will rapidly precipitate. This rapid precipitation at higher pH values can provide favourable conditions for the nucleation of metastable or poorly crystalline phases such as ferrihydrite or schwertmannite.

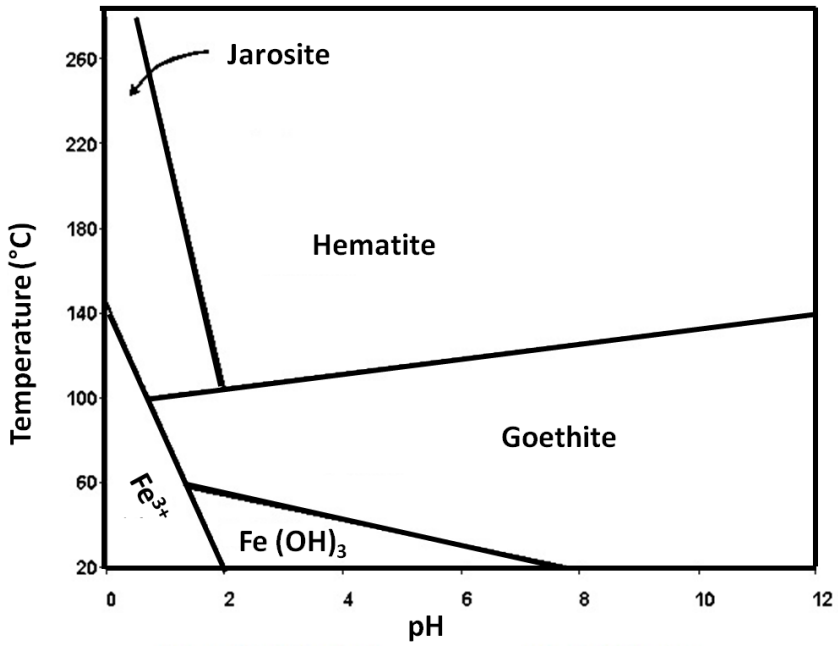

Figure 2.10 Stability regions of various compounds in the Fe-S-O system (Babacan, 1971).

Figure 2.10 does not show ferrihydrite or schwertmannite regions as these are metastable phases that transform to more stable phases upon ageing. Ferrihydrite is considered to be the first product of Fe (III) hydrolysis (Murad and Schwertmann, 1980) and it is believed to be a precursor for stable iron oxide phases. Ferrihydrite is unstable and transforms to more stable goethite and/or hematite. If the transformation process does not go to completion, a substantial amount of poorly crystalline or X-ray amorphous phase (refer to section 4.2 for details) will exist in the residue (Claassen *et al*., 2002; Loan *et al.*, 2005).

The name ferrihydrite commonly refers to a range of poorly crystalline iron oxide/hydroxide phases of which 2-line (exhibiting 2 broad XRD peaks) ferrihydrite and 6-line (exhibiting 6 broad XRD peaks) ferrihydrite are most common. It has been represented

with the general formula $5Fe_2O_3 \cdot 9H_2O$ (Murad and Schwertmann, 1980). However, considerable debate as to its formula remains and no single formula has yet been agreed upon. A number of other formulae have been suggested e.g. $Fe_5HO_8 \cdot 4H_2O$ (Towe and Bradley, 1967), $2FeOOH \cdot 2.6H_2O$ (Russel, 1979). Jambor and Dutrizac (1998) and Janney *et al*. (2000a, 2000b, 2001) identified that ferrihydrite is not strictly amorphous but has poor long-range order and very small crystallite size (2 – 6 nm). Ferrihydrite has high sorbent capacity due to very high (200-300 m^2/g) BET (Brunauer-Emmett-Teller) surface area (Cornell and Schwertmann, 2003). It has a higher tendency to adsorb divalent cations such as copper and nickel and therefore increases the loss of these metals to the residue (Cornell and Giovonali, 1988). In concentrated ferric sulphate solutions, in the pH range 2 – 4, a similarly structured schwertmannite is a more common phase than ferrihydrite (Bigham *et al*., 1994). Schwertmannite is represented by the ideal formula $Fe_8O_8(OH)_6SO_4$ and is a complex hydroxy ferric sulphate with poorly crystalline nature. Claassen *et al*. (2006) suggested that schwertmannite is nothing but ferrihydrite with high sulphate values. However, Loan *et al*. (2002a) stated that schwertmannite can be distinguished from ferrihydrite at least qualitatively on the basis of its hedgehog morphology. Ferrihydrite and schwertmannite have been widely discussed in iron control literature. Jambor and Dutrizac (1998) have provided an excellent review of ferrihydrite while Bigham *et al*. (1992, 1994 and 1996) have described schwertmannite in detail.

Ferrihydrite has been positively identified in a number of hydrometallurgical systems. For example, Loan *et al*. (2006) identified that paragoethite process residue, in zinc

hydrometallurgy, consists of approximately 40 – 50 % 6-line ferrihydrite with the remaining fraction being a mixture of poorly crystalline goethite and other iron oxides and oxyhydroxides. Claassen *et al*. (2002) studied residues produced in zinc rich processing solutions and found that approximately 50 % of the iron was associated with ferrihydrite, schwertmannite and a third unknown phase. Steel *et al*. (2010) characterized leach residues from the Vale demonstration plant and found that approximately 10 % of the nickel was associated with phases leached by hydroxylamine hydrochloride (HaHC). Hydroxylamine hydrochloride is considered a reagent that selectively dissolves amorphous iron oxides/oxyhydroxides including ferrihydrite (Chao and Zhou, 1983; Tessier *et al*., 1979). Sahu and Asselin (2011) characterized 13 different leach residue samples generated under CESL conditions and identified the presence of amorphous iron oxide/oxyhydroxide phases in the residues. These authors demonstrated that the amorphous component was responsible for ~5 times more copper loss to the residue as compared to the crystalline counterparts. Ferrihydrite was only positively identified in one of the samples, which was later confirmed to have the largest amount of amorphous phase. Characterization of 3 residue samples, in this study, from CESL and Vale processes also confirmed the presence of poorly crystalline iron oxide phases and higher associated metal loss. Dyer *et al*. (2012) also identified ferrihydrite in their study of the Caron leach residue. Before the identification of ferrihydrite in the Caron leach process, the cobalt losses were attributed to co-precipitation of ferric hydroxide or passivation of the iron based alloys that report to the leaching step. The fact that the existence of ferrihydrite or poorly crystalline iron oxide phases results in

higher metal loss to the residue indicates that the formation of these phases should be avoided.

2.6 Transformation of metastable phases

In the hydrometallurgical processes where retention time is short, a higher proportion of ferrihydrite may exist as the transformation kinetics is slow. Das *et al*. (2011) confirmed that only 50 % of ferrihydrite was transformed to hematite and/or goethite after 9 hours at 100 °C and a pH of 2.0. Zic *et al*. (2011) also observed slow transformation of ferrihydrite at 160 °C. Transformation of ferrihydrite to crystalline products proceeds via two competing mechanisms. Hematite nucleates and grows within the solid precursor (ferrihydrite) by an internal dehydration and rearrangement process. The formation of goethite involves dissolution of iron from ferrihydrite followed by re-precipitation of the crystalline oxide in solution (Cornell and Schwertmann, 2003). Which mechanism predominates depends upon a number of factors such as pH, temperature and solution chemistry.

From the above discussion it is clear that the formation of ferrihydrite in the medium temperature processes is quite probable. Precipitation of ferrihydrite leaves a high amount of X-ray amorphous phase in the residue, making the residue difficult to characterize. It also causes higher valuable metal loss to the residue and decreases the percentage of iron precipitated as a stable phase. Therefore, it is important to optimize any

process parameters that can lead to higher proportions of a stable phase and lower amounts of ferrihydrite/amorphous phase in the residue.

Leaching of concentrates in a real hydrometallurgical process results in complex solution chemistry and it is difficult to pinpoint the factors leading to a particular phase in the residue. Therefore, several authors carried out experiments using simulated solutions to predict the effect of a particular parameter on the composition of residue phases. Among these studies, the most pertinent work done recently is by Dutrizac and Chen (2009, 2010 and 2011). These authors studied factors affecting hematite precipitation from nickel-sulphate-chloride and pure acidic ferric sulphate solutions by varying the solution conditions over a broad range. It was concluded that increasing retention time to 5 – 6 hours increased the proportion of hematite in the precipitates. Precipitates made at temperatures greater than 170 °C exhibited better crystallinity than those at 130 °C. Addition of hematite seed suppressed jarosite precipitation and promoted hematite precipitation. Mineralogical studies of the precipitates in their study indicated the presence of 3 – 4 % SO_4^{2-} which was thought to be adsorbed onto the individual hematite crystallites. However, the factors responsible for associated metal loss with a specific precipitation product were not widely discussed.

Umetsu *et al*. (1977) studied the hydrolysis of ferric sulphate solutions at elevated temperatures (185 and 200 °C) for long retention times (up to 30 hours). These authors found that the rate of hydrolysis decreases with an increase in the initial concentration of

iron. It was suggested that the hydrolysis of ferric sulphate takes place in one of three ways, depending upon the acidity of the solution.

1. at low acidity

$$Fe_2(SO_4)_3 + 3H_2O \rightarrow Fe_2O_3 + 3H_2SO_4 \quad (2.19)$$

2. at moderate acidity

$$3Fe_2(SO_4)_3 + 14H_2O \rightarrow 2(H_3O)Fe_3(OH)_6(SO_4)_2 + 5H_2SO_4 \quad (2.20)$$

$$2(H_3O)Fe_3(OH)_6(SO_4)_2 + 3H_2SO_4 \rightarrow 4Fe(OH)SO_4 + Fe_2(SO_4)_3 + 10H_2O \quad (2.21)$$

$$2Fe(OH)SO_4 + H_2O \rightarrow Fe_2O_3 + 2H_2SO_4 \quad (2.22)$$

3. at high acidity

$$Fe_2(SO_4)_3 + 2H_2O \rightarrow Fe(OH)SO_4 + H_2SO_4 \quad (2.23)$$

The equilibrium hydrolysis of ferric sulphate solutions was studied by Sasaki *et al*. (1993) in the temperature range 150 to 220 °C. These authors also observed that lower acid concentrations favour hematite while at higher acid concentration basic ferric sulphate $Fe(OH)SO_4$ becomes the dominant phase. This is also consistent with the earlier work by Posnjak and Merwin (1922). Sasaki *et al*. (1993) also determined the stability region of hematite in terms of sulphur content of the precipitates and free sulphuric acid concentration of the solutions in the temperature range 150 to 220 °C. The results of their study are shown in Figure 2.11. Figure 2.11 shows that at lower acid concentrations hematite is precipitated, however, beyond a certain acid concentration, sulphur content of

the product increases rapidly and hydronium jarosite becomes the major product of precipitation.

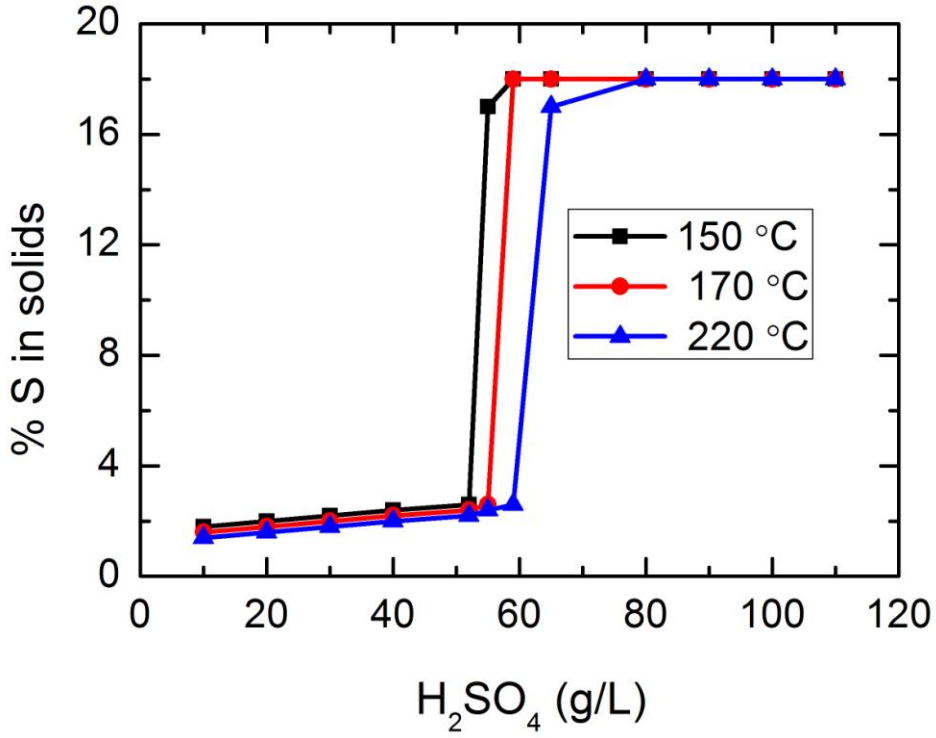

Figure 2.11 The stability region of hematite as a function of free acid concentration from 150 to 220 °C (with modification from Sasaki *et al*., 1993)

Sasaki *et al*. (1993) determined the minimum acid concentration above which sulphur content of the product increased and jarosite precipitation predominated. The minimum free acid concentration was determined to be up to 53.4, 54.8 and ~60-67.5 g/L free H_2SO_4 for temperatures 150, 170 and 220 °C, respectively. Above these acid concentrations the sulphur content of the precipitates increased abruptly and hydronium jarosite/basic ferric sulphate became the dominant phase. The relationship between equilibrium ferric and H_2SO_4 concentration is shown in Figure 2.12. Figure 2.12 shows that an increase in temperature results in a decrease in the equilibrium ferric levels at a given

H_2SO_4 concentration i.e. as the temperature increases to higher values more and more iron is precipitated.

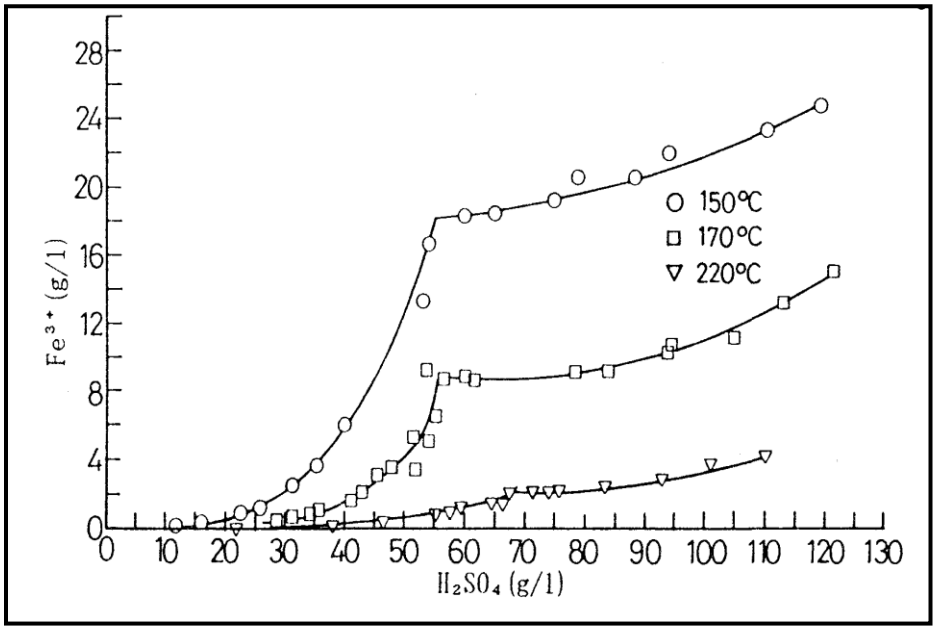

Figure 2.12 Relationship between equilibrium ferric and H_2SO_4 concentration at different temperatures (Sasaki *et al*., 1993).

Umetsu *et al*. (1977) and Tozawa and Sasaki (1986) observed that the ferric oxide stability region is extended by the addition of other soluble sulphate salts e.g. $ZnSO_4$, $MgSO_4$ and $CuSO_4$. For example, when 70 g/L Zn^{2+} in the form of zinc sulphate was added to the ferric solution at 185 °C, precipitation of ferric oxide was favoured instead of $Fe(OH)SO_4$ until a free sulphuric acid concentration of 83 g/L, as compared to 56 g/L H_2SO_4 in the absence of zinc sulphate. This stability was further extended to 92 g/L at 100 g/L Zn^{2+}.

Dutrizac and Chen (1993) studied the effect of initial iron concentration on the precipitation of hematite by conducting experiments at 225 °C for 4 hours. Hematite was precipitated when the initial ferric concentration was < 0.3 M Fe (III) (16.8 g/L Fe (III)). At

higher iron concentrations typically > 0.4 M Fe(III) (22.4 g/L Fe(III)) basic iron sulphate $Fe(OH)SO_4$ was the principal phase. For initial Ferric concentration of 0.4 M, about 60 % of iron was precipitated in 4 hours in their study. The stoichiometry of the basic ferric sulphate precipitation reaction, Equation (2.23), suggests the final free acid concentration to be ~11.8 g/L (0.12 M) which is within the stability region of hematite as determined by Umetsu *et al*. (1993). At lower acid concentrations one should expect the precipitation of hematite to occur. The precipitation of basic ferric sulphate instead of hematite was thought to be a manifestation of Stranski's rule or Ostwald's step rule as described by Demopoulos (2009). According to which, in a system dominated by homogeneous nucleation, the least stable phase forms first, which upon ageing transforms to a more stable phase. Hydronium jarosite and basic ferric sulphates are metastable relative to hematite and transform to hematite at higher temperature and/or longer time, as shown in Equation (2.24). Therefore, the kinetic stability in spite of thermodynamic instability, of these phases at higher ferric concentration is quite probable (Cheng and Demopoulos, 2004).

$$Hydronium\ jarosite \xrightarrow{>150\ ^{\circ}C} Basic\ ferric\ sulphate \xrightarrow{>200\ ^{\circ}C} Hematite \qquad (2.24)$$

Voigt and Gobler (1986) studied the hydrolysis of ferric sulphate solutions in the temperature range 100 – 300 °C, with an initial ferric concentration of 1.0 M Fe (III) (56 g/L) and zero initial free acid. The precipitation product in their study was hydronium jarosite up to 200 °C, above which basic ferric sulphate was precipitated. The maximum amount of hematite formed in their experiments was 35 wt. % at 250 °C after 24 hour retention. At

150 °C only 3 % of initially present iron was precipitated and the precipitation product was 100 % hydronium jarosite. When these authors increased the retention time from 6 to 100 hours, the % iron precipitation increased from 3 to 9 % only and the product was still hydronium jarosite. Stoichiometric calculations for the final free acid concentration (Equation (2.20) i.e. 1.46 g/L acid per gram of Fe (III) precipitation) show the final free acid to be 7.4 g/L (0.08 M). This again shows the formation of hydronium jarosite within the stability region of hematite at higher ferric levels. Levy and Quemeneur (1964) studied the hydrolysis of ferric sulphate in the temperature range 25 to 200 °C and obtained equilibrium after 5 days at 200 °C. These authors found an increase in hematite at the expense of $Fe(OH)SO_4$ in their experiments for longer retention times. This observation suggests the precipitation of $Fe(OH)SO_4$ in the first step, which in a second step converts to hematite. Umetsu *et al*. (1977) also studied the effect of initial ferric concentration on iron precipitation in the temperature range 185 to 200 °C for retention times up to 30 hours. These authors found that after precipitation started there occurred a retardation period before the precipitation started again and finally achieved the equilibrium. The retardation period extended to more than 14 hours at 180 °C with an initial ferric concentration of 25 g/L. However, the retardation period was not observed when the initial ferric concentration of the solution was less than 7.5 g/L. The presence of a retardation period for higher ferric concentrations also suggests the formation of metastable phases, i.e. $Fe(OH)SO_4$, at first which go through a dissolution-recrystallization mechanism and finally convert to hematite.

2.7 Iron oxides/oxyhydroxides formation mechanism

Addition of base to the ferric solutions results in the formation of monomeric and dinuclear species such as: $Fe(OH)^{2+}$, $Fe(OH)_2^{+}$ and $Fe_2(OH)_4^{2+}$. Other higher order polynuclear species may also exist (Cornell *et al*. 1989). Higher temperatures accelerate the hydrolysis process and the existence of poly nuclear species becomes more favourable (Matijevic *et al*., 1975). Monomers and dimers combine to form larger polymers by formation of Fe-OH-Fe (olation) and Fe-O-Fe (oxolation) bridges. The mechanism of formation of polycations as described by Cornell *et al*. (1989), Misawa *et al*. (1974) and Dutrizac (1980, 1987) is summarized in Figure 2.13. The monomers exist as octahedral complexes $[Fe(OH_2)_6]^{3+}$ with the deprotonated species having the formulae: $[Fe(OH_2)_5(OH)]^{2+}$ and $[Fe(OH_2)_4(OH)_2]^{+}$ etc. The first step in polycation formation, referred to as olation, involves the development of a dimer bound by double $-OH$. When the polymers grow to large spheres, oxolation (replacing of OH bridging with O bridging) takes place (Figure 2.13). The polycations formed by oxobridging are comparatively more stable than the ol-bridging. The aging process of the polycations is very slow at room temperature and takes years to complete at neutral to acidic pH (Schwertmann and Murad, 1983). However, elevated temperature and higher pH promote the transformation. The large oxolated polymers are of colloidal size and may range in diameter from 1.5 nm to 9 nm (Spiro *et al*., 1966; Murphy *et al*., 1976). The growth of polymer precursors occurs by the addition of monomers as expressed in reaction (2.25).

$$Fe_2(OH)_2^{4+} + FeOH^{2+} + H_2O \longrightarrow Fe_3OH_4^{3+} + H^+ \quad (2.25)$$

These polymeric species eventually age either to amorphous (such as ferrihydrite) or crystalline iron oxides/hydroxides. Amorphous iron oxides/hydroxides are unstable and transform to stable hematite or goethite. Hematite forms within the polycation nuclei by dehydration and internal rearrangement while transformation to goethite takes place by dissolution and re-precipitation. Aggregation of ferrihydrite into dense masses promotes ordering and from this ordered region hematite nucleates. Due to the energy required for dehydration and rearrangement, hematite precipitation requires high temperature (Fischer and Schwertmann, 1975; Cornell *et al*., 1989).

When precipitation occurs from ferric sulphate solutions, the polymers contain a significant amount of the anion from the solution (Cornell and Schwertmann, 2003). Margulis *et al*. (1976) isolated a polymer from the sulphate solution, the polymer had the following composition: $Fe_4O_5(SO_4).xH_2O$, this suggests that the sulphate is bound to the iron in the polymer. Such polymers lead to the formation of schwertmannite instead of ferrihydrite. Similarly, precipitation from chloride containing environments can also lead to the incorporation of Cl^- into the polymer structures resulting in the formation of akaganeite (β-FeOOH) (Dousma *et al*., 1978).

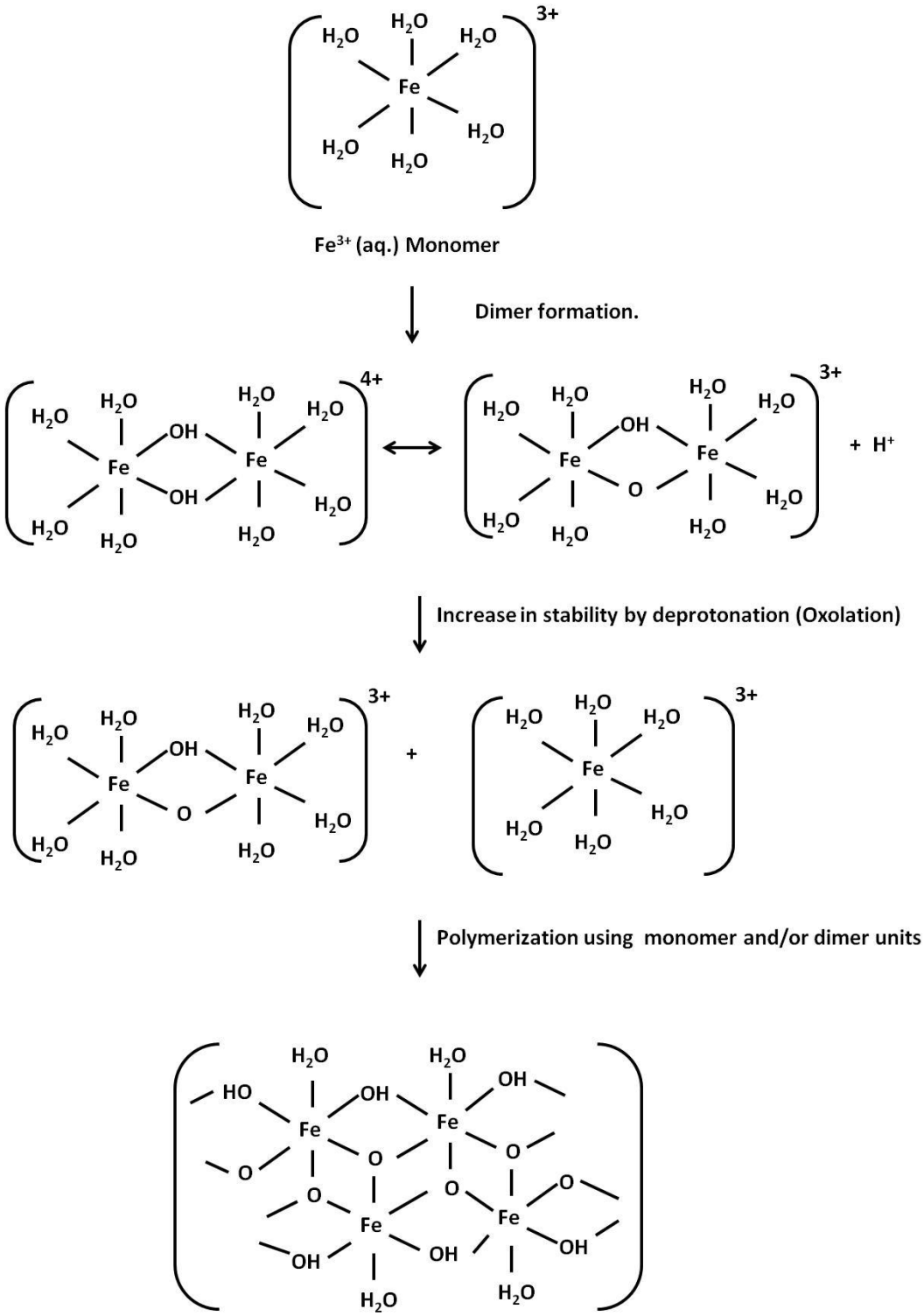

Figure 2.13 Mechanism for the formation of polymers by the linking of dimmers (Dutrizac, 1980, 1987; Cornell *et al*., 1989; Misawa *et al*., 1974).

2.8 Nucleation and crystallization

The process of precipitation involves the creation of supersaturation followed by nucleation and crystal growth. The supersaturation of a solution may be expressed in terms of supersaturation ratio or relative supersaturation "S" as follows:

$$S = \frac{a}{a^*} \tag{2.26}$$

where "a" is the activity of the solute and "a^*" is the activity of the pure solute in equilibrium with the macroscopic crystal.

Nucleation can occur spontaneously or it can be induced artificially. It can be categorized into primary and secondary nucleation. Primary nucleation can take place either spontaneously from the supersaturated solution (homogeneous nucleation) or it can be induced by foreign particles (heterogeneous nucleation). On the other hand, nucleation on the surface of a solid of the same kind as the new precipitate is often referred to as secondary nucleation. Secondary nucleation can be further divided into: apparent (small fragments washed from seed), true (nucleation on the surface of seed) and contact (induced by walls of the crystallizer or crystal-crystal contact) nucleation. Various nucleation mechanisms are summarized in Figure 2.14 (Dirksen and Ring, 1991; Mullin, 2000).

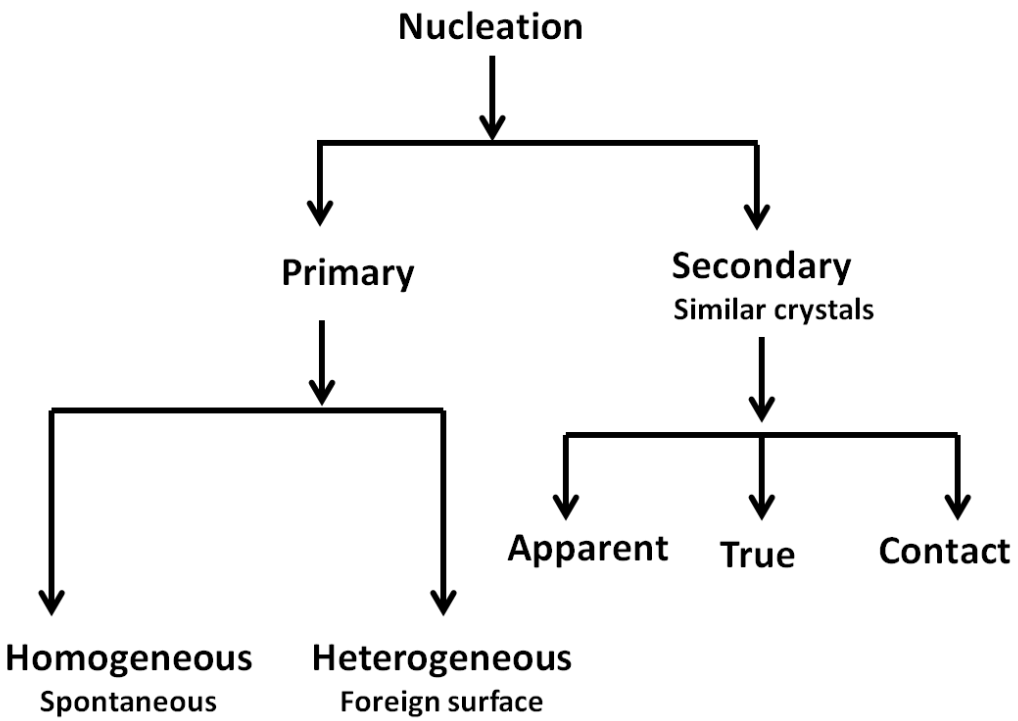

Figure 2.14 Classification of nucleation processes (Dirksen and Ring, 1991; Mullin, 2000; Demopoulos, 2009).

In a supersaturated solution, solute atoms, molecules or their polymers combine to form ordered structures or embryos. The overall free energy of these embryos goes through a maximum (ΔG^*) at some critical size (r^*) corresponding to a critical supersaturation ($S_{crit.}$), see Figure 2.15. The embryos lower their free energy by formation of stable nuclei. The behavior of a newly created crystalline structure in a supersaturated solution depends on its size; it can either grow or redissolve to decrease its free energy. The critical size (r^*), therefore, represents the critical size of a stable distinct nucleus. Particles smaller than r^* will dissolve and those larger than r^* will continue to grow. Once a critical value of supersaturation is achieved the nucleation rate suddenly increases and then reaches a maximum. This critical value of supersaturation is different for each nucleation type and is

shown in Figure 2.16. An increase in supersaturation results in an increase in the number of nuclei and a decrease in their size in a homogeneous nucleation.

Figure 2.15 shows that nucleation on the surface of a crystal already present in the system (heterogeneous nucleation) requires lower activation energy. Once heteronuclei are consumed heterogeneous nucleation stops, thus limiting the heterogeneous nucleation rate. Because of the difference in the critical supersaturation level for homogeneous and heterogeneous nucleation they are not likely to take place at the same time, see Figure 2.16 (Dirksen and Ring, 1991; Mullin, 2000).

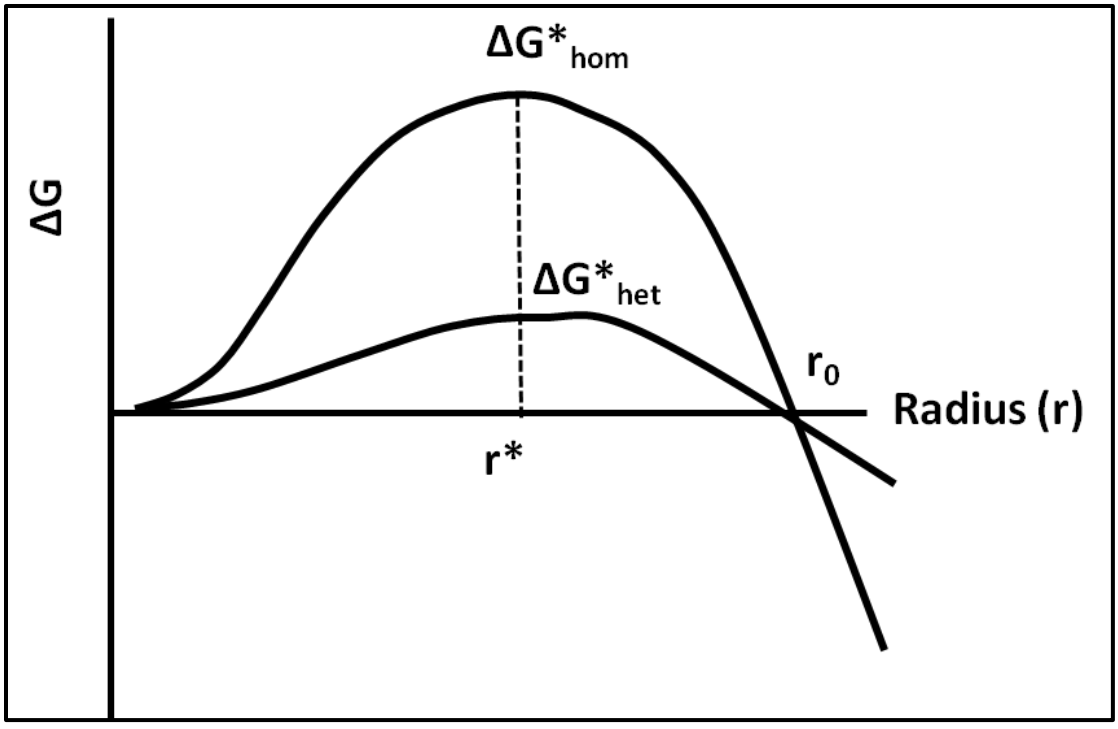

Figure 2.15 Plot of free energy versus critical radius for homogeneous and heterogeneous nucleation (Ragone, 1994).

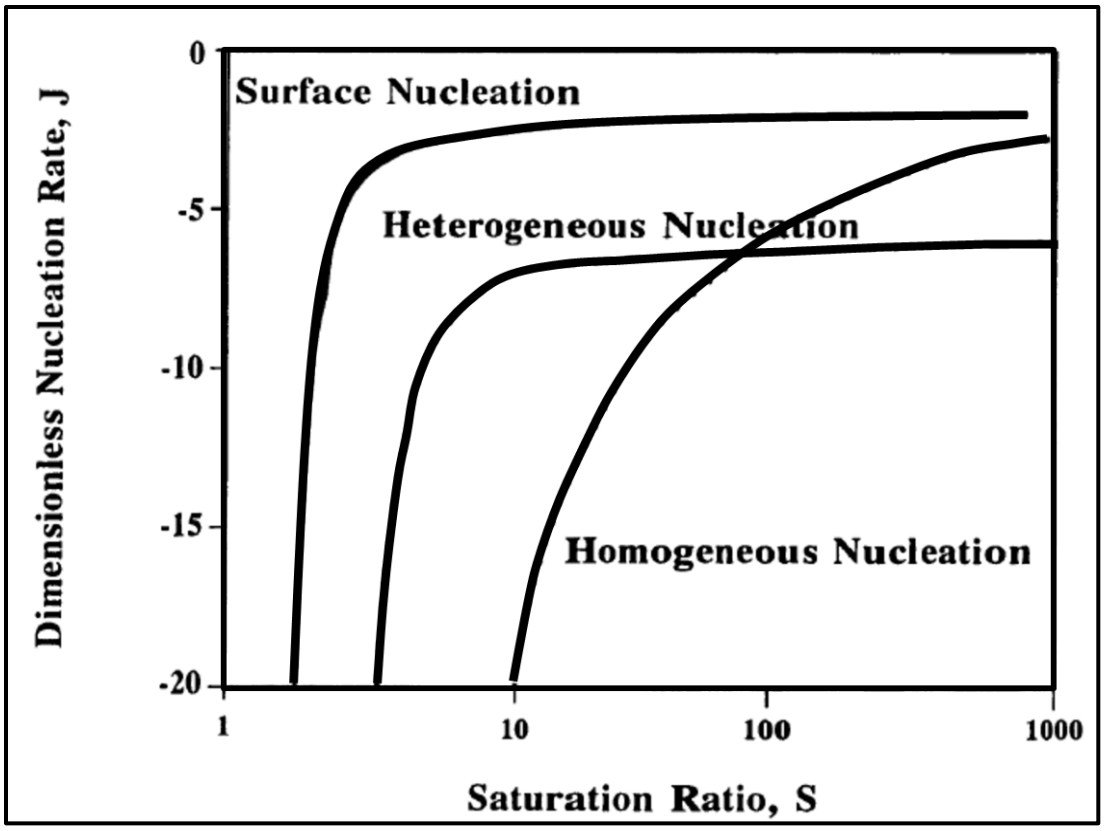

Figure 2.16 Generalized nucleation rate diagram describing the characteristic differences between homogeneous and heterogeneous nucleation as a function of saturation ratio, S (Dirksen and Ring, 1991).

2.8.1 Secondary nucleation and seeding

Seeding is considered to be the best method of inducing crystallization in a supersaturated solution. Seed material crystal size is also an important consideration for the nucleation process as it can influence secondary nucleation. Larger seed particles generate more secondary nuclei as compared to smaller seeds because of their greater contact probabilities and collision energies (Dirksen and Ring, 1991). In highly agitated systems, very small crystals may follow the streamline eddies and may not be very effective in the

nucleation process. Crystals smaller than 10 μm grow more slowly than the larger crystals. Some defragmented parts may not grow at all, which can increase the amount of fine fraction in the final product. Secondary nuclei can originate from different sources. Three sources: apparent, true and contact, are generally believed to contribute to the generation of secondary nuclei (Dirksen and Ring, 1991; Mullin, 2000). Apparent secondary nucleation usually refers to small fragments of crystals washed from the seed surface when it is added to the solution. True secondary nucleation refers to the surface nucleation of the new crystals on the seed material. Contact nucleation is the type of secondary nucleation which induces nucleation in the system by crystal-crystal contact and contact with the walls of the crystallizer. Collision in a liquid medium can induce different behaviours e.g. fracture at a point of contact, elastic and plastic deformation due to substantial hydrodynamic forces in the vicinity of point of contact and defragmentation of a crystal by collision forces (Dirksen and Ring, 1991). The defragmented part of the crystal contains many dislocation and mismatch surfaces. In fact, it is nearer to the amorphous glassy condition than to a crystal. These smaller crystals also grow at a slower rate than the larger crystals, and in some cases may not grow at all.

However, it should be noted that seed alone is not always enough to improve the quality or extent of precipitation. Proper initial conditions i.e. low initial saturation (less than that required for homogeneous nucleation) and extensive recycling of the solids may prove to be an effective approach for the production of well crystallized precipitates.

2.8.2 Nucleation of metastable phases

The Ostwald step rule states that during homogeneous nucleation the least stable or metastable phases nucleate first, which upon ageing transform to more stable phases. The nucleation rate of a metastable phase can be expressed in terms of the saturation ratio in the simplified form (Mullin, 2000) as:

$$J = A^* \, exp \left\{ \frac{\gamma}{(\ln S)^2} \right\} \qquad (2.27)$$

where the pre exponential term A^* represents the attachment frequency and γ is the interfacial energy required for the formation of a critical nucleus. Metastable phases are more easily attached than the stable phases, therefore it is expected that the factor A^* is greater for metastable phase than the stable phase i.e. $A^*_{met.} > A^*_{st}$. Similarly, less energy is required for the formation of metastable nuclei than the stable nuclei i.e. $\gamma_{met.} < \gamma_{st.}$ Since S, and γ are inversely proportional to each other, the exponential term in Equation (2.27) becomes negligible when precipitation occurs at high supersaturation. The nucleation rate is controlled by the pre-exponential term A^*, and formation of the metastable phase is kinetically favoured in the high supersaturation zone i.e. where homogeneous nucleation prevails as shown in Figure 2.17 (Dirksen and Ring, 1991; Mullin, 2000).

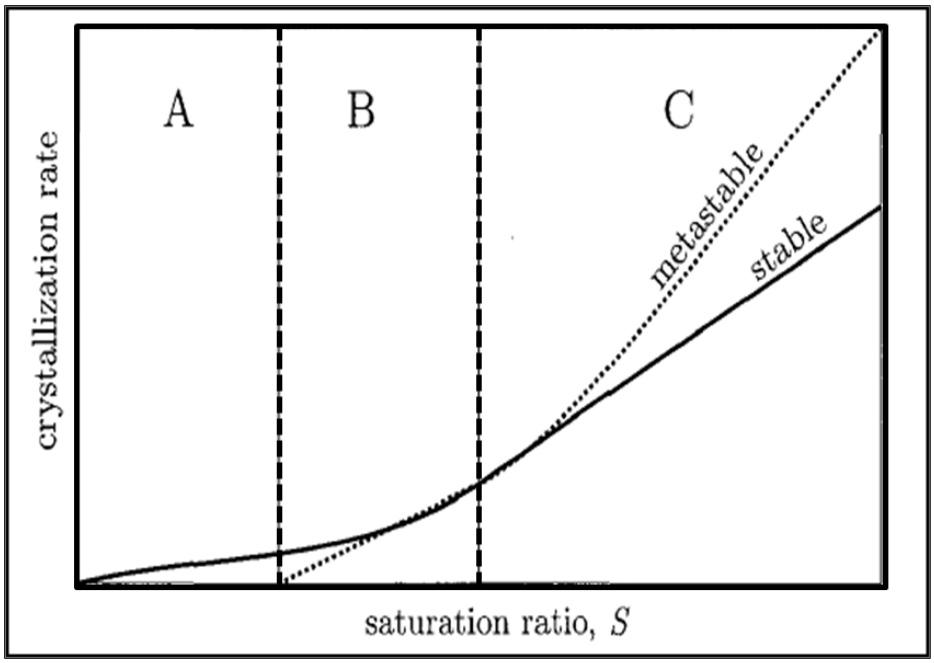

Figure 2.17 Crystallization rate of the stable and metastable phases as a function of saturation, S. In region A only stable phase can form; in region B there is kinetic competition between the two phases; in region C formation of metastable phase dominates (Nyvlt, 1995).

In systems dominated by homogeneous nucleation, aggregation becomes the major growth mechanism. Tiny particles generated by the homogeneous nucleation event have very high surface to volume ratios, therefore surface energy becomes an important term. A system in non-equilibrium state will tend to lower its energy by forming large particles at the expense of small particles (also called Ostwald ripening). Certain factors such as: population density, agitation and particle size can affect the agglomeration growth process. Higher population densities or agitation favour agglomeration, while larger particles tend to agglomerate less (Mullin, 2000; Demopoulos, 2009). In a system where supersaturation control is not possible once the supersaturation exceeds a certain level, homogeneous

nucleation starts (as described above). With the progress of the reaction, supersaturation drops and surface nucleation followed by crystal growth occurs.

For saturation values less than the homogeneous saturation, growth dominates and well grown crystals are expected to be produced. On the other hand, for saturations values greater than the homogeneous saturation value, nucleation prevails, thus resulting in production of ultrafine particles. In the region where saturation is much larger than that required for homogeneous nucleation, growth is not expected even in the presence of seed Figure 2.18.

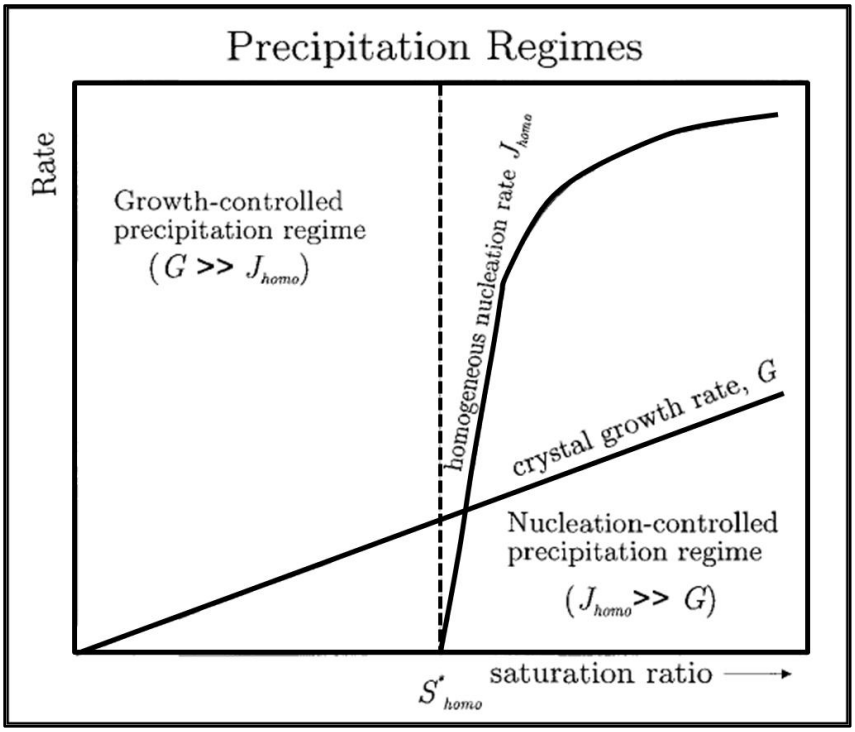

Figure 2.18 Separation of precipitation regime on the basis of rate versus supersaturation relationships (Demopoulos, 1993).

2.9 Summary

Iron is a major constituent of sulphide concentrates, present either as a structural component such as in chalcopyrite or in the form of iron sulphides such as pyrite and pyrrhotite. For efficient recovery of the valuable metals downstream processing of the leach solutions demands that all iron should be removed before the leach solutions are fed to the electro winning circuits. CESL and Vale are operating medium temperature hydrometallurgical processes for sulphide concentrates where iron is simultaneously leached and precipitated in the pressure oxidation step. Analysis of the CESL pilot and demonstration plant leach residue samples indicated that rejection of iron to the leach residue in the form of amorphous iron oxide phases must be avoided because of their characteristic to retain higher amounts of valuable metals. CESL and Vale aim to precipitate iron in an eco-friendly form with minimum loss of valuable metal to the iron residue. Comparison of different iron precipitation processes showed that hematite process has the potential to offer both of these qualities. The hematite process, as practiced in the past, required prior reduction of iron, higher temperature and longer retention times. However, in the CESL and Vale processes there is no need for prior reduction of iron and by carefully controlling the process parameters iron can be precipitated as hematite under the prevailing process conditions.

The literature review indicated that precipitation of iron occurs via a metastable phase i.e. the metastable phase precipitates first, which upon ageing converts to a more

stable phase. A higher amount of metastable phase in the residue will adversely affect its characteristics in terms of residue stability and metal intake. This suggests the need to explore the kinetics aspect of the precipitation and factors that accelerate or decelerate the precipitation kinetics under the CESL and Vale medium temperature processes.

Finally, nucleation & growth mechanisms and seeding also play an important role in defining the nature of the precipitate, its particle size and the uptake of impurities. Once the precipitation product is controlled to give mainly hematite, careful selection of the right combination of the process parameters can generate a better quality hematite with minimum valuable metal loss.

It is concluded that there is a need to better understand the effect of various process parameters on the complex chemistry of iron oxide precipitation and associated metal loss to the precipitation product, especially for the conditions relevant to CESL and Vale. The avenues that require further investigation are: characterization of leach residue samples to confirm whether amorphous iron oxide phases are responsible for higher associated metal loss to the leach residue as witnessed by characterization of the early stage test work (Sahu and Asselin, 2011); study of the process variables in a systematic manner to pinpoint the factors that have a more pronounced effect on iron precipitation and associated metal loss; examine the kinetics of the precipitation; characterization of the precipitation product(s); and finally the effect of impurities on iron precipitation behavior and its kinetics. These identified aspects will help to better understand the CESL and Vale iron precipitation processes and ultimately will lead to rejection of iron to the leach residue

with minimum associated metal loss and a stable form of the residue. This in turn will provide a step towards a more efficient iron rejection process. Secondly, improved understanding of the general aspects of iron precipitation can also be of benefit to the general audience of iron control in hydrometallurgy. The various identified aspects are in accordance with the objectives of this work, as discussed in Chapter 3 and each will be dealt-with in a separate chapter in this thesis.

Chapter 3. Objectives

The overall goal of this study is to identify the modes of metal loss to the leach residue and to find the optimum process conditions leading to a better quality iron precipitation product with minimum valuable metal loss. This will be achieved through the following steps.

1. Initially three different leach residue samples from CESL and Vale pilot and demonstration plant medium temperature hydrometallurgical processes will be characterized to identify the nature of the iron residue and phases responsible for metal losses.
2. In the second stage simulated process solutions will be used to identify the major factors affecting hematite precipitation from ferric sulphate-chloride solutions and metal loss to the precipitates.
3. The major variables identified will be optimised for conditions leading to maximum iron precipitation as hematite with minimum metal loss to the precipitation product.
4. In the last stage, the effect of certain variables on the kinetics of iron precipitation will be studied. The variables will include; acid, seed as well as the most common impurity elements.

The secondary goals of this study, which are intrinsically related to the primary goals, are to:

5. Investigate the relationship between iron precipitation and metal loss to the precipitation product from the solution containing only iron, copper and chloride in an

acidic medium. The variables studied will be: initial ferric concentration, acid concentration, time, hematite seed, and chloride and copper concentrations.

6. Identify the factors controlling the product yield and the quality of the precipitation product as well as the crystallinity of the product.
7. Identify the timescale involved in the precipitation of amorphous/poorly crystalline iron precipitates and their transformation to stable crystalline iron phases under the conditions relevant to medium temperature leaching.
8. Identify the factors which affect the transformation of amorphous/poorly crystalline precipitates; initially nucleated during the precipitation process.
9. Study direct precipitation from ferric solutions in the presence of arsenic, aluminum, magnesium and sodium.

Chapter 4. Characterization of the CESL and Vale leach residues

CESL and Vale leach residue samples produced during pilot and demonstration scale medium temperature (150 °C) hydrometallurgical processing of sulphide concentrates were characterized using different techniques. The residue samples contained amorphous/poorly crystalline and metastable nano-scale iron oxides/oxyhydroxide phases. These phases controlled the properties of the residue and contained a relatively high loading of the valuable (Cu, Ni) metals. Poor agreement between total iron analysis by inductively coupled plasma optical emission spectroscopy (ICP-OES) and quantitative X-ray powder diffraction (QXRPD) indicated the presence of amorphous/poorly crystalline iron oxide phases in the samples. QXRPD coupled with sequential extraction was used for quantification of the amorphous iron oxide phases and their associated metal loss. Amorphous iron oxides/oxyhydroxides were found to be a major source of copper and/or nickel loss to the residue. The distribution of copper and nickel into the amorphous and crystalline iron oxide phases was determined by a two-stage sequential extraction process. Association of copper and nickel to the amorphous phases was found to be approximately 2-4 times higher than with the crystalline iron oxide phases.

This chapter is based on: Javed, T., Abdul, B., Ryan, D., Raudsepp, M., Asselin, E., 2016. Amorphous iron phases in medium temperature sulphide concentrate leach residues from pilot and demonstration plants. Intl. J. Mineral processing, 148, 65-71.

4.1 Experimental

Sulphide concentrate leach residue samples (labeled as S1, S2 and S3) were supplied from CESL (S1 and S2) and Vale (S3) operations. Mineralogy of the ore concentrates from which the samples were produced is given in Table 4-1.

Table 4-1 Concentrate mineralogy for samples: S1, S2 and S3.

Phase name	Formula	Phase %		
		S1	S2	S3
Chalcopyrite	$CuFeS_2$	38	35	7
Cubanite	$CuFe_2S_3$		30	
Enargite	Cu_3AsS_4	20	1	
Pyrite	FeS_2	18		
Bornite	Cu_5FeS_4	7		
Covellite	CuS	5		
Tennantite	$(Cu, Fe)_{12}As_4S_{13}$	2		
Sphalerite	(Zn,Fe)S	2		
Pentlandite	$(Fe,Ni)_9S_8$		5	63
Pyrrhotite	$Fe_{1-x}S$		7	29
Others	Gangue	8	22	1

The general process conditions under which samples were leached are given in Table 4-2. The leach residues samples received from the CESL and Vale were thoroughly washed with de-ionized water, sampled using coning and quartering and dried in an oven at 60 °C for overnight (~10 hr). Dried samples were lightly ground with the help of a mortar and pestle and a portion was analyzed by ICP-OES after complete multi acid digestion.

Quantitative X-ray powder diffraction (XRPD) was done on the as received solid residue samples, except for drying and size reduction necessary for QXRPD analysis. QXRPD phase analysis was performed using Rietveld method and X-ray powder diffraction data.

For this purpose, each sample was reduced to fine powder to the optimum grain-size range for X-ray analysis (< 10 μm) by grinding under ethanol in a vibratory McCrone Micronising Mill for 7 min. Corundum was used as an internal standard for quantification of the relative amounts of crystalline and amorphous phases present. Amorphous content was estimated by adding a weighed amount of a spike (corundum; NIST Standard Reference Material 676a) with known crystallinity (99.02 wt. %). The determination of amorphous phase in a given sample from Rietveld quantitative analysis is straightforward. Initially, a mixture with a weighed amount of a suitable standard, with negligible or at least a well known amorphous content and the investigated material is prepared. Then, the mixture is analyzed by powder diffraction and Rietveld phase analysis. If the sample has an amorphous phase, the crystalline phases present in the sample will have a smaller Rietveld refined weight ratio. Consequently, the standard phase fraction will be overestimated. From overestimation of the standard, the amorphous content can be determined. It enables the measurement of the amorphous content with accuracy close to 2 % (De La Torre *et al*., 2001). Continuous-scan X-ray powder-diffraction data were collected over a range 3–80° 2θ with CoK_{α} radiation on a Bruker D8 Focus Bragg-Brentano diffractometer. The X-ray diffractograms were analyzed using the International Centre for Diffraction Database PDF-4 and Search-Match software DiffracPlus Evaluation 19.0.0.0 prior to the Rietveld analysis.

Table 4-2 Leaching conditions for samples: S1, S2 and S3.

Operating Parameters	Unit	S1	S2	S3
Total pressure	kPa	1300	1264	1030
Temperature	°C	150	150	150
Retention Time	Min	91	58	80
Autoclave free acid	g/L	10.7	0.0	10-12
Solids loading	%	10.2	23.2	5*
$[Cl^-]$	g/L	11.2	10.4	5

*Concentrate feed slurry is diluted with coolant and anolyte from electro winning before entering the autoclave

To determine the amounts of amorphous and crystalline iron oxides/ohyhydroxides in the leach residue samples and the distribution of copper/nickel into these phases, a two stage sequential extraction was employed. Comparisons between different sequential extraction methods (Kostka and Luther, 1994; Raiswell *et al.*, 1994; Poulton and Canfield, 2005) have shown that hydroxylamine hydrochloride (HaHC) is the most selective for dissolution of amorphous iron oxides/oxyhydroxides. The 1st stage extraction used in this study had been successfully used by many authors (Chao and Zhou, 1983; Chester and Hughes, 1967; Berger *et al.*, 2008; Sahu and Asselin, 2011). This technique has several advantages over the conventional oxalate method (Raiswell *et al.*, 1994). The Sequential extraction scheme is given in Figure 4.1. Amorphous iron oxide phases together with water soluble phases are recovered in the first stage while crystalline phases are recovered in the second stage. In the first stage extraction, about 5 g of the leach residue (R) was leached with 0.25 M HaHC + 0.25 M hydrochloric acid at 50 °C under atmospheric pressure for 30 minutes, keeping the solid to liquid mass ratio at 1:50. The reaction mixture was then filtered. The filtrate was analyzed for Cu, Fe, Ni, As, Si and Ca. The remaining residue (R_1)

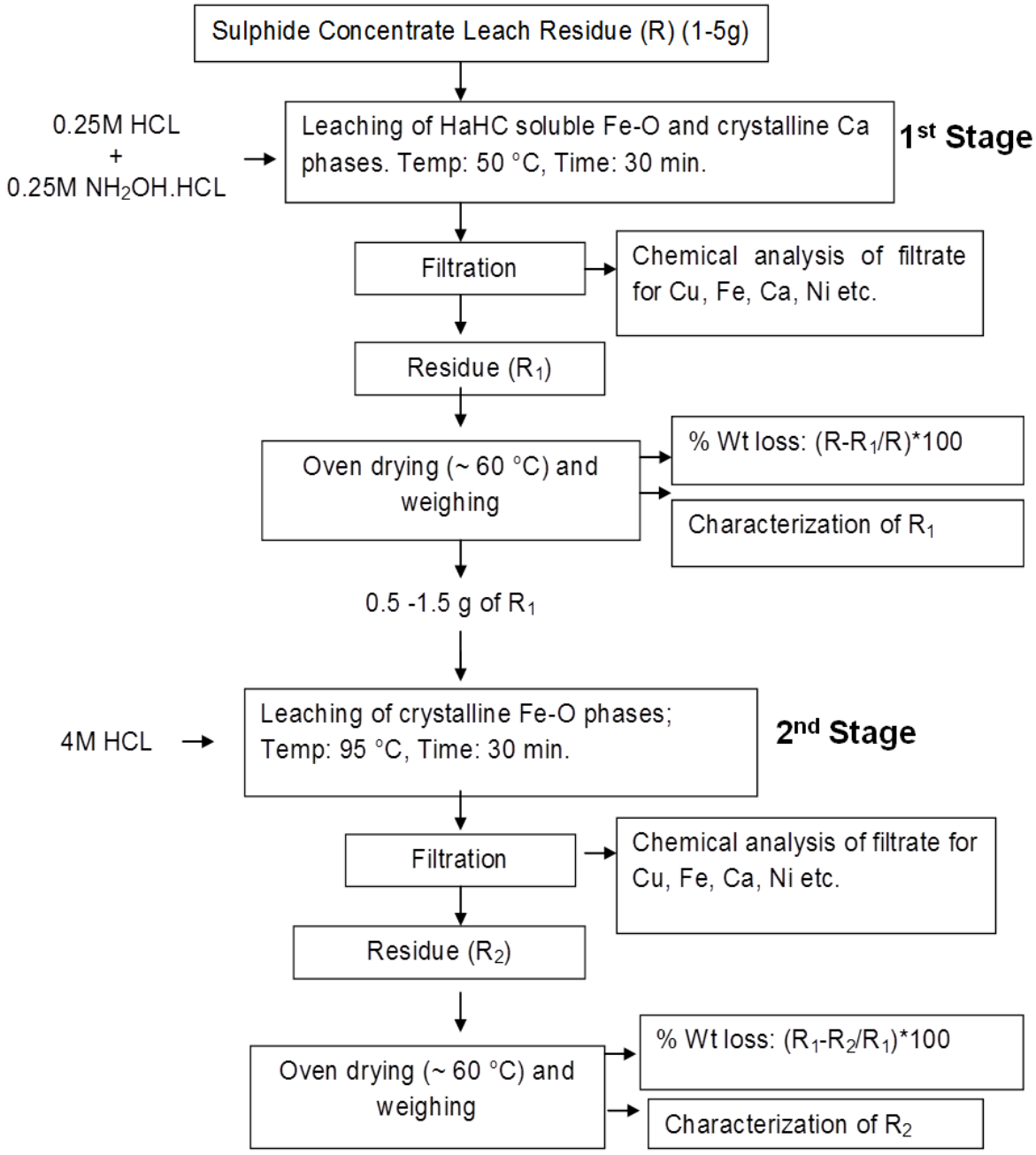

Figure 4.1 Sequential extraction scheme for the determination of HaHC soluble and crystalline iron oxide phases.

was dried in an oven at 60 °C, weighed and percent weight loss was calculated. In the second stage approximately 1.5 g of R_1 was leached with 4 M hydrochloric acid at 95 °C and

atmospheric pressure for 30 minutes keeping the solid to liquid mass ratio 1:40. The filtrates were analyzed for Cu, Fe, Ni, As, Si and Ca. The remaining residue (R_2) was dried in an oven at 60 °C, weighed and the percent weight loss was determined. In some of the experiments where residue R_2 was less than a gram, experiments were repeated several times to make enough sample for characterization.

After necessary correction for the water soluble phases from the weight loss in the first stage extraction, the amounts of amorphous phases were determined. Weight loss in the second stage extraction gives the amount of crystalline iron oxide phases. Each sample was put through the two stage sequential extraction process eight times. In addition, for every stage, two different solid to liquid ratios were employed to check the reproducibility. The weight loss was within a standard deviation of ±2 %.

Scanning electron microscopy/energy dispersive X-ray spectroscopy (SEM/EDS) was carried out by mounting the residue samples onto 26 x 46 mm, 200µm thick glass slides using epoxy, samples were polished and coated with carbon prior to analysis. The samples for Mössbauer spectroscopy were prepared by mixing approximately 40 mg of powdered material with boron nitride powder. The ^{57}Fe Mössbauer spectra were obtained with a 50mCi ^{57}Co(Rh) source on a conventional spectrometer operated in constant-acceleration mode. The spectra were fitted using a conventional nonlinear least-squares minimization routine to a sum of Lorentzian lines with positions and intensities calculated using a simple first-order perturbation model.

4.2 Results and discussion

The mineralogy of the leach residue samples consisted of elemental sulphur and iron oxide phases along with associated gangue minerals. The chemistry of iron oxide phases was quite complex, iron oxides were found to exist in different crystalline forms with variable crystallinity. Considering crystallinity of the iron oxides, iron precipitates were divided into three regimes (i) Crystalline (ii) Poorly crystalline and (iii) Amorphous iron oxides. Regime (i) normally contains hematite, goethite and jarosite. Possible phases in regime (ii) can be hematite and goethite, as both of these phases have been shown to exhibit variable crystallinity (Machala *et al.*, 2007, Schwertmann *et al*., 1985, Johnston and Glasby, 1978), and regime (iii) can contain phases such as ferrihydrite and schwertmannite. Ferrihydrite although considered amorphous is not strictly amorphous (Jambor and Dutrizac, 1998; Janney *et al*., 2000a, 2000b, 2001) and commonly refers to a range of poorly crystalline iron oxide phases of which 2 line (exhibiting 2 broad XRD peaks) ferrihydrite and 6 line (exhibiting 6 broad XRD peaks) ferrihydrite are more common.

Several studies of the hydrometallurgical residues have identified the presence of regime (iii) phases (Loan *et al*., 2006; Steel *et al*., 2010; Sahu and Asselin, 2011). However, true quantification of these phases and associated valuable metal loss remained an issue. Additionally, in all the studies mentioned above, the possible presence of regime (ii) phases was not addressed.

Amorphous/poorly crystalline phases do not respond to the X-ray diffraction as crystalline phases do. Therefore, the presence of regime (ii) and regime (iii) phases, if not taken into account properly, can result in inaccurate quantification of the crystalline phases determined by routine XRD. It should be noted that leach residues have heterogeneous mineralogy and gangue minerals can also contribute to regime (ii) and regime (iii) phases. This study will focus only on iron oxide phases in regime (ii) and (iii). As regime (ii) and (iii) both lead to X-ray amorphous content of the residue, these collectively will be called as X-ray amorphous phases which, in fact, is the total amorphous content of the residue as determined by QXRPD. A fraction of this X-ray amorphous content is due to regime (iii) i.e. the phases responsible for higher valuable metal loss to the residue, and was determined by hydroxyl amine hydrochloride (HaHC) extraction, therefore it will be called HaHC phase in the remainder of the document.

4.2.1 Quantitative X-ray powder diffraction (QXRPD)

QXRPD phase analysis of the samples is given in Table 4-3. The X-ray amorphous content was found to vary between 30.5 and 52.7 wt. % as shown in Table 4-3. Sample S1 exhibiting highest amorphous content did not have any of the crystalline iron oxide phases except jarosite (13.5 %). In sample S2 and S3 major iron oxide phases are hematite (S2= 20.6 %, S3= 35 %), goethite (S2= 3.5 %, S3= 8 %) and minor amounts of jarosite (S2= 0.6 %, S3= 1 %). When iron was present mostly in the crystalline form (hematite), less total amorphous

phase was found to be present. After 1st and 2nd stage extractions the amorphous content was found to decrease in all the samples, see Table 4-4. The fraction of the amorphous phase due to the presence of regime (ii) and regime (iii) phases was determined by sequential extraction scheme and is discussed in next section.

Table 4-3 Comparison of phases in samples: S1, S2 and S3 as determined by routine XRD and QXRPD. X-ray amorphous content varies from 30.5 to 52.7 % (error ±2 %).

Phase Name	Ideal Formula	Routine XRD			QXRPD		
		S1	S2	S3	S1	S2	S3
Albite low	$NaAlSi_3O_8$	2	4.4		0.9	2.5	
Chalcopyrite	$CuFeS_2$			0.3			0.2
Goethite	α-$Fe^{3+}O(OH)$		6.3	11.5		3.5	8.0
Gypsum	$CaSO_4.2H_2O$	6.8		1.5	3.2		1.0
Hematite	α-Fe_2O_3		37.1	50.4		20.6	35.0
Jarosite	$KFe^{3+}{}_3(SO_4)_2(OH)_6$	28.6	1.1	1.5	13.5	0.6	1.0
Lizardite 1T	$Mg_3Si_2O_5(OH)_4$	2.8			1.3		
Muscovite	$KAl_2(Si_3Al)O_{10}(OH,F)_2$	8.3	4		3.9	2.2	
Pyrite	FeS_2	3.3			1.5		
Quartz low	SiO_2	9			4.2		
Sulfur	S_8	34.5	34.9	34.8	16.3	19.6	24.2
Talc 1A	$Mg_3Si_4O_{10}(OH)_2$	3.8	12.1		1.8	6.7	
Tennantite	$(Cu, Fe)_{12}As_4S_{13}$	1.1			0.5		
Amorphous					**52.7**	**44.5**	**30.5**
Total		100	100	100	100	100	100

4.2.2 Sequential extraction

Chemical analysis of the, as received, solid residue samples showed the presence of 1.1 and 1.4 wt. % copper, in samples S1 and S2, respectively, and approximately 1.0 wt. % nickel in sample S3. The distribution of copper and nickel into different iron oxide phases was determined by the two-stage sequential extraction technique shown in Figure 4.1 and

the results are presented in Table 4-5. Chemical analysis for Cu, Fe, As, Si, Ca and Ni was carried out on both the 1st stage and 2nd stage filtrates of sequential extraction. Cu/Ni recovered during 1st stage extraction was attributed to regime (iii) phases i.e. when these phases are recovered in the 1st stage extraction, Cu/Ni adsorbed onto these phases is also recovered. The 2nd stage extraction selectively dissolved crystalline iron oxide phases. Therefore, Cu/Ni recovered during the 2nd stage extraction was associated with regime (i) and (ii) phases.

All elemental percentages are reported as a percentage of R. For example, "10 % Fe" means that 10 % of R was Fe. Total iron calculated from the two-stage extraction agreed well with the ICP analysis of solids in all three samples as shown in Table 4-5. The only small difference between sequential extraction iron content and that obtained by ICP was due to iron-containing phases that remained un-recovered throughout the two-stage extraction (i.e. tennantite, pyrite and chalcopyrite).

Table 4-4 QXRPD analysis of samples: S1, S2 and S3; as received (R) and after 1st (R_1), 2nd (R_2) stage extractions. Weight loss during sequential extraction, X-ray amorphous phase and HaHC amorphous phases are also compared. Weight losses under R_1 and R_2 are due to first and second stage extractions, respectively. Results are within 2 wt. % error. R_1 and R_2 were corrected for weight loss using Rietveld refinement, see appendix A.

Phase name	Ideal Formula	R (wt. %)			R_1 (wt. %)			R_2 (wt. %)		
		S1	S2	S3	S1	S2	S3	S1	S2	S3
Albite low	$NaAlSi_3O_8$	0.9	2.5			1.5			1.5	
Alunite	$KAl_3(SO_4)_2(OH)_6$							0.2	0.2	
Boehmite	AlO(OH)							0.4	0.2	
Calcite	$CaCO_3$					0.3	0.9	0.4	0.5	
Chalcopyrite	$CuFeS_2$			0.2						0.3
Goethite	α-$Fe^{3+}O(OH)$		3.5	8.0		3.4	9.1			
Gypsum	$CaSO_4.2H_2O$	3.2		1.0						
Hematite	α-Fe_2O_3		20.6	35.0		20.2	34.6			
Jarosite	$NaFe^{3+}{}_3(SO_4)_2(OH)_6$	13.5	0.6	1.0	10.2					
Lizardite 1T	$Mg_3Si_2O_5(OH)_4$	1.3			0.7			0.3	1.1	
Magnetite	Fe_3O_4								0.3	
Muscovite	$KAl_2(Si_3Al)O_{10}(OH,F)_2$	3.9	2.2		1.0			1.5		
Pyrite	FeS_2	1.5			1.0			1.1	0.3	0.1
Quartz low	SiO_2	4.2			3.4			4.7	0.9	
Sulfur	S_8	16.3	19.6	24.2	16.2	19.4	23.4	20.7	21.6	22.9
Talc 1A	$Mg_3Si_4O_{10}(OH)_2$	1.8	6.7			4.6			4.0	
Tennantite	$(Cu, Fe)_{12}As_4S_{13}$	0.5			0.5			0.7		
X-ray amorphous		**52.7**	**44.5**	**30.5**	**28.1**	**38.6**	**27.5**	**24.0**	**15.4**	**8.8**
SX* Wt. loss					**38.8**	**12.0**	**4.6**	**46.0**	**54.0**	**68.0**
Total		100	100	100	100	100	100	100	100	100
HaHC amorphous		**25.8**	**7.2**	**2.2**						

*SX = Sequential extraction

Table 4-5 Distribution of Fe, Cu, Ni and Ca into 1st and 2nd stage extraction filtrates. ICP of the dried but otherwise as-received solids is also provided for comparison. All elemental percentages are reported as a percentage of R.

Sequential Extraction	S1	S2	S3
Fe 1st stage extraction (%)	12.1	4.5	1.1
Fe 2nd stage extraction (%)	9.7	27.8	38.0
Total Fe (sequential extraction) (%)	21.8	32.3	39.1
Total Fe (ICP of R) (%)	22.6	32.8	40.0
% Fe recovered by sequential extraction	96.5[a]	98.5[b]	97.5[c]
Cu 1st stage extraction (%)	0.50	0.38	0.05
Cu 2nd stage extraction (%)	0.23	0.94	0.46
Total Cu (Sequential extraction) (%)	0.73	1.32	0.51
Total Cu (ICP of R) (%)	1.1	1.38	0.57
% Cu recovered by Sequential extraction	66[a]	96[b]	89.5[c]
Ni 1st stage extraction (%)	-	-	0.05
Ni 2nd stage extraction (%)	-	-	0.70
Total Ni (sequential extraction) (%)	-	-	0.75
Total Ni (ICP of R) (%)	-	-	0.90
% Ni recovered by sequential extraction	-	-	83.3[d]
Ca 1st stage extraction (%)	0.72	0.03	0.2
Ca 2nd stage extraction (%)	0.061	0.37	0.03
Total Ca (%)	0.78	0.40	0.23

[a]S1 contained approximately 0.5 % tennantite (0.24 % Cu, 0.02 % Fe) and approximately 1.5 % pyrite (0.7 % Fe), both of which remained unrecovered in sequential extraction. Phase percentages are from QXRPD results, Table 4-4.

[b]S2 contained approx. 0.9 % unrecovered (after 2nd stage extraction) pyrite (0.4 % Fe)

[c]S3 (after 2nd stage extraction) contained approximately 1 % un-recovered chalcopyrite (0.35 % Cu, 0.31 % Fe) and approximately 0.2 % un-recovered pyrite (0.1 % Fe)

[d]In case of sample S3 SEM showed the presence of pentlandite which also remained unrecovered during sequential extraction.

When percentage ratios of Cu/Fe and Ni/Fe for the 1st and 2nd stage extractions were compared it was realized that, in all cases, the ratios were higher for 1st stage extraction than for 2nd stage extraction, see Table 4-6.

Figure 4.2 presents the percentage of copper and iron recovered during 1st stage extraction. It is clear from Figure 4.2 that a higher amount of amorphous iron leads to higher loss of Cu to the residue. Figure 4.3 shows the SEM – EDS elemental mapping of the amorphous iron oxide phase in sample S1. It can be seen that the distribution of Cu in the amorphous phase is higher than other regions of the sample.

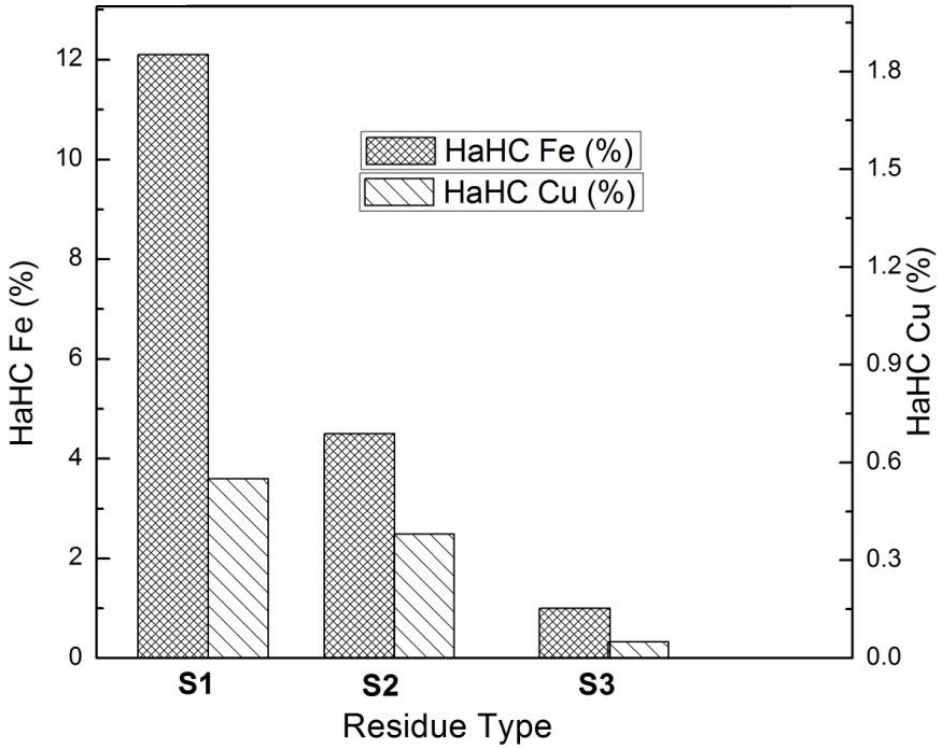

Figure 4.2 % Fe and Cu dissolved by HaHC extraction for the samples: S1, S2 and S3.

Table 4-6 Comparison of Cu/Fe and Ni/Fe ratios in the 1st and 2nd stage extractions for S1, S2 and S3.

Sample	1st stage Cu/Fe x100	2nd stage Cu/Fe x100	1st stage Ni/Fe x100	2nd stage Ni/Fe x100
S1	4.13	2.37	-	-
S2	8.44	3.38	-	-
S3	5.0	1.33	4.5	1.84

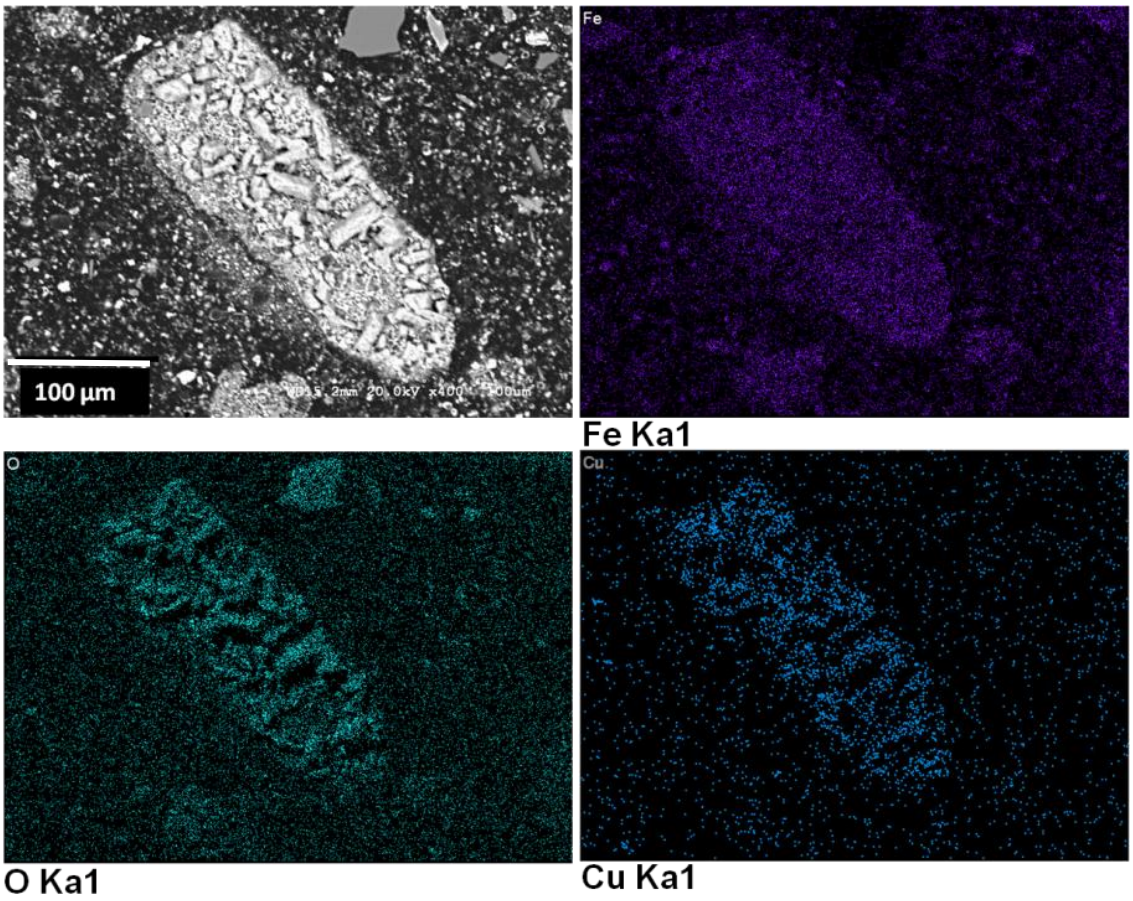

Figure 4.3 SEM image of the iron oxide phase in sample S1 along with elemental mapping for Fe, O and Cu.

4.2.3 Comparison of elemental analysis

Total iron content determined from QXRPD and ICP analysis of the residues is compared in Table 4-7. All elemental percentages are reported as percentage of R as mentioned above. Only 5.3 % iron in sample S1 was found to be present in the crystalline form as detected by QXRPD (Table 4-3). If the remaining iron (17.3 %, Table 4-7) in S1 is present in the form of HaHC soluble phases, then chemical analysis of the 1st stage filtrates

should have detected the remaining 17.3 % iron. However, only 12.1 % iron was recovered during the 1st stage extraction. The 2nd stage extraction recovered 9.7 % iron. All iron oxides which are not recovered during 1st stage are recovered in the 2nd stage. Jarosite is also recovered during 2nd stage extraction but other non-oxide iron phases (e.g. pyrite and tennantite) remain intact. After taking into account the iron from jarosite it was found that approximately 5 % iron remained unaccounted-for in unknown phases. This unaccounted-for iron was assigned to regime (ii) phases. Similarly about 11.5 % and 9.1 % iron was found to be associated with regime (ii) phases in S2 and S3, respectively.

Table 4-7 Comparison of total Fe from ICP, QXRPD and 1st stage extraction for S1, S2 and S3.

	Total Fe (wt. %)			
Sample No.	QXRPD	ICP	ICP – QXRPD	1st stage
S1	5.3	22.6	17.3	12.1
S2	16.8	32.8	16.0	4.5
S3	29.9	40.0	10.1	1.1

4.2.4 Determination of "Hydroxyl amine hydrochloride (HaHC) soluble amorphous" phases

Based on the mass loss during 1st stage sequential extraction and the QXRPD analysis (Table 4-4): the hydroxylamine hydrochloride (HaHC) soluble phases were determined as follows:

$$HaHC\ (\%) = \left(\frac{R - R_1}{R}\right) * 100 - X \qquad (4.1)$$

Where R is total mass of residue, R_1 is the mass of the residue left after first stage of extraction and X is the difference between the weight % of phases in R and R_1 calculated from the QXRPD data in Table 4-4 (The difference was not considered when it was less than 2 wt. %).

The difference between the QXRPD amorphous content of R and R_1 and the amorphous phases calculated from sequential extraction were in good agreement, see Table 4-4. These values also agreed well with the mass balance of the ICP iron from first stage filtrates, see Table 4-4. For example for sample S1, the difference between QXRPD amorphous content of R and R_1 was 24.6 wt. % while amorphous phase determined by sequential extraction was 25.8 wt. %. Similarly, ICP analysis of the first stage sequential extraction filtrates showed the presence of ~12.1 wt. % Fe. The stoichiometry of the iron compound dissolved during the first stage is not known, if it is supposed that the compound dissolved is ferrihydrite with the generally accepted formula $5Fe_2O_3 \cdot 9H_2O$, the mass balance of the iron dissolved in first stage extraction suggests the presence of ~20 wt. % ferrihydrite which is very close to the amorphous content calculated from QXRPD and sequential extraction.

Amorphous/poorly crystalline iron oxyhydroxides identified in many soils (Taylor, 1959; Schwertmann *et al*., 1982; Schulze, 1981) and hydrometallurgical residues (Claassen *et al*., 2002; Loan *et al*., 2002, 2006; Steel *et al*., 2010; Sahu and Asselin, 2011) were found to be ferrihydrite. However, ferrihydrite was not conclusively identified in this study.

4.2.5 Mössbauer spectroscopy

^{57}Fe Mössbauer spectroscopy (Gütlich *et al*., 1978) is a solid-state nuclear-probe technique that yields information on the chemical and physical environments of iron within a solid material. Unlike XRD, spectral signals can be obtained from both crystalline and non-crystalline samples.

Mössbauer analysis of the sample which has the highest amount of amorphous phase i.e. sample S1 presented a broadened, slightly asymmetric doublet with no trace of a magnetic component (< 1 %). The Mössbauer spectra of the sample S1 and sample S1 after 1st stage extraction are shown in Figure 4.4. Figure 4.4 (S1-R1) shows that leaching by HaHC leads to a distinctly better defined spectrum for sample S1. The spectral asymmetry and broad lines of the leached material appear to be consistent with a mineral from the ferrihydrite/schwertmannite family. However, while the fitted quadrupole splittings of the two components (1.10(1) mm/s and 0.62(1) mm/s) are certainly within the range seen for ferrihydrite (Murad, 1988), the area ratios are reversed so that we observe a much larger average splitting (0.90 mm/s) than is reported for ferrihydrite (0.72 mm/s) or schwertmannite (0.71 mm/s; Cashion *et al*., 2012). Cooling to 11 K should provide some further discrimination. The hyperfine field of sample S1-R1, after cooling to 11 K, was consistent with, but slightly higher than that reported for both ferrihydrite and schwertmannite.

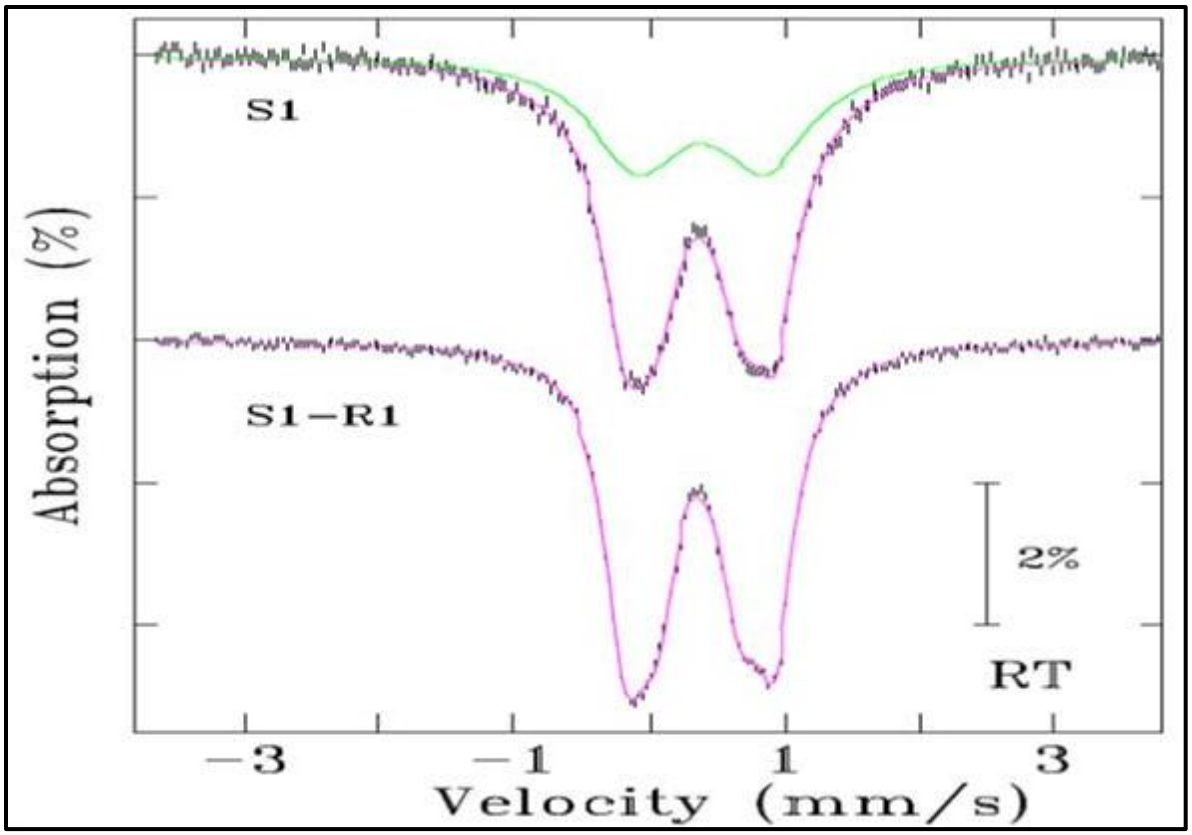

Figure 4.4 Room temperature Mössbauer spectra for sample S1: before (S1) and after (S1−R1) leaching. The doublet shown at the top is the difference between the two spectra and reflects the Mössbauer spectrum of the material removed by the HaHC extraction.

4.3 Conclusions

Characterization of the leach residues samples from CESL and Vale pilot and demonstration scale medium temperature hydrometallurgical processes showed that the residues contain a significant amount of the X-ray amorphous material that should be taken into account for true quantification of the phases. X-ray amorphous and HaHC soluble phases were determined by QXRPD and sequential extraction. Poor agreement between quantification of total iron from QXRPD and sequential extraction indicated the presence of

iron in amorphous as well as poorly crystalline iron oxide phases. Chemical analysis of the sequential extraction filtrates revealed that HaHC soluble phases were the major source of copper and nickel loss to the residue. HaHC soluble phases contained about 2-4 times more Cu/Ni compared to the crystalline iron oxide phases. Selection of a copper/nickel hydrometallurgical process which produces minimum amount of amorphous phase can reduce the loss of copper/nickel to the residue. The process conditions described for S3 in Table 4-2 i.e. 1030 kPa total pressure, 80 min retention time, 10-12 g/L acid concentration with 5 g/L chloride concentration and 5 % solids loading generated comparatively lower amount of HaHC soluble phases. The HaHC soluble phases were suspected to be ferrihydrite or a mixture of amorphous iron oxides/oxyhydroxides. However, these were not positively identified.

Chapter 5. Thermal behavior of medium temperature leach residues

5.1 Introduction

As a part of the work to characterize the leach residue samples generated under CESL and Vale conditions, the samples S1, S2 and S3 were further analyzed for their thermal behavior and spectroscopic studies. Derivative samples were prepared by extracting gypsum and sulphur from the original samples: S1, S2 and S3, to help understand the modes of amorphous iron oxide phases in the samples. Thermal behavior of the samples was studied by using thermal gravimetric analysis (TGA) – differential thermal analysis (DTA) in the temperature range 30 to 800 °C in both air and nitrogen atmospheres, with XRD analyses both before and after heating. Thermal transformation temperatures of the iron oxides/oxyhydroxides in the residue samples varied over a wide range which suggested the presence of different kinds of iron oxide phases. Spectroscopic analysis was carried out to further augment the analysis. Given the compositions of the residues, presence of thermal events in the temperature range 200 °C to 480 °C was attributed to amorphous/poorly crystalline iron oxide phases.

5.2 Experimental

Primary samples (CESL, S1 and S2 and Vale, S3) were treated to extract gypsum and sulphur from the samples. Sulphur extraction was carried out using a Soxhlet extractor. For sulphur extraction about 10 grams of the samples were taken and placed in cellulose made cylindrical-shaped thimble inside a Soxhlet extractor. The samples were extracted with a known amount of toluene for 24 hours. A schematic of the Soxhlet extractor is shown in Figure 5.1. Gypsum extraction as carried out by washing in water for up to 24 hours.

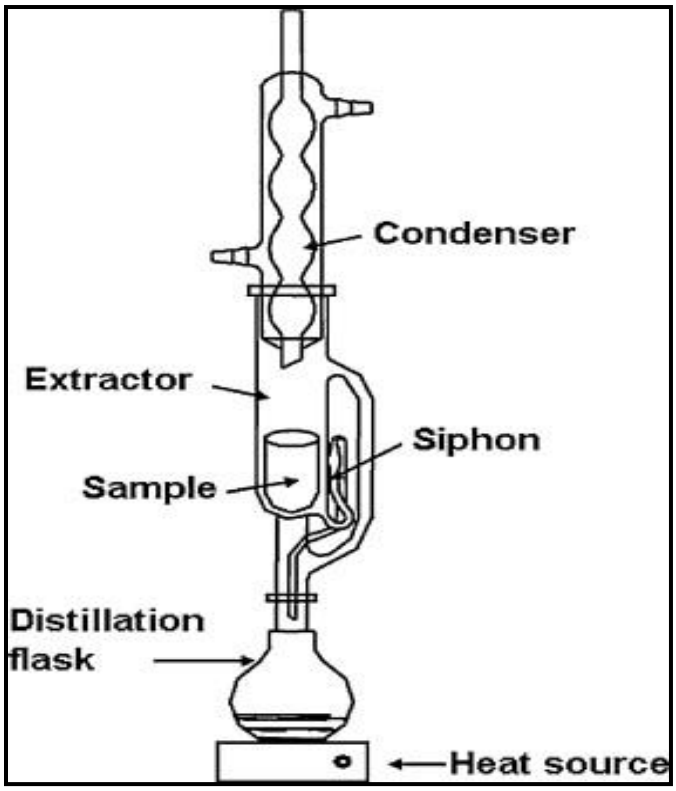

Figure 5.1 Schematic of the Soxhlet extractor used in this study.

Thermal gravimetric analysis coupled with differential thermal analysis was carried out using a Perkin Elmer simultaneous thermal analyzer STA-6000. For this purpose about 25-35 mg of the sample was placed in a ceramic pan. The sample was then heated from 30-800 °C with a heating rate of 10 °C/min in both air and nitrogen atmospheres.

Raman spectra were obtained using 632.81 nm radiations from a 17 mW air cooled laser and the laser beam was focused on the sample by using a lens to give a spot size of *ca.*1 µm with a resolution better than 2 cm^{-1}. The laser power was always kept below 0.1 mW at the sample, to avoid sample degradation, except in the laser power dependence experiments.

Fourier transform infrared spectra were recorded using a Perkin-Elmer FTIR-ATR (Fourier transform infrared spectrometer-Attenuated total reflection) apparatus in the range 400-4000 cm^{-1}. Quantitative phase analysis of all the samples was done both before and after thermal analysis using the same method as described in Chapter 4.

5.3 Results and discussion

5.3.1 Thermal gravimetric/differential thermal analysis (TGA/DTA)

TGA/DTA was carried out on as received samples as well as gypsum and sulphur extracted samples. After gypsum and sulphur extraction samples are left only with stable

gangue minerals and iron oxide/oxyhydroxide phases. Attribution of a certain behavior to iron oxides/oxyhydroxides, under such circumstances, becomes easier.

Elemental analysis of the as received samples S1, S2 and S3 after washing and drying is provided in Table 5-1, while phase analysis is given in Table 5-2. The dehydroxylation temperatures of various forms of iron oxides and oxyhydroxides as reported in the literature are summarized in Table 5-3.

Table 5-1 Elemental analysis of samples: S1, S2 and S3 (wt. %).

Element	S1	S2	S3
S	28.5	27.7	31.3
Fe	22.6	32.8	40.0
Ca	1.01	0.48	0.26
Cu	1.1	1.38	0.57
As	6.1	0.34	<0.01
Si	6.6	9.5	0.23
Al	0.83	1.0	0.07
Mg	0.02	0.91	0.01
K	0.23	0.08	0.01
Na	0.22	0.24	0.26
Ni	<0.01	0.31	0.90
Pb	0.48	0.043	0.013
Sb	0.26	0.014	<0.01
Ti	0.04	0.08	<0.01

TGA-DTA traces of as received sample S1 are shown in Figure 5.2, a large exothermic peak between 200-300 °C in the air atmosphere, as shown in Figure 5.2a, appeared due to sulphur oxidation (Sammut and Welham, 2002), with associated weight loss of ~25%.

Table 5-2 XRD phase analysis (wt. %) of the as received samples: S1, S2 and S3 before and after thermal (air atmosphere) analysis, (error ±2 %).

Phase Name	Ideal Formula	Before Thermal Analysis			After Thermal Analysis		
		S1	S2	S3	S1	S2	S3
Akaganeite	$Fe^{3+}O(OH,Cl)$				0.4		
Albite low	$NaAlSi_3O_8$	0.9	2.5			3.8	
Anhydrite	$CaSO_4$				1.8		
Chalcopyrite	$CuFeS_2$			0.2			
Goethite	α-$Fe^{3+}O(OH)$		3.5	8.0	0.2		
Gypsum	$CaSO_4.2H_2O$	3.2		1.0	0.3		0.4
Hematite	α-Fe_2O_3		20.6	35.0	27.2	42.2	55.1
Jarosite	$MFe^{3+}{}_3(SO_4)_2(OH)_6$	13.5	0.6	1.0			
Lizardite 1T	$Mg_3Si_2O_5(OH)_4$	1.3					
Magnetite	Fe_3O_4				1.1	4.8	6.1
Muscovite/ Biotite	$KAl_2(Si_3Al)O_{10}(OH,F)_2$	3.9	2.2				
Pyrite	FeS_2	1.5					
Quartz low	SiO_2	4.2			3.0	0.6	
Sulfur	S_8	16.3	19.6	24.2			
Talc 1A	$Mg_3Si_4O_{10}(OH)_2$	1.8	6.7				
Tennantite	$(Cu, Fe)_{12}As_4S_{13}$	0.5					
Amorphous		52.7	44.5	30.5	12.0	17.6	5.4
Heating Wt. loss %					54.0	31.0	33.0
Total		100	100	100	100	100	100

Table 5-3 Transformation/dehydroxylation temperatures for different iron oxides and oxyhydroxides.

Compound	Formula	Transformation temperature	Reference
Ferrihydrite	$5Fe_2O_3.9H_2O$	150-400 °C	Eggleton and Fitzpatrick (1988), Schwertmann and Cornell (2000)
Goethite	α-FeOOH	285-380 °C	Rizov (2012)
Akaganeite	β-FeOOH	190-350 °C	Goni-Elizalde and Garcia Clavel (1988b)
Lepidocrocite	γ-FeOOH	180-200 °C	Schwertmann and Cornell (2000)
Feroxyhite	δ-FeOOH	240-250 °C	Carlson and Schwertmann (1980)
Maghemite	γ -Fe_2O_3	325-460 °C	Schwertmann (1987)
Magnetite	Fe_3O_4	200-450 °C	Schmidt and Vermaas (1955)

Two small peaks below 150 °C are due to sulphur melting at ~120 °C and gypsum associated water at~95-100 °C. However, sulphur allotrope transformation can also produce a shoulder between ~84-97 °C (Timmons and Goertz, 1994). After gypsum and sulphur extraction (Figure 5.2b), a very small exothermic peak centered at 200 °C was due to remaining traces of sulphur. This peak was followed by a broad endothermic peak between ~220-410 °C with associated weight loss of ~6 %. In this temperature range dehydroxylation or dehydration of hydrous ferric oxides takes place which then transform to a more stable phase i.e. hematite. The dehydration/dehydroxylation is an endothermic process as it consumes heat and usually occurs with an associate weight loss. Transformation is an exothermic process because the material releases heat and transforms to a more stable phase, however, it may go without any change in the sample weight. The presence of endothermic peak between ~220-410 °C followed by a small exothermic peak~420 °C suggests the presence of some sort of less stable iron oxide phases.

It is believed that hematite is formed by the dehydration and internal rearrangement mechanism of ferrihydrite or hydrous ferric oxide phases (Cornell and Giovanoli, 1988) i.e. during Fe (III) hydrolysis ferrihydrite is first formed, which after dehydration and structural rearrangement transforms to hematite. Therefore, the endothermic peak between 220-410 °C (dehydration) and the exothermic peak (transformation) at~420 °C for sample S1 can be attributed to the presence of ferrihydrite type phases in the sample. The presence of hematite was confirmed in the post thermal

XRD analysis, see Table 5-2. Pre thermal XRD analysis did not show the presence of hematite in the sample.

Any thermal event above ~440 °C was attributed to the decomposition of jarosite. Jarosite dissociates in two steps producing two endothems starting at ~446 °C and ~683 °C due to dehydroxylation and sulphate losses, respectively (Chen *et al*., 2013). In certain cases evolved sulphate can sequester as ferric sulphate into the sample which can lead to a weight gain step as observed in Figure 5.2b (Sammut and Welham, 2002).

When TGA/DTA was carried out under nitrogen atmosphere for sample S1, an endothermic peak between ~220-320 °C (with two small exotherms , centered at 262 and 290 °C) appeared due to sulphur volatilization. In this temperature range dehydroxylation of iron oxides/oxyhydroxides also takes place (Rizov, 2012). After gypsum and sulphur extraction (Figure 5.2d), a broad endothermic peak in the temperature range 220-410 °C, which also contains a small exotherm at ~300 °C appeared. This was followed by an exothermic peak afterwards (420 °C). According to the sample chemical composition, thermal events in the temperature range 200-480 °C appear due to the presence of poorly crystalline iron oxide phases. Therefore a small exotherm at ~300 °C could appear due to the formation of an intermediate phase during transformation of poorly crystalline/amorphous iron oxides to hematite. During ferrihydrite transformation, an intermediate phase, maghemite has been reported in the literature (Cornell and Schwertmann, 2003).

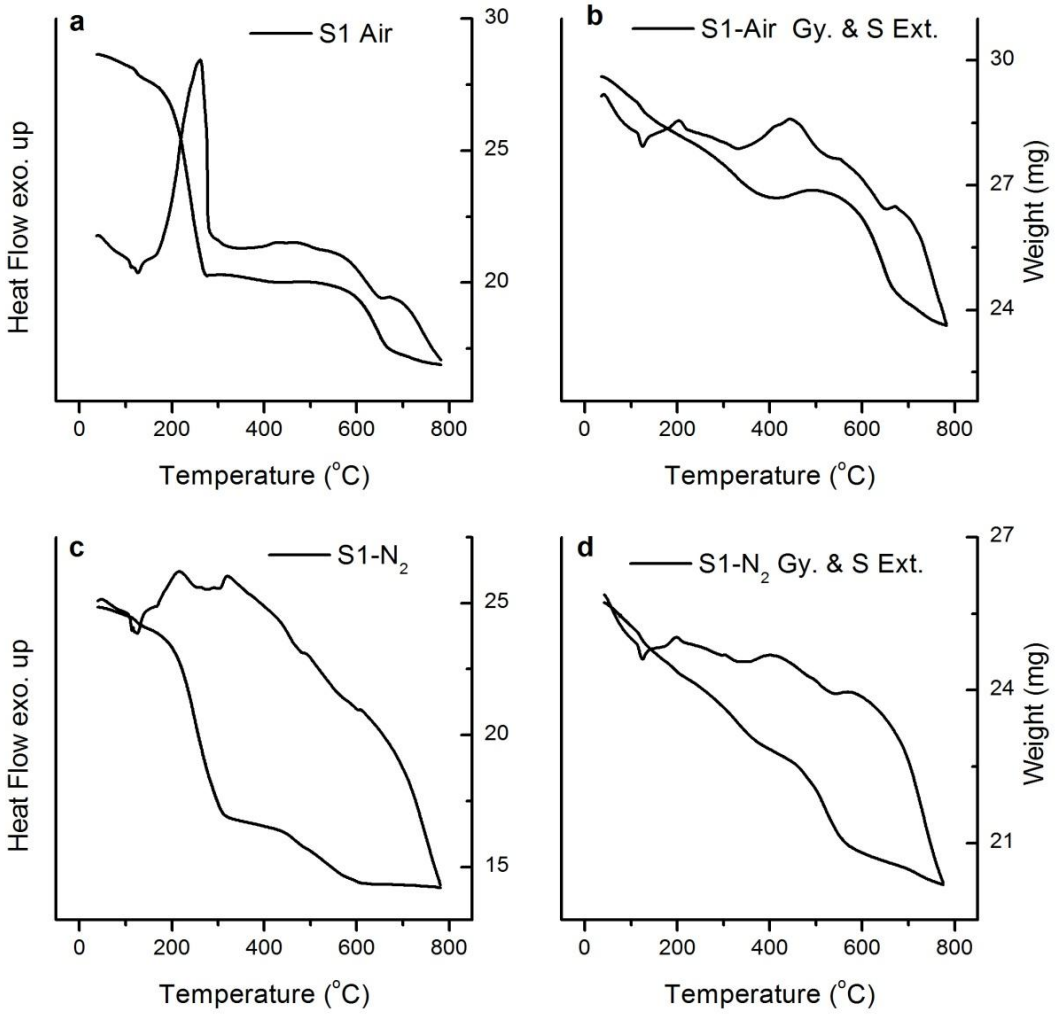

Figure 5.2 TGA-DTA traces of sample S1 in air and nitrogen atmospheres: a) as received S1 in air, b) S1 after gypsum and sulphur extraction in air, c) as received S1 in nitrogen, d) S1 after gypsum and sulphur extraction in nitrogen.

Figure 5.3 shows the TGA-DTA traces for S2 wherein the peaks below 150 °C and in the range 200-300 °C are the same as described earlier for S1. However, after gypsum and sulphur extraction (Figure 5.3b, d), an endothermic peak was observed in the temperature range 190-240 °C (in both air and nitrogen atmospheres). Considering the chemical

composition of S2, this endothermic peak (190-240 °C) can be attributed to the presence of amorphous/poorly crystalline ferric oxide phases. Dehydration of such phases can produce endotherms in this region (Table 5-3). After gypsum and sulphur extractions, there is no compound, other than iron oxides/oxyhydroxides, left in the sample that can produce a peak in this temperature range (*cf.* Table 5-2, XRD S2).

Dehydroxylation of goethite takes place between ~365-410 °C. Generally, the goethite-hematite transformation peak is sharp at 385 °C for highly crystalline goethite, however for finely grained and poorly crystalline goethite, the dissociation temperature varies (Rizov, 2012; Swamy *et al*., 2003). Therefore, the peak between ~365-410 °C (Figure 5.3b) was attributed to dehydroxylation of goethite in S2. However, under nitrogen atmosphere this peak was not clearly distinguishable.

Similarly Figure 5.4 shows TGA-DTA traces of sample S3. After gypsum and sulphur extraction a small endothermic peak in the temperature range 200-300 °C (Figure 5.4b,d) indicated the presence of a small amount of amorphous/poorly crystalline ferric oxide (Walter *et al*., 2001). Comparison of the three samples (i.e. Figure 5.2b, Figure 5.3b, Figure 5.4b) shows that dehydroxylation (~200-400 °C) of sample S1 exhibits a broad peak as compare to S2 and S3. This is consistent with HaHC extraction results in Chapter 4 as this sample was found to have the highest amount of amorphous iron oxide phase.

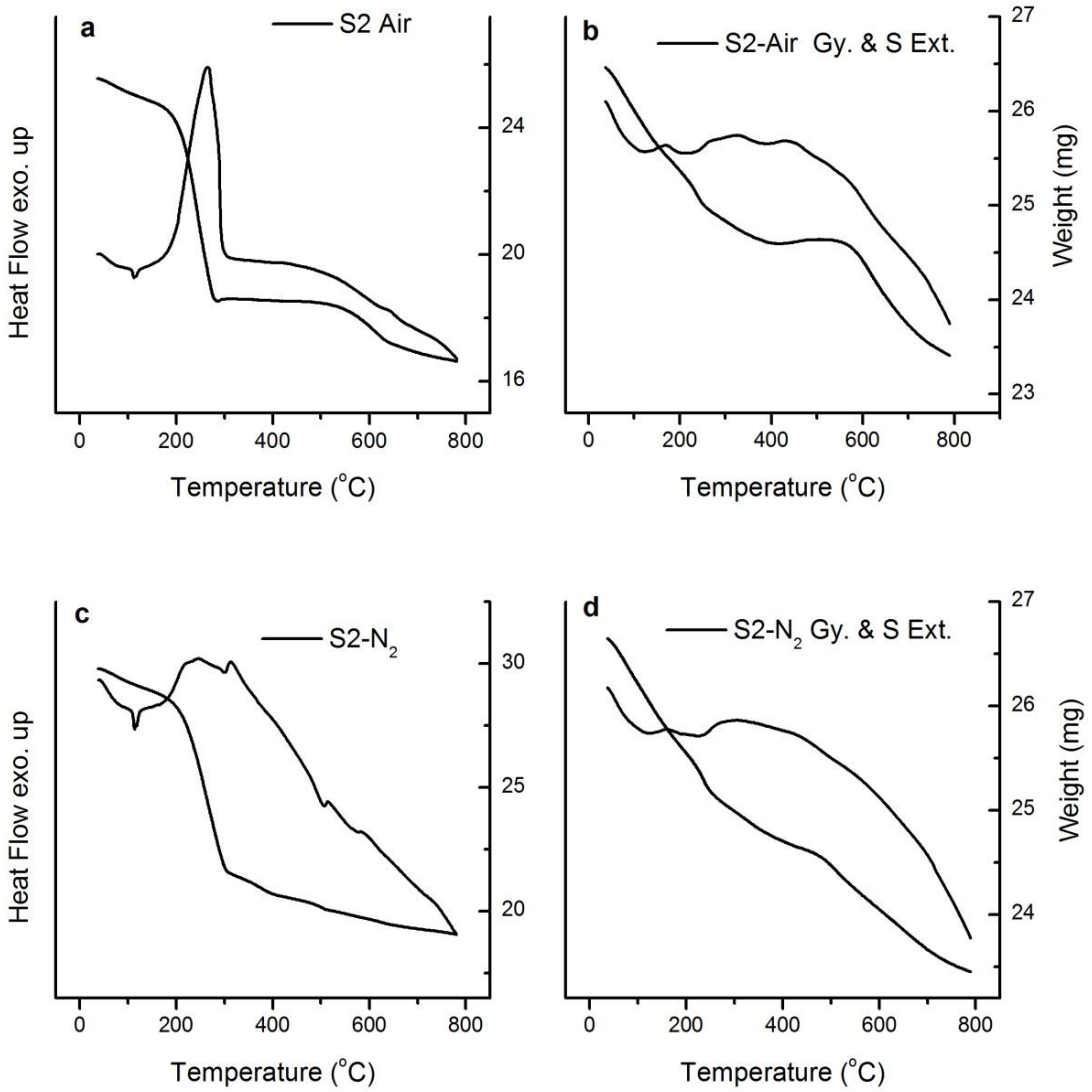

Figure 5.3 TGA-DTA traces of sample S2 in air and nitrogen atmospheres: a) as received S2 in air, b) S2 after gypsum and sulphur extraction in air, c) as received S2 in nitrogen, d) S2 after gypsum and sulphur extraction in nitrogen.

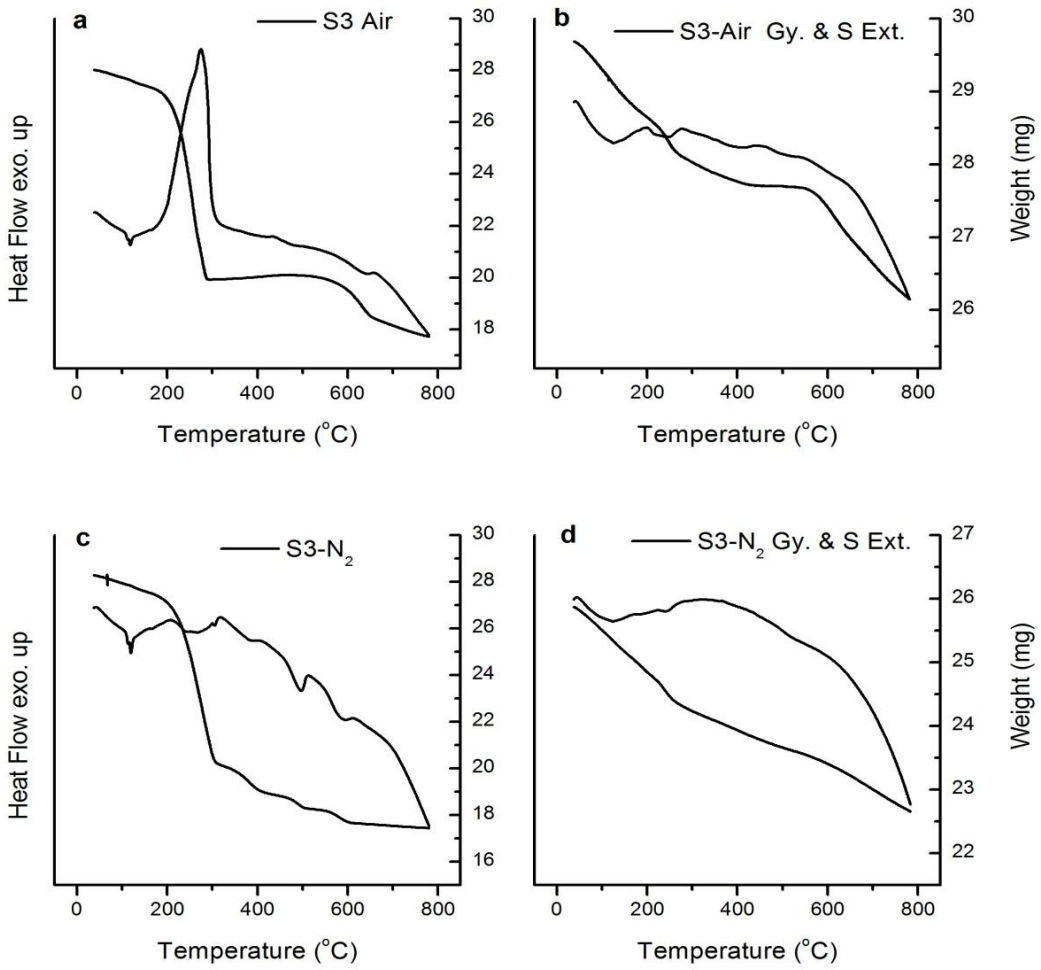

Figure 5.4 TGA-DTA traces of sample S3 in air and nitrogen atmospheres: a) as received S3 in air, b) S3 after gypsum and sulphur extraction in air, c) as received S3 in nitrogen, d) S3 after gypsum and sulphur extraction in nitrogen.

5.3.2 Raman spectroscopy

Structural information obtained from Raman spectra is related specifically to the short range bonding environment within the material. It can provide useful information for the study of poorly crystalline phases. Raman spectroscopy of the leach residue samples

was carried out with the aim to confirm the presence of different iron oxides and oxyhydroxides. A major challenge with Raman spectroscopic studies of amorphous or poorly crystalline iron oxide/oxyhydroxides is the fast transformation of metastable iron oxide phases under high laser powers. Poorly crystalline iron oxides can also lead to broadening of Raman bands (Rull et al., 2004) or variation in the relative intensity of bands (De Faria *et al*., 1997); however these characteristics do not result in a change in the position of the band.

Different laser powers were applied to select an optimum power for analysis. Figure 5.5 shows the effect of laser power on sample S1. The full power used was 17 mW and it was reduced successively down to 25 %, 10 %, 1 % and 0.01 % of the full power. A different spectrum for 25 % laser power indicates that the laser power was high enough to transform the labile/poorly crystalline phases. For all the laser powers ≤ 1 % of the full power, the spectra produced were similar. A laser power of 0.01% was selected to analyze the samples to avoid the complications induced by the higher laser powers.

Among iron oxides and oxyhydroxides, hematite (α-Fe_2O_3), goethite (α-FeOOH), and lepidocrocite (γ-FeOOH) produce strong Raman scattering, whereas magnetite (Fe_3O_4) and maghemite (γ-Fe_2O_3, which has magnetic and superparamagnetic forms) are relatively weak Raman scatterers. The Raman spectral peaks of hematite can vary in position due to variation in crystallinity or grain size. Goethite and lepidocrocite both have orthorhombic symmetry, but have different space groups and produce different Raman spectra. The main peaks of goethite and lepidocrocite occur at 386 cm^{-1} and 252 cm^{-1} respectively. Magnetite

has its main Raman peak near 667 cm^{-1}, and is distinguishable from other iron oxides of spinel (or inverse-spinel) structure. The six-line ferrihydrite has three bands 370, 510 and 710 cm^{-1} that can be distinguished in the spectrum measured at low laser powers (0.1 mW). In the spectrum of the two-line ferrihydrite, only the strong 710 cm^{-1} band is distinguishable (Hanesch, 2009; de Faria *et al*., 1997).

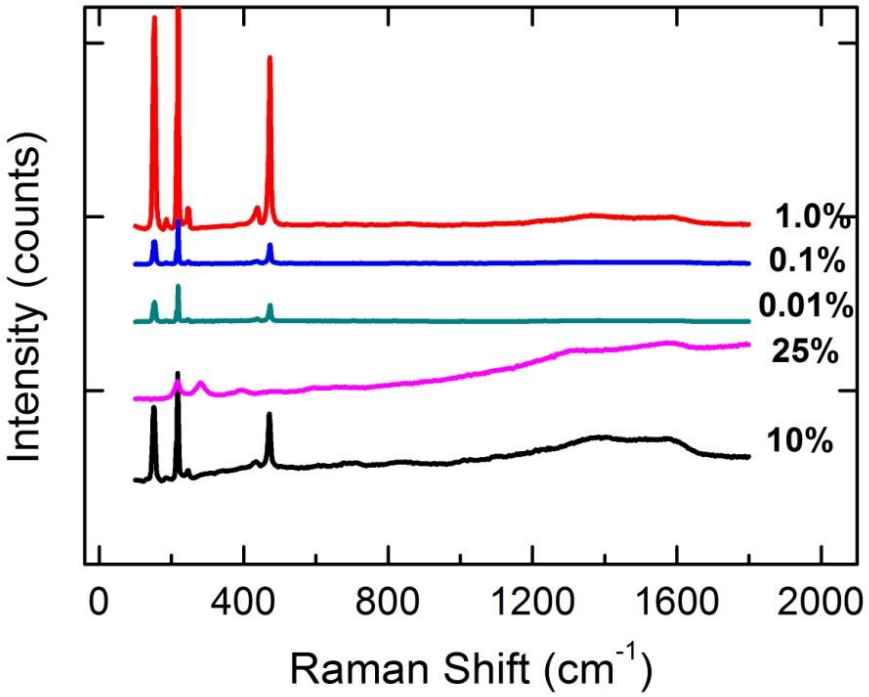

Figure 5.5 Series of Raman spectra showing effect of laser power on sample S1. The percentages shown are the percent of 17 mW full power.

Six different peaks (150, 221, 244, 292, 439, 500 cm^{-1}) were observed in the Raman spectra of the residue samples as shown in Figure 5.6. Considering the sample chemical composition, peaks below 200 cm^{-1} were attributed either to sulphur or gypsum (Krishnamurthy and Soots, 1971). The peaks at 221, 244 and 292 cm^{-1} were attributed to the presence of hematite in the samples (Hanesch, 2009; de Faria *et al*., 1997). The peak at

439 cm^{-1} was attributed to jarosite (Frost *et al*., 2005; Sasaki *et al*., 1998). The peak at 500 cm^{-1} was attributed to ferrihydrite type phases; minerals containing Si-O bonding can also contribute to this peak. The ferrihydrite peak usually appears at 510 cm^{-1}, however, the peak position can vary with structural order (Hanesch, 2009; de Faria *et al*., 1997). After HaHC extraction the peak at ~510 cm^{-1} was reduced in intensity in samples S1 and S3, see Figure 5.6; S1, S1-R1 and S3, S3-R1. This suggests the presence of poorly ordered or ferrihydrite type phases in these samples. However, the spectra produced by S2 were not clearly distinguishable due to structural variations and possibly due to interference by the gangue minerals.

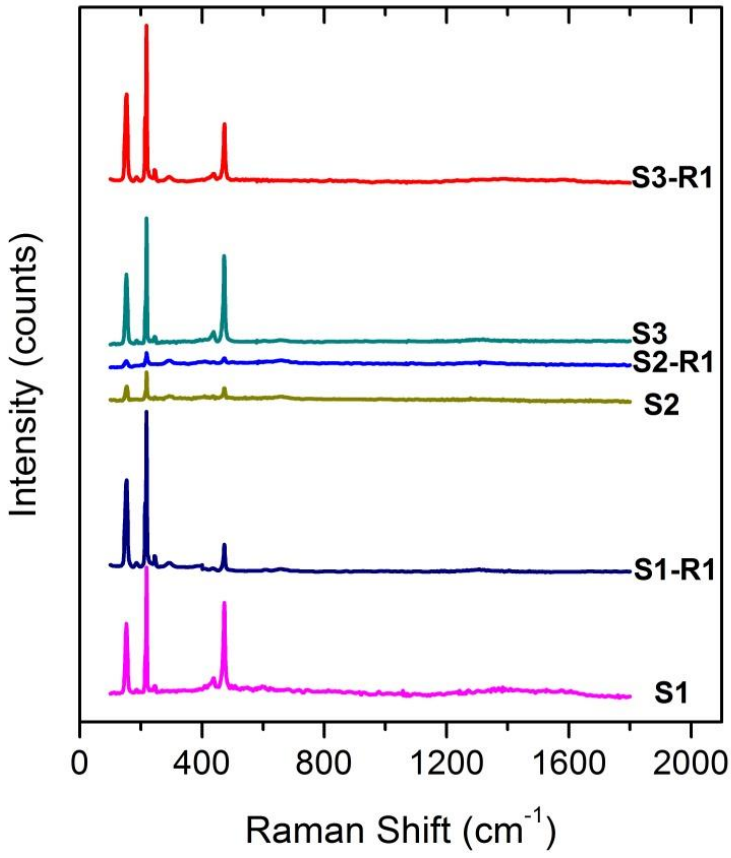

Figure 5.6 Raman spectra of the samples: S1, S2 and S3. Samples: S1-R1, S2-R1 and S3-R1 are the residues left after HaHC extractions of S1, S2 and S3 respectively.

5.3.3 Fourier transformed infrared spectroscopy.

The infrared spectra obtained for the sulphide leach residue samples S1, S2 and S3 are shown in Figure 5.7 and summarized in Table 5-4. Although there are many species contributing to the IR bands making it complex to interpret and identify contribution from the individual species, a good agreement was found to be present between experimental results and data from the literature. The various peaks observed in all the samples are labeled in Figure 5.7. In general peaks in the 400-1500 cm^{-1} region appear due to SO_4^{2-} vibrations, 1500-2400 cm^{-1} due to H_2O bending vibrations and 2400-4000 cm^{-1} due to OH^- stretching vibrations (Powers *et al*., 1975; Schwertmann and Cornell, 1991; Bigham *et al*., 1994).

In this study, the band at approximately 3383 cm^{-1} is attributed to adsorbed water in all the samples. In sample S1, the bands at (628, 1005, 1083, 1201, 1621 cm^{-1}) are attributed to jarosite and were in good agreement with the literature (Baron and Palmer, 1996; Powers et. al., 1975). The band at ~1420 cm^{-1} can appear due to Fe-OH bonding, indicating the presence of iron oxyhydroxide in S1 (Tang and Liu, 2012). The band at 797 cm^{-1} is attributed to goethite in all the samples. Bands between ~435-526 cm^{-1} are attributed to hematite.

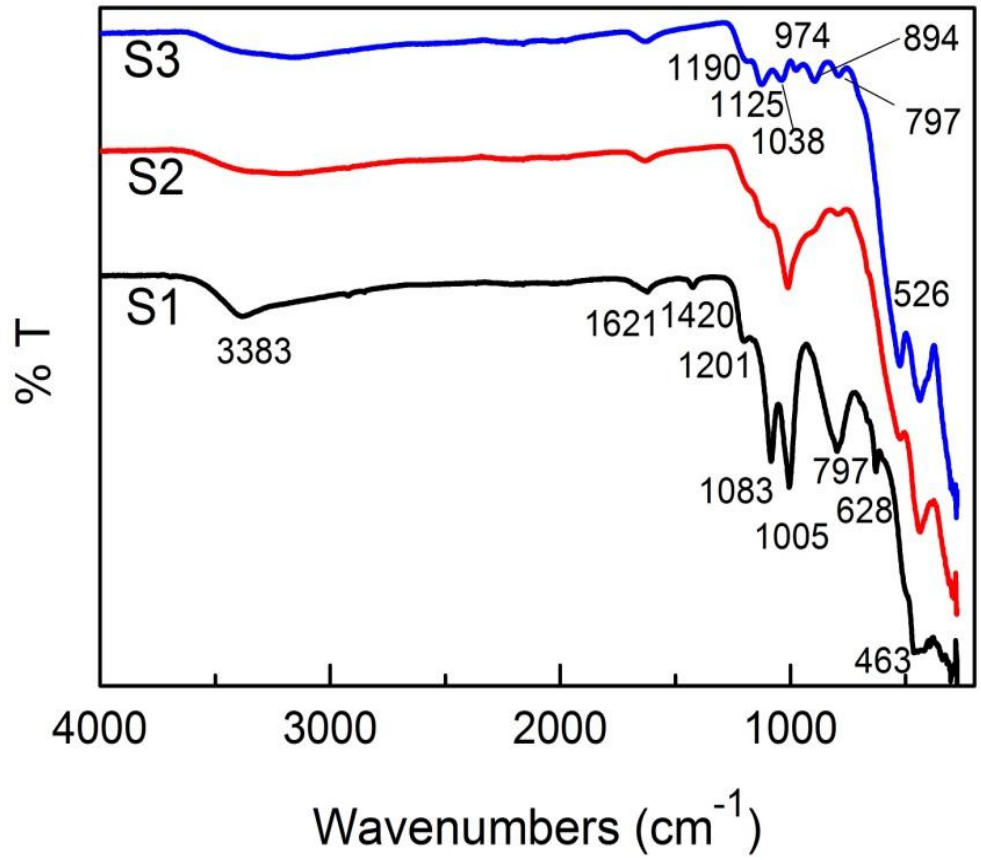

Figure 5.7 Infrared spectra of the leach residue samples: S1, S2 and S3.

A series of bands in sample S3 between 894 and 1190 cm^{-1} were attributed to the chemisorbed or surface coordinated sulphate on hematite (Cheng and Demopoulos, 2004). Since sample S1 also contained quartz (4.2 %), therefore contribution to the IR bands because of quartz was also considered. The bands at 463 cm^{-1} (Si-O asymmetrical bending vibrations), 797 cm^{-1} (Si-O symmetrical stretching vibrations); Al-O-Si (out of phase deformation) and 1083 cm^{-1} (Si-O asymmetrical stretching vibrations) in S1 could also be because of SiO_2 (Suresh *et al*., 2011). Albite and muscovite were also present in sample S1; these can also contribute to the band at 1005 cm^{-1}. After HaHC extraction the band

at ~1420 cm^{-1} was removed (results were reproducible) as shown in Figure 5.8. However, no other significant changes were observed in the spectrum after HaHC extraction. Because of the various species contributing to the IR bands it was difficult to conclusively assign the bands to a single phase; however, the absence of Fe-OH band after HaHC extraction indicates the presence of iron oxyhydroxide phases. This further confirms that the HaHC leached material is an iron oxyhyroxide phase.

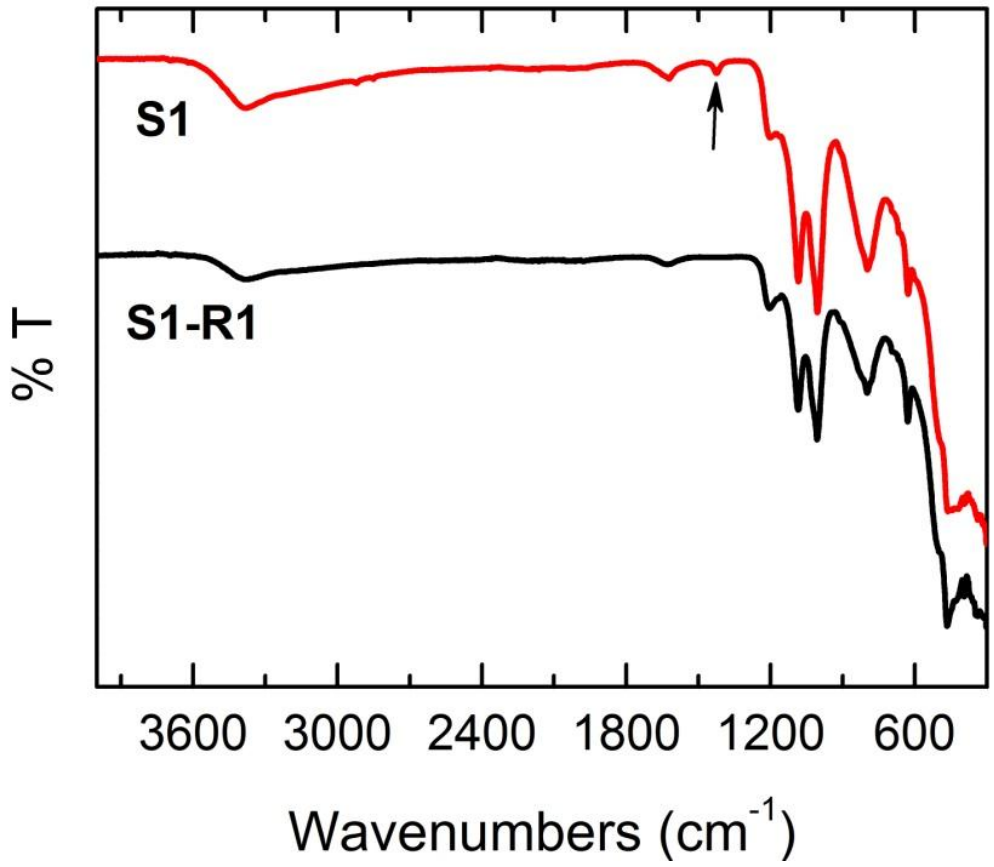

Figure 5.8 Infrared spectra of sample S1: before (S1) and after (S1-R1) HaHC extraction.

Table 5-4 Assignment of FTIR bands in S1, S2 and S3 to different bonds.

Sample	Band Position (cm^{-1})	Attribution	Source
S1	3383	OH stretching vibrations	H_2O
	1621	HOH bending vibrations	H_2O
	1420	Fe-OH	Fe oxide/hydroxide
	1201, 1083, 1005, 628, 463	SO_4^{2-} vibrations	Jarosite
	1005	OH deformation	Jarosite
	463	Fe-O	Hematite
	797	Si-O, Al-O-Si, Fe-OH	Quartz, Muscovite, Albite, Goethite
S2	3215	OH stretching vibrations	H_2O
	1627	HOH bending vibrations	H_2O
	439,523	Fe-O	Hematite
	797, 894	Fe-OH	Goethite
	1008	OH deformation	Jarosite
	1083	SO_4^{2-} vibrations	Jarosite
S3	3136	OH stretching vibrations	H_2O
	1627	HOH bending vibrations	H_2O
	435, 526	Fe-O	Hematite
	797, 894	Fe-OH	Goethite
	974, 1038, 1125, 1190	Fe-O, Fe-S, SO_4^{2-}	Hematite, Pyrite, Jarosite

5.4 Conclusions

The thermal transformation behaviour of medium temperature sulphide concentrate leach residues was studied. All the residue samples contained variable amounts

of iron oxides/oxyhydroxides which dehydroxylate and transform to hematite over a broad temperature range. The dehydroxylation of amorphous ferric oxide phases over a range of temperature suggests the wide variation in the composition of the amorphous phases. TGA/DTA and Raman spectroscopic analysis gave some indication of the resemblance of amorphous phase to ferrihydrite type phases in sample S1.

Raman spectroscopic analysis showed that iron oxides/oxyhydroxides present in the samples are very labile and transform to hematite even at low laser powers. The results suggest that widely varying structures are obtained during medium temperature leaching. Thermal transformations of the iron oxides/oxyhydroxides were found to vary over a wide range of temperature due to lack of purity and crystallinity. The knowledge of thermal transformation temperatures is useful when residues are evaluated for safe disposal. The various observations made in this chapter point to study the leaching conditions which can lead to a better crystalline residue so that iron chemistry can be manipulated to obtain a stable and eco-friendly residue, with attendant benefits to process efficiency/ metal recovery.

Chapter 6. Iron precipitation and copper loss from simulated sulphate-chloride solutions at 150 °C – one variable approach

6.1 Introduction

It has been seen in the previous chapters that the precipitation of iron in the form of crystalline phases minimizes the valuable metal loss to the residue and produces a more suitable residue for tailings. In this chapter, the effect of controllable process parameters and their relative importance on precipitation conditions will be presented. The overarching goal is again to maximize hematite yield while minimising Cu loss to the precipitation product. The experimental range of each factor was selected to simulate the process conditions encountered in typical CESL and Vale medium temperature hydrometallurgical processes. As explained earlier, both of these processes employ a chloride "catalyst" in the form of soluble chloride salts as this is believed to enhance the leaching kinetics by breaking the passive sulphur layer that forms around the sulphide minerals as they leach, and by activating the cuprous/cupric couple. Therefore, the experiments presented in this chapter were carried out in the presence of chloride i.e. mixed sulphate-chloride solutions.

Experiments were carried out to study the effect of initial concentrations of: ferric iron, chloride, H_2SO_4; retention time, temperature and reagent grade hematite seed. One factor was varied at a time while keeping all others constant. The effect of each variable was recorded against two responses i.e. % Fe precipitation and % Cu in solids.

6.2 Experimental work

Reagent grade chemicals ($CuSO_4 \cdot 5H_2O$, $Fe_2(SO_4)_3 \cdot 7H_2O$, LiCl) and de-ionized water (10 MΩ) were used for all the experiments. The superscript notation (i.e. Fe^{3+}, Cu^{2+} and Cl^-) will be used, in the remainder of the document, to represent the amounts of initially added elements. However, due to formation of metal ion complexes in the solution, it does not always represent the total amount of free ions.

The experiments were carried out using 1 litre of solution contained in a glass liner (24.7 x 9.65 cm) in a 2 litre Parr autoclave fitted with titanium internals to resist the chloride effect. Agitation was provided at 500 rpm by two 45° pitched-blade impellers with a 5.7 cm diameter. The experiments were carried out at 150 °C for 1 hour retention time (except time and temperature dependent experiments). LiCl was used instead of NaCl to avoid sodium jarosite formation. The chemicals were dissolved in 1 litre of de-ionized water in a beaker before being transferred to the autoclave. Hematite seed, where employed, was of reagent grade with average particle size of about 18 µm and was added immediately before the contents were sealed in the autoclave. About 35 minutes were required for the sealed contents to reach the desired temperature of 150 °C. Retention time was calculated from the moment the contents reached the reaction temperature (150 °C) to the end of the heating. No oxygen overpressure was used, except for the enclosed oxygen from air, and the contents in the autoclave were under a steam pressure of 400 – 500 kPa. At the end of heating, the contents were immediately cooled to room temperature within~5 minutes. The

slurries were filtered on a Buchner vacuum filter with Whatman 42 ash less filter paper, washed with 3 – 4 litres of warm de-ionized water and dried overnight in an oven at 60 °C. Dried samples were analyzed by ICP-OES after complete multi acid digestion. About 2 – 3 g of the precipitates were analysed by quantitative X-ray powder diffraction (QXRPD). Quantitative phase analysis of all the precipitates was done using the Rietveld method and X-ray powder diffraction data. Corundum was used as an internal standard for quantification of the relative amounts of crystalline and amorphous phases in a similar way as described in Chapter 4. The size distribution of the precipitates was determined with a Malvern Mastersizer 2000 Laser Diffraction Particle Size Analyser. Hydroxyl amine hydrochloride (HaHC) extractions were carried out as described in Chapter 4.

Acid is produced during the hematite precipitation reaction, which affects the final equilibrium position of the reaction. Final acid concentration of the solutions was measured by titration with 0.1N NaOH. A solution of Mg-EDTA (0.2M $MgSO_4$ + 0.1M EDTA) was used to complex metal ions that would normally contribute protons by reaction with hydroxide ions in the water (Rolia and Dutrizac, 1984).

Transmission electron microscopy (TEM) was performed using a 120 kV tungsten filament Hitachi H7600 Transmission Electron Microscope capable of 0.35 nm point-to-point resolution. To prepare samples, a small amount of the washed and dried powder was dissolved in ethanol. A few drops of the faintly coloured water were placed on a holey carbon film supported by a copper mesh TEM grid.

6.3 Results and discussion

6.3.1 Effect of initial iron concentration

Figure 6.1 shows that an increases in the initial iron concentration of the solution results in a decrease in apparent % Fe precipitation. A similar trend for H_2SO_4 concentration confirms that addition of $Fe_2(SO_4)_3$ is similar to the addition of H_2SO_4 to the solutions i.e. the presence of higher amounts of ferric ion in the solution increases the hydronium ion activity and decreases pH. Secondly, higher initial ferric concentrations slow the hydrolysis rate due to differences in the nature and kinetics of the precipitating phases; however, under equilibrium conditions higher initial ferric levels are expected to result in more precipitation to occur.

Hydrolysis of ferric iron generates acid ($K = [H^+]^6/[Fe^{3+}]^2$). The equilibrium constant depends upon both, the concentration of acid and ferric ions in the solution. Because of the exponential effect of acid on the equilibrium constant, it effectively controls the extent of reaction. Increasing acid concentration, in fact, increases the equilibrium ferric concentration of the solution which results in a decrease in the % Fe precipitation.

QXRPD analysis of the precipitates (Table 6-1) showed that hematite was the dominant phase below 15 g/L initial Fe^{3+}, while hydronium jarosite was the dominant phase above that ferric concentration. The phase, volaschioite, given in Table 6-1 is from the family of hydroxy sulphate phases explained elsewhere (Biagioni *et al.*, 2011). Analysis of

the final free acid concentration (Table 6-1) showed that in all the cases final free acid concentration was less than the upper stability limit of hematite i.e. 53.4 g/L free H_2SO_4 as determined by Sasaki *et al*. (1993). At low acid (< 53.4 g/L H_2SO_4) concentrations one should expect the formation of hematite, however, QXRPD analysis showed the formation of jarosite when higher initial ferric levels were used. The formation of hydronium jarosite or hydroxy-sulphate phases at higher initial ferric concentrations is attributed to the kinetic stability of these phases at higher initial ferric concentrations. The kinetic stability of hydronium jarosite or hydroxy-sulphate despite their thermodynamics instability is, in fact, the manifestation of Stranski's rule or Ostwald's step rule as discussed earlier. Hydronium Jarosite and volaschioite are metastable relative to hematite and transform to hematite at higher temperatures and/or longer retention times. Formation of these phases at higher initial ferric concentrations can occur within the stability region of hematite (Umetsu *et al*., 1977; Levy and Quemeneur, 1964). For detailed discussion about the presence of metastable phases and their transformation refer to section 2.6 of the thesis.

Figure 6.2 illustrates the effect of initial iron concentration on the composition of the product. The Fe content decreased from about 59 to 36 % and SO_4^{2-} content increased from about 7 to 35 % as the initial iron concentration increased from 1.5 to 30.0 g/L Fe^{3+}. The relationship between the initial ferric or acid concentrations and the corresponding Cu/Fe ratios of the solid precipitates is shown in Figure 6.3. The relatively higher Cu content of the precipitates for lower initial Fe^{3+} concentrations is in fact related to the hydrolysis rate and its effect on the supersaturation and nucleation – growth mechanism. The rate of

hydrolysis increased initially and then decreased for higher initial ferric concentration (> 15 g/L Fe^{3+}), see Figure 6.4. A similar relationship between higher initial ferric concentrations and hydrolysis rate was observed by Umetsu *et al*. (1977).

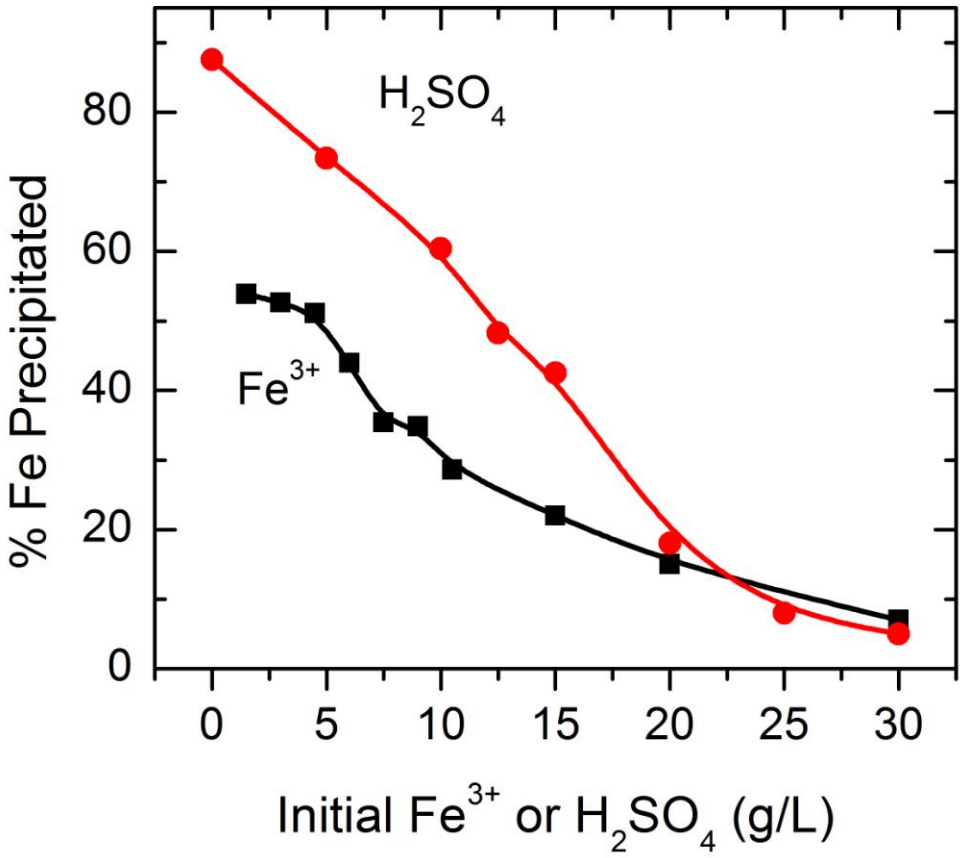

Figure 6.1 Variation of % Fe precipitation with initial concentrations of Fe^{3+} and H_2SO_4; for the experiments carried out for 1 hr. at 150 °C in the system containing 11.0 g/L Cl^- and 30.0 g/L Cu^{2+}.

Note: In case of Fe^{3+} experiments an initial amount of 15 g/L H_2SO_4 was added to all the experiments while in case of H_2SO_4, 6.0 g/L initial Fe^{3+}, added as $Fe_2(SO_4)_3$, was used for all the experiments.

Table 6-1 Phases identified by QXRPD when the concentration of iron was varied from 1.5 – 30 g/L for the experiments carried out for 1 hr at 150 °C in the system containing 15.0 g/L H_2SO_4, 11.0 g/L Cl^- and 30.0 g/L Cu^{2+}.

Fe (g/L)	Final Free acid (g/L)	Phase (Wt. %) error (± 2 %)			
		Hematite α-Fe_2O_3	Volaschioite $Fe_4(SO_4)O_2(OH)_6.2H_2O$	Jarosite $(H_3O)Fe^{3+}{}_3(SO_4)_2(OH)_6$	Amorphous
1.5	17.0	87.3	-	-	12.7
3.0	19.0	85.7	-	-	14.3
4.5	21.0	85.8	-		14.2
6.0	22.0	86.0	1.0	-	13.0
7.5	22.0	78.6	6.9		14.4
9.0	23.0	67.6	12.8	-	19.6
10.5	23.0	65.2	16.9		17.9
15.0	23.0	52.3	20.0	7.7	20.0
20.0	20.0	8.7	4.1	72.8	14.5
30.0	20.0	2.7	-	81.0	16.2

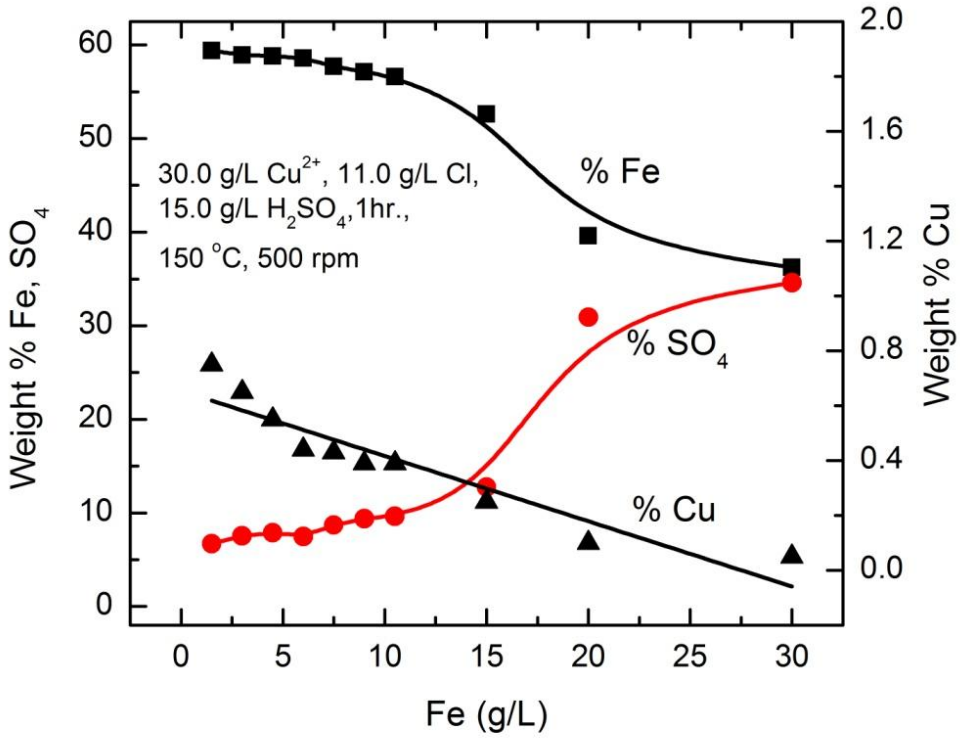

Figure 6.2 Effect of initial concentration of iron on the composition of the precipitates.

Apparent precipitation rate in g/L/hr and particle size analysis results are compared in Figure 6.4. At lower initial ferric concentrations growth to nucleation ratio increased as the ferric concentration of the solution increased. However, when precipitation rate was highest growth to nucleation ratio decreased i.e. more nuclei formed than the growth of the existing nuclei and finally at higher initial ferric concentrations (> 15 g/L) growth to nucleation again increased (high ferric levels result in a slower hydrolysis rate), see Figure 6.4. Higher ferric concentrations in fact increase the activity of the hydronium ion as explained earlier, which results in a slower precipitation rate and prefer growth over nucleation. Particle size analysis of the precipitates also showed that in the regions where the hydrolysis rate was highest, particle growth was not preferred.

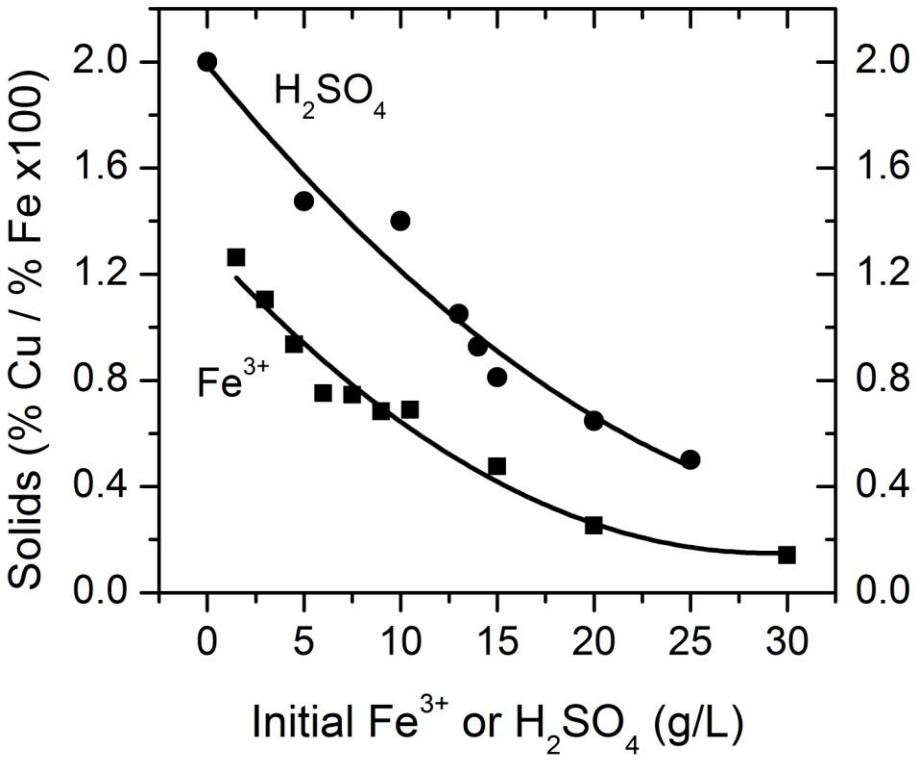

Figure 6.3 Effect of initial iron and acid on Cu/Fe ratio of the precipitates. Note: For higher acid concentration product mass was not enough for characterization.

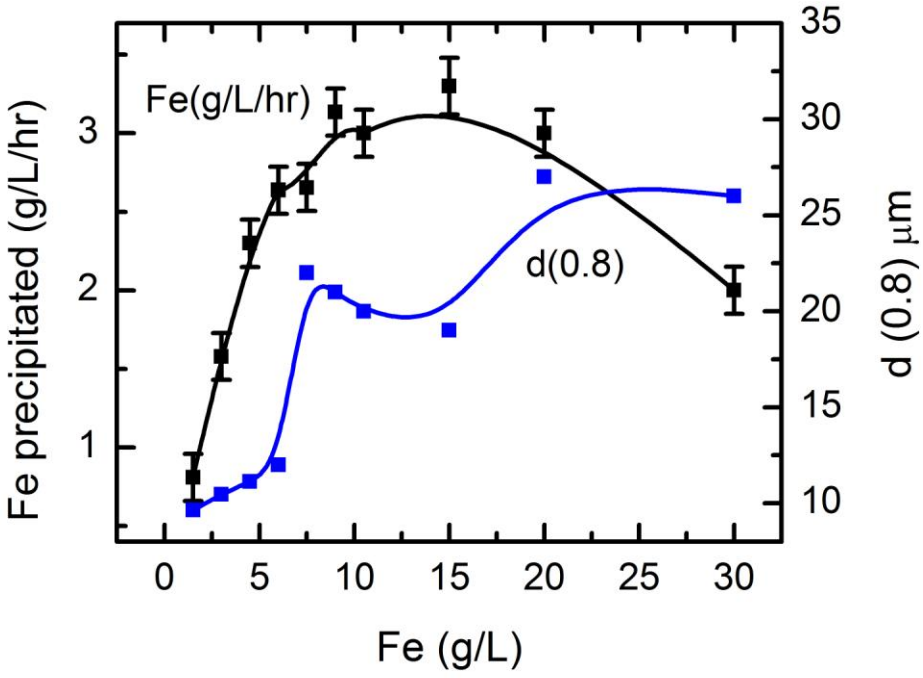

Figure 6.4 Effect of initial ferric concentration on the apparent iron precipitation and particle size of the precipitates. Other conditions: 15 g/L H_2SO_4, 11 g/L Cl^-, 30 g/L Cu^{2+}, 150 °C.

6.3.2 Effect of initial sulphuric acid concentration

The effect of initial acid concentration on the % Fe precipitation is shown in Figure 6.1. Figure 6.1 shows that % Fe precipitation decreases with an increase in the initial acid concentration of the solution in a nearly linear manner because of increase in the equilibrium ferric concentration of the solutions. Almost negligible amounts of the initially present iron were precipitated when the acid concentration was 30 g/L or higher. X-ray diffraction analysis of the precipitates showed the precipitates consist of poorly crystalline hematite. However, at lower initial acid concentration (< ~12.5 g/L) certain amounts of

goethite were also precipitated along with hematite. The relative amount of goethite decreased as the concentration of H_2SO_4 increased from 0.0 to ~12.5 g/L. The precipitates made from the solutions containing ≥ ~12.5 g/L H_2SO_4 consisted of poorly crystallized hematite as the dominant phase, see Table 6-2.

Table 6-2 Phases identified by QXRPD when initial H_2SO_4 concentration was increased from 0 to 20 g/L for the system containing 6 g/L Fe^{3+}, 11 g/L Cl^-, 30.0 g/L Cu^{2+} at 150 °C for 1 hr.

H_2SO_4 (g/L)	Phase (Wt. %) error (± 2 %)			
	Hematite α-Fe_2O_3	Goethite α-FeOOH	Volaschioite $Fe_4(SO_4)O_2(OH)_6.\ 2H_2O$	Amorphous
0	79.3	7.1	1.2	12.4
5	80.5	4.7	1.4	13.4
10	81.8	2.7	1.6	13.9
12.5	82.8	0	2.5	14.7
13.5	83.6	0	2.6	13.8
15	84.8	0	3.1	12.1
20	84.1	0	4.6	11.3

Figure 6.5 shows the composition of the precipitates for different initial acid concentrations. The Fe content decreased from ~56 % to 54 % and sulphate content increased from ~5 to 9 % as the acid concentration increased from 0 to 20 g/L H_2SO_4. Increase in sulphate content was due to the precipitation of relatively higher amounts of valoaschiote at higher initial acid concentrations, see Table 6-2. However, noticeable effect was the decrease in cu content from ~1.2 to < 0.4 %.

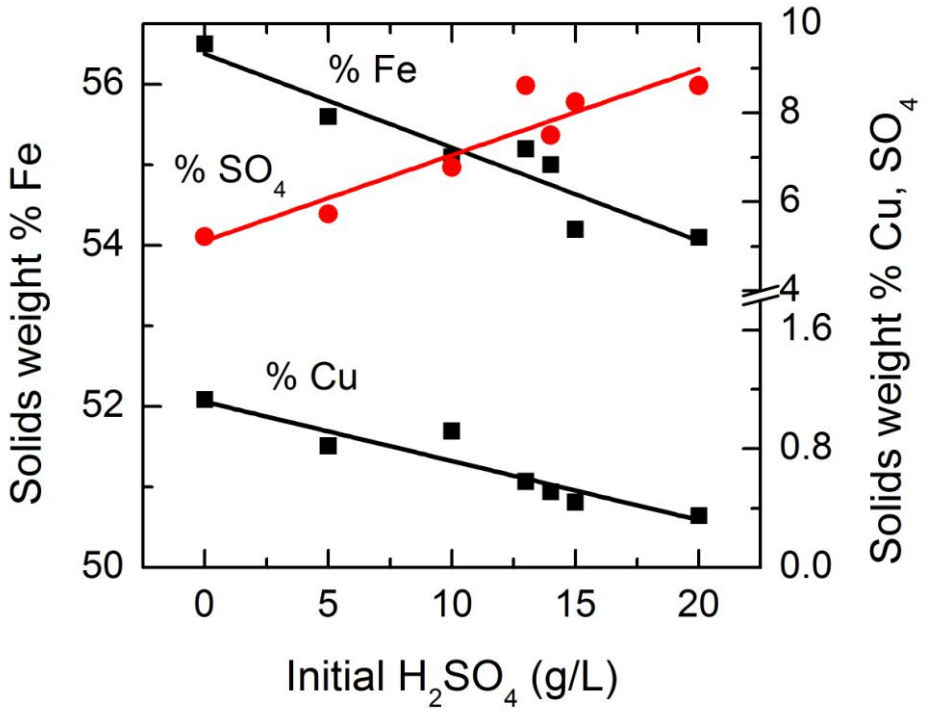

Figure 6.5 Effect of initial H_2SO_4 on the composition of the solid precipitates for the experiments carried out for 1 hr. at 150 °C in the system containing 6.0 g/L Fe^{3+}, 15.0 g/L H_2SO_4, 11.0 g/L Cl^- and 30.0 g/L Cu^{2+}.

Acid concentration was found to play an important role on the supersaturation and nucleation growth of the precipitating solid. Higher acid concentrations increase the equilibrium ferric concentration of the solution (i.e. decrease supersaturation) leading to a slower nucleation rate and coarser particles, which results in less solution occlusion and relatively lower adsorption of the divalent ions such as Cu^{2+}. The relationship between the final acid concentration and the Cu/Fe ratio of the solid product when experiments were carried out using different initial acid concentrations is plotted in Figure 6.6. Figure 6.6 shows a decrease in the Cu/Fe ratio of the solid precipitates with an increase in the final acid concentration, while increase in particle size is evident in Figure 6.7.

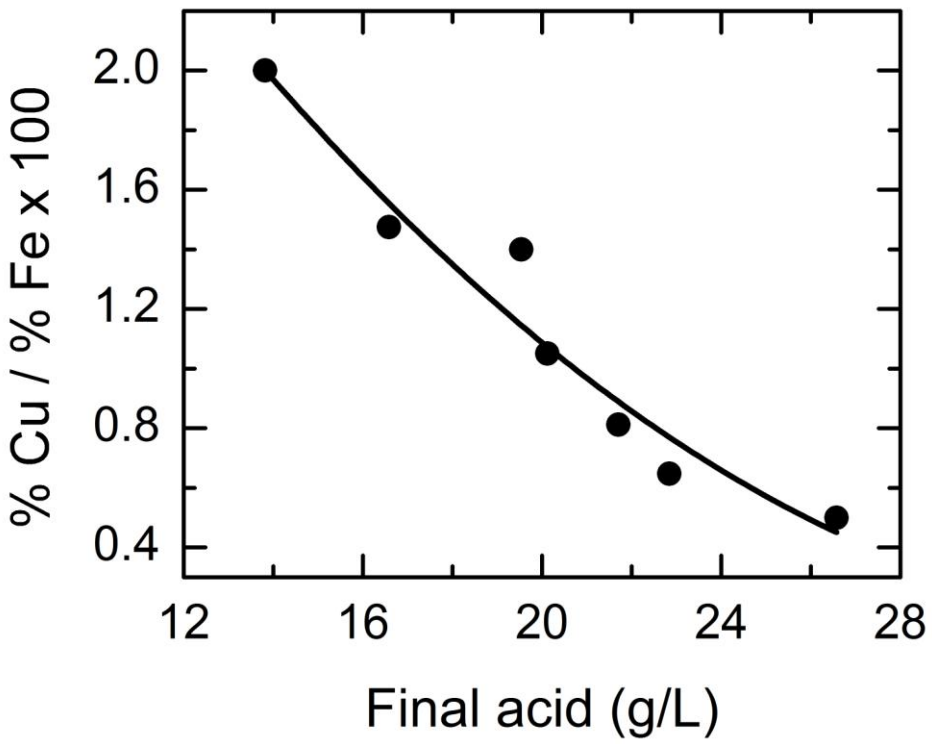

Figure 6.6 Relationship between final acid concentration and the Cu/Fe ratio of the solids.

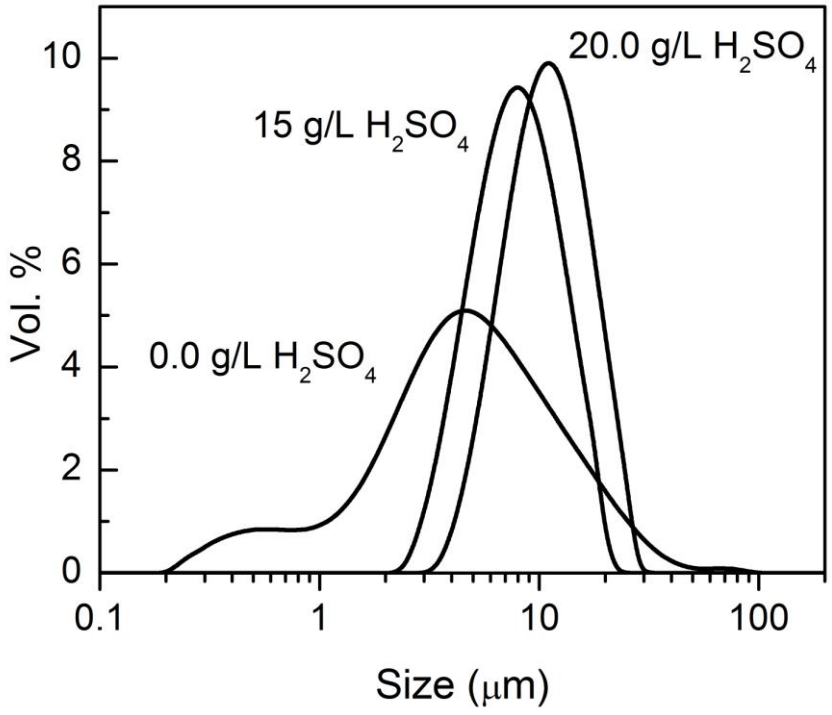

Figure 6.7 Particle size distribution of the precipitates: Other conditions: 6 g/L Fe^{3+}, 11g/L Cl^{-}, 30 g/L Cu^{2+}, 1 hr, 150 °C.

6.3.3 Effect of chloride concentration

It has been explained earlier (section 2.2 of thesis) that the presence of chloride in the medium temperature leaching enhances the leaching kinetics. However, the effect of chloride on the precipitation of iron in sulphate media is not well understood. In this regard experiments were carried out to study the effect of chloride on iron precipitation at 150 °C. Figure 6.8 shows the effect of chloride concentration on % Fe precipitation. It can be seen that the % Fe precipitation increases with an increase in the chloride concentration of the solution.

It is suggested that the hydrolysis of ferric iron starts with the formation of monomeric and dimeric species. These species then rapidly grow to form small and large polymers by formation of Fe-OH-Fe (olation) and Fe-O-Fe (oxolation) bridges, Equation (6.1). Once the polymers reach a critical size, colloid size particles are formed which grow by further addition. The subsequent growth of the nuclei takes place by incorporation of additional growth units from the solution, until the supersaturation level drops to the extent that the supply of growth units is insufficient (Dousma et. al., 1978, 1979, Diz et. al., 2006).

$$\text{Monomer, Dimers} \xrightarrow{polymerizations} \text{Polymers} \xrightarrow{nucleation+growth} \underbrace{\overbrace{Fe_8O_8(OH)_6SO_4}^{\substack{Fe_2O_3 \\ growth\uparrow oxolation}}}_{\substack{growth\downarrow olation \\ \text{FeOOH}}} \qquad (6.1)$$

Both sulphate and chloride have different tendency toward coordination with the ferric ion. The ΔG_f^o value for the anion coordination reaction $Fe^{3+} + A^{z-} \leftrightarrow (Fe^{(3-z)})^+$ is

reported to be $-143.9\ kJ.mol^{-1}$ for the Cl^- complex and $-772.8\ kJ.mol^{-1}$ for the SO_4^{2-} complex (Welham *et al*., 2000). Moreover, speciation studies of the ferric sulphate systems have shown $FeSO_4^+$ to be the dominant species at 150 °C and low pH values (Welham *et al*., 2000; Yue *et al*., 2014). Therefore, it is assumed that the system is dominated by the sulphate species which polymerize to provide precursor for nucleation. As polymerized species are removed from solution to form nuclei, iron is released from the $FeSO_4^+$ complexes to restore equilibrium. The released iron hydrolyzes and slowly incorporates into the existing surface. This phenomenon can be represented by the following reaction, Equation (6.2).

$$FeSO_4^+ + 2H_2O \rightarrow Fe(OH)_2^+ + 2H^+ + SO_4^{2-} \quad (6.2)$$

Diz *et al*. (2006) found that greater numbers of charged species are produced than being destroyed. The accelerated iron precipitation rate in the presence of chloride can be attributed to the higher extinction rate of the charged species by the excess amount of negatively charged chlorides (electrostatic attraction) ions in the system. Murphy *et al*. (1976) also observed accelerated precipitation kinetics in the presence of chloride. These authors attributed the increase in precipitation rate to a decrease in surface charge of the polycations by adsorption of negatively charged Cl^- on the polycation surface, which reduces the overall charge and increases mobility and collision rate (resulting in permanent association). Riveros and Dutrizac (1997) observed partial neutralization of iron complexes by chloride ion in a pure ferric chloride medium, see Equation (6.3).

$$2Fe(OH)_2^+ + 2Cl^- \rightarrow Fe_2O_3 + 2HCl + H_2O \quad (6.3)$$

This reaction, Equation (6.3), produces 2 protons as compare to ferric precipitation reaction (i.e. $Fe^{3+} + 3H_2O \rightarrow Fe_2O_3 + 6H^+$) which generates 6 protons. If in the above reaction i.e. Equation (6.3), hematite is partially replaced with goethite the proton yield will be even lower. The low proton yield in turn will result more precipitation to occur. Secondly, higher concentration of chloride in solution will favour free ferric to form ferric chloride complexes (Brown and Ekberg, 2016). This in turn will result more precipitation to occur. The other possible mechanism for the higher precipitation rate could be as observed by Dousma *et al*. (1978) for the ferric chloride system. These authors attributed the accelerated particle formation to the replacement of the OH^- in the polymer bridges by Cl^- i.e. $(Fe\langle^{OH}_{OH}\rangle Fe)^{4+}$ by $(Fe\langle^{Cl}_{Cl}\rangle Fe)^{4+}$ or in case of partial replacement: $(Fe\langle^{Cl}_{OH}\rangle Fe)^{4+}$. Replacement of OH^- by Cl^- in the polymeric bridges also causes pH relaxation (i.e. release of OH^- from its complex to solution) which can result in more precipitation. However, this mechanism leads to incorporation of chloride in the final product (i.e. β-FeOOH). Almost negligible (< 0.01 %) incorporation of chloride into the precipitating solids, in this study, suggest that this mechanism may not be responsible for higher precipitation rate.

The initially precipitated phase is metastable (Stranski's rule) and transforms to a more stable phase as the product ages. According to the mechanism described by Sapieszko *et al*., (1977) the precipitation of metastable phase can be represented by the following reaction, Equation (6.4).

$$7Fe(OH)_2^+ + FeSO_4^+ \rightarrow Fe_8O_8(SO_4)(OH)_6 + 8H^+ \qquad (6.4)$$

The metastable amorphous phase, in this study, is hypothesized to be schwertmannite, however formation of other hydroxy sulphate phases ($Fe_4SO_4(OH)_{10}$ etc.) is also possible (Sapieszko, 1977). XRD analysis of the precipitates showed an increase in the amount of hematite and goethite and decrease in the amount of amorphous and other iron hydroxy sulphate phases as the chloride concentration increased see Table 6-3.

Table 6-3 Phases identified by QXRPD when chloride concentration was increased from 0 to 30 g/L for the system containing 6 g/L Fe^{3+}, 15.0 g/L H_2SO_4, 30.0 g/L Cu^{2+} at 150 °C for 1 hr.

Chloride (g/L)	Phase (Wt. %) error (± 2 %)			
	Hematite α-Fe_2O_3	Goethite α-FeOOH	Volaschioite $Fe_4(SO_4)O_2(OH)_6.\ 2H_2O$	Amorphous
0	69.2	-	20.3	10.5
6	75.7	-	12.4	11.9
11	83.8	-	5.1	11.7
15	84.4	3.4	4.3	7.9
20	84.8	5.8	2.2	7.2
30	85.1	11.6	-	3.3

The composition of the precipitates made with various concentrations of chloride is illustrated in Figure 6.9. The increase in Fe content of the precipitates from ~53 to 56 % and decrease in SO_4^{2-} content from ~9 to 6 % is due to the preferential precipitation of iron oxides over iron hydroxy sulphate phases.

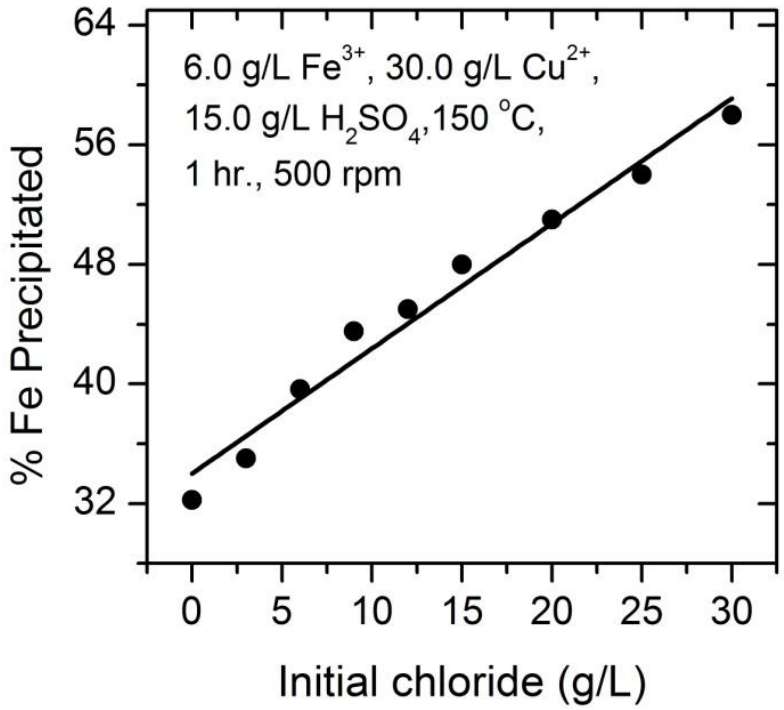

Figure 6.8 Variation of % Fe precipitation with initial concentration of chloride as LiCl.

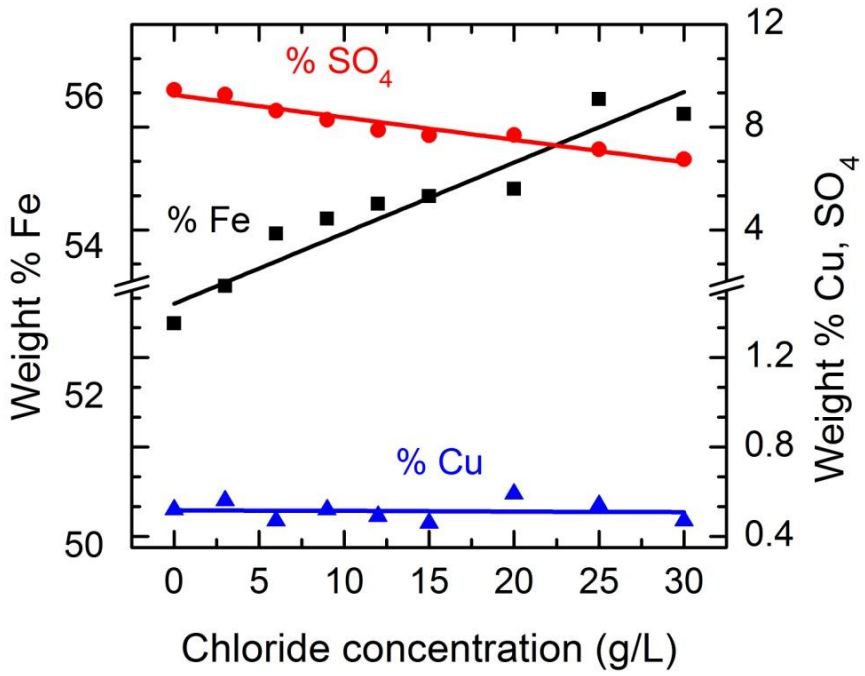

Figure 6.9 Effect of chloride concentration on the composition of the precipitates; for the experiments carried out for 1 hr. at 150 °C in the system containing 6.0 g/L Fe^{3+}, 15.0 g/L H_2SO_4 and 30.0 g/L Cu^{2+}.

6.3.4 Effect of retention time

The focus in this study was the investigation of iron precipitation under short retention time, as practised by CESL and Vale. However, a few experiments were carried out for longer retention times to see how the precipitation product and associated metal loss change with the retention time. In this regard the effect of time on the amount, composition and crystallinity of the product was investigated. Figure 6.10 shows that negligible precipitation occurs during the first~35 minutes required to heat the autoclave to the reaction temperature 150 °C i.e. 0 hour retention time. Prolonging the retention time increased the amount of iron precipitation and this trend continued to ~6 hours. Further increase in the retention time had little effect on the percentage iron precipitation.

Table 6-4 Phases identified by QXRPD when the retention time was increased from 1 to 12 hours; for the experiments carried out at 150 °C in the system containing initial concentrations: 15.0 g/L H_2SO_4, 11.0 g/L Cl^-, 30.0 g/L Cu^{2+}.

Time (hr)	Phase (Wt. %) error (± 2 %)		
	Hematite α-Fe_2O_3	Volaschioite $Fe_4(SO_4)O_2(OH)_6.\ 2H_2O$	Amorphous
1	86.6	1	12.4
2	86.4	-	13.6
4	100	-	-
6	100	-	-
8	100	-	-
12	100	-	-

Quantitative phase analysis of the precipitates, for longer retention times, is given in Table 6-4. It can be seen that the reaction product after 1 hour contains about 86 %

hematite and ~13 % amorphous phase. When retention time was increased to 4 hours or higher, the precipitates consisted only of hematite.

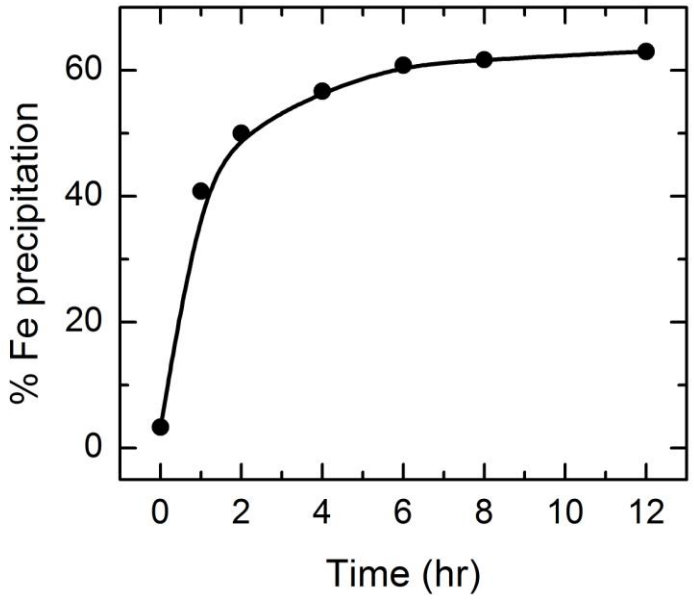

Figure 6.10 Effect of retention time on % iron precipitation; for the experiments carried out for 1 hr. at 150 °C in the system containing 6.0 g/L Fe^{3+}, 15.0 g/L H_2SO_4, 30.0 g/L Cu^{2+} and 11.0 g/L Cl^-.

Elemental analysis of the precipitates, Figure 6.11, showed an increase in the Fe content of the solid product from ~57 % Fe to ~61 % Fe and a decrease in the SO_4^{2-} content from ~7.5 to ~4.4 % SO_4^{2-} as the retention time increased from 0.5 to 12 hours. The data suggests that the first product of hydrolysis is a sulphate containing metastable phase which transforms to a more stable phase upon ageing. Figure 6.12 shows the particle size distribution for different retention times. Particle growth is preferred with an increase in retention time. The decrease in the Cu content (~0.6 to ~0.3 % Cu), for longer retention times, as shown in Figure 6.11, can be attributed both to the absence of metastble phase and increase in particle size for longer retention times. Increasing retention time increased

the percentage iron precipitation; however, it did not affect the crystallinity of the precipitates to a significant extent, see Figure 6.13.

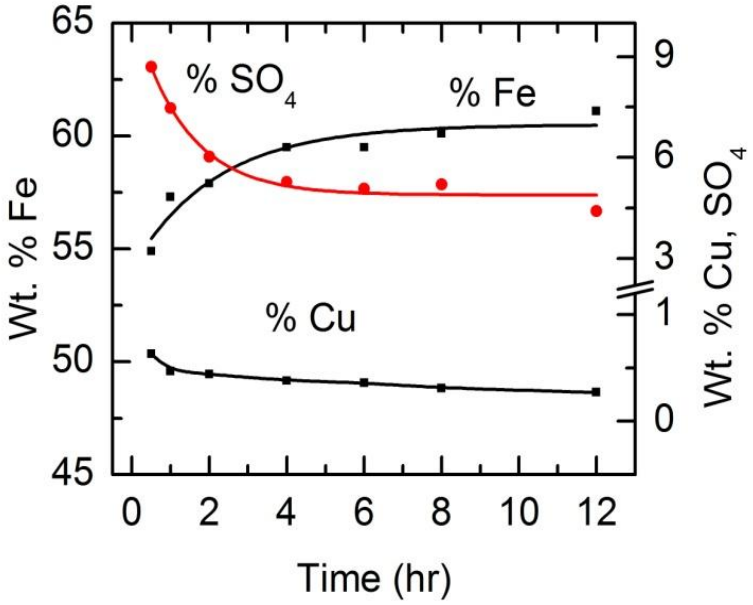

Figure 6.11 Effect of retention time on the composition of the solid precipitates for the experiments carried out at 150 °C in the system containing 6.0 g/L Fe^{3+}, 15.0 g/L H_2SO_4, 11.0 g/L Cl^- and 30.0 g/L Cu^{2+}.

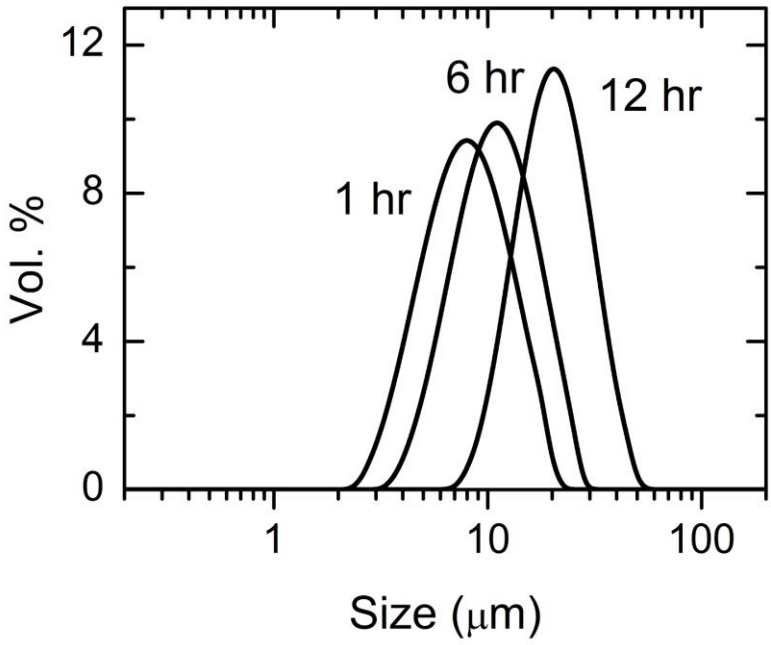

Figure 6.12 Effect of retention time on the particle size distribution of the precipitates: initial conditions: 6 g/L Fe^{3+}, 15 g/L H_2SO_4, 11g/L Cl^-, 30 g/L Cu^{2+}, 150 °C.

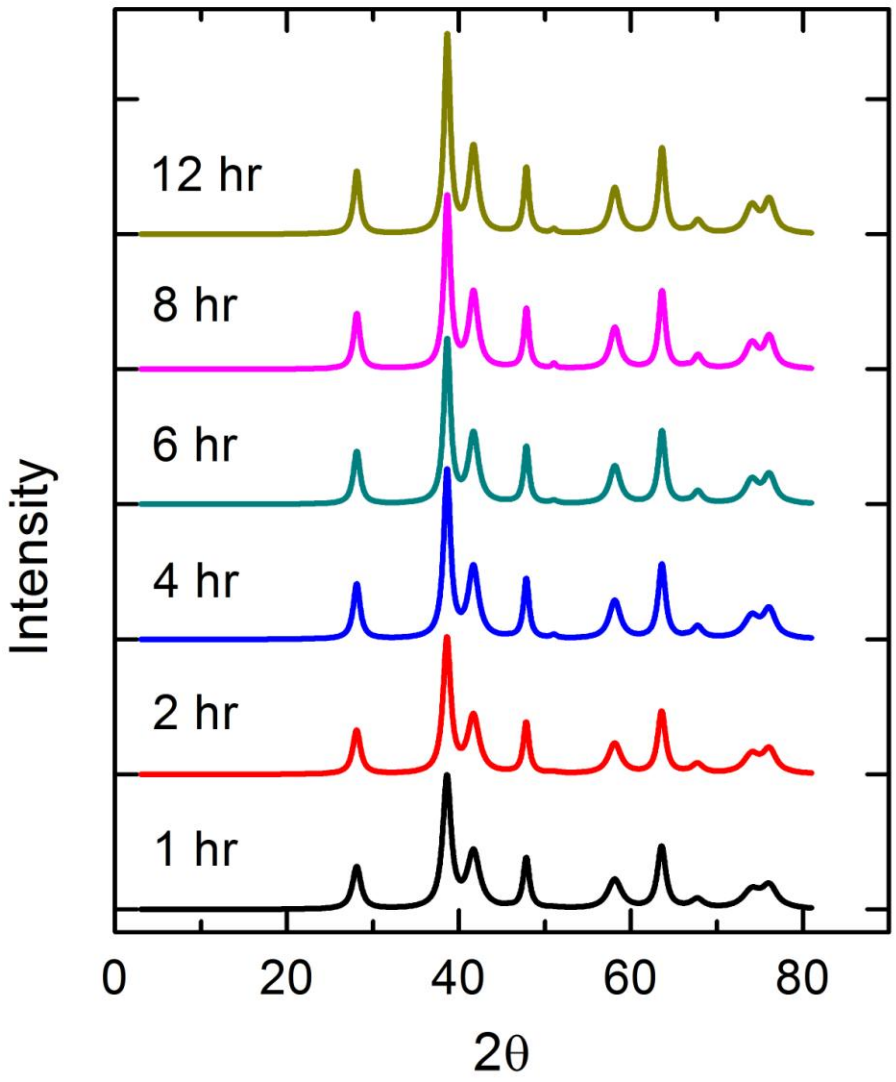

Figure 6.13 Effect of retention time on the crystallinity of the hematite; for the experiments carried out at 150 °C in the system containing 6.0 g/L Fe^{3+}, 15.0 g/L H_2SO_4, 11.0 g/L Cl^- and 30.0 g/L Cu^{2+}.

6.3.5 Effect of hematite seed

In a continuous process a certain amount of seed is always present. In this study experiments were carried out using reagent grade hematite seed to study the effect of

different seed levels on the extent of iron precipitation. The Fe and SO_4^{2-} contents of the seed were: 69.5 % Fe and < 0.01 % SO_4^{2-} respectively. As the concentration of seed increased the % iron precipitation also increased i.e. more iron precipitated in 1 hour retention time (because of lower activation energy barrier for secondary nucleation). There was little difference between % Fe precipitations for seed concentrations of 15 g/L and higher, because of the system being close to equilibrium. Solution containing higher initial ferric concentrations may require higher seed levels before the precipitation plateau. A rough estimation, based on this study, is that an iron to seed ratio of 1:3 can provide enough secondary nucleation sites to achieve higher precipitation rate. Figure 6.14 compares the % iron precipitation in the absence and presence of 15 g/L seed. It can be seen in Figure 6.14 that the presence of 15 g/L seed in the system results in the precipitation curve to plateau after 2 hours, which in the absence of seed is attained almost after 6 hours. However, the presence of seed is not expected to affect the final equilibrium state of the system and both curves will meet eventually at a single point.

QXRPD analysis of the precipitates showed the precipitation of only hematite irrespective of the retention time. In comparison to the absence of initially added seed, 100 % hematite phase was only obtained after 4 hour of retention. Addition of hematite seed promotes the precipitation of hematite phase relative to other iron oxide/hydroxy sulphate phases. Increasing seed concentration decreased the copper content of the precipitates. However, higher seed levels (≥ 15 g/L) resulted in more fine fractions in the precipitation product. One possible reason for this behaviour seems that higher seed levels result in

defragmentation of the crystals growing on the seed surface and these defragmented parts exist mainly as separate particles, this hypothesis is further discussed in Chapter 7. The presence of higher amounts of the fine fractions results in an increase in the total surface area in the system which is expected to affect the adsorption behaviour of the precipitating solid. Detailed discussion about the effect of seeding on the copper content/adsorption of the precipitates will be addressed in Chapter 7.

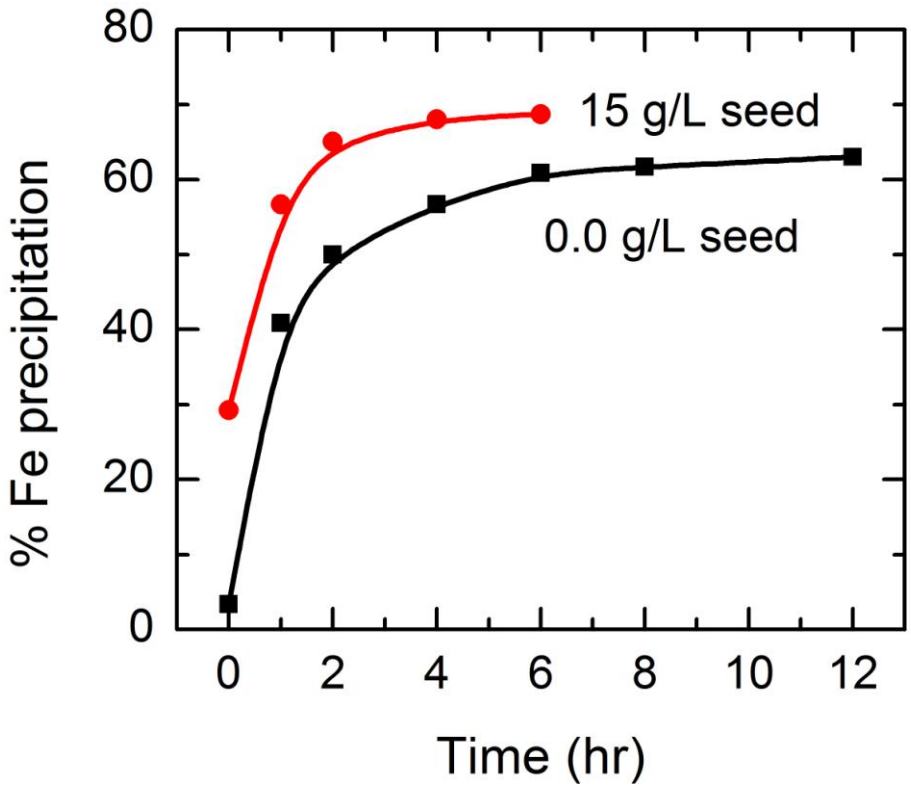

Figure 6.14 Relationships between retention time and % iron precipitation both in the presence and absence of hematite seed. In case of seed added experiments, mass of the new precipitates was calculated by subtracting the mass of seed from the total mass.

6.3.6 Effect of temperature

The baseline temperature for this study was selected to be 150 °C, as per Vale and CESL operations. However, some experiments were carried out at higher temperatures to compare the nature of the precipitation products. Temperature was varied in the range 150 – 220 °C. Figure 6.15 illustrates the effect of temperature on % iron precipitation after 1 hour of reaction time, in the system containing 6.0 g/L Fe^{3+}, 15.0 g/L H_2SO_4, 11.0 g/L Cl^- and 30.0 g/L Cu^{2+}. Figure 6.15 shows that increasing temperature results in an increase in the % iron precipitation. At higher temperatures equilibrium solubility of ferric ion decreases which results in more iron precipitation. XRD analysis of the precipitates showed the precipitates to consist of 100 % hematite phase when the temperature was ≥ 200 °C, see Table 6-5. The presence of metastable/amorphous phase at lower temperatures (< 200 °C) and its absence at higher temperatures (≥ 200 °C) suggests that transformation kinetics are faster at higher temperatures. Chemical analysis of the precipitates showed an increase in Fe content and decrease in SO_4^{2-} content of the precipitates see Figure 6.16. As the temperature increased, sulphate was rejected out from the precipitates, see Figure 6.16. However, at higher temperatures ≥ 200 °C even though XRD detected 100 % hematite phase, subsequent leaching of the precipitates with 0.1 M H_2SO_4 showed the presence of 1-2 % basic ferric sulphate.

Figure 6.16 illustrates the composition of the precipitates made in the system containing 6.0 g/L Fe^{3+}, 15.0 g/L H_2SO_4, 11.0 g/L Cl^- and 30.0 g/L Cu^{2+} for 1 hour reaction at

various temperatures. The Fe content of the precipitates increased from 57 to 66 % and the SO_4^{2-} content deceased from about 8 % to 2 %, as the temperature increased from 150 °C to 220 °C. The Cu content remained < 0.5 % in all cases. However, Cu to Fe ratio decreased as the temperature increased, see Figure 6.15.

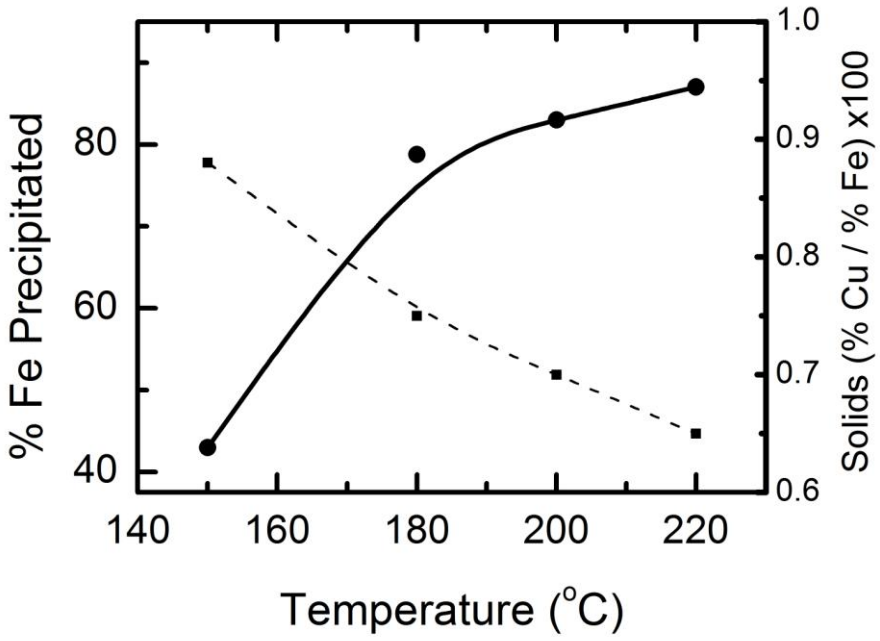

Figure 6.15 Effect of temperature on % iron precipitation. Dashed line shows the Cu/Fe ratio in the solid product. Note: Solids mass increased with temperature which resulted in more Cu loss to the precipitates therefore only a small difference in the Cu/Fe ratio was observed as the temperature increased from 150 to 220 °C, see appendix D, Table D-1.

Table 6-5 Phases identified by QXRPD when the temperature was increased from 150 to 200 °C; for the experiments carried out for 1 hr in the system containing 15.0 g/L H_2SO_4, 11.0 g/L Cl^-, 30.0 g/L Cu^{2+}.

Temperature (°C)	Phase (Wt. %) error (± 2 %)		
	Hematite α-Fe_2O_3	Volaschioite $Fe_4(SO_4)O_2(OH)_6.\ 2H_2O$	Amorphous
150	86.6	1	12.4
180	86.2	-	13.8
200	100	-	-
220	100	-	-

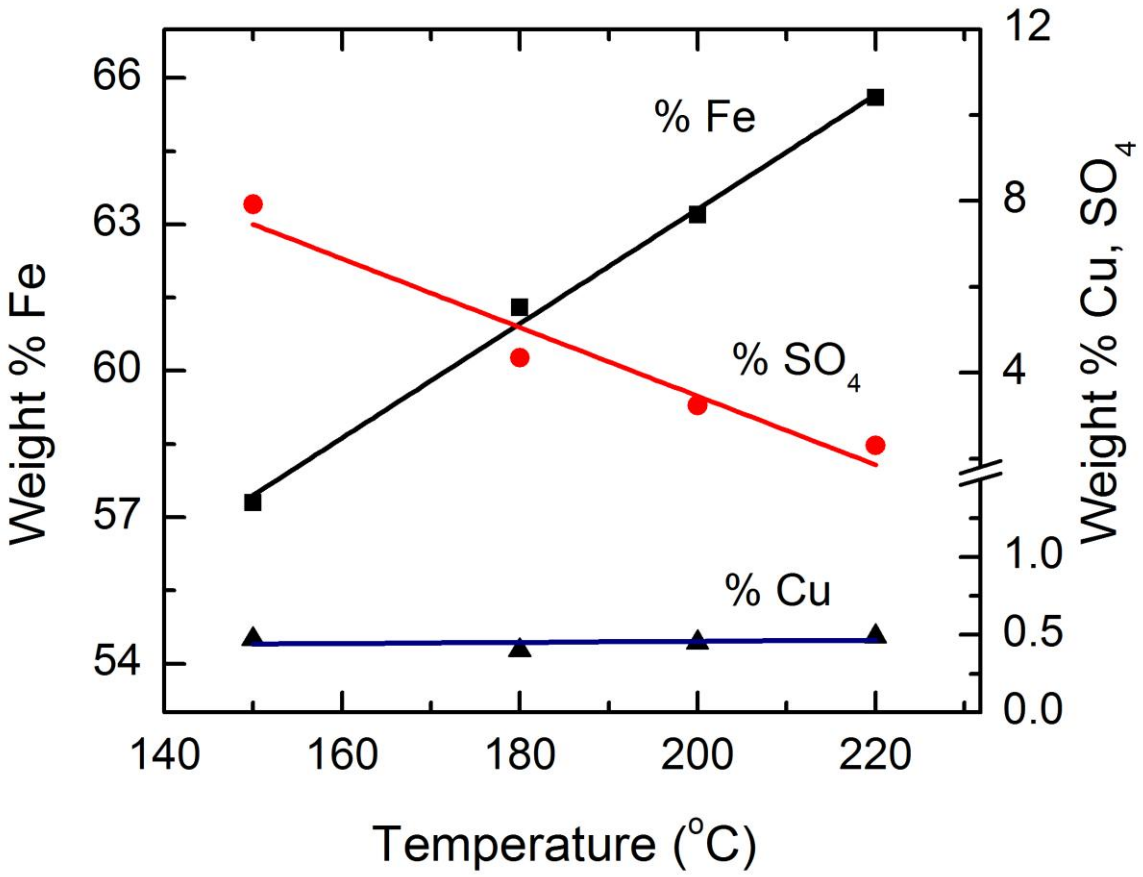

Figure 6.16 Effect of temperature on the composition of the solid product.

Figure 6.17 demonstrates that temperatures above 200 °C are required to produce a more crystalline product. A comparison of the XRD patterns for different temperatures and retention times is given in Figure 6.18. Longer retention times were not as effective to produce a crystalline product as the higher temperature was. Precipitates made from a 1 hour test at 220 °C exhibited better crystallinity than those made from a 12 hour test at 150 °C.

Chemical analysis of the precipitates showed the precipitates to consist of ~8 % SO_4^{2-} for the 1 hour and ~4.2 % SO_4^{2-} for the 12 hour product compared to the ~2.0 % SO_4^{2-} for

the product made at 220 °C. It should be noted that for 1 hour product a certain amount of amorphous phase is co-precipitated with hematite which results in higher sulphate content. Similarly at higher temperatures a certain amount of basic ferric sulphate coexists.

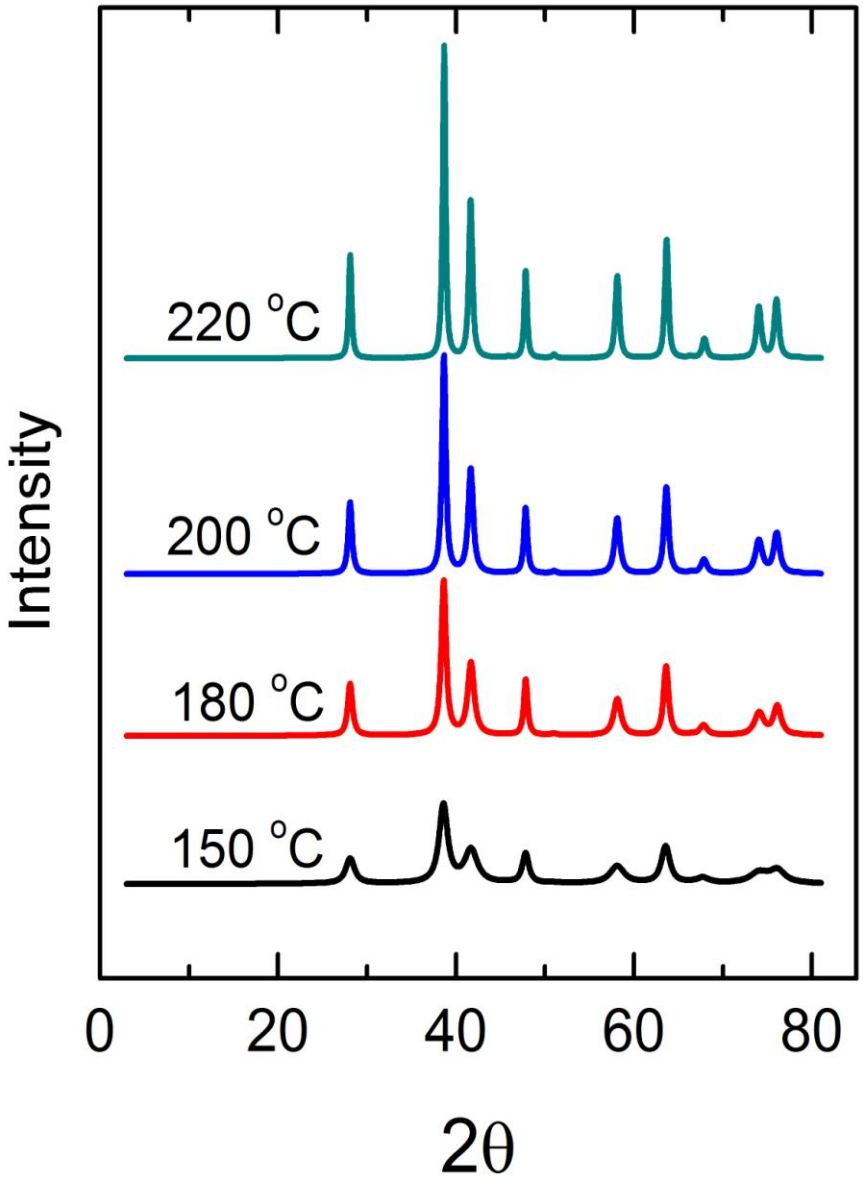

Figure 6.17 Comparison of XRD patterns for different temperatures.

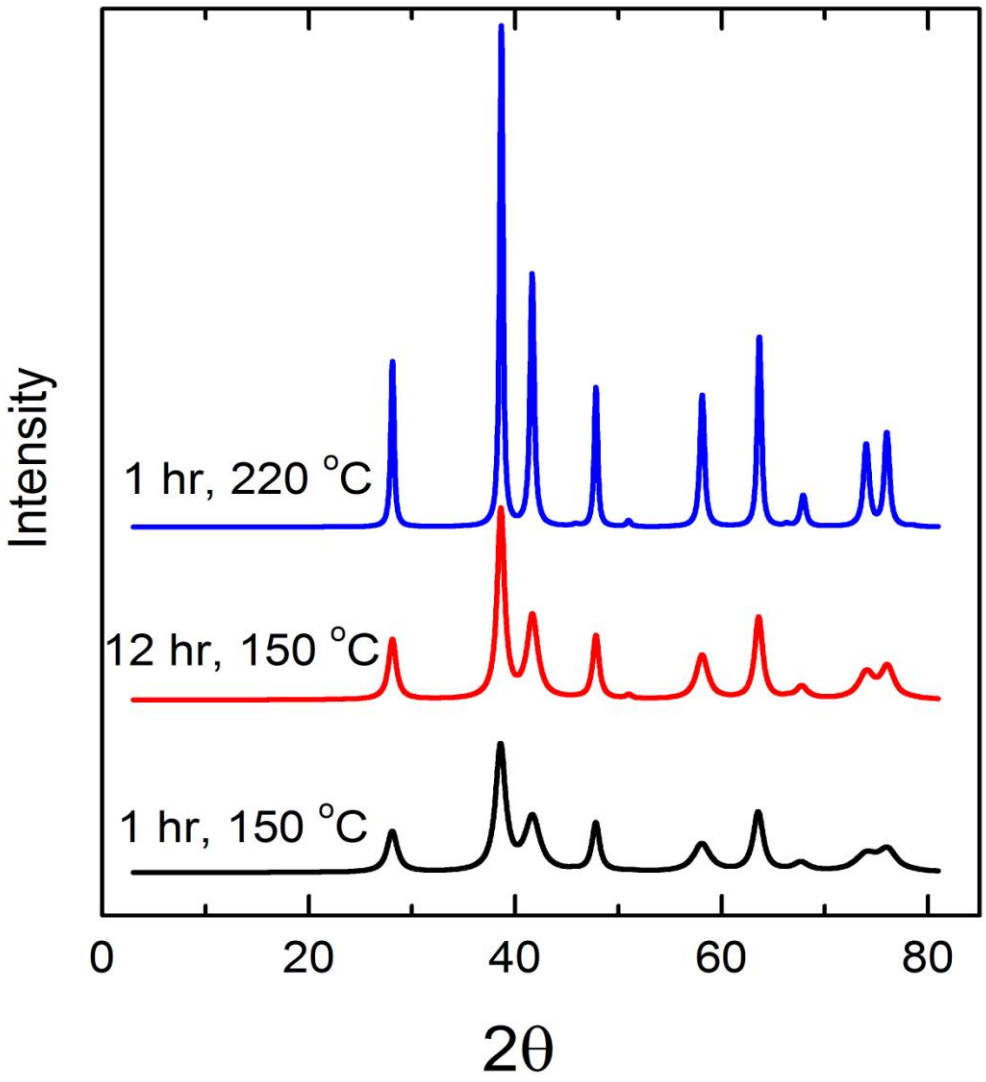

Figure 6.18 Comparison of XRD patterns for different temperatures and retention times.

6.3.7 Effect of pre-neutralization

Increasing the room temperature pH of the solution i.e. pre-neutralization, increased the amount of precipitation product and nearly complete iron precipitation was achieved in 1 hour for pH values of ≥ 2.5. However, pre-neutralization (higher pH values) resulted in precipitation to start at room temperature. The precipitates formed at room

temperature were found to be amorphous and did not transform to the crystalline product after 1 – 3 hours of retention at 150 °C. As a result, the product formed at higher pH values was contaminated by significant amounts of the amorphous phase (~20 – 40 %), see Table 6-6. In certain cases the precipitates also contained goethite along with hematite and amorphous phase.

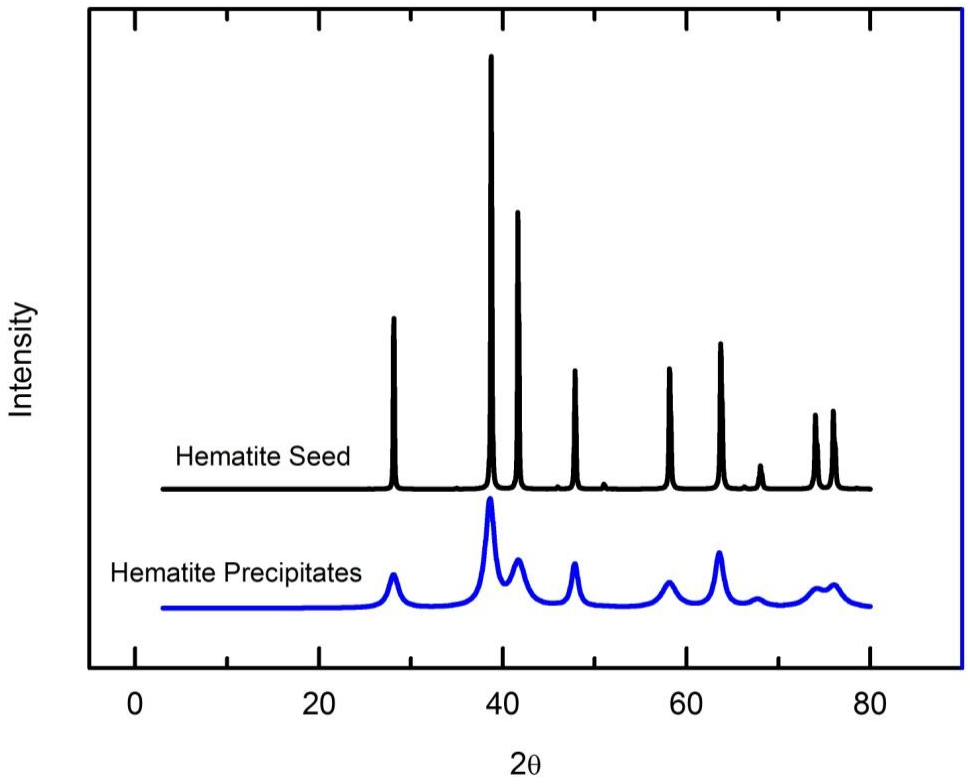

Figure 6.19 Comparison of the XRD patterns of reagent grade hematite seed and representative pattern of hematite precipitates.

Figure 6.19 shows the XRD pattern of the reagent grade hematite seed and a representative pattern of hematite precipitates made in this study. It can be seen that the freshly prepared hematite lacks in crystallinity. XRD patterns of the experiments carried out at higher pH values (i.e. initial neutralization of the solution) were separated from the

amorphous phase and are shown in Figure 6.20. Figure 6.20 demonstrates that comparatively better crystalline hematite is formed at higher initial pH values.

As described above, precipitation of iron takes place by formation of small polymers which convert to large polymers and eventually to the colloidal size solids which grow by the further addition of the precursor species or by agglomeration. At lower pH values dominance of the species such as $FeSO_4^+$, $Fe(SO_4)_2^-$ etc. is expected. The matrix anion ligand (SO_4^{2-}) is incorporated in the precipitating solid due to incomplete exchange of SO_4^{2-} with the precipitating anion ligand (OH^-) (Demopoulos, 2009; Grundl and Delwiche, 1993). A complete anion ligand exchange reaction is shown in Equation (6.2). However, an incomplete ligand exchange will result in mixed stoichiometry such as the one shown in Equation (6.4). Secondly, adsorption of SO_4^{2-} onto the active surface sites of the precipitating solid will also result in a mixed stoichiometry. Sugimoto and Wang (1998) have shown that sulphate adsorption on hematite increases as the pH decreases. The presence of matrix anion interferes with the dehydration process and may result in poor crystallinity.

Table 6-6 Phases identified by QXRPD when solution were neutralized at room temperature to get the desired pH; other conditions: 6.0 g/L Fe^{3+}, 11.0 g/L Cl^- and 30.0 g/L Cu^{2+}, 1 hr. at 150 °C.

pH	Phase (Wt. %) error (± 2 %)		
	Hematite α-Fe_2O_3	Goethite α-FeOOH	Amorphous
~1.5*	86.0	-	14.0
2.0	47.2	34.4	18.4
2.5	57.5	19.6	22.9
3.0	61.1	-	38.9

*pH 1.5 is the solution pH in the presence of 15 g/L initially added H_2SO_4 and without any initial neutralization. Neutralization was carried out using $LiCO_3$.

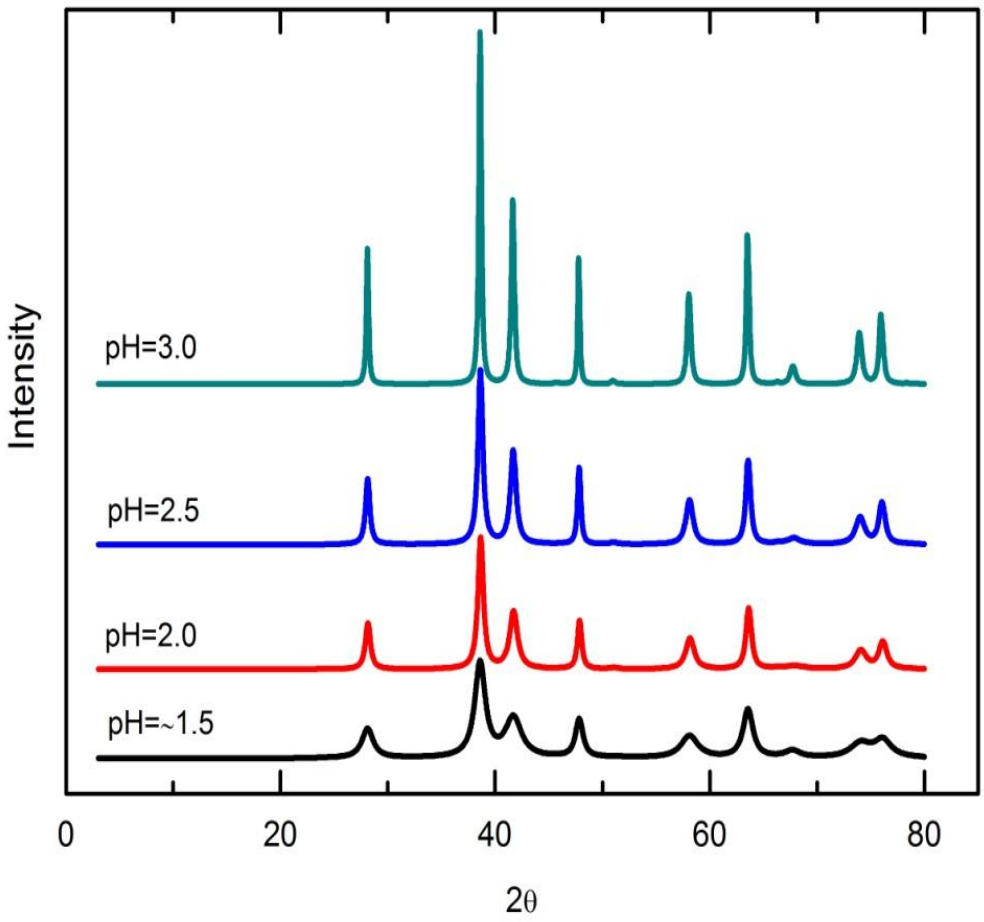

Figure 6.20 Effect of initial solution pH on the hematite crystallinity; for the experiments carried out for 1 hr at 150 °C in the system containing 6.0 g/L Fe^{3+}, 11.0 g/L Cl^{-}, 30.0 g/L Cu^{2+}. pH was raised at room temperature using $LiCO_3$.

Note: pH before addition of base was ~1.5 which is the pH of the lowest diffractogram. pH was raised at room temperature using $LiCO_3$. The diffractograms shown are the calculated patterns of hematite while the precipitates also contain other phases.

To further investigate whether adsorption and/or incorporation of sulphate on the active surface sites of hematite results in poor crystallinity of the product, experiments were carried out in the absence of sulphate in the solution i.e. chloride salts of the respective metals were used to prepare the initial solutions. The results are presented in

Figure 6.21. It can be seen in Figure 6.21 that the absence of sulphate in the medium results in a more crystalline product.

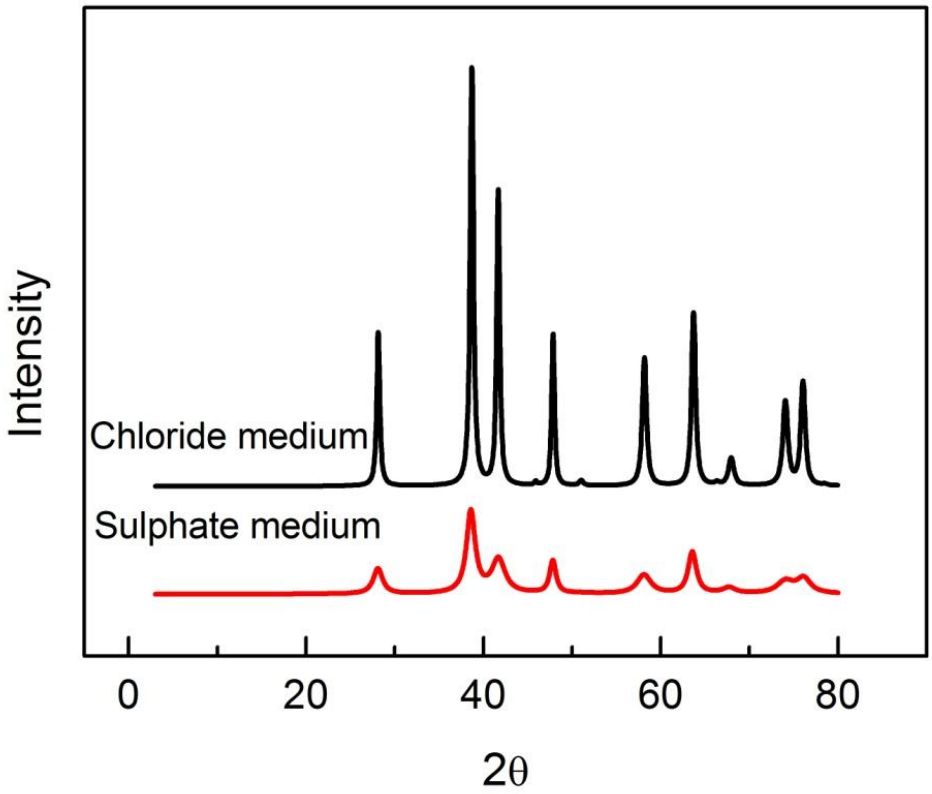

Figure 6.21 Effect of precipitation medium on the hematite crystallinity; for the experiments carried out for 1 hr at 150 °C.

XRD analysis of the powder hematite from both sulphate and chloride media showed almost identical lattice parameters (i.e. a = 5.031 Å, c = 13.816 Å from sulphate and a = 5.027 Å, c = 13.805 Å from chloride medium) and there was no indication of peak shifts. Therefore, structural incorporation of SO_4^{2-} (diameter 0.5 nm), which is expected to change the lattice parameters significantly, in the hematite does not seem to be taking place.

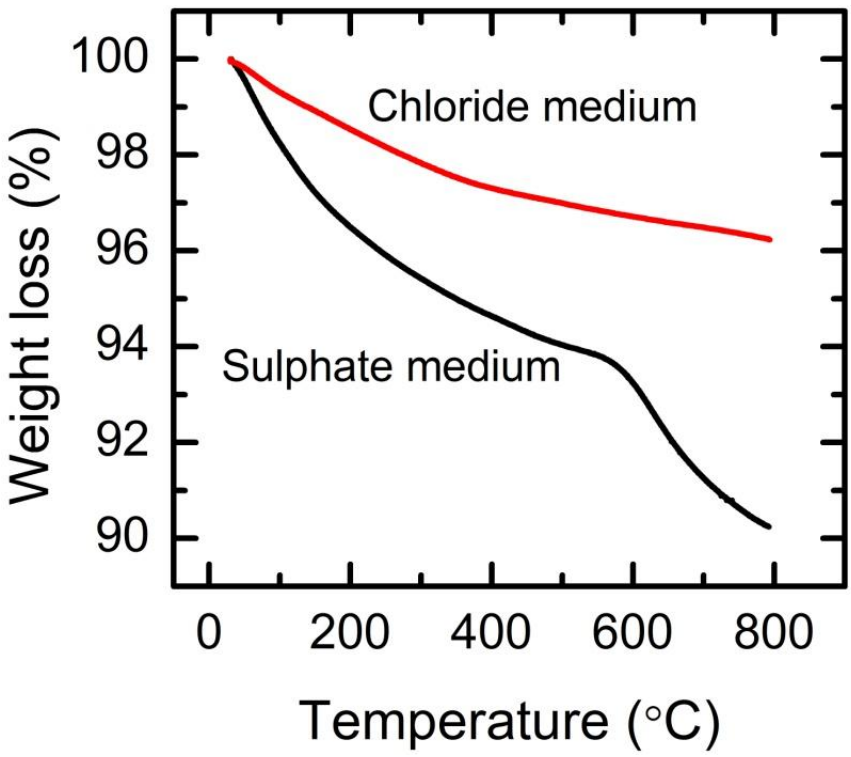

Figure 6.22 TGA weight loss behaviour of the hematite precipitates from: sulphate medium (150 °C, 48 hr retention) and chloride medium (150 °C, 4 hr retention). Other conditions: 30 g/L Cu^{2+}, 11 g/L Cl^{-}, pH ~1.5. Longer retention times were chosen to ensure that the precipitation product contains only hematite phase.

Dutrizac and Chen (1993) studied hematite precipitation from sulphate medium. Although, SEM-EDX analysis in their study did not detect any sulphate containing phase within the hematite, these authors were able to confirm the presence of 2.81 % sulphate using quantitative electron microprobe analysis of the individual hematite particles. Dissolution of hematite, in their study, in the hydrochloric acid followed by $BaSO_4$ precipitation confirmed the presence of S as SO_4^{2-}. Similarly, TEM-EDX of the individual hematite crystallites showed the presence of sulphate consistent with the bulk composition of their product. Therefore, it seems that it is the strongly held sulphate on the surface of

the individual hematite crystallites which results in poor crystallinity. Sulphate covering of the hematite surface changes the surface electronic configuration and atomic scattering from the planes resulting in low intensity peaks. It is believed that SO_4^{2-} adsorption takes place through a ligand exchange with the surface FeOH groups in the presence of protons where some of FeOH are protonated to give $FeOH_2^+$ and resultantly binuclear bridging complexes i.e. Fe—O—SO_2—O—Fe are formed at the surface (Parfitt and Smart, 1978).

Wolska (1981) observed that hematite precipitates from aqueous medium contain about 3 – 4.5 % tightly held water which requires temperatures up to 1000 °C for complete withdrawal. Wolska (1981) and Dutrizac and Chen (2001) believed that this tightly held water is in the form of OH^- partly replacing the O^{2-} in the hematite structure i.e. "hydrohematite". With such a replacement, electrostatic neutrality is disturbed, to preserve this charge imbalance Fe^{3+} deficient cites are created in the cation positions. Such Fe^{3+} deficiency results in low intensity peaks (Wolska, 1981).

TO investigate this hypothesis thermal gravimetric analysis of the precipitates was carried out. TGA weight loss analysis of the precipitates from both sulphate and chloride mediums, Figure 6.22, showed about ~9.6 ± 1.0 % weight loss from sulphate medium and ~3.7 ± 1.0 % weight loss from the chloride medium. QXRD analysis of the precipitates showed the presence of 100 % hematite in both the samples, therefore the weight loss due to the presence of other impurities can be excluded. The weight loss from chloride medium took place steadily as the temperature increased from 30 to 800 °C. However, a rapid weight loss occurred after approximately 580 °C for the precipitates from sulphate medium.

The change in slope of the weight loss curve at ~580 °C indicates two distinct reactions to be taking place. The weight loss of ~3.8 % after ~580 °C is very close to the ~4.0 % sulphate content of the precipitates as determined by ICP. Secondly, Dutrizac and Chen (2001) have shown that SO_2 gas is evolved when hematite, precipitated from sulphate media, is heated above 580 °C. Therefore, the second weight loss is almost certainly due to the sulphate desorption from the precipitates. Weight loss comparison shows that the precipitation product from sulphate medium results in ~6.8 % extra weight loss, of which ~3.8 % is due to sulphate and ~3.0 % is due to extra water content of this sample. Therefore, the implication is that it is the combined effect of adsorbed sulphate and structural water which results in the mixed stoichiometry and poor crystallinity of the product from the sulphate medium.

Figure 6.23(a), shows a general morphology of the hematite precipitated in this study. However, under short retention times (< 4 hour, when the product contained ~13 % amorphous phase) two types of morphologies were found in the precipitation product as shown in Figure 6.23(b), (c). For longer retention times (≥ 12 hour), the hedgehog type morphology as seen in Figure 6.23(b), (c) seemed to have more compact agglomerates and hematite was found to grow within as small round particles, see Figure 6.23(d), (e). On the other hand, the precipitation product from chloride only medium (i.e. in the absence of sulphate in the system) had a higher tendency for agglomeration and consisted of large agglomerates made up of tiny hematite particles, see Figure 6.23(f) and Figure 6.23(f) inset.

The morphology found in Figure 6.23(c) has some resemblance to the hedgehog morphology attributed to schwertmannite by Loan *et al*., (2002a, 2005). Claassen *et al*.,

(2002) also found the amorphous phase to be schwertmannite from the acidic sulphate medium in the Zincor process. These latter authors used Mössbauer effect spectroscopy to identify its presence. However, positive identification of the metastable/amorphous phase, in this study, needs further investigation using techniques such as X-ray absorption near edge spectroscopy, TEM-EDS.

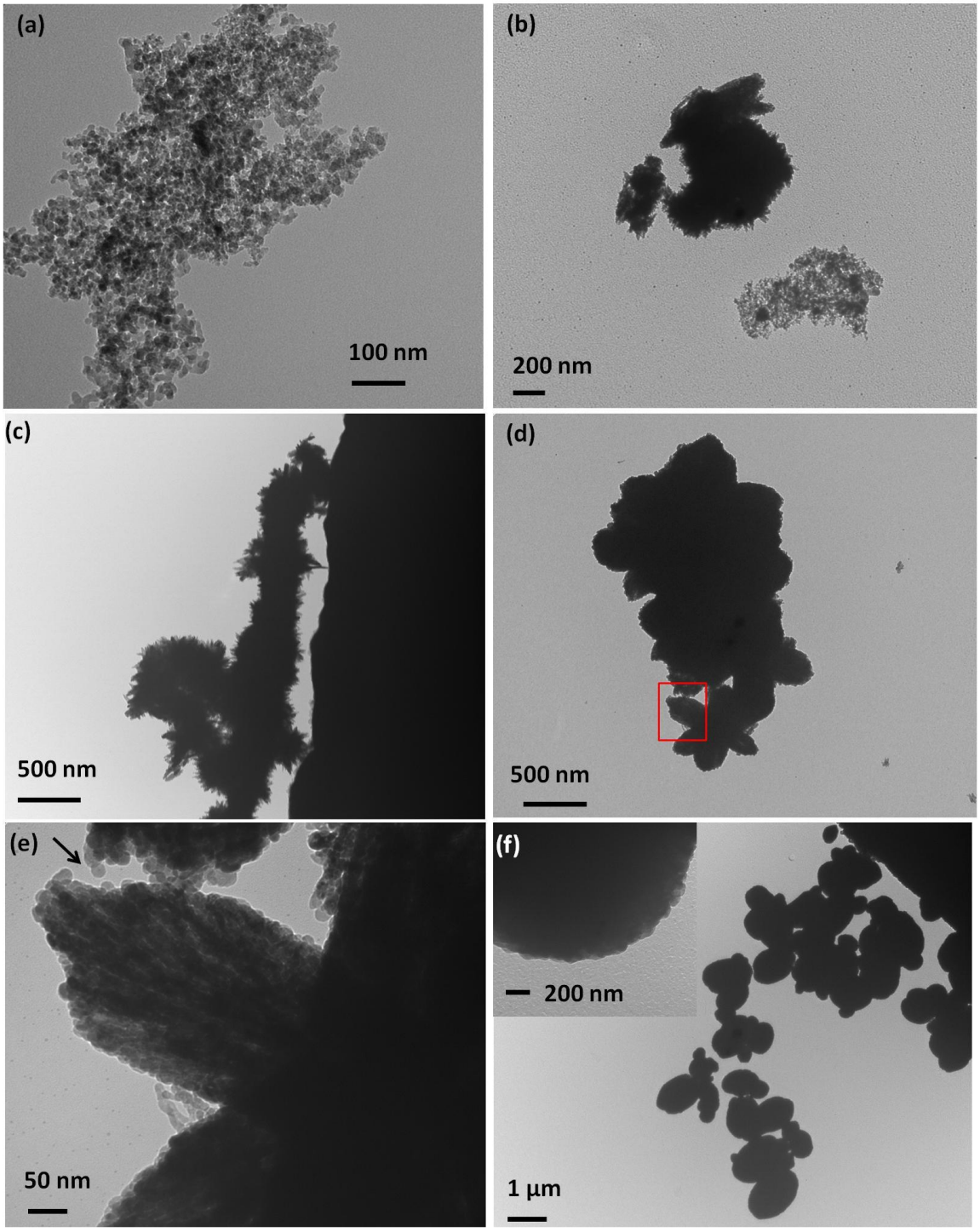

Figure 6.23 TEM images of: (a) hematite precipitates; (b) precipitation product after 1 hr retention; (c) another image of the hedgehog type morphology seen in (b); (d) morphology of (c) after 12 hr retention; (e) image of the highlighted area in (d) at higher magnification; (f) precipitation product from chloride medium, the inset image shows the fine details of an edge of large agglomerates seen in (f).

6.3.8 Hydroxylamine hydrochloride (HaHC) extraction

Figure 6.24 shows the Cu/Fe ratio in the solutions when the precipitates made under various conditions were leached with HaHC (i.e. selective leaching of the amorphous phase). It can be seen that an increase in the retention time, acid or seed concentration leads to a decrease in the Cu/Fe ratio resulting from the leaching of the precipitates. A lower Cu/Fe ratio means that less copper is lost to the products during the precipitation process.

It has been seen in the previous sections of this chapter that increasing retention time decreased the amorphous phase and increased the particle size; similarly presence of seed increased the proportion of hematite and presence of higher acid concentrations promoted particle growth. These changes in the product result in lower Cu/Fe ratios with HaHC leaching. It should be noted that seed itself is inert to HaHC leaching.

Figure 6.25 shows the Cu/Fe ratio in the solutions when the precipitates made at different pH values, i.e. pre-neutralization, were extracted with HaHC. As mentioned earlier, pre-neutralization of the solution results in the precipitation starting at room temperature, contaminating the product with a significant amount (20-40 %) of amorphous component. The room temperature product was amorphous and did not transform to a crystalline phase under the temperature and time used in this study. Therefore the HaHC leaching resulted in higher Cu/Fe ratios.

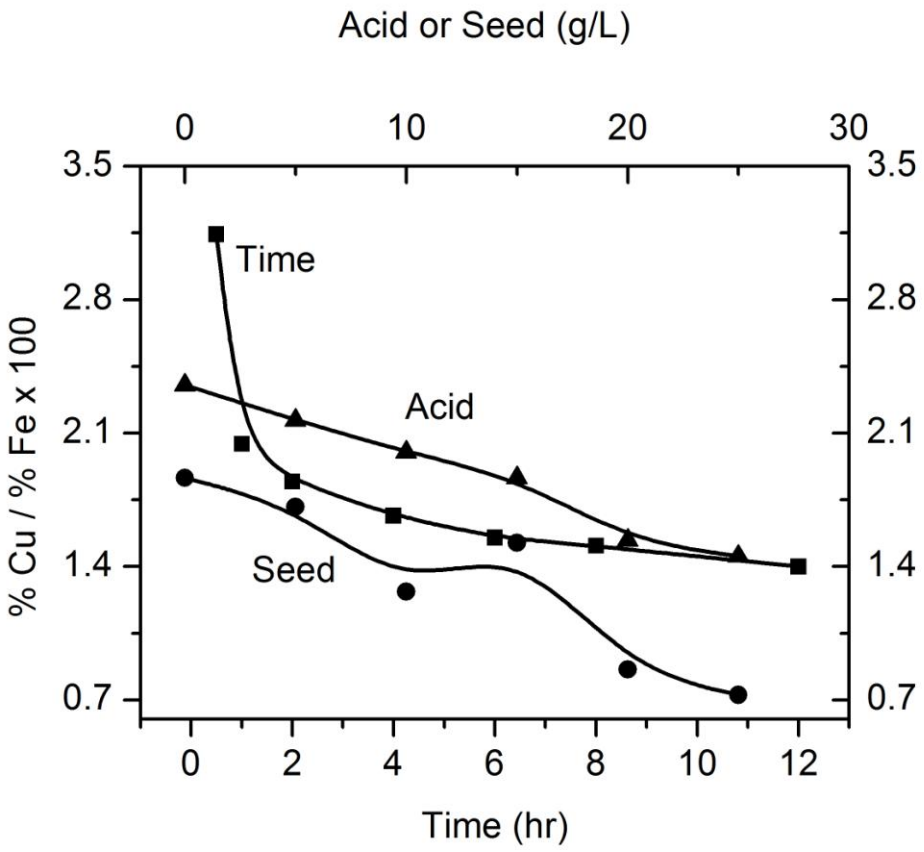

Figure 6.24 Cu/Fe ratios in the solution when the Fe precipitates were dissolved with HaHC. Results are based on the experiments carried out for varying time, seed and acid concentrations.

The product left after the first HaHC treatment i.e. the crystalline component was dried and given a second HaHC treatment. In the second treatment almost negligible amount of Cu and Fe iron were reported to the solutions (result not reported in detail). The lower Cu/Fe ratios for the second treatment suggest that the amorphous components were mostly responsible for the higher copper loss to the precipitates.

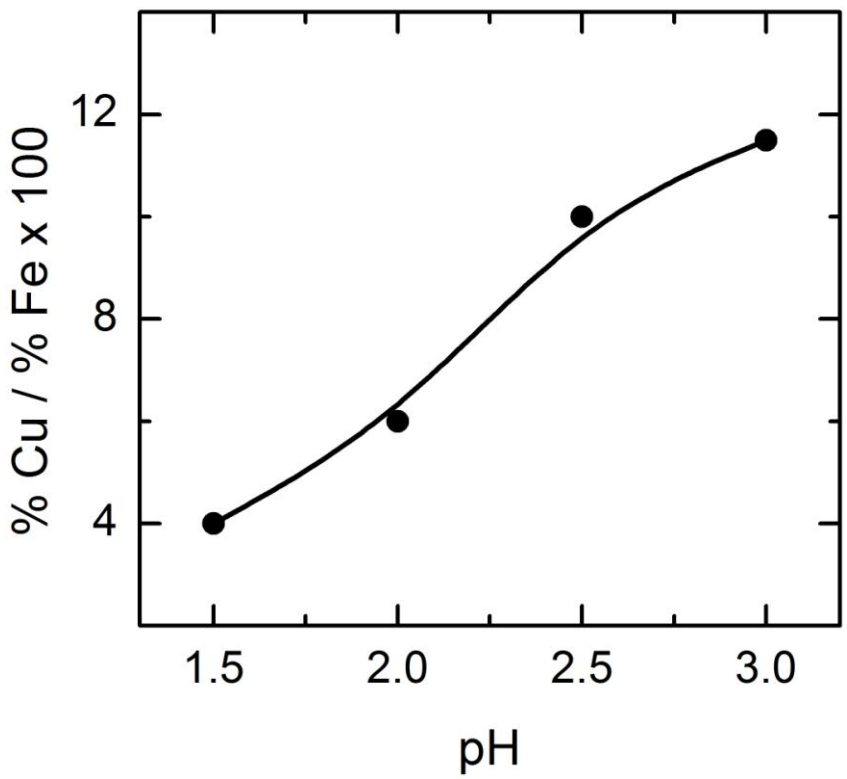

Figure 6.25 Cu/Fe ratios in the HaHC extracted solutions for the precipitates made at different pH values.

6.3.9 Effect of copper concentration

The copper concentration of a commercial processing solution increases as copper is dissolved from the copper sulphide concentrates in the autoclave. Therefore, in another set of experiments, copper concentration was varied from 0 – 60 g/L in the system containing 6.0 g/L Fe^{3+}, 15 g/L H_2SO_4, 11 g/L Cl^- at 150 °C for 1 hour. Figure 6.26 shows that a negligible amount of iron precipitates in the absence of copper sulphate. However, as the copper sulphate concentration of the solution increased the amount of iron precipitation also increased up to 40 g/L Cu^{2+} and became constant thereafter. Increase in iron precipitation

for higher concentrations of Cu (added as $CuSO_4$) is related to the formation of bisulphate (HSO_4^-) by the extra sulphate added to the system, which results in a decrease in the activity of the hydronium ion (i.e. pH increase). Tozawa and Sasaki, (1986) and Umetsu *et al*., (1977) have shown that the addition of certain sulphate salts (Cu, Zn, Mg) shifts the maximum concentration of free sulphuric acid above which basic iron sulphates precipitate instead of hematite. For example, in their study, at 185 °C hematite existed as a stable phase up to 76 g/L H_2SO_4 in the presence of 15 g/L Mg as $MgSO_4$ and up to 100 g/L H_2SO_4 in the presence of 30 g/L Mg. Similarly the upper limit of sulphuric acid at 200 °C was shifted to 79 and 102 g/L H_2SO_4 in the presence of 15 and 30 g/L Mg, respectively.

Figure 6.27 shows the composition of the precipitates for different initial copper sulphate concentrations. The increase in iron and decrease in the sulphate content of the precipitates for higher concentrations of $CuSO_4$ indicates that the product is less contaminated with iron hydroxy sulphates (or basic ferric sulpahte) due to the shift in upper limit of formation of basic ferric sulphate. Slight increase in the copper content of the precipitates could possibly be due to the incorporation of Cu into the hematite structure or due to the higher amount of product formed in the same retention time which is expected to result in finer size. However, the exact mechanism of Cu loss needs further investigation.

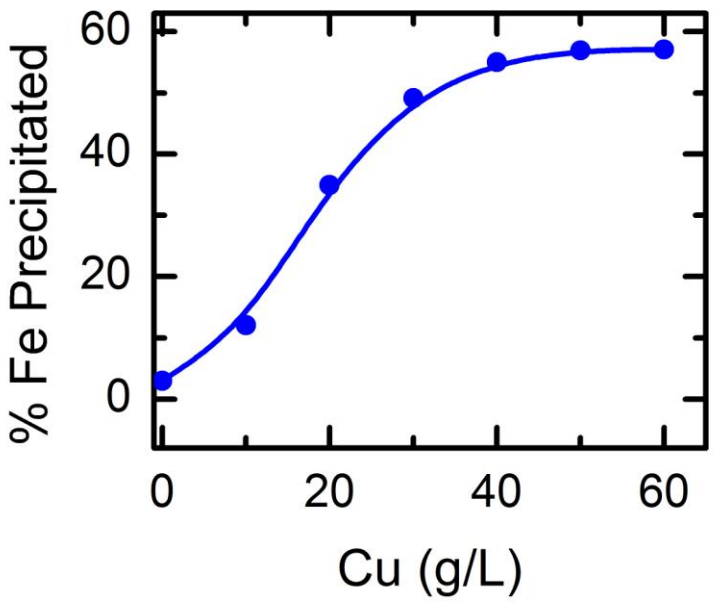

Figure 6.26 Effect of initial copper added as copper sulphate on the % Fe precipitation.

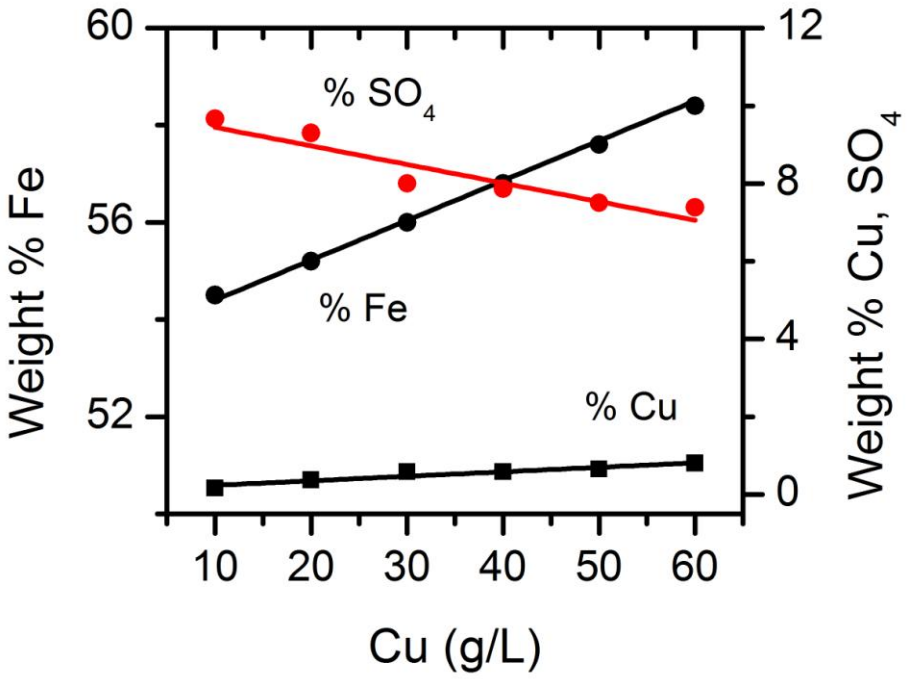

Figure 6.27 Effect of copper added as copper sulphate on the composition of the solid product.

6.4 Conclusions

Results of the preliminary experiments showed that % Fe precipitation increased as the initial H_2SO_4 concentration decreased from 30 to 0 g/L. However, due to increase in the equilibrium ferric concentration of the solution at higher acidities, almost negligible amounts of iron were precipitated when the initial H_2SO_4 concentration of the solution was > 30 g/L. QXRPD analysis of the precipitates showed the precipitates to consist of hematite as the dominant phase. However, in the absence of initially added acid small amounts of goethite were precipitated along with hematite.

Higher initial ferric levels (>15 g/L Fe^{3+}) reduced the % Fe precipitation to a significant extent because of the acid produced upon hydrolysis which shifted the equilibrium and due to slower kinetics of the precipitating phases. QXRPD analysis of the precipitates showed the precipitates to consist of predominantly hematite at lower initial ferric concentrations (< 15 g/L Fe^{3+}). At higher ferric concentrations (> 15 g/L Fe^{3+}) hydronium jarosite and hydroxy sulphate phases were kinetically favoured. Higher initial ferric concentrations resulted in the precipitation of hydronium jarosite and other iron hydroxy sulphate phases even where hematite was expected to precipitate.

Increasing retention times increased the % Fe precipitation. Virtually constant amounts of iron were precipitated for retention times of 6 hour and higher. XRD analysis of the precipitates showed the precipitates to consist of 100 % hematite for retention times 4 hours and longer.

It was found that a small amount of copper was always required for iron precipitation from the system containing 15 g/L H_2SO_4, 6 g/L Fe^{3+}, 11 g/L Cl^-, for 1 hour at 150 °C. Negligible (< 5%) iron precipitation occurred in the absence of initially added Cu^{2+} (as $CuSO_4$). Increasing copper concentration increased the % Fe precipitation and a nearly constant amount of iron was precipitated for copper concentrations of 40 g/L and higher. XRD analysis of the precipitates showed the precipitates to consist of hematite as the dominant phase.

Increasing chloride concentration from 0 to 30 g/L also increased the % Fe precipitation in the system containing 15 g/L H_2SO_4, 6 g/L Fe^{3+}, 1 hour and 150 °C. XRD analysis of the precipitates showed a relatively higher amount of hematite at higher chloride concentrations.

Increasing hematite seed levels from 0 to 15 g/L increased the % Fe precipitation but a virtually constant amount of iron precipitation was obtained at higher seed levels. Increasing temperature increased the % Fe precipitation and amount of hematite in the final product. A comparatively more crystalline product was produced at higher temperatures. Precipitation conditions which resulted in particle growth over nucleation lead to a precipitation product with lower Cu/Fe ratio. Sulphate adsorption and incorporation of OH^- into the hematite structure resulted in a poorly crystalline product.

Chapter 7. Iron precipitation and copper loss from sulphate-chloride solutions at 150 °C: A statistical approach.

7.1 Introduction

As discussed in the previous chapters, the precipitation of iron in the hydrometallurgical process solutions is a common and large scale industrial operation. This step is notorious for leading to valuable metal loss with the iron precipitation product, which is usually directed to tailings. In this study, factors affecting iron precipitation and associated copper loss were studied in synthetic process solutions using statistical analysis and modelling. The variables studied were: initial acid concentration, retention time, seed addition, initial ferric, copper and chloride concentrations. The importance of each variable and their interaction effects were studied against two responses i.e. % Fe precipitated and % copper to the solids. The range of each variable was selected based on the results from the one variable approach, as discussed in Chapter 6, in such a way that the precipitation product contained a maximum amount of hematite with a minimum copper loss to the precipitates. Initial screening was performed by using a fractional factorial method for the variables that have important effect on % Fe precipitation and % Cu in the solids. The important factors determined by fractional factorial design were further optimized by using a Box-Behnkin design.

7.2 Experimental

The experiments were carried out using 1 litre of solution contained in a glass liner (24.7 x 9.65 cm) in a 2 litre Parr instruments autoclave fitted with titanium internals as discussed in Chapter 6.

The relative importance and interaction effects were studied by using statistical design of experiments (Oehlert, 2000). The important factors were first screened by using one quarter fractional factorial design (Box et. al., 1978). Significant factors and their interaction effects were then further optimized using a Box-Behnken design (Myers and Montgomery, 2002). This experimental strategy was skeptically analyzed by Burkin (1984) and has been successfully applied to goethite precipitation by Agatzini and Burkin (1985), agglomeration-growth of iron precipitates by Claassen and Sandenbergh (2006) and iron precipitation from atmospheric nickel sulphate solutions (Wang et. al., 2011). A best fit mathematical model was developed by multiple regression analyses of the data. The corresponding contour plots were obtained using the software package Design-Expert® version 9.0.5.1 (STAT-EASE trial version). In certain cases originPro 8SR0 v8.0724 (B724) was used to plot the graphs.

For scanning electron microscopy (SEM), a small amount of the washed and dried sample was suspended in water and a few drops of the sonicated suspension were dried on carbon tape before analysis. The images were collected using the secondary electron (SE)

mode. Additionally, the size distribution of the precipitates was determined by using Malvern Mastersizer 2000 Laser Diffraction Particle Size Analyser.

7.3 Fractional factorial design

Studying one variable at a time allows for simple interpretation. However, the way each variable is interrelated with another cannot be interpreted through the single variable technique. The advantage of the fractional factorial technique is the fact that several variables are changed together so that interaction between variables can be identified using only a small number of experiments.

The significance of the factors and their levels identified by one variable approach, as detailed in Chapter 6, was tested by designing a one quarter 2^{5-2} fractional factorial design of resolution III. An un-replicated fractional factorial design at two levels, low (—) and high (+) was employed. The layout of the design is given in Table 7-1 and the levels of the variables are given in Table 7-2. The selection of the low (—) and high (+) levels of the variables was based on the one variable approach, as discussed in Chapter 6, and represent the range of a typical CESL and Vale medium temperature hydrometallurgical process leach liquor (Jones *et al*., 2009). Because of the short retention times used, the final conditions of the precipitation were not always in equilibrium.

Table 7-1 Screening experiments for the fractional factorial design in coded and actual forms.

Exp. No.	Variables studied									
	A		B		C		D=AB		E=BC	
	coded	actual	coded	actual	Coded	actual	coded	actual	coded	actual
F-1	+	15	—	0	—	1	—	0	+	15
F-2	+	15	—	0	+	6	—	0	—	0
F-3	+	15	+	15	—	1	+	30	—	0
F-4	+	15	+	15	+	6	+	30	+	15
F-5	—	6	+	15	—	1	—	0	—	0
F-6	—	6	—	0	+	6	+	30	—	0
F-7	—	6	—	0	—	1	+	30	+	15
F-8	—	6	+	15	+	6	—	0	+	15

Table 7-2 Variables and their ranges used for the factorial design experiments. Hematite was the dominant precipitate within these ranges.

Factor	Variable	Low level (—)	High level (+)	Units
A	Initial Fe	6	15	g/L
B	Initial H_2SO_4	0	15	g/L
C	Retention time	1	6	Hour
D	Initial chloride	0	30	g/L
E	Seed	0	15	g/L

7.4 Box-Behnken design

The important variables identified by fractional factorial design and their interaction effects were studied in more detail by using a Box-Behnken design (Box and Behnken, 1960). Details of the Box-Behnken design are given in appendix C. The factors studied were initial H_2SO_4 concentration, Initial ferric concentration and concentration of seed. The factors were studied at three levels: low (—), medium (0) and high (+). The factors and their

levels are given in Table 7-3. The Box-Behnken design with three factors and fifteen experiments including three central points is given in Table 7-4.

Table 7-3 Factors and their ranges used for the Box-Behnken experiments.

Factor	Variable	Low level (—)	Medium (0)	High level (+)	Units
A	Initial Fe	6	10.5	15	g/L
B	Initial H_2SO_4	0	7.5	15	g/L
C	Seed	0	7.5	15	g/L

Table 7-4 Design matrix for Box-Behnken experiments.

Experiment No.	Variables studied					
	A		B		C	
	coded	actual	Coded	actual	coded	actual
G-1	—	6	+	15	0	7.5
G-2	+	15	0	7.5	0	7.5
G-3	—	6	0	7.5	0	7.5
G-4	+	15	+	15	0	7.5
G-5	+	15	—	0	—	0
G-6	0	10.5	+	15	—	0
G-7	0	10.5	0	7.5	—	0
G-8	—	6	—	0	—	0
G-9	—	6	—	0	+	15
G-10	0	10.5	0	7.5	+	15
G-11	0	10.5	+	15	+	15
G-12	+	15	—	0	+	15
G-13	0	10.5	0	7.5	0	7.5
G-14	0	10.5	0	7.5	0	7.5
G-15	0	10.5	0	7.5	0	7.5

7.5 Results and discussion

7.5.1 Fractional factorial design

Experimental results of the fractional factorial design are given in Table 7-5. As in a fractional factorial design there are not enough degrees of freedom left, therefore conventional analysis of variance (ANOVA) cannot be applied. In this study, data was analysed by plotting half normal probability plots for the effect estimates (Daniel, 1959). Half normal probability plots are recommended for experiments utilizing a small number of tests (Myers and Montgomery, 2002). These are plots of the absolute value of the effect estimates against their cumulative normal probabilities. It is assumed that only the main factors (A, B, C etc.) and their low order interactions (i.e. two factor interactions: AB, BC etc.) are dominant and the higher order interactions (three factor and higher i.e. ABC, ABCD etc.) are negligible. In these graphs the factors with small and/or insignificant effects fall on a straight line on the plot while the factors with large and significant effects will visually fall off the straight line.

Figure 7.1 and Figure 7.2 show half normal probability graphs for “% Fe precipitation” and “% Cu content” of the precipitates, respectively. Due to large variation in the amount of product formed; the Cu uptake of the product was gauged by % Cu content of the precipitates, instead of % Cu loss to solids. For example, if two experiments generate solids having same Cu content but different product yield or total mass of the precipitates.

The experiment with higher product yield will result in higher % Cu loss to the solids, even though the Cu content of the two products remained same.

Table 7-5 Elemental analysis of the fractional factorial design experiments

Experiment No.	Precipitates Fe, S content (%)		% Fe precipitated	Cu in solids (%)
	Fe	S		
F-1	62.3	1.33	57.03	0.157
F-2	59.7	2.57	73.36	0.194
F-3	47.8	5.72	10.20	0.094
F-4	64.0	1.09	48.30	0.084
F-5	56.2	2.47	14.99	0.045
F-6	61.6	1.58	86.65	0.046
F-7	64.5	0.91	94.60	0.035
F-8	66.2	0.62	79.99	0.074

Figure 7.1 shows that the factors: A (initial Fe^{3+}), B (initial H_2SO_4), C (time) and E (seed) have large effects on % Fe precipitation for the system under study. While Figure 7.2 shows that the factors: A (initial Fe^{3+}), B (H_2SO_4) and their interaction AB are the most important factors for the copper loss to solids. The interaction term AB becomes more important because the equilibrium constant for the ferric hydrolysis reaction ($K = [H^+]^6/[Fe^{3+}]^2$) is defined by both the ferric and acid concentrations.

Ferric hydrolysis involves the nucleation of hematite particles and subsequent growth of the solid nuclei to larger particles. The agglomeration-growth mechanisms depend upon the ferric iron supersaturation of the solution where the growth of the particles occurs by the attachment of molecules to the surface of the crystal or by agglomeration of the crystals. Both processes play an important role in defining the copper content and quality of the final product.

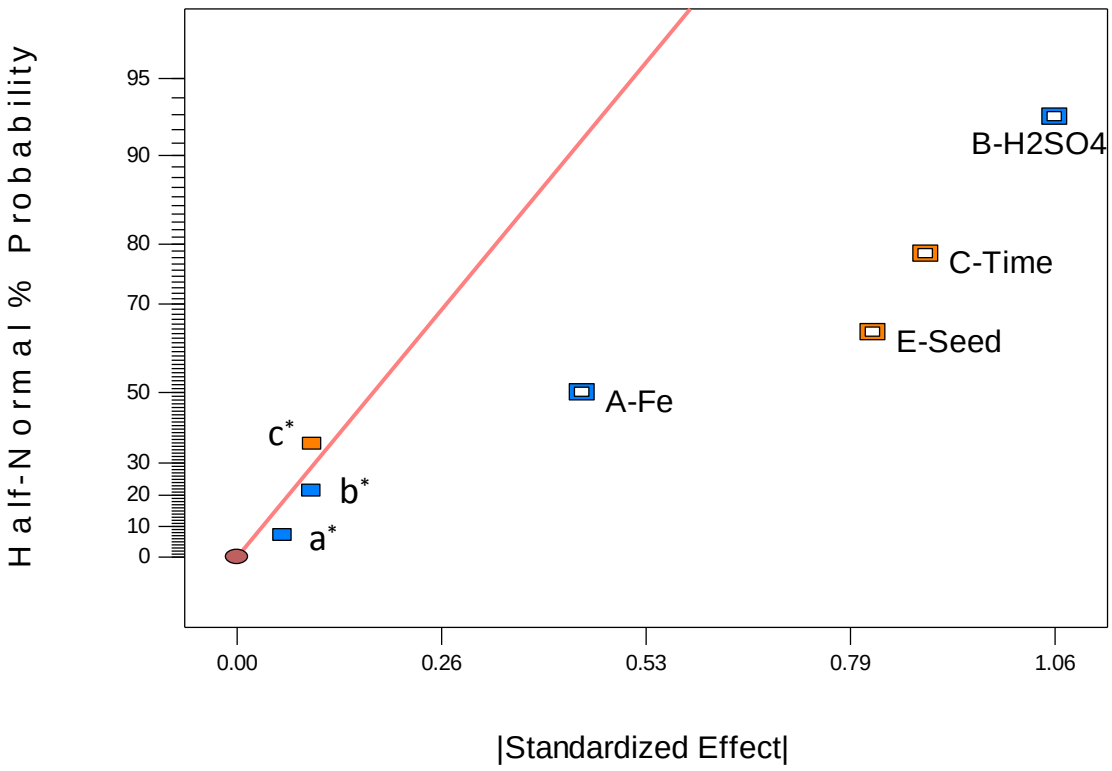

Figure 7.1 Half-normal probability plot for the factors and their interactions for Log (% Fe precipitated). a^*=D+AB+BCE, b^*=BC+DE+ACD+ABE, c^*=BE+CD+ABC+ADE.

Higher supersaturation leads to a faster nucleation rate, which results in small particles, larger surface area and a relatively higher adsorption of divalent ions (Dutrizac and Riverose, 1999; Ruiz *et al*., 2007). At lower supersaturation the nucleation rate is slower, initially fewer nuclei are formed which grow by further addition i.e. particle growth is preferred. In such cases larger particles and relatively lower adsorption or solution entrapment are achieved (Dirksen and Ring, 1991; Dutrizac and Riverose, 1999; Ruiz *et al*., 2007).

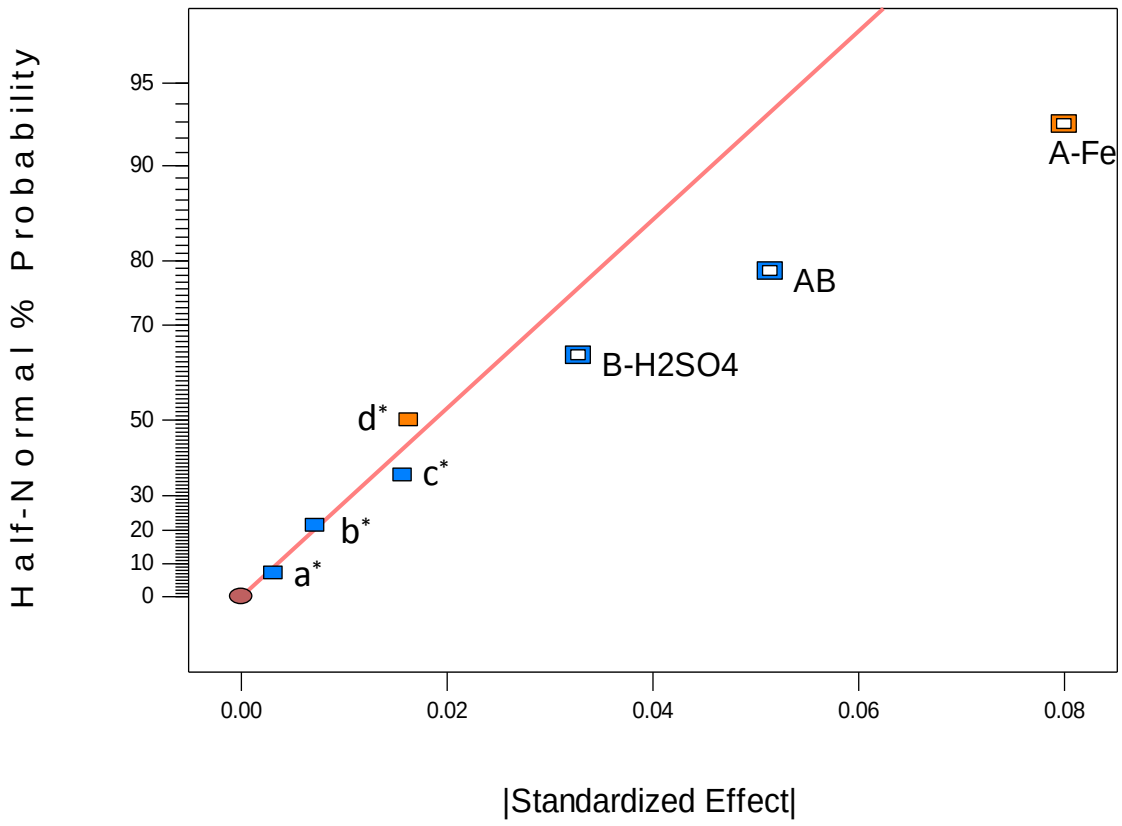

Figure 7.2 Half-normal probability plot for the factors and their interactions for "% Cu content" of the precipitates. a^*=C+AE+BDE, b^*=E+AC+BCD, c^*=BC+DE+ACD+ABE, d^*=BE+CD+ABC+ADE.

Due to large variation in the response values, the data for % Fe precipitation in Figure 7.1 was described by a log transformation (appendix B). Such transformations are often used for stabilizing the variance of the response, making the distribution of the response closer to the normal distribution and improving the fit of the model to the data (Myers and Montgomery, 2002). Details of the procedure have been discussed by Box and Cox (1964) and Box *et al*. (1978). Transformation procedure used in this study is given in appendix B.

Fractional factorial designs usually have low resolution, where the main effects can be differentiated from one another but the main effects cannot be differentiated from some of the low order interactions (AB, BC etc.). Further, some of the low order interactions also cannot be differentiated from one another (Myers and Montgomery, 2002). Therefore, the effects of A, B, C, E and AB, in Figure 7.1 and Figure 7.2, are confounded with BD+CE, AD+CDE, AE+BDE, AC+BCD and D+BCE respectively. Higher order interaction effects are usually negligible in a fractional factorial design, and the system is left with the main factors and two factor interactions only. Although the main factors cannot be differentiated from the two factor interactions, yet, A (initial ferric) and B (initial H_2SO_4) concentrations, have a significant effect on "% Cu content" and the same two effects along with C (time) and E (Seed) have significant effect on "% Fe precipitation". Since longer retention times put economic constraints on hydrometallurgical processes by limiting reactor throughput, and since a certain amount of seed in always present in a continuous commercial process; the factors: A (initial ferric concentration), B (initial H_2SO_4) and E (seed) were studied in more detail in a Box-Behnken design.

Variables which might possibly affect the chosen responses, but were fixed throughout the experimental work for Box-Behnken design were: retention time, 1 hour, temperature, 150 °C, initial Cu^{2+} concentration, 30 g/L and agitation speed, 500 rpm.

7.6 Optimization for the factors

The important factors (initial Fe^{3+}, initial H_2SO_4 and seed) as identified by fractional factorial design were further investigated using a Box Behnken design at three levels with fifteen experiments. The factors and their levels are given in Table 7-3 and the experimental results are given in Table 7-6.

Table 7-6 Compositional analysis of the Box-Behnken design experiments.

Experiment No	Precipitates Fe, S content (%)		% Fe precipitated	Cu in solids (%)
	Fe	S		
G-1	64.6	0.89	60.72	0.031
G-2	63.4	1.36	34.24	0.132
G-3	58.5	1.18	72.54	0.252
G-4	61.2	1.23	22.85	0.051
G-5	48.0	4.04	44.24	0.497
G-6	53.4	2.87	10.00	0.288
G-7	51.8	2.91	39.14	0.522
G-8	54.8	1.98	75.81	0.865
G-9	60.4	0.86	86.57	0.532
G-10	62.6	1.00	65.58	0.152
G-11	63.3	0.95	56.00	0.067
G-12	59.5	1.20	52.00	0.164
G-13	60.5	1.37	54.00	0.121
G-14	60.9	1.39	53.00	0.151
G-15	60.7	1.38	55.00	0.141

The method of least squares was applied to the data to fit a quadratic model for the "% Fe precipitated" and "% Cu content" of the precipitates. The predicted models for the two responses are given in Equations (7.1) and (7.2), with the analysis of variance (ANOVA) results in Table 7-7. The statistical significance of the models was tested by Fisher's F-test.

Normally, p-values of less than 0.05 for significant terms and greater than 0.05 for "lack of fit" are considered good to explain the statistical significance of the model. It can be seen in Table 7-7 that significant terms in both the fitted quadratic models have very small p-values, while p-values for "lack of fit" are greater than 0.05 in both the models. The "R-Squared" values, for % Fe precipitated and % Cu content of the solids, were 0.9911 and 0.9729 respectively. For both the models, the "Predicted R-Squared" values were in good agreement with the "Adjusted R-Squared" i.e. the difference was less than 0.1, demonstrating the statistical significance of the models (Daniel, 1976). The model results were plotted as 2D contour plots as shown in Figure 7.3 and Figure 7.4. The results show that the interaction of factors A (initial ferric concentration) and B (initial H_2SO_4) has significant effect on the % Cu content of the precipitates while the interaction of B (initial H_2SO_4) and C (seed) has significant effect on the % Fe precipitated (see Table 7-7, p-value <0.05).

$$\%\ \boldsymbol{Fe\ precipitated} = 101.738 - 3.953 \times [Fe] - 3.188 \times [H_2SO_4] + 1.825 \times [Seed] + 0.162 \times [H_2SO_4] \times [Seed] - 0.082 \times [Seed]^2 \quad (7.1)$$

$$\%\ \boldsymbol{Cu\ content} = 1.292 - 0.086 \times [Fe] - 0.050 \times [H_2SO_4] - 0.070 \times [Seed] + 0.003 \times [Fe] \times [H_2SO_4] + 0.002 \times [\mathrm{Fe}]^2 + 0.003 \times [\mathrm{Seed}]^2 \quad (7.2)$$

where, $[Fe]$, $[H_2SO_4]$ and $[Seed]$ are the initial concentrations, in g/L, for ferric iron, sulphuric acid and hematite seed, respectively.

Table 7-7 Analysis of variance for the fitted quadratic models.

Source	% Fe precipitated					% Cu content				
	Sum of Squares	df*	Mean Square	F Value	p-value Prob> F	Sum of Squares	df*	Mean Square	F Value	p-value Prob> F
Model	5578.98	5	1115.80	199.90	<0.0001	0.77	6	0.13	126.66	<0.0001
A-Fe	2531.87	1	2531.87	453.59	<0.0001	0.047	1	0.047	45.74	0.0001
B-H_2SO_4	1512.89	1	1512.89	271.04	<0.0001	0.12	1	0.12	117.56	<0.0001
C-Seed	1366.95	1	1366.95	244.89	<0.0001	0.20	1	0.20	194.17	<0.0001
AB						0.054	1	0.054	53.48	<0.0001
BC	458.45	1	458.45	82.13	<0.0001					
A^2						0.006	1	0.006	6.07	0.0391
C^2	67.93	1	67.93	12.17	0.0068	0.11	1	0.11	103.52	<0.0001
Residual	50.24	9	5.58			0.008	8	$1.017x10^{-3}$		
Lack of Fit	48.24	7	6.89	6.89	0.1325	0.008	6	$1.279x10^{-3}$	5.50	0.1617
Pure Error	2.00	2	1.00			$4.647x10^{-4}$	2	$2.323x10^{-4}$		
Corrected- Total	5629.22	14				0.78	14			

*df=degree of freedom.

Figure 7.3(a) contour plot shows that in the presence of 15 g/L initially added H_2SO_4, 6 g/L Fe^{3+} and 0.0 g/L seed about 35 % of the iron is precipitated in 1 hour. However, by the addition of 15 g/L seed under the same conditions this amount increases to about 75 %. The presence of hematite seed increased the precipitation kinetics (by lowering the critical energy for nucleation) as well as the proportion of iron precipitated as hematite (mineralogy of the precipitates is discussed later in section 7.9). In the presence of higher amounts of initially added ferric, the amount of iron precipitation again decreased, see

Figure 7.3(b) and (c). This decrease is due to generation of acid by the hydrolysis of excess ferric in the system, which in fact increases the equilibrium ferric concentration of the solution. The initial and final H_2SO_4 concentrations of each experiment are given in Table 7-8.

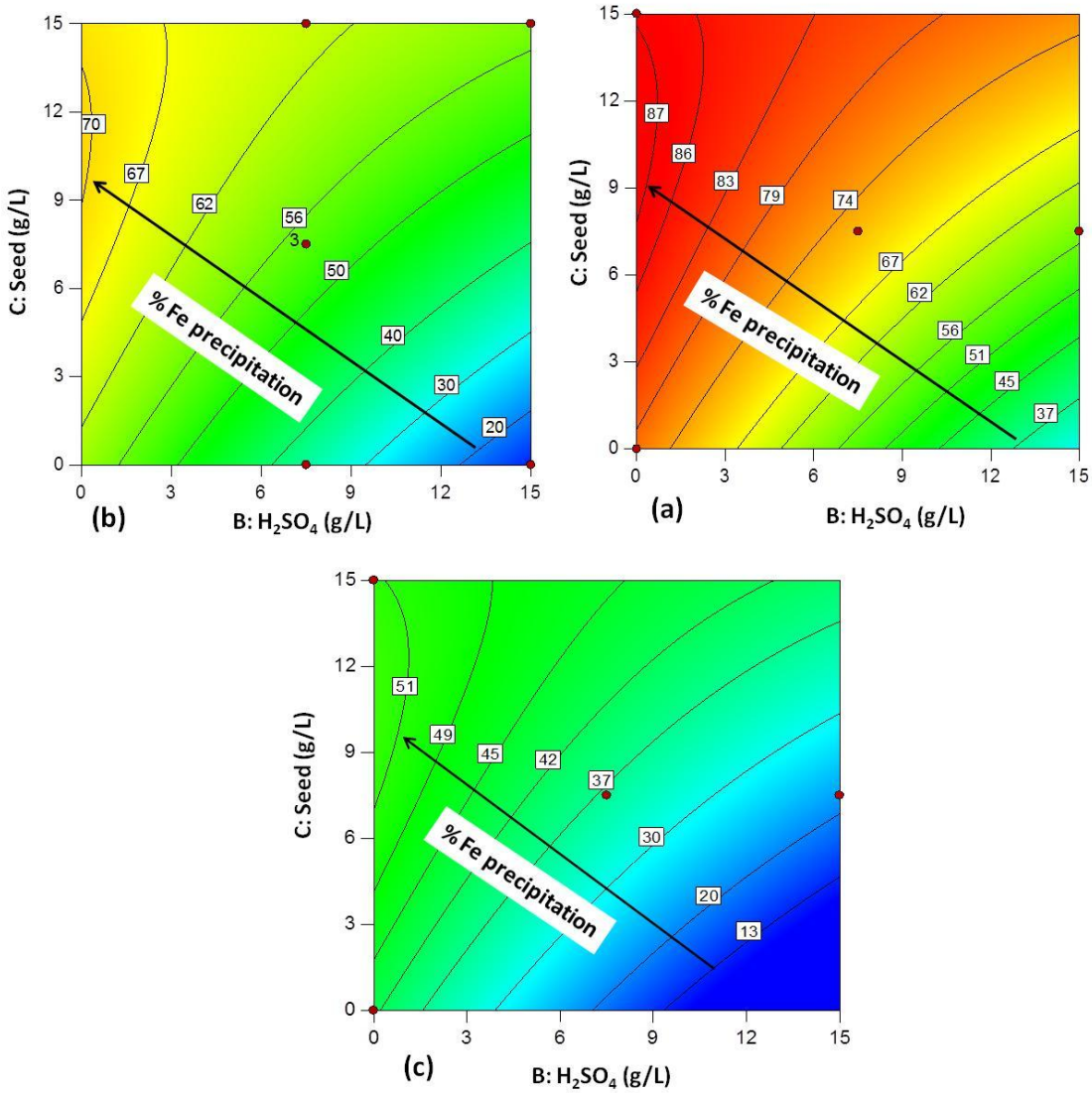

Figure 7.3 2D contour plots for the interaction effect of initial H_2SO_4 and seed concentrations on % Fe precipitation: (a) initial Fe^{3+} = 6.0 g/L; (b) initial Fe^{3+} = 10.5 g/L; (c) initial Fe^{3+} = 15 g/L.

Figure 7.4(a) shows that increasing acid concentration from 0 to 15 g/L decreases the Cu content of the precipitates from about 0.8 % to about 0.4 %. Figure 7.4(b) and (c) show that addition of seed further reduces the copper content of the precipitates. Comparison between Figure 7.4(b) and (c) shows that difference between % Cu content of the precipitates for medium and high levels of seeding is not significant (even though the solids are diluted with higher amount of seed which does not take Cu). It was observed that seed itself does not result in the copper loss in the absence of fresh precipitates. After necessary correction for the dilution effect of seed, the Cu/Fe ratio of the fresh precipitates is plotted in Figure 7.5. The presence of hematite seed promotes the precipitation of hematite relative to other iron bearing species, which in fact reduces the copper content of the precipitates as seen in Figure 7.5. Figure 7.5(a) and (b) show that presence of high acid low ferric and medium seed levels generates the precipitates with least amount of copper to the solids. However, high seed levels, as shown in Figure 7.5(c), did not improve the Cu uptake of the precipitates. For a constant ferric concentration of solution, higher seeding levels provide more surface area for surface nucleation, which result in more surface nucleation sites and less growth. XRD analysis of the precipitates for high seeding level detected two generations of hematite: one with well crystallized narrow peaks and the other nanoscale with broad diffused peaks. The more probable explanation seems that the new nuclei are formed and some of the newly precipitated material was present as distinct separate particles. This observation suggests that during the precipitation event a first burst of nuclei is formed by homogeneous nucleation which drops the supersaturation level and

thereafter surface growth i.e. surface nucleation becomes the dominant mechanism. Because of the fine sizes of the initially formed nuclei, larger seed particles grew preferentially and the fine fractions remained mainly as separate particles.

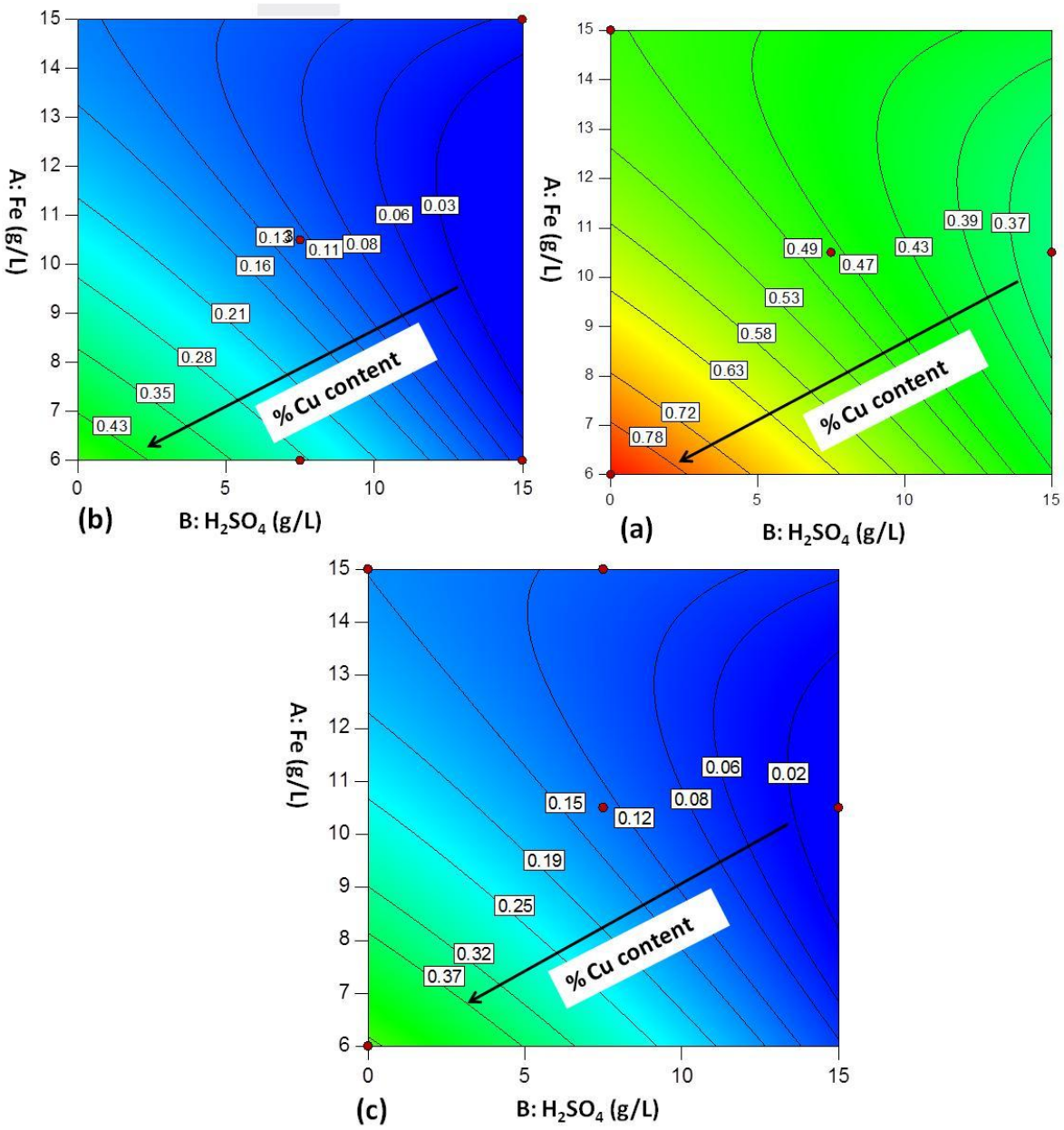

Figure 7.4 2D contour plots for the interaction effect of initial H_2SO_4 and initial Fe^{3+} concentrations on % Cu content of precipitates: (a) seed = 0.0 g/L; (b) seed = 7.5 g/L; (c) seed = 15 g/L.

The mechanism as pointed out in Chapter 6 i.e. high seeding levels result in higher secondary nucleation rate, collisions (i.e. crystal-crystal contact) may also contribute to the fine fractions by defragmentation of the newly deposited crystals. Particle size distribution of the precipitates is compared in Figure 7.6. The presence of fine fractions (0.8-3 μm) and bimodal particle size distribution for high seeding levels further supports the behaviour observed by XRD. These observations are consistent with Hutchison and Phipps (1977) and Claassen and Sandenbergh (2006). These authors also observed a similar trend for high seeding levels in their system.

It was difficult in this study to differentiate the individual effect of the factor A (initial Fe^{3+}) due to the fact that more acid is generated at higher ferric concentrations, which is confounded with the effect of factor B (initial H_2SO_4). Therefore, instead of the individual term 'A' the interaction term AB (initial ferric and H_2SO_4) is more important for % Cu loss to the precipitates. A decrease in the copper content of the precipitates at higher acid concentrations, as seen in Figure 7.5(a) – (c), is attributed to an increase in equilibrium ferric concentration of the solution (lower supersaturation) leading to a slower nucleation rate, which results in larger particles and relatively lower adsorption of divalent ion, see Figure 7.7 and Figure 7.8. These figures show that at lower initial acid concentrations rapid homogeneous nucleation occurs which results in the generation of a large number of fine particles at once. However, at higher initial acid concentration fewer nuclei are formed at first which further grow to large particles as seen in Figure 7.8. Ruiz *et al*., (2007) also observed an increase in the particle size of precipitates at higher acid concentrations.

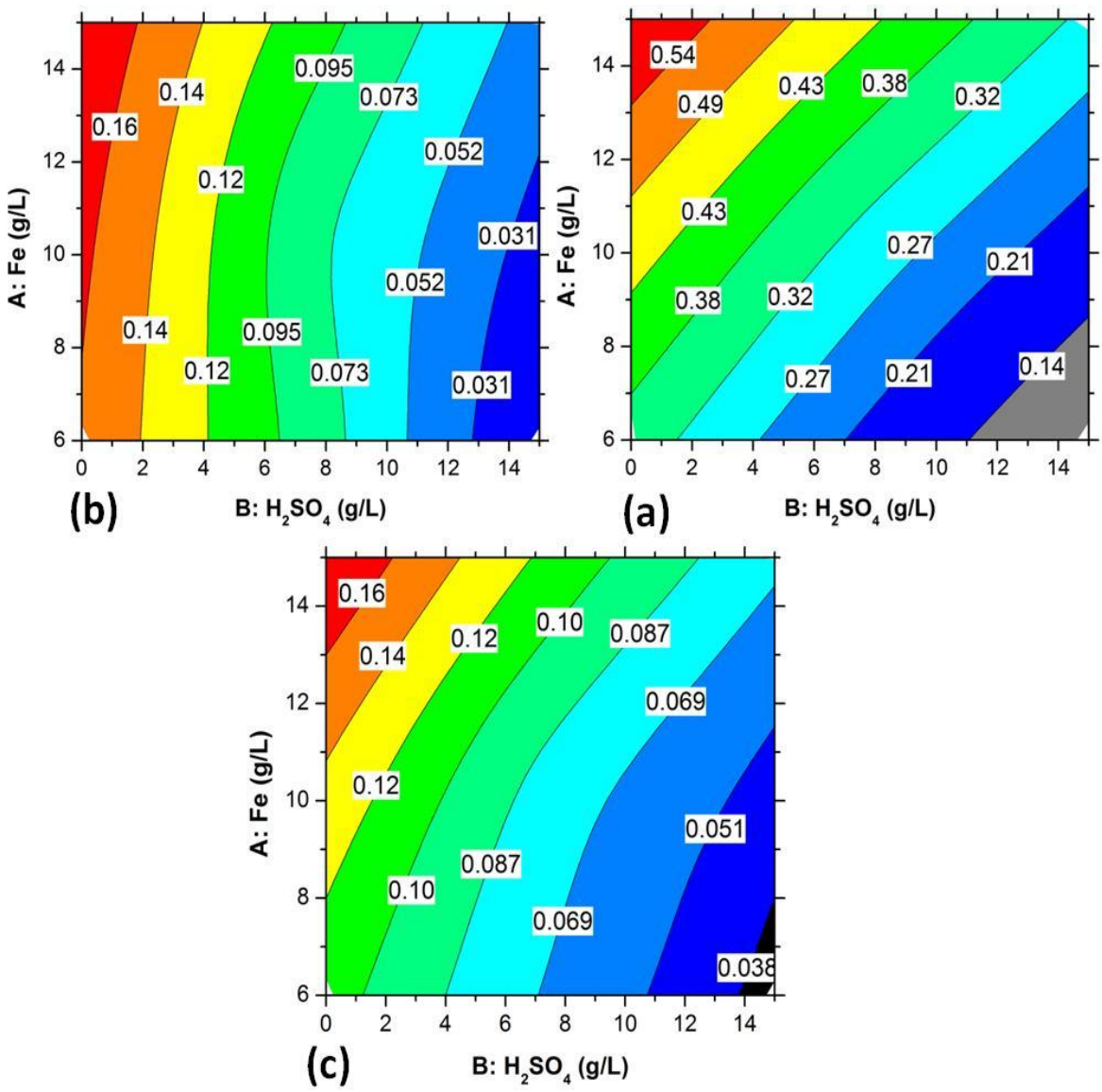

Figure 7.5 Cu/Fe ratio (%Cu/%Fe x 100) of precipitates for the interaction effects of initial H_2SO_4 and initial Fe^{3+} concentrations: (a) seed = 0.0 g/L; (b) seed = 7.5 g/L; (c) seed = 15 g/L.

Table 7-8 Initial and final conditions of the solutions and X-ray structure of the precipitates.

Experiment	Fe (g/L)		Cu (g/L)		H_2SO_4 (g/L)		Solid phase
No.	Initial	Final	Initial	Final	Initial	Final	precipitated*
F-1	15	6.2	30	29.3	0	22.7	H
F-2	15	4.0	30	28.8	0	29.2	H
F-3	15	13.1	30	29.8	15	19.1	H + V
F-4	15	7.3	30	29.5	15	34.5	H
F-5	6	5.0	30	29.8	15	17.6	H
F-6	6	0.58	30	29.9	0	14.6	H
F-7	6	0.29	30	29.7	0	15.2	H
F-8	6	1.0	30	29.7	15	27.9	H
G-1	6	2.3	30	29.8	15	24	H
G-2	15	9.6	30	29.5	7.5	21.3	H
G-3	6	1.6	30	29.5	7.5	20.3	H
G-4	15	11.5	30	28.9	15	24.2	H
G-5	15	7.9	30	27.5	0	18.2	H + V
G-6	10.5	9.4	30	29.6	15	18	H
G-7	10.5	6.3	30	28.8	7.5	19.6	H
G-8	6	1.3	30	27.8	0	12.5	H + G
G-9	6	0.6	30	28.4	0	14.2	H
G-10	10.5	3.5	30	29.3	7.5	26.1	H
G-11	10.5	5	30	29.7	15	28.4	H
G-12	15	5.5	30	29.3	0	23.2	H
G-13	10.5	4.8	30	29.5	7.5	22.5	H
G-14	10.5	4.6	30	29.4	7.5	22.8	H
G-15	10.5	4.7	30	29.7	7.5	22.3	H

*H = Hematite, V = Volaschioite, G = Goethite

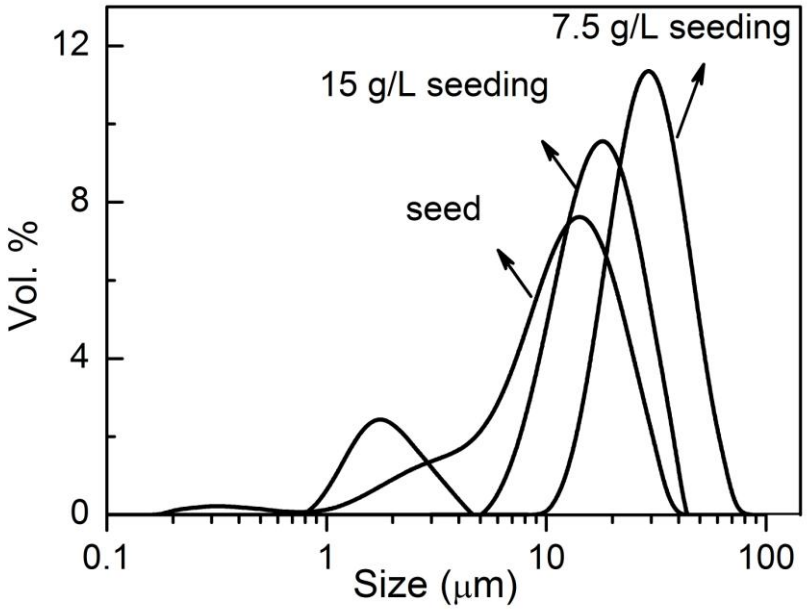

Figure 7.6 Particle size distribution of the seed and precipitates for different seeding levels.

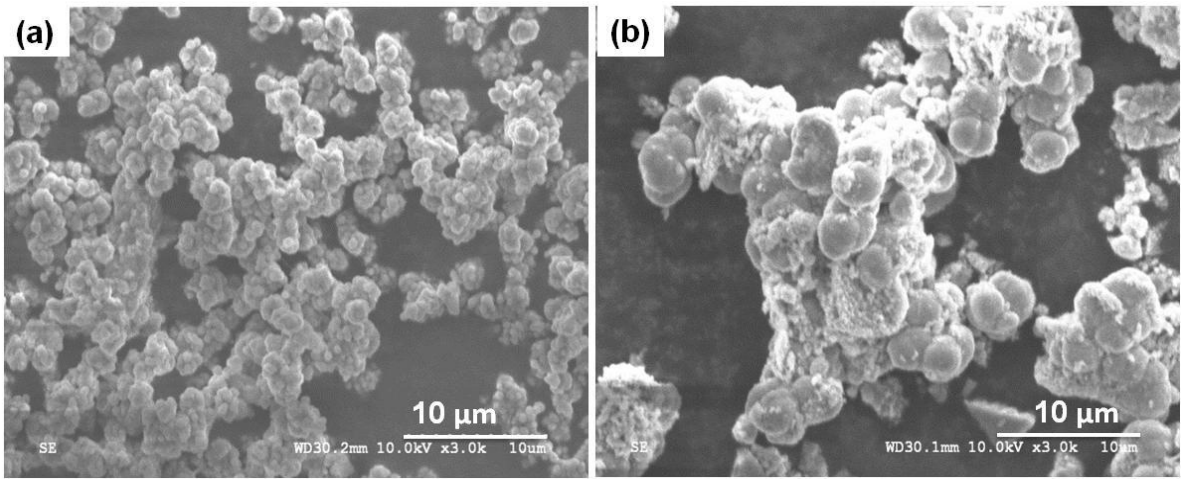

Figure 7.7 SEM images of the precipitates: (a) 0.0 g/L initial H_2SO_4; (b) 15 g/L initial H_2SO_4. Other conditions: 6 g/L Fe^{3+}, 30 g/L Cu^{2+}, 1 hr, 150 °C.

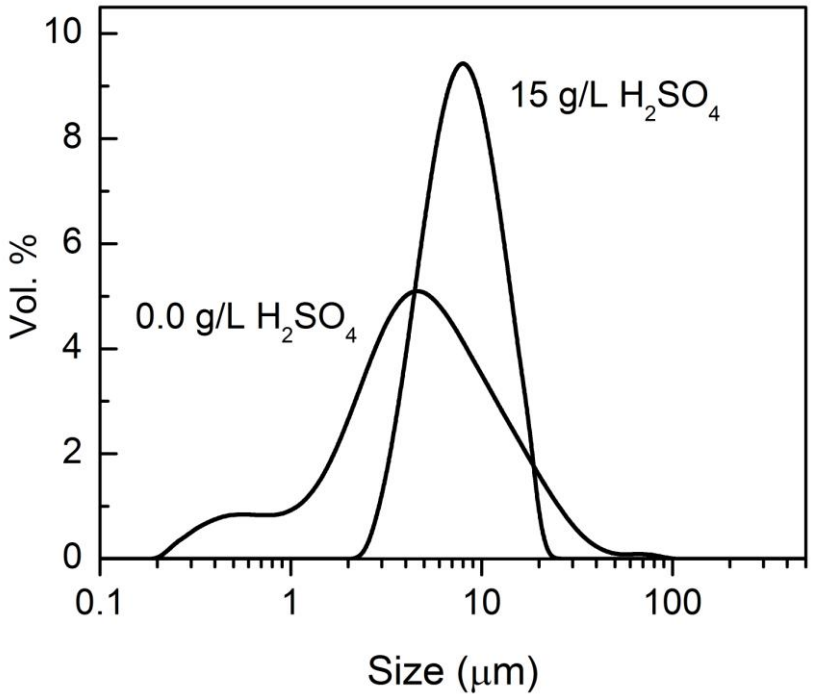

Figure 7.8 Particle size distribution of the precipitates: (a) 0.0 g/L initial H_2SO_4; (b) 15 g/L initial H_2SO_4. Other conditions: 6 g/L Fe^{3+}, 30 g/L Cu^{2+}, 1 hr, 150 °C.

7.7 Mechanism of Cu loss to the precipitates

Various studies (Rose and Bianchi-Mosuera, 1993; Peacock and Sherman, 2004; Chen and Li, 2010, Grover *et al*., 2012) have shown the adsorption of Cu^{2+} on fine particles of hematite. Peacock and Sherman (2004) described the adsorption of Cu^{2+} by considering surface complexes ($Fe - O^- + Cu^{2+} \rightarrow Fe - OCu^+$) on the hematite particles, see Figure 7.9. Unpaired bonds at the surface of hematite create a localized electric field. Electric potential further increases if the particles approach nanosize (typically < 7 nm, because of a decrease in the symmetry of the bonding environments on the smaller particles relative to the larger particles), resulting in relatively higher uptake of the cations (Madden *et al*.,

2006). However, Tombácz *et al*., (2004) suggested that at lower pH values, where activity of proton is high, protonation ($Fe - O^- + H^+ \rightarrow Fe - OH + H^+ \rightarrow Fe - OH_2^+$) of the surface sites of the hematite particles takes place. These positively charged protonated sites are complexed with negatively charged SO_4^{2-} in the solution. This mechanism leads to hematite with relatively higher sulphate content. Charge reversal of the surface sites takes place when the SO_4^{2-} adsorption capacity of the hematite is reached making the surface suitable for cation uptake.

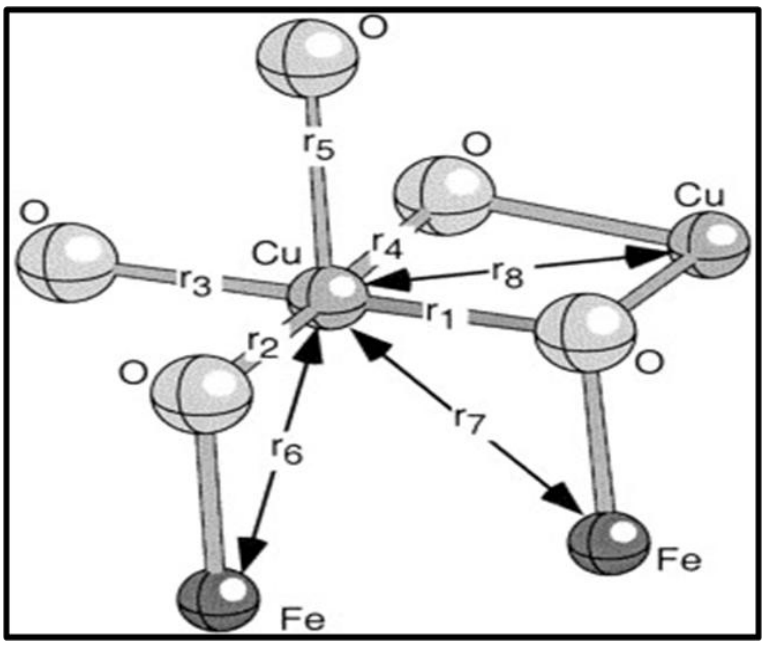

Figure 7.9 Hypothetical model cluster for Cu^{2+} sorbed to hematite (with modification from Peacock and Sherman, 2004).

On the other hand, substitution of Cu^{2+} into the hematite structure can serve as another means of copper loss to precipitates. Cu^{2+} and Fe^{3+} have a large difference in ionic radii (0.073 and 0.0645 nm respectively) and can cause charge neutrality issues when

replacing the other. However, in highly acidic environments Cu^{2+} can replace Fe^{3+}. This is suggested to be due to the fact that charge balance is achieved by uptake of protons on the particle surface and an enlarged cell parameter "c" is observed due to the Jahn-Teller effect of copper ions in the hematite structure (Cornell and Schwertmann, 2003).

It is of further interest to study the exact mechanism of copper loss to the precipitates by using a combination of techniques such as: X-ray absorption fine structure spectroscopy (XAFS), XRD and TEM.

7.8 Optimum parameters

Figure 7.3 and Figure 7.4 show that, in the absence of seed, if the target is set to achieve maximum “% Fe precipitation” lower acid levels should be used, but if the target is to reduce the % Cu content of the precipitates, higher acid levels will be favorable. Hence, both targets cannot be achieved at the same time. However, in the presence of moderate amounts of seed, Cu loss can be minimized with moderate to high iron precipitation levels from the acidic media. For example, Figure 7.3(a) and Figure 7.4(b) show that in the presence of 15 g/L initially added H_2SO_4, 7.5 g/L seed and 6 g/L initial Fe^{3+} about 60 % of the iron is precipitated with < 0.1 % Cu content of the precipitates. Under the same conditions but in the absence of seed about 35 % iron is precipitated with about 0.45 % Cu content of the precipitates. The predicted models and contour plots suggest that the presence of a high acid and moderate seeding produces best results. As discussed earlier, the high acid

environment creates low supersaturation (because of higher equilibrium ferric solubility in acid) and results in slower nucleation rate or prefers particle growth over nucleation, resulting in relatively coarser particles as shown in Figure 7.7 and Figure 7.8. Demopoulous (2009) and Claassen and Sandenbergh (2006) have described the effect of supersaturation on particle growth and product quality in detail.

7.9 Phase analysis of the precipitates

The precipitation products generated under different experimental conditions were analyzed by XRD and the X-ray structures of the solid phases are given in Table 7-8. Hematite was the dominant phase in all cases. However, under certain experimental conditions the precipitates contained certain amounts of either Volaschioite ($Fe_4(SO_4)O_2(OH)_6.2H_2O$) or goethite. The restriction of Volaschioite to samples F-3 and G-5 and goethite to G-8 alone shows that these are precipitated only under the conditions of high or zero initial acid concentrations, respectively, and only in the absence of hematite seed. The quantitative powder diffraction analysis of the precipitates, in this study, showed the precipitates to consist of about 10 – 15 % amorphous phase when retention time was ≤ 4 hour or when hematite seed was absent. The kinetic stability of amorphous phase, despite its thermodynamic instability in the domain of hematite was attributed to the short retention times used.

7.10 Conclusions

The statistically designed experiments successfully identified the significant factors and their interactions affecting the "% Fe precipitation" and "% Cu content" of the precipitates. The factors: initial ferric and H_2SO_4 concentrations were found to have significant effect on "% Cu content" in the solids, while the factors: initial ferric, H_2SO_4 concentrations, retention time and seed were identified by fractional factorial design to be the important factors for the "% Fe precipitation". The factors: initial ferric, H_2SO_4 and seed were further studied at three levels using a Box-Behnken design and the data was used to create contour plots. Mathematical models for "% Fe precipitated" and "% Cu content" of the precipitates were developed by fitting the data to quadratic models. The predicted models were successful to explain the factors and their interactions which maximize "% Fe precipitation" and minimize "% Cu content". The results can be applied to improve the existing processes as well as for those being in the development stages. However, care should be taken to use the predicted models and contour plots for the conditions outside the range of conditions used in this study.

The data show that the presence of high acid and moderate amount of seed are the more suitable conditions to minimize % Cu content of the solids with moderate to high levels of % Fe precipitation. The results also show that the supersaturation and the nucleation to growth ratios determine the final product quality i.e. the final particle size and Cu and SO_4^{2-} content of the precipitates. High acid concentrations create a low

supersaturation environment which results in slower nucleation rate and prefers particle growth. The presence of a certain amount of seed was always beneficial for the two responses. However, high seed levels resulted in more fine fractions in the final product.

Chapter 8. Precipitation kinetics and effect of impurities

8.1 Introduction

It has been discussed in Chapter 6 and Chapter 7 that the rate of precipitation affects the particle size of the solid product and its copper uptake. Secondly, knowledge of precipitation rate can help to manipulate the process characteristics inherently related to the kinetics. In this chapter precipitation experiments were carried out to study the effect of different variables on the rate of iron precipitation. Several factors, which either increase or impede the iron precipitation rate, such as: H_2SO_4, time and seed concentration were studied.

Sulphide concentrates fed to the autoclave are usually not pure and may contain significant amounts of other elements such as As, Al, Mg and Na which are leached along with the target metal. The presence of these elements can also affect the iron precipitation step. Therefore, the effect of the presence of these elements on the nature of precipitation product and precipitation rate was also investigated. It has been seen in Chapter 6 that the presence of chloride accelerates the precipitation kinetics; secondly the beneficial effect of chloride on leaching kinetics has also been discussed in Chapter 6. In these experiments chloride concentration was kept constant at 11 g/L Cl^-.

Despite numerous studies on the hydrolysis of ferric sulphate solutions (Dutrizac and Chen, 2009, 2011; Umetsu *et al*., 1977; Tozawa and Sasaki, 1986; Vöigt and Gobler, 1986;

Posnjak and Merwin, 1922), there is not much data for the kinetic effect of the parameters on iron precipitation under medium temperature conditions from sulphate-chloride solutions. This study focuses on how certain factors affect the precipitation kinetics and the solution conditions which cause those effects.

Precipitation of hematite at elevated temperature from pure ferric chloride solutions (Riveros and Dutrizac, 1997), ferric nitrate solutions (van Weert and Shang, 1993; Shang and van Weert, 1993) and ferric sulphate solutions (Dutrizac and Chen, 2009, 2011, Ruiz *et al*., 2007) has been studied in the past. However, there is not much data available for the mixed sulphate chloride system under medium temperature conditions, except for the work done by Dutrizac and Chen (2009). The simultaneous presence of sulphate and chloride in the solution makes the system more complex because an abundance of species can form. In the literature outside hydrometallurgy (Knight and Sylva, 1974; Murphy *et al*., 1976; Sapieszko *et al*., 1977; Dousma *et al*., 1978, 1979; Flynn, 1984; Grundl and Delwiche, 1993 and Diz *et al*., 2006); precipitation kinetics and product type have been linked to the solution species and how they form monomer, dimmers and polynuclear complexes or large polymers and ultimately colloid sized particles. These mechanisms are greatly affected by the presence of various types of ions and solution temperature. It is not the goal of this study to carry out speciation studies of the system under consideration. However, the speciation knowledge from the literature, where necessary, will be applied to explain certain behaviours observed.

8.2 Experimental work

Reagent grade chemicals ($CuSO_4 \cdot 5H_2O$, $Fe_2(SO_4)_3 \cdot 7H_2O$, LiCl, Na_2SO_4, $Al_2(SO_4)_3 \cdot 18H_2O$, $As_2O_5 \cdot 0.5H_2O$, $MgSO_4$) and de-ionized water (10 MΩ) were used for all the experiments. The experiments were carried out using a 2 litre Parr autoclave with 1 litre of solution contained in a glass liner (24.7 x 9.65 cm). Experiments were carried out using the same procedure as outlined in Chapter 6.

8.3 Results and discussion

8.3.1 Effect of acid on hydrolysis rate

The effect of various initial H_2SO_4 concentrations on the hydrolysis of ferric ion for longer retention times is shown in Figure 8.1. Figure 8.1a and Figure 8.1d respectively show that in the presence of 13 g/L initial H_2SO_4 the equilibrium is reached after about 6 hours. However, at 27 g/L initial H_2SO_4, equilibrium is not reached even after 12 hours. The slower hydrolysis rate for higher acid concentrations is evident in Figure 8.1a and Figure 8.1d by comparison between solid and dashed lines.

During the first ~35 minutes (i.e. time=0) required to heat the autoclave to the required temperature (150 °C), only a small amount (3 – 10 %) of iron was precipitated (i.e. most of the iron remained in the solution)

At any time "t", during hydrolysis, the ferric concentration in the final solutions can be expressed in the form of an exponential relationship given in Equation (8.1):

$$Fe_t = A\exp(-Bt) + Fe_{eq.} \tag{8.1}$$

where $t = 0$ represents the time when the contents in the autoclave reach the reaction temperature 150 °C, Fe_t is the ferric concentration at any time "t", $Fe_{eq.}$ is the equilibrium ferric concentration and A and B are constants.

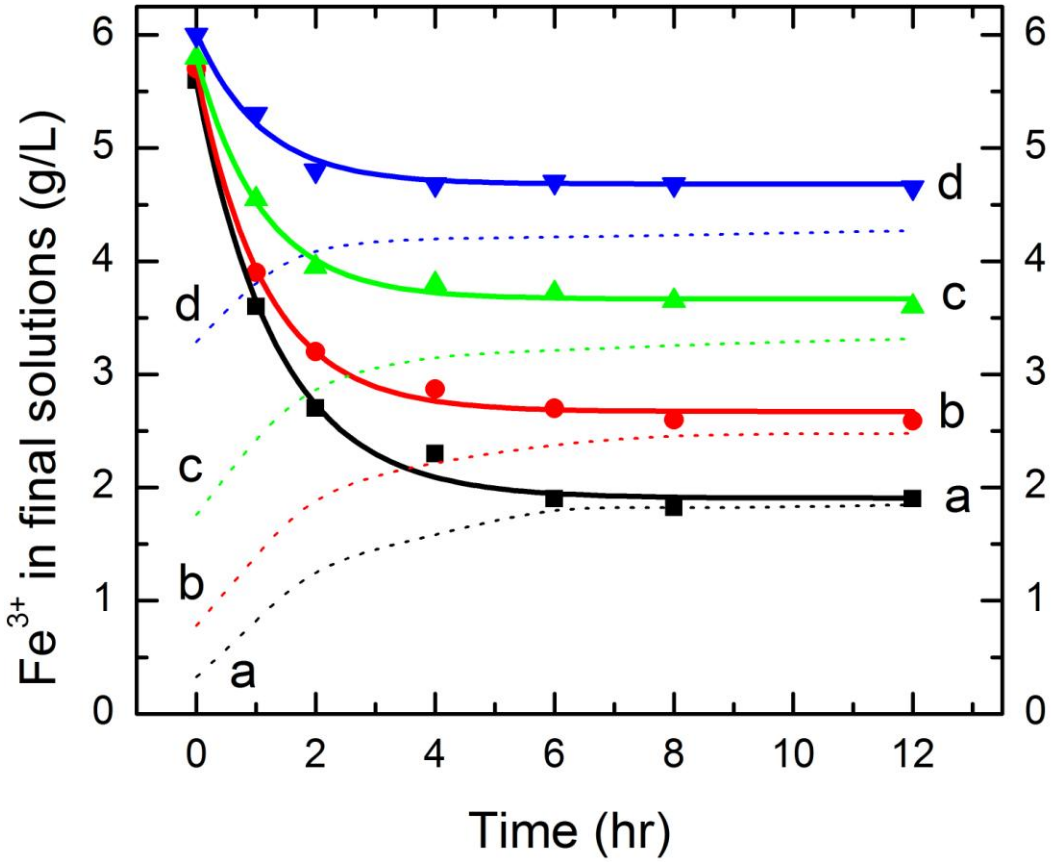

Figure 8.1 Relationship between Fe^{3+} in final solutions and retention time for different initial acid concentrations: a) 13 g/L, b) 17 g/L, c) 22 g/L, d) 27 g/L initial H_2SO_4. Dotted lines show the equilibrium values for the acid present, calculated using Equation (8.2). Other conditions: 6 g/L Fe^{3+}, 30 g/L Cu^{2+}, 11g/L Cl^-, 150 °C.

The equilibrium ferric concentration ($Fe_{eq.}$) is a function of final H_2SO_4 concentration of the solution. It was determined by carrying out experiments at different acid concentrations for long retention times (48 hours). It was assumed herein that equilibrium was established after 48 hours. When equilibrium was established in different acid concentrations, the relationship between the final acid and final iron concentration of solutions resulted in a straight line in the $log - log$ plot as shown in Figure 8.2. The relationship based on the least square fit of the data is given in Equation (8.2). This equation can be used to determine the equilibrium ferric concentration for the hematite precipitation reaction.

$$Log(Fe_{eq}) = 3.42\ Log(H_2SO_4) - 4.46 \tag{8.2}$$

where Fe and H_2SO_4 are the final ferric and sulphuric acid concentrations, respectively, in g/L.

After finding the equilibrium ferric concentration ($Fe_{eq.}$), the data in Figure 8.1 was fitted to Equation (8.1). By using the method of least squares the constants A and B of Equation (8.1) were determined for different acid concentrations and are given in Table 8-1.

The hydrolysis reaction rate (R_{hyd}) was determined using the power law given in Equation (8.3) (Cheng and Demopoulos, 2004; Söhnel and Garside, 1992).

$$R_{hyd} = k_{hyd}\ (Fe_t - Fe_{eq.})^{\alpha} \tag{8.3}$$

On a $log - log$ scale it can be written as Equation (8.4).

$$\log\ (R_{hyd}) = \log\ \left(k_{hyd}\right) + \alpha \log\ (Fe_t - Fe_{eq.}) \tag{8.4}$$

where R_{hyd} is in $g/L/hour$, k is the kinetic constant with units "per hour" and α is the reaction order.

By differentiating Equation (8.1) with respect to time, the hydrolysis reaction rate at any time "t" can be expressed as shown in Equation (8.5).

$$R_{hyd} = -\frac{d}{dt}(Fe_t) = AB\exp(-Bt) \tag{8.5}$$

at time $t = 0$ it becomes as given in Equation (8.6).

$$R_{hyd} = -\frac{d}{dt}(Fe_{t=0}) = AB \tag{8.6}$$

R_{hyd} at time $t = 0$ was determined for different acid concentrations using values of A and B and it was plotted against $\log\ (Fe_t - Fe_{eq.})$, see Equation (8.4). The plot resulted in a straight line as shown in Figure 8.3. The slope of the line was equal to the reaction order "α" which was found to be approximately equal to 1. By using the values of the α and R_{hyd}, the kinetic constant k_{hyd} was determined and was found to be "$\log\left(k_{hyd}\right) = -0.34 \pm 0.024$". Hence, the final rate equation for the hydrolysis of ferric iron can be expressed as Equation (8.7):

$$R_{hyd} = 0.46\ (Fe_t - Fe_{eq}) \tag{8.7}$$

It should be noted that there are various sources of error during the calculations of k_{hyd}. Secondly, the reaction order cannot be confirmed because of the acid generation and change in equilibrium ferric concentration as the hydrolysis reaction proceeds. Therefore, due to the higher errors associated with the determination of the rate constant, it only represents an approximate value. However, it is still useful to predict the precipitation rate.

For example, in the presence 15 g/L initial H_2SO_4, the equilibrium ferric concentration calculated using Equation (8.2) turns out to be 0.37 g/L. If an experiment is designed with 6 g/L initial Fe^{3+} and 15 g/L initial H_2SO_4, Equation (8.7) suggests the precipitation of about 42 % iron in an hour which is in reasonably good agreement with the 45 % iron precipitation as observed experimentally, under the same conditions in Chapter 6, Figure 6.1.

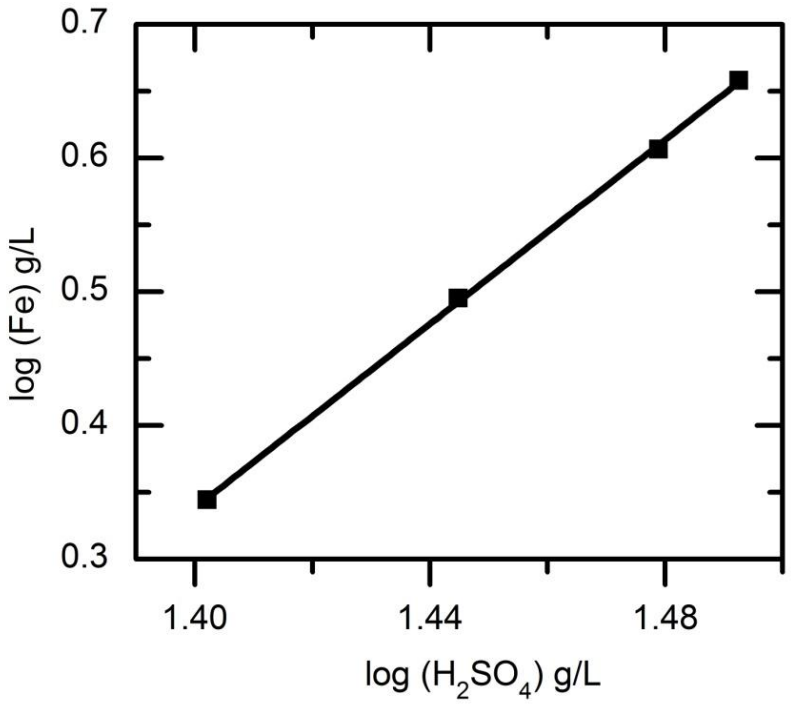

Figure 8.2 Log – Log plot for the determination of equilibrium ferric concentration: Other conditions: 6 g/L Fe^{3+}, 30 g/L Cu^{2+}, 11g/L Cl^-, 48 hr, 150 °C.

Table 8-1 Values of constants A and B obtained from least square fitting of Equation (8.1), for the experiments carried out at various initial acid concentrations.

Initial H_2SO_4 (g/L)	A	B
13.0	3.67	0.750
17.0	3.02	0.870
22.0	2.14	0.910
27.0	1.33	0.910

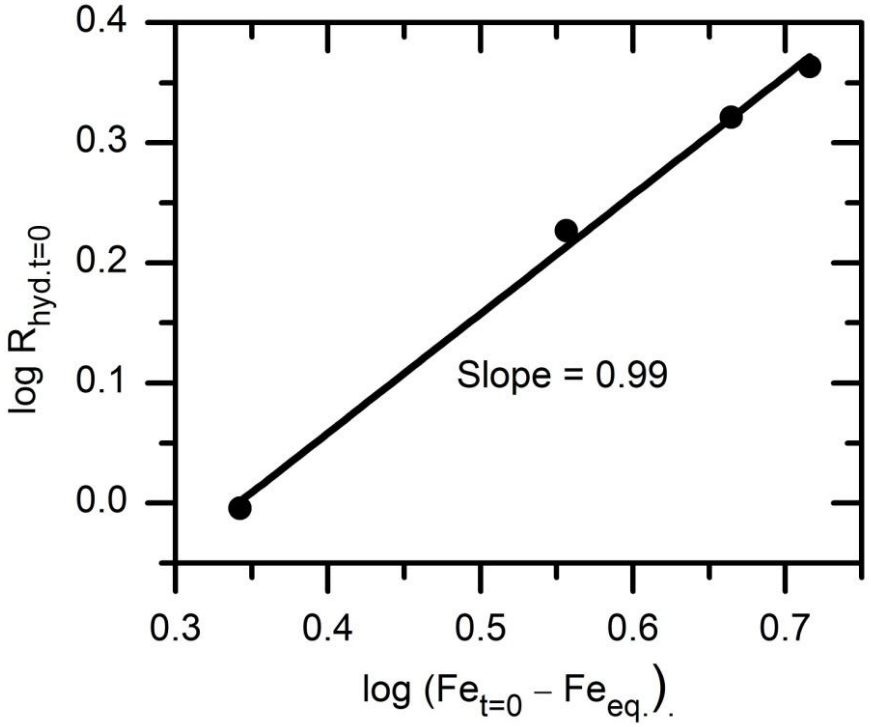

Figure 8.3 Log – log plot for the determination of reaction order (α).

8.4 Effect of impurities

The presence of Mg and Na increased the amount of iron precipitation while Al and As decreased the extent of iron precipitation from the system containing 6.0 g/L Fe^{3+}, 15.0 g/L H_2SO_4, 11.0 g/L Cl^-, 30.0 g/L Cu^{2+} at 150 °C and 1 hour retention. The behaviour of arsenic was noticeably different from other elements. Figure 8.4 shows that in the absence of arsenic about 45 % of iron is precipitated. Addition of small amounts of As (< 500 mg/L As^{5+}) impeded the iron precipitation to a significant extent. In the concentration range (50 – 500 mg/L As^{5+}) less than 10 % of iron was precipitated. The % iron precipitation remained less than 10 % even when the retention time was increased to 4 hours or when 15 g/L

hematite or scorodite seed was employed. However, in the concentration range (0.5 – 2 g/L As) the % Fe precipitation increased and resulted in the precipitation of scorodite.

In the simultaneous presence of sulphate, arsenate and chloride in the system, arsenate-ferric complexes are more stable, with $FeH_2AsO_4^{2+}$ as the dominant species at pH < 1 having a ΔG_f^o value of ($-793.7\ kJ.mol^{-1}$) compared to $FeSO_4^+$ ($-772.8\ kJ.mol^{-1}$) and $FeCl_2^+$ ($-279.1\ kJ.mol^{-1}$) (Welham *et al*., 2000). The lower iron precipitation rate for initial arsenic concentrations (< 500 mg/L) may be attributed to the lower concentration of polymeric species in the solution which are responsible for nucleation and growth of scorodite. Once the precipitation starts there are not enough supply units in the solution for the formation of more scorodite nuclei or the growth of the existing nuclei. At higher arsenic concentrations (> 500 mg/L) the supply to the growth units increases (i.e. monomers and dimers combine to produce enough polymers) resulting in a higher precipitation rate. However, the exact mechanism of how arsenic affects the precipitation behaviour is not completely understood and needs further investigation. Droppert (1996) and Singhania *et al*. (2006) also observed a similar effect of arsenic on iron precipitation for higher ferric to arsenic ratios (Fe:As ≥ 2) or low arsenic levels under atmospheric conditions. These authors were also of the opinion that the retardation of precipitation is related to the solution speciation and complexation. However, the details of the speciation were not discussed.

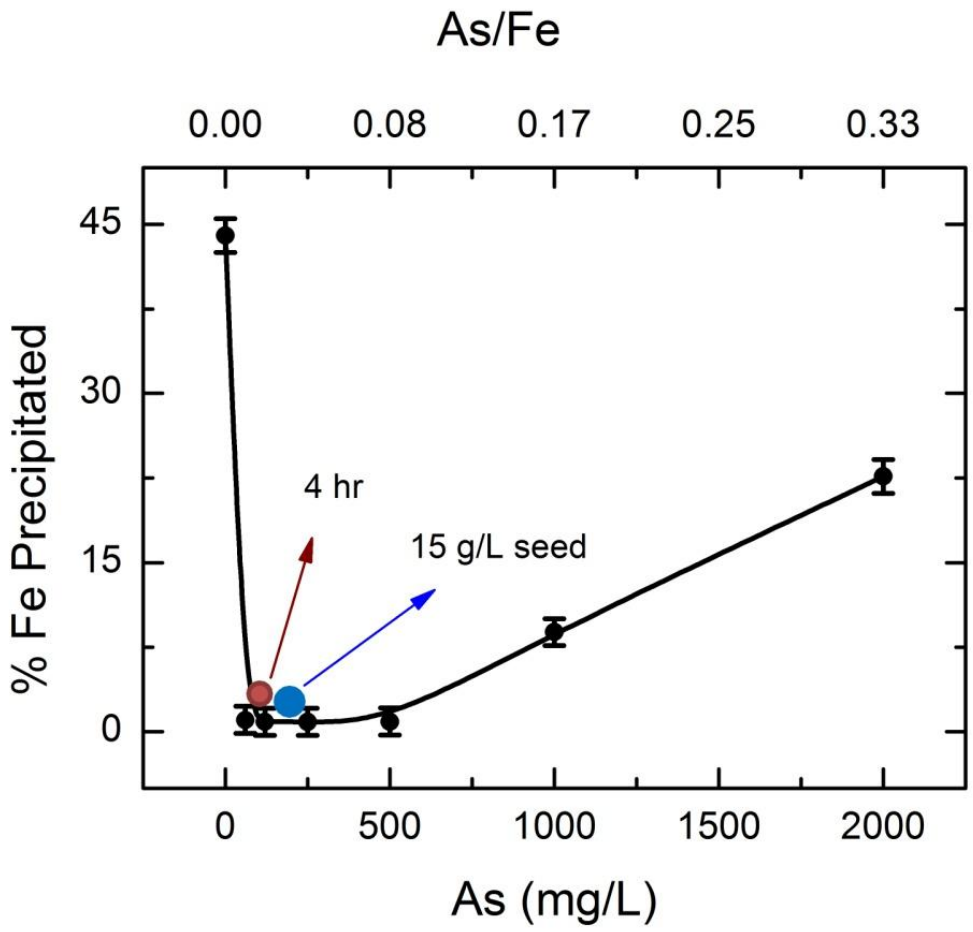

Figure 8.4 Effect of arsenic concentration on % Fe precipitation; for the experiments carried out for 1 hr at 150 °C in the system containing 6.0 g/L Fe^{3+}, 15.0 g/L H_2SO_4, 11.0 g/L Cl^- and 30.0 g/L Cu^{2+}.

As the effect of Na on iron precipitation from acidic solutions is well understood (Dutrizac, 1987), the results shown here are more for the comparison purposes i.e. the rate of % Fe precipitation. Figure 8.5 shows that nearly complete (> 95 %) iron precipitation can be achieved in 1 hour in the presence of Na but the precipitation product is Na-jarosite instead of hematite.

An increase in iron precipitation in the presence of Mg added as $MgSO_4$ (Figure 8.5) is due to the formation of bisulphate (HSO_4^-) by the extra sulphate added to the system,

which results in a decrease in the activity of the hydronium ion (i.e. pH increase). Similar behaviour was observed when Mg in the solutions was replaced with Cu. Umetsu, *et al*. (1977) and Tozawa and Sasaki, (1986) also observed the formation of bisulphate and shift in the upper limit of free acid for hematite precipitation.

A decrease in the extent of iron precipitation in the presence of Al (Figure 8.5) is due to formation of Al complexes in the solution e.g. $Al(OH)^{2+}$, $Al(OH)^{+}_{2}$ etc. which increase the hydronium ion activity (i.e. pH decrease).

Figure 8.6 and Figure 8.7 show the composition of the product in the in the presence of As and Na, respectively. The compositions are typical of scorodite and Na-jarosite. Precipitation of scorodite or Na-jarosite resulted in higher Cu uptake, see Figure 8.6 and Figure 8.7.

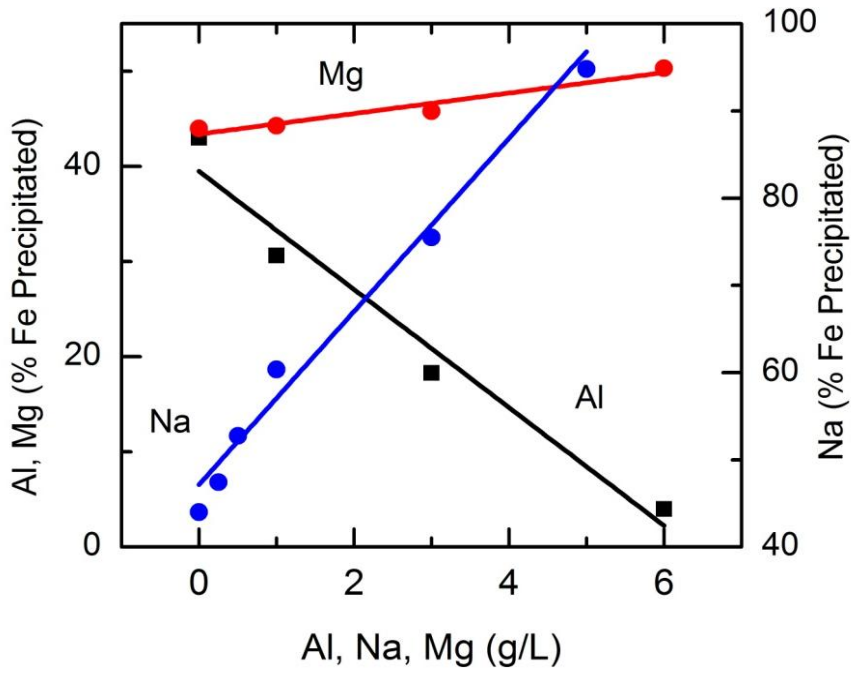

Figure 8.5 Effect of Al, Na and Mg on iron precipitation: for the experiments carried out for 1 hr at 150 °C in the system containing 6.0 g/L Fe^{3+}, 15.0 g/L H_2SO_4, 11.0 g/L Cl^- and 30.0 g/L Cu^{2+}.

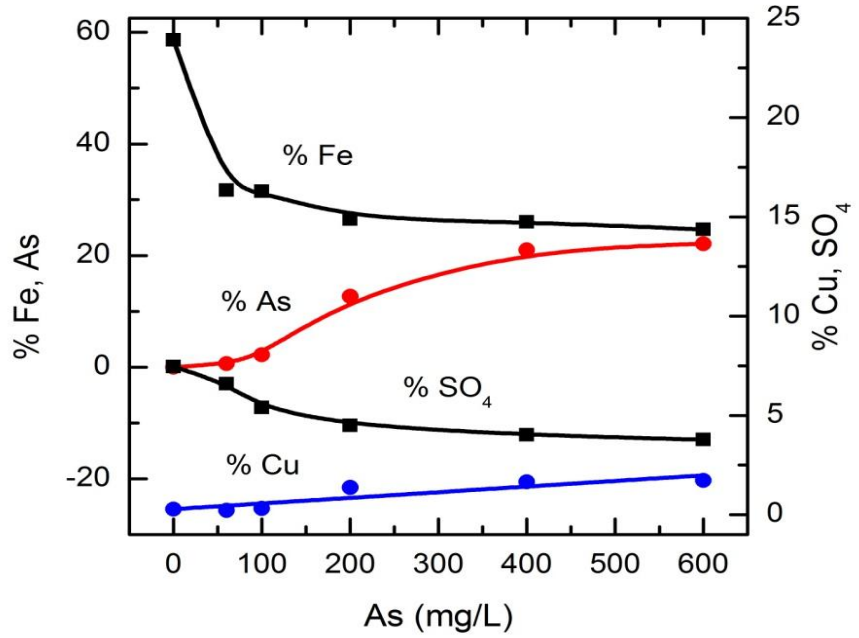

Figure 8.6 Effect of arsenic on the composition of the precipitates; for the experiments carried out for 1 hr at 150 °C in the system containing 6.0 g/L Fe^{3+}, 15.0 g/L H_2SO_4, 11.0 g/L Cl^- and 30.0 g/L Cu^{2+}.

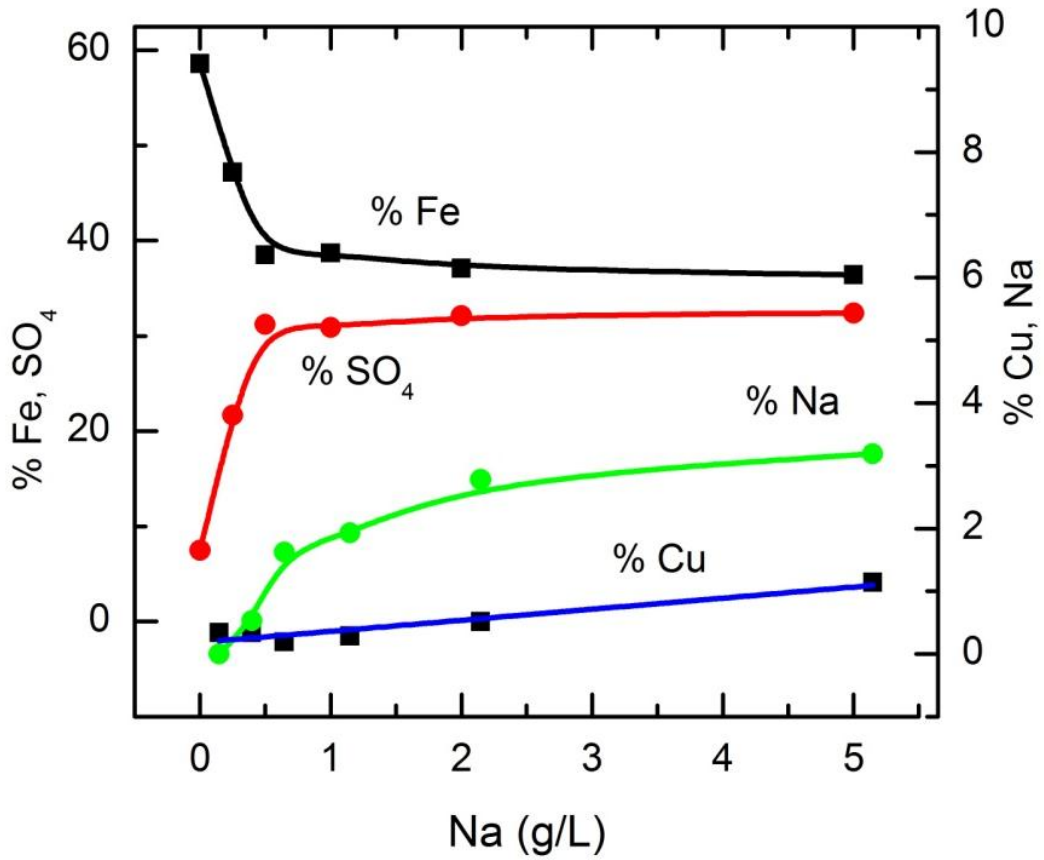

Figure 8.7 Effect of sodium on the composition of the precipitates; for the experiments carried out for 1 hr at 150 °C in the system containing 6.0 g/L Fe^{3+}, 15.0 g/L H_2SO_4, 11.0 g/L Cl^- and 30.0 g/L Cu^{2+}.

8.5 Conclusions

Ferric hydrolysis and hematite precipitation kinetics were affected by the amount of initial acid, hematite seed and the presence of other cations or anions such as: As^{5+}, Al^{3+}, Na^{2+}, Mg^{2+} and SO_4^{2-}. Low levels of arsenic (< 500 mg/L) significantly retarded the ferric precipitation reaction. However, higher arsenic levels (> 500 mg/L) increased the precipitation rate and resulted in the precipitation of scorodite. Presence of higher amounts

of the sulphate salts of Mg and Cu increased the extent of ferric precipitation due to the formation of bisulphate (i.e. decreasing H^+ activity). Precipitation kinetics was much faster in the presence of Na, but this lead to the precipitation of Na-jarosite instead of hematite. Presence of sulphate salt of Al decreased the extent of ferric precipitation due to its complexing behavior i.e. release of proton by aqueous complex formation.

Chapter 9. Summary and future work

9.1 Summary

Detailed conclusions have been drawn at the end of each chapter. In this chapter the overall conclusions and suggestions for future work are briefly summarised. The work in this thesis mainly consisted of three parts. 1) Characterization of the residue from the CESL and Vale medium temperature hydrometallurgical processes for the quantification of poorly crystalline phases and associated metal loss. 2) Use of simulated process solutions to determine the optimum conditions for hematite precipitation with minimum metal loss to the precipitates, using conventional one variable approach and statistical design of experiments. 3) Effect of various impurities on the precipitation behaviour of iron and the precipitation kinetics.

9.1.1 Characterization of CESL and Vale leach residues

Residue samples from CESL and Vale medium temperature hydrometallurgical processes contained a significant portion of amorphous or poorly crystalline and metastable iron oxides phases. These phases controlled the properties of the residue and contained a high loading of the valuable (Cu, Ni) metals. Residues samples were characterized by using a combination of characterization techniques. Poor agreement between total Fe analysis by

ICP-OES and QXRPD indicated the presence of amorphous iron oxides phases. It was determined that amorphous iron oxide phases were the major source of Cu and/Ni loss to the residue. Distribution of Cu and Ni into amorphous and crystalline iron oxide phases was determined by a two stage sequential extraction process. Association of Cu and Ni to the amorphous iron oxide phases was found to be approximately 2-4 times higher than the crystalline iron oxide phases. The amorphous iron oxide phases determined by QXRPD and sequential extraction were in good agreement; see section 4.2.4 (Table 4-4). In general the techniques used in this study i.e. QXRPD and sequential extraction can be used to determine total X-ray amorphous content and amorphous iron oxide phases in the scenarios where routine XRD fails to provide true quantification of the phases.

9.1.2 Simulated process solutions

Simulated process solutions were used to establish the relationship between the precipitation product and copper loss to the precipitates. In the first stage, one variable approach i.e. variation of one variable at a time while keeping all others constant was used to study the effect of various process parameters on % Fe precipitation and % Cu in the solids. The variables were studied over a broad range. The variables and their ranges which resulted in maximum amount of hematite with minimum amount of Cu to the precipitates were selected for further investigation. Fractional factorial design methods were then applied, where several variables were changed simultaneously. The results of one variable

approach showed that the factors: initial ferric concentration, initial acid concentration, retention time, initial chloride and seed concentrations were the important factors governing the iron precipitation and associated copper loss to the precipitates. The results of the factorial design experiments showed that the factors: initial ferric and H_2SO_4 concentrations and the same two along with retention time and seed have more significant effects on "% Cu content" and "% Fe precipitation", respectively. Further screening of the significant factors by using a Box-Behnken design showed that the factors: initial ferric, H_2SO_4 and seed concentrations have the largest effect on "% Cu content" and "% Fe precipitation" of the precipitates. By controlling these factors iron can be rejected in the form of a stable phase with minimum associated metal loss. Box-Behnken results showed that for a given ferric level i.e. 6 g/L initial ferric in the solutions, higher acid levels (≥ 15 g/L H_2SO_4) and moderate amount of seed (7.5 g/L) were the most suitable conditions to minimize % Cu content of the solids with moderate to high levels of Fe precipitation. For a fixed ferric level in the solution, higher acid concentrations resulted in lower supersaturation and promoted particle growth over nucleation which in turn resulted in a decrease in the Cu content of the precipitates. The results clearly showed that a low supersaturation environment with a moderate amount of seeding significantly improved the product quality in terms of % hematite and % Cu content in the final product. In the existing processes either supersaturation is not controlled or the amount of seed is too high (which in fact results in higher fine fractions in the residue) and resultantly the residue has a broad range of particle size distribution. Mathematical models for "% Fe precipitated" and

"% Cu content of precipitates" were predicted by fitting the data to quadratic models. The predicted models can be used for an estimation of the iron precipitation and copper loss if the process starting conditions are known. However, care should be taken to use the predicted models for the conditions outside of the range used in this study.

The presence of chloride in the solution accelerated precipitation kinetics and promoted the precipitation of iron oxides over iron hydroxy sulphate phases. This in turn produced precipitates with lower sulphate content. The presence of the sulphate salts of the metals such as: Mg and Cu increased the extent of precipitation, while the sulphate salts of the metals with extensive hydrolysis nature such as aluminum decreased the extent of precipitation. The presence of sodium and arsenic in the solution changed the precipitate nature completely from hematite to hydronium jarosite and scorodite, respectively. However, the presence of sodium ion in the system accelerated the precipitation kinetics and almost all (> 95 %) of the iron was precipitated in about an hour of retention at 150 °C, but the product was sodium jarosite. The presence of low levels of arsenic (As:Fe ≤ 0.08) severely retarded the precipitation rate and only about 5 % of the initially present iron was precipitated in 1-4 hours of retention and even in the presence of 15 g/L hematite or scorodite seed.

A comparison of the HaHC soluble Fe and Cu from the CESL and Vale leach residue samples, characterized in this study, and selected hematite precipitates made using simulated process solutions is provided in Figure 9.1. It is clear from Figure 9.1 that a significant amount of the target metal can be saved from deporting to the residue by

controlling the process variables and iron precipitation chemistry. Secondly, by controlling the process parameters iron can be rejected to the residue in an environmentally stable form.

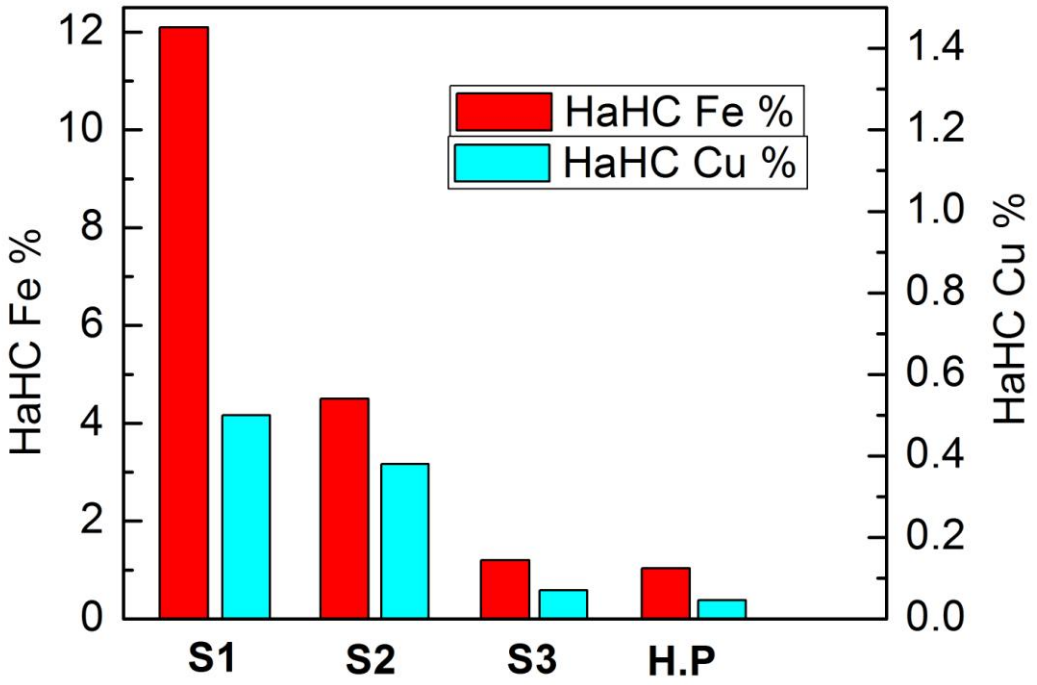

Figure 9.1 Comparison of HaHC dissolved iron and copper for the leach residue samples: S1, S2, S3 and hematite precipitates (H.P) made in this study.
Note: The Cu, Fe percentages for the hematite precipitates (H.P) leached by HaHC represent the average values of three selected precipitates made at 150 °C, 1 hour, 12.5, 15, 20 g/L initial H_2SO_4, 11.0 g/L Cl^-, 30.0 g/L Cu^{2+} and 6.0 g/L Fe^{3+}.

If control of the process parameters does not limit copper deportment to the residue, then residue treatment to liberate copper seems to be an alternative. The association of copper with amorphous/poorly crystalline iron oxide phases in the CESL residue suggests that a low temperature (< 350 °C) treatment would be enough to liberate

copper form the amorphous iron oxide phases in the residue. This is because of the fact that most of the amorphous iron oxide phases, present in the leach residue samples, were found to have transformation temperatures in the range 200-350 °C, see Chapter 5 for more details. Ward (2015) found that a prolonged low temperature (95 °C) water aging of the CESL residue can result in recovery of about 22 % of total copper in the residue. However, this technique resulted in only partial transformation of amorphous iron oxide phases and was not suitable to liberate copper from most of the amorphous and nanoscale crystalline iron oxides.

The results in this thesis clearly demonstrate: what factors are responsible for higher valuable metal loss to the residues, generated under medium temperature hydrometallurgical process conditions. How the amorphous phases and associated metal loss can be quantified. What are the key process parameters to control the residue characteristics. How the presence of various ions in the solution affects the extent of iron precipitation and product mineralogy. The overall results also provide an improved understanding of the physico-chemical nature of the iron precipitation process in the medium temperature sulphate-chloride systems. This in fact answers the aims of the thesis as outlined in Chapter 3.

9.2 Recommendations for future work

Future work that may advance the knowledge of the subject in the thesis is proposed below.

1. A chemical model for the speciation in the system Fe (III)-H_2SO_4-Cu (II)-Cl at 150 °C that should be able to calculate the hydrogen ion activity and corresponding pH at a given ionic strength and temperature is needed to better understand the changes in the equilibrium relationships between the species in the system. The model can be further extended to accommodate the high ionic strength caused by the metals which are leached along with iron and copper from the ore concentrates during the medium temperature leaching process.
2. Characterization of the precipitates made in this study showed that the precipitates are contaminated with a significant amount of amorphous phase under short retention times. The exact nature and distribution of the amorphous phase can be determined by using the sophisticated techniques such as: extended X-ray absorption fine spectroscopy (EXAFS) and X-ray absorption near edge structure (XANES). The hematite produced in this study also contained a significant amount of sulfate (3-4 %). Advanced characterization techniques as mentioned above can also be applied to determine the distribution of sulphate into the hematite precipitates.
3. In this study the precipitation behavior was studied by starting with ferric iron. Hydrolysis of ferric ion is an integral step of the ferrous oxidation-precipitation process. Further work can be done by starting with ferrous iron to shed light on the precipitation behavior and product nature. The oxidation of ferrous in highly acidic environment is difficult compared to low acid environments. It will be worth examining the effect of ferrous oxidation on solution supersaturation and product quality and particle size. Hui

et al. (2007, 2008) suggested that the presence of ferrous ion in the solution catalysis the dissolution of ferrihydrite to the monomers $Fe(OH)^{2+}$ and $Fe(OH)_2^{+}$ before transformation to goethite or hematite therefore it will be worthy to know if there is any change in the mineralogy of the precipitates. Experiments can be designed in a similar fashion as the factorial design methods used in this study.

4. The hematite product produced in one experiment can be recycled as seed for the next experiments for at least 10-20 cycles to assess any changes in the product quality and sulphate uptake.
5. It was observed in this study that about 0.1-0.8 % copper is lost with the hematite precipitation product. However, it was not clear whether the copper loss occurred through adsorption or incorporation into the hematite structure. The exact mechanism of copper loss to the precipitates can be confirmed by synchrotron based radiation techniques such as X-ray absorption spectroscopy (XAS).
6. Batch reactors encounter variable supersaturation environment and are not good for supersaturation control. A constant supersaturation autoclave can be designed to keep control on the supersaturation levels with the progress of precipitation reaction.
7. The results in this study showed that the presence of low levels of arsenic in the solution significantly retard the iron precipitation. However, the exact mechanism responsible for this behavior was not clear. Further investigation to the mechanism can be carried out by carrying the solution speciation study and expanding the experiments over a

wide arsenic concentration range. The results can be augmented by replacing the ferric ion with ferrous ion.

8. The leach residues containing amorphous iron oxide phases from medium temperature conditions can be treated at higher temperature (≥ 230 °C) to liberate copper from the residues. Further, residue from the copper smelting (i.e. slag) can be treated to liberate copper and a benchmark can be established for copper recovery from both the residue types.

References

Agatzini, S., Burkin, A.R., 1985. Statistical approach to the precipitation of iron as “goethite”. Trans. Inst. Min. Metall. Sect. C 94, C105-114.

Aguilar, R.A.L., Rodríguez, C.I.M., Rangel DE, H.R., Liu, H., 2013. Removal of ferric iron as hematite at atmospheric pressure. https://www.google.ch/patents/WO2013188922A1.

Allan, R.W., Haigh, C., Hamdorf, J., 1973. Method of removing dissolved ferric iron from iron-bearing solutions. https://www.google.com/patents/US3781405.

Baba, A.A., Kuranga, I.A., Adekola, F.A., Ghosh, M.K., Ayanda, O.S., Bale, R.B., Sheik, A.R., Pradhan, S.R., 2012. A review on novel techniques for chalcopyrite ore processing, Int. J. Min. Eng. Miner. Process. 1, 1-16.

Babčan, J., 1971. Synthesis of jarosite $KFe_3(SO_4)_2(OH)_6$. Geologicky Zbornik-Geologica Carpathica. 22, 299-304.

Baron, D., Palmer, C.D., 1996. Solubility of jarosite at 4-35 °C. Geochimica et Cosmochimica Acta. 60(2), 185-195.

Barr, G., Defreyne, J., Mayhew, K., 2005. CESL process - an economic alternative to smelting. CESL publications. www.cesl.com/downloads/intermin_2005.pdf.

Baxter, K.G., Pavlides, A.G., Dixon, D.G., 2004. Testing and modelling a novel iron control concept in a two-stage ferric leach/pressure oxidation process for the Sepon copper project. In: Collins, M.J., Papangelakis, V.G. (Eds.), Pressure hydrometallurgy,

international conference on the use of pressure vessels for metals extraction, CIM, Montreal, 57–76.

Beaulieu, R., Gagne, G., Nasmyth, M., Cooper, G., Inostroza, C., 2006. Iron control and management in the zinc industry. In: Dutrizac, J.E., Riveros, P. A. (Eds.), Iron control technologies: proceedings of the third international symposium on iron control in hydrometallurgy. CIM, Montreal, Canada, October 1-4. 45-55.

Berezowsky, R., Trytten, L., 2002. Commercialization of the acid pressure leaching of chalcopyrite. In: ALTA copper-7 forum, Perth. ALTA metallurgical services, Melbourne.

Berger, C.J., Lippiat, S.M., Lawrence, M.G., Bruland, K., 2008. Application of a chemical leach technique for estimating labile particulate aluminium, iron and manganese in the Columbia River plume and coastal waters off Oregon and Washington. Journal of Geophysical Research. doi:10.1029/2007JC004703.

Biagioni, C., Bonaccorsi, E., Orlandi, P., 2011. Volaschioite, $Fe_4(SO_4)O_2(OH)_6.2H_2O$, a new mineral species from Fornovolasco, Apuan Alps, Tuscany, Italy. The Canadian Mineralogist. 49, 605-614.

Bigham, J.M., Carlson, L., and Murad, E., 1994. Schwertmannite, a new iron oxyhydroxysulfate from Pyhlsalmi, Finland, and other localities. Miner. Mag. 58, 641-648.

Bigham, J.M., Schwertmann U., Carlson, L., 1992. Mineralogy of precipitates formed by the biogeochemical oxidation of Fe(II) in mine drainage. In: Biomineralization processes of iron and manganese: modem and ancient environments, 21, Catena Verlag, 219-232.

Bigham, J.M., Schwertmann, U., Carlson, L., Murad, E., 1996. Schwertmannite and the chemical modeling of iron in acid sulfate waters. Geochimica et Cosmochimica Acta. 54, 2743-2758.

Bonan, M., Demarthe, J.M., Renon, H., Baratin, F., 1981. Chalcopyrite leaching by $CuCl_2$ in strong NaCl solutions. Metallurgical Transactions. B, Process Metallurgy 12B, 269-274

Box, G.E.P., Behnken, D.W., 1960. Some new three level designs for the study of quantitative variables. Technometrics 2, 455-475.

Box, G.E.P., Cox, D.R., 1964. An analysis of transformations. J. R. Stat. Soc. 26B, 211-246.

Box, G.E.P., Hunter, W.G., Hunter, J.S., 1978. Statistics for experiments: an introduction to design, data analysis, and model building. John Wiley and Sons, Inc., New York.

Brantley, S.L., 2003. Reaction kinetics of primary rock-forming minerals under ambient conditions. In: Holland, H.D., Turekian, K.K. (Eds.), Treatise in Geochemistry Volume 5, Surface and Ground Water, Weathering, and Soils, 73–117.

Brook Hunt, metals cost service summary and analysis, copper, March 2011, a wood Mackenzie company.

Brown, P.L., Ekberg, C., 2016. Hydrolysis of metal ions. Wiley, Weinheim.

Burkin, A.R., 1984. Use of statistical methods of experimental design in optimizing hydrometallurgical processes. Hydrometallurgical Process Fundamentals. NATO Conference Series, 10, 529-538.

Carlson, L., Schwertmann, U., 1980. A natural occurrence of feroxyhite (δ'-FeOOH). Clays and Clay Minerals., 28, 272-280.

Cashion, J.D, Suzuki, K., Murad, E., 2012. Mössbauer spectra of the acid mine drainage mineral Schwertmannite from the Sokolov basin, Czech Republic. Proc. 36th Ann. Condens. Matter and Mater. Mtg. TP30:1.

Chao, T.T., Zhou, L., 1983. Extraction techniques for selective dissolution of amorphous iron oxides from soils and sediments. Soil Sci. Soc. Am. J., 47, 225-232.

Chen, L., Li, J.W., Rye, R. O., Benzel, W. M., Lowers, H. A., and He, M.Z., 2013. Mineralogical, chemical, and crystallographic properties of supergene jarosite-group minerals from the Xitieshan Pb-Zn sulfide deposit, northern Tibetan Plateau, China. Mineralogy and Petrology, 107, 487-499.

Chen, T.T., Cabri, L.J., 1986. Mineralogical overview of iron control in hydrometallurgical processing. In: Dutrizac, J.E., Monhemius, A.J. (Eds.), Iron control in hydrometallurgy, Ellis Horwood Ltd., Chichester, U.K. 19-55.

Chen, Y.H., Li, F.A., 2010. Kinetic study on removal of copper (II) using goethite and hematite nano-photocatalysts. Journal of Colloid and Interface Science. 347, 277-281.

Cheng, T.C, Demopoulos, G.P., 2006. The hematite process – new concepts for increased throughput and clean hematite production. In: Dutrizac, J.E., Riveros, P.A. (Eds.), Iron control technologies: proceedings of the third international symposium on iron control in hydrometallurgy. CIM, Montreal, Canada, October 1-4, 965-980.

Cheng, T.C., 2002. Production of hematite in acidic zinc sulphate media, PhD Thesis, Dept. of mining and metallurgical engineering, McGill University, Montreal, Canada.

Cheng, T.C., Demopoulos, G.P., 2004. Hydrolysis of ferric sulfate in the presence of zinc sulfate at 200 °C: Precipitation kinetics and product characterization. Ind. Eng. Chem. Res., 43, 6299-6308.

Chester, R., Hughes, M.J., 1967. A chemical technique for the separation of ferro-manganese minerals, carbonate minerals and adsorbed trace elements from pelagic sediments. Chem. Geol., 2, 249-262.

Claassen, J.O., Meyer, E.H.O., Rennie, J., Sandenbergh, R.F., 2002. Iron precipitation from zinc-rich solutions: defining the Zincor Process. Hydrometallurgy, 67, 87-108.

Claassen, J.O., Sandenbergh, R.F., 2006. Particle growth parameters in the precipitation of metastable iron phases from zinc-rich solutions. Hydrometallurgy, 84, 165-174.

Córdoba, E.M., Muñoz, J.A., Blázquez, M.L., González, F., Ballester, A., 2008. Leaching of chalcopyrite with ferric ion. Part I: General aspects. Hydrometallurgy, 93, 81-87.

Cornell, R.M., Giovanoli, R., 1987. Effect of manganese on the transformation of ferrihydrite into goethite and jacobsite in alkaline media. Clay Miner., 35, 11-20.

Cornell, R.M., Giovanoli, R., 1988. The influence of copper on the transformation of ferrihydrite ($5Fe_2O_3.9H_2O$) into crystalline products in alkaline media. Polyhedron, 7, 385-391.

Cornell, R.M., Giovanoli, R., Schneider, W., 1989. Review of hydrolysis of iron(III) and the crystallisation of amorphous iron(III) hydroxide hydrate. J. Chem. Tech. Biotechnol., 46, 115-134.

Cornell, R.M., Schwertman, U., 2003. The Iron oxides: Structure, properties, reactions, occurrences and uses, second ed. Wiley-VCH, Weinheim. DOI: 10.1002/3527602097.

Cubeddu, F., Piasentin, M., Reilly, F., 1996. The para-goethite process at the Enirisorse-Porto Vesme plant. In: Dutrizac, J.E., Harris, G.B. (Eds.), Iron control and disposal. CIM, Montreal, Canada, 147-162.

Daniel, C., 1959. Use of half-normal plots in interpreting factorial two-level experiments. Technometrics, 1, 311-341.

Daniel, C., 1976. Applications of statistics to industrial experimentations. New York: Wiley.

Das, R.P., Sarveswara, R., Jena, P.K., 1987. Leaching behaviour of copper converter slag obtained under different cooling conditions. Trans. Inst. Mm. Metall., Sect. C: Miner. Process Extr. Metall., 96, 156-161.

Das, S., Hendry, M.J., Essilfie-Dughan, J., 2011. Transformation of two-line ferrihydrite to goethite and hematite as a function of pH and temperature. Environ. Sci. Technol. 45, 268-75.

Davenport, W.G., King, M., Schlesinger, M., Biswas, A.K., 2002. Extractive metallurgy of copper 4 th edition, Pergamon, Oxford, ISBN 9780080440293.

Davey, P.T., Scott, T.R., 1976. Removal of iron from leach liquors by the goethite process. Hydrometallurgy, 2, 25-33.

David, B., Mathe, R., 1983. Recovery of sulphur trioxide, iron (III) oxide and potassium sulphate (or sodium sulphate and potassium hydroxide) from jarosite. Rom. R0 82, 155.

De Faria, D.L.A., Venancio Silva, S., de Oliveira, M.T., 1997. Raman microspectroscopy of some iron oxides and oxyhydroxides, J. Raman Spectrosc., 28, 873-878.

De La Torre, A.G., Bruque, S., Aranda, M. A. G., 2001. Rietveld quantitative amorphous content analysis. J. Appl. Crystallogr., 34, 196-202.

Defreyne, J., Cabral, T., 2009. Early copper production results from Vale's hydrometallurgical CESL refinery. ALTA copper technical proceedings, Perth, Australia.

Defreyne, J., Grieve, W., Jones D.L., Mayhew, K., 2006. The role of iron in the CESL process. In: Dutrizac, J.E., Riveros, P.A. (Eds.), Iron control technologies: Proceedings of the third international symposium on iron control in hydrometallurgy. CIM, Montreal, Canada, October 1-4, 205-221.

Demopolous, G.P., 2009. Aqueous precipitation and crystallization for the production of particulate solids with desired properties. Hydrometallurgy, 96, 199-214.

Demopoulos, G.P, 1993. Precipitation in aqueous processing of inorganic materials: a unified colloid-crystallization approach to the production of powders with controlled properties. In: Henein, H., Oki, T., (Eds.), First conference on processing materials for properties, TMS, Warrendale, Pa, 537-540.

Dirksen, J.A., Ring, T.A., 1991. Fundamentals of crystallization: kinetic effects on particle size distributions and morphology. Chem. Engg. Sci., 46, 2389-2427.

Dousma, J, De Bryun, P.L., 1979. Hydrolysis-precipitation studies of iron solutions-III. Application of growth models to the formation of colloidal α-FeOOH from acid solutions. J. Colloid Interface Sci., 72, 314-320.

Dousma, J., Van Den Hoven, T.J., De Bruyn, P.L., 1978. The influence of chloride ions on the formation of iron(III) oxyhydroxide. J. inorg. nuel. Chem., 40, 1089-1093.

Dreisinger, D.B., 2004. New developments in hydrometallurgical treatment of copper concentrates. Engineering and Mining Journal, 205, 5, 1-27.

Dreisinger, D.B., 2006. Copper leaching from primary sulfides: Options for biological and chemical extraction of copper. Hydrometallurgy, 83 (1-4), 10-20.

Dreisinger, D.B., Richmond, G., Hess, F. and Lancaster, T., 2002. The competitive position of the Mt. Gordon copper process in the copper industry, Proceedings of ALTA Cu conference, ALTA metallurgical services Australia.

Droppert, D.J., 1996. The ambient pressure precipitation of crystalline scorodite from sulphate solutions. M.Eng. thesis. Dept. of mining and metallurgical engineering, McGill University, Montreal, Canada.

Dutrizac, J.E, Chen, T.T, 2009. Factors affecting the precipitation of hematite rather than jarosite in nickel sulphate-chloride solutions. In: Budac, J.J. (Ed.), Proceedings of hydrometallurgy of nickel and cobalt. CIM, Montreal, Canada, 295-319.

Dutrizac, J.E, Chen, T.T, 2011. Precipitation of hematite directly from ferric sulphate solutions. World of Metallurgy – ERZMETALL, 64, 134-150.

Dutrizac, J.E., 1980. The physical chemistry of iron precipitation in zinc industry. In: Cigan, J.M, Mackey, T.S, O'Keefe, T.J. (Eds.), Lead-Zinc-Tin '80, TMS – AIME, Warrandale, 532-564.

Dutrizac, J.E., 1984. The behavior of impurities during jarosite precipitation. In: Bautista, R.G. (Ed.), Hydrometallurgical process fundamentals. Plenum Press, New York, 125-169.

Dutrizac, J.E., 1987. An overview of iron precipitation in hydrometallurgy, In: Strathdee, G.L., Klein, M.O, Melis, L.A. (Eds.), crystallization and precipitation: proceedings of the international symposium, Saskatoon, Saskatchewan, 259-283.

Dutrizac, J.E., Chen, T.T., 1987. Mineralogical characterization of the residues of the two stage oxygen pressure leaching of a pyritic Zn-Pb-Cu-Ag concentrate with SO_2 reduction of the jarosite fraction. Canadian Metallurgical Quarterly, 26, 189-205.

Dutrizac, J.E., Chen, T.T., 1993. Surface and structural impurity incorporation in iron precipitates. In: Emerging separation technologies for metals and fuels. Lakshmanan, V.l. Bautista, R.G., Somasundaran, P. (Eds.), TMS, Warrendale, PA., U.S.A. 183-198.

Dutrizac, J.E., Chen, T.T., 2001. Characterization of hematite residues from commercial zinc circuits. In: Rao, S.R. (Ed.): proceedings of the fourth international symposium on waste processing and recycling in mineral and metallurgical industries, August 26-29, 2001, Ontario, Canada. CIM, Montreal, Canada.

Dutrizac, J.E., Chen, T.T., 2010. Precipitation of $Fe_4(SO_4)(OH)_{10}$ and hydronium jarosite, $(H_3O)Fe_3(SO_4)_2(OH)_6$, in ferric sulphate-sulphuric acid media. World of Metallurgy-ERZMETALL, 63, 181-96.

Dutrizac, J.E., Harris, G.B. (Eds.), 1996. Iron control and disposal: Second international symposium on iron control in hydrometallurgy, CIM, Montreal, Canada.

Dutrizac, J.E., Jambor, J.L, Chen, T.T., 1987. The behaviour of arsenic during jarosite precipitation: Reactions at 150 ^{o}C and the mechanism of arsenic precipitation. Canadian Metallurgical Quarterly, 26, 103-115.

Dutrizac, J.E., Monhemius, A.J. (Eds.), 1986. Iron Control in Hydrometallurgy. Ellis Horwood Ltd., Chichester, U.K.

Dutrizac, J.E., Riveros, P.A. (Eds.), 2006. Iron Control Technologies: Proceedings of the third international symposium on iron control in hydrometallurgy. CIM, Montreal, Canada, October 1-4.

Dutrizac, J.E., Riveros, P.A., 1999. The precipitation of hematite from ferric chloride media at atmospheric pressure. Metallurgical and Materials Transactions B, 30B, 993-1001.

Dyer, L., Su, B., Asselin, E., 2012. Cobalt loss due to iron precipitation in ammoniacal carbonate solutions. Hydrometallurgy, 125-126, 144-147.

Eggleton R.A., Fitzpatrick R.W., 1988. New data and a revised structural model for ferrihydrite. Clays and Clay Minerals, 36, 111-124.

Fischer, W.R., Schwertmann, U., 1975. The formation of hematite from amorphous iron (Ill) hydroxide. Clays and Clay Minerals, 23, 33-37.

Flynn, C.M. Jr., 1984. Hydrolysis of inorganic iron (III) salts. Chem. Rev. 84, 31-41.

Frost, R.L., Rachael-Anne Wills, Weier, M.L.,Martens, W., 2005. Comparison of the Raman spectra of natural and synthetic K- and Na-jarosites at 298 and 77 K. J. Raman Spectrosc. 36, 435-444.

Goni-Elizalde, S., Garcia-Clavel, M.E., 1988b. Thermal behavior in air of iron oxyhydroxides obtained from the method of homogeneous precipitation: Part I. Goethite samples of varying crystallinity. Thermochimica Acta, 124, 359-369.

Grover, V.A., Hu, J., Engates, K.E., Shipley, H.J., 2012. Adsorption and desorption of bivalent metals to hematite nanoparticles. Environ. Toxicol. Chem. 31, 86-92.

Grundl, T., Delwiche, J., 1993. Kinetics of ferric oxyhydroxide precipitation. Journal of Contaminant Hydrology, 14, 71-97.

Gütlich, P., Link, R., Trautwein, A., 1978. Mössbauer spectroscopy and transition metal chemistry. Inorganic Chemistry Concepts, v. 3. Berlin: Springer-Verlag.

Hackl, R.P., 1995. The leaching and passivation of chalcopyrite in acid sulphate media. PhD thesis, Dept. of materials engineering, University of British Columbia, Vancouver, Canada.

Hanesch, M., 2009. Raman spectroscopy of iron oxides and (oxy)hydroxides at low laser power and possible applications in environmental magnetic studies. Geophys. J. Int., 177, 941-948.

Hanusch, K., 1984. Processing of precipitates and residues of hydrometallurgical zinc production. In: Donato, M. (Ed.), resources workshop on lead, commission of the European communities, Brussels. EUR 10169, 57-63.

Hershel, F., 2011. Chalcopyrite mineral. The mineral and gemstone kingdom. http://www.minerals.net/mineral/chalcopyrite.aspx.

Hirato, T., Majima, H., Awakura, Y., 1987. The leaching of chalcopyrite with cupric chloride. Metallurgical Transactions B-Process Metallurgy, 18(1), 31-39.

Hui, L., Guo, H., Li, P.,Wei, Y., 2008. The transformation of ferrihydrite in the presence of trace Fe(II): The effect of the anionic media. Journal of Solid State Chemistry 181, 10, 2666-2671.

Hui, L., Li, P., Zhu, M., Wei, Y., Sun, Y., 2007. Fe(II)-induced transformation from ferrihydrite to lepidocrocite and goethite. Journal of Solid State Chemistry, 180, 7, 2121-2128.

Hutchison, R.F.S., Phipps, P.J., 1977. Formation and particle size of jarosite. The Aus. I.M.M. conference Tasmania, 319-327.

Jambor, J.L., Dutrizac, J.E., 1998. Occurrence and constitution of natural and synthetic ferrihydrite, a widespread iron oxyhydroxide. Chem. Rev. 98, 2549-2585.

Janney , D.E., Cornell, R.M., Buseck, P.R., 2000a. Transmission electron microscopy of synthetic 2- and 6-line ferrihydrite. Clay Miner. 48, 111-119.

Janney, D.E., Cornell, R.M., Buseck, P.R., 2000b. Structure of synthetic 2-line ferrihydrite by electron nanodiffraction. American Mineralogist, 85, 1180-1187.

Janney, D.E., Cornell, R.M., Buseck, P.R., 2001. Structure of synthetic 6-line ferrihydrite by electron nanodiffraction. American Mineralogist 86, 327-385.

Javed, T., Abdul, B., Ryan, D., Raudsepp, M., Asselin, E., 2016. Amorphous iron phases in medium temperature sulphide concentrate leach residues from pilot and demonstration plants. Intl. J. Mineral processing, 148, 65-71.

Javed, T., Asselin, E., 2014. Thermal behaviour of medium temperature sulphide concentrate leach residues, In: Asselin, E., Dixon, D.G., Doyle, F.M., Dreisinger, D.B., Jeffrey, M.I., Moats, M.S. (Eds.), Hydrometallurgy 2014. CIM, Montreal, Canada, 1, 113-126.

Johnston, J.H., Glasby G.P., 1978. The secondary iron oxidehydroxide mineralogy of some deep-sea and fossil manganese nodules: A Mössbauer and X-ray study. Geochem. J., 12, 153 -164.

Jones, D.L., 1999. Chloride assisted hydrometallurgical extraction of nickel and cobalt from sulphide or laterite ores. https://www.google.com/patents/WO1999009226A1.

Jones, D.L., Mayhew, K., Connor, L.O., 2009. Nickel and cobalt recovery from a bulk copper-nickel concentrate using the CESL process. In: Budac, J.J., Fraser, R., Mihaylov, I., (Eds.), Hydrometallurgy of nickel and cobalt. CIM, Montreal, Canada, 45-58.

Jones, D.L., Moore, R., Stocker, S.K., 2008. Pressure oxidation leaching in the presence of an acidic solution of halide and sulfate ions from copper and base metal containing ore/concentrate. https://www.google.com/patents/US7438874.

Kerfoot, D.G.E., Krause, E., Love, B.L., Singhal, A., 2002. Recovery of nickel and cobalt values from a sulfidic flotation concentrate by chloride assisted oxidative pressure leaching in sulfuric acid. http://www.google.ca/patents/WO2002024966A1.

Knight, R. J., Sylva, R. N., 1974. Precipitation in hydrolyzed iron(Ill) solutions. J. inorg. nucl. Chem., 36, 591-597.

Kostka, J.E., and G.W. Luther III. 1994. Partitioning and speciation of solid phase Fe in saltmarsh sediments. Geochim. Cosmochim. Acta., 58, 1701-1710.

Krishnamurthy, N., Soots, V., 1971. Raman Spectrum of Gypsum. Canadian Journal of Physics, 49, 885-896.

Lahtinen, M., Lehtinen, L., Takala, H., 2007. A method for precipitating iron from a zinc sulphate solution as hematite. http://www.google.ch/patents/US7294319.

Lahtinen, M., Svens, K. 2006. Hematite versus jarosite precipitation in zinc production. In: Dutrizac, J.E., Riveros, P.A. (Eds.), Iron control technologies: Proceedings of the third international symposium on iron control in hydrometallurgy. CIM, Montreal, Canada, October 1-4. 93-107.

Levy, W.L., Quemeneur, 1964. On the hydrolysis of ferric sulphate solutions at elevated temperatures. C.R. Acad. Soc. Paris, 258, 3028-3031.

Loan, M., Newman, O. G. M., Cooper, R. M. G., Farrow, J. B., Parkinson G. M., 2006. Defining the paragoethite process for iron removal in zinc. Hydrometallurgy, 81, 104-129.

Loan, M., Parkinson, G.M., Newman, M., Farrow, J.B., 2002. Iron oxy-hydroxide crystallization in a hydrometallurgical residue. Journal of Crystal Growth, 235, 482-488.

Loan, M., Pierre, T.G.St., Parkinson, M., Newman, O., Farrow, J. 2002. Identifying nanoscale ferrihydrite in hydrometallurgical residues. JOM, 54, 40-43.

Loan, M., Richmond, W.R., Parkinson, G.M., 2005. On the crystal growth of nanoscale schwertmannite. Journal of Crystal Growth, 275, 1875-1881.

Machala, L., Zboril, R., Gedanken, A., 2007. Amorphous Iron (III) oxides: A review. J. Phys. Chem. B, 111, 4003-4018.

Madden, A.S., Hochella, M.F., Luxton, T.P., 2006. Insights for size-dependent reactivity of hematite nanomineral surfaces through Cu^{2+} sorption. Geochim. Cosmochim. Acta, 70, 4095-4104.

Majima, H., Awakura, Y., Mishima, T., 1985. The leaching of hematite in acid solution. Metallurgical transactions B, 16, 23-30.

Margulis, E.V., Getskin, L.S., Zapuskalova, N.A., Beisekeeva, L.I., 1976. Hydrolytic precipitation of iron in the $Fe_2(SO_4)_3$-KOH-H_2O system. Russ. J. Inorg. Chem., 21, 996-999.

Marsden, J.O., Wilmot, J.C., Hazen, N., 2007a. Medium- temperature pressure leaching of copper concentrates - Part I: Chemistry and initial process development. Minerals and Metallurgical Processing, 24, 4, 193-204, SME, Littleton, Colorado.

Martin, A., Feltz, A., 1984. Method for the preparation of iron oxide from jarosite and related compounds. Ger. Dem. Rep. Patent DD 215 999 A1.

Matijevié, E., Sapieszko, R.S., Melville, J.B., 1975. Ferrie hydrous oxide sols 1. Monodispersed basic iron(III) sulphate particles., J. Colloid and Interface Science, 50, 567-581.

Mayhew, K., Parhar, P., Salomon-de-Friedberg, H., 2010. CESL Process as applied to enargite-rich copper concentrates. Proceedings of the 7th international copper-cobre conference, 5, 1983-1998.

McDonald, R.G., Muir, D.M., 2007a. Pressure oxidation leaching of chalcopyrite. Part I. Comparision of high and low temperature reaction kinetics and products. Hydrometallurgy, 86, 191-205.

McDonald, R.G., Muir, D.M., 2007b. Pressure oxidation leaching of chalcopyrite. Part II. Comparision of medium temperature kinetics and products and effect of chloride ion. Hydrometallurgy, 86, 191-205.

Meyer, E.H.O., Howard, G., Haegele, R., Beck, R.D., 1996. Iron control and removal at the zinc corporation of South Africa. In: Dutrizac, J.E., Harris, G.B. (Eds.), Iron control and disposal. CIM, Montreal, 163-182.

Misawa, T., Hashimoto, K., Shimodaira, S., 1974. The mechanism of formation of iron oxides and oxyhydroxides in aqueous solutions at room temperature. Corrosion science, 14, 131-149.

Mullin, J. W., 2000. Crystallization fourth edition. Butterworth Heinemann, Oxford, UK.

Murad, E., 1988. The mössbauer spectrum of “well-crystallized” ferrihydrite. J. Magn. Magn. Mater., 74, 153-157.

Murad, E., Schwertmann, U., 1980. The Mössbauer spectrum of ferrihydrite and its relations to those of other iron oxides. American Mineralogist, 65, 1044-1049.

Murphy, P.J., Posner, A.M., Quirk, J.P., 1976. Characterization of hydrolyzed ferric ion solutions: A comparison of the effects of various anions on the solutions. Journal of Colloid and Interface Science, 56, 312-319.

Myers, R.H.,Montgomery, D.C., 2002. Response surface methodology: Process and product optimization using designed experiments. JohnWiley and Sons, Inc., New York.

Nazari, G., Dixon, D.G., Dreisinger, D.B., 2011. Enhancing the kinetics of chalcopyrite leaching in the Galvanox™ process. Hydrometallurgy, 105, 251-258.

Nyvlt, J., 1995. The Ostwald rule of stages. Cryst. Res. Technol., 30, 443-449.

Oehlert, Gary W. 2000. A first course in design and analysis of experiments. New York: W.H. Freeman.

Onozaki, A., Sato, K., Kuramochi, S. 1986. Effect of some impurities on iron precipitation at Iijima Zinc Refinery. In: Dutrizac, J.E., Monhemius, A.J. (Eds.), Iron control in hydrometallurgy, Ellis Horwood Ltd., Chichester, U.K 742-752.

Pammenter, R.V, Kershaw, M.G, Horsham, T.R., 1986. The low contaminant jarosite process-further developments, and implementation of the process. In: Dutrizac, J.E., Monhemius, A.J. (Eds.), Iron control in hydrometallurgy, Ellis Horwood Ltd., Chichester, U.K., 603-617.

Parfitt, R.L., Smart, R.St.C. 1978. The mechanism of sulfate adsorption on iron oxides. Soil Science Society of America Journal, 42, 1, 48-50.

Peacock, C.L., Sherman, D.M., 2004. Copper(II) sorption onto goethite, hematite and lepidocrocite: a surface complexation model based on ab initio molecular geometries and EXAFS spectroscopy. Geochim. Cosmochim. Acta, 68, 2623-2637.

Peek, E.M.L., Dutrizac, J.E., Buarzaiga, M., Filippou, D., Becze, L., Ghahremaninezhad, A., Nakamura, T., Vandenbroucke, J., Somanathan, M., (Eds.), 2016. Iron control in

hydrometallurgy: Proceedings of the fourth international symposium on iron control in hydrometallurgy. CIM, Montreal, Canada, September 11-15.

Pelino, M., Cantalini, C., Abbruzzese, C., Plescia, P., 1996. Treatment and recycling of goethite waste arising from the hydrometallurgy of zinc. Hydrometallurgy, 40, 2087-2094.

Piret, N.L., Melin, A.E., 1993. Impact of environmental issues on iron removal process evolution in electrolytic zinc production. In: Hiskey, J.B., Warren, G.W. (Eds.), Hydrometallurgy: fundamentals, technology, and innovation. SME, Littleton, CO, USA, 499-520.

Posnjak, E., Merwin, H.E., 1922. The Fe_2O_3-SO_3-H_2O system. J. Am. Chem. Soc. 44, 1965-1994.

Poulton S.W., Canfield D.E., 2005. Development of a sequential extraction procedure for iron: implications for iron partitioning in continentally derived particulates. Chemical Geology, 214, 209-221.

Powers, D.A., Rossman G.R., Schugar H.J., and Gray H.B., 1975. Magnetic behavior and infrared spectra of jarosite, basic iron sulfate, and their chromate analogs. J. Solid State Chem., 13, 1-13.

Ragone, D.V., 1994. Thermodynamics of materials, John Wiley and sons Inc, ISBN-10: 0471308854. New York, Chichester, Brisbane, Toronto, Singapore.

Raiswell, R., Canfield., D.E., and Berner, R.A., 1994. A comparison of iron extraction methods for the determination of degree of pyritization and recognition of iron-limited pyrite formation. Chemical Geology, 111, 101-111.

Riveros, P.A., Dutrizac, J.E., 1997. The precipitation of hematite from ferric chloride media. Hydrometallurgy, 46, 85-104.

Rizov, B., 2012. Phase transformations from goethite to hematite and thermal decomposition in various nickeliferrous laterite ores. Journal of the University of Chemical Technology and Metallurgy, 47, 207-210.

Rodriguez, M., Wedderburn, B.J., 2007. Hematite precipitation at elevated temperature and pressure. https://google.com/patents/WO2007095689A1.

Rolia, E., Dutrizac, J.E., 1984. The determination of free acid in zinc processing solutions. Canadia Metallurgical Quarterly, 23, 159-167.

Rosato, L.I., Agnew, M.J., 1996. Iron disposaI options at Canadian electrolytic zinc. In: Dutrizac, J.E., Harris, G.B. (Eds.), Iron control and disposal: Second international symposium on iron control in hydrometallurgy, 77-89. CIM, Montreal, Canada.

Rose, A.W., Bianchi-Mosquera, G.C., 1993. Adsorption of Cu, Pb, Zn, Co, Ni, and Ag on goethite and hematite: A control on metal mobilization from red beds into stratiform copper deposits. Econ. Geol., 88, 1226-1236.

Ruiz, M.C., Zapata, J., Padilla, R., 2007. Effect of variables on the quality of hematite precipitated from sulfate solutions. Hydrometallurgy, 89, 32-39.

Rull, F., Martinez-Frias, J., Sansano, A., Medina, J., Edwards, H.G.M., 2004. Comparative micro-Raman study of the Nakhla and Vaca Muerta meteorites, J. Raman Spectrosc., 35, 497-503.

Russel, J.D., 1979. Infrared spectroscopy of ferrihydrite: Evidence for the presence of structural hydroxyl groups. Clay Miner., 14, 109-114.

Sahu, S.K., Asselin, E., 2011. Characterization of residue generated during medium temperature leaching of chalcopyrite concentrate under CESL conditions. Hydrometallurgy, 110, 107-114.

Sammut, D., Welham, N. J., 2002. The Intec copper process: A detailed environmental analysis. Proceedings of the green processing conference, Cairns, Queensland , 29-31 May, 115-124.

Sapieszko, R.S., Patel, R.C., Matijevic, E., 1977. Ferric hydrous oxide sols. 2. Thermodynamics of aqueous hydroxo and sulfato ferric complexes. The Journal of Physical Chemistry, 81, 1061-1068.

Sasaki, K., Ootsuka, K., Tozawa, K., 1993. Hydrometallurgical studies on hydrolysis of ferric sulphate solutions at elevated temperatures. II. Equlibrium diagram in the system, Fe_2O_3- SO_3-H_2O, at elevated temperatures. Shigen to Sozai (in Japanese), 109, 11, 871-877.

Sasaki, K., Tanaike, O., Konno, H., 1998. Distinction of jarosite-group compounds by Raman spectroscopy. The Canadian Mineralogist, 36, 1225-1235.

Schemidth, E.R., Vermaas, F.H.S., 1955. Differential thermal analysis and cell dimensions of some natural magnetites. Ann. Mineral., 40,422-431.

Schmidt, E.R., Vermaas, F.H.S., 1955. Differential thermal analysis and cell dimensions of some natural magnetites. American Mineralogist, 40, 422-431

Schulze, D.G., 1981. Identification of soil iron oxide minerals by differential X-ray diffraction. Soil Sci. Soc. Am. J., 45, 437-440.

Schulze, D.G., Schwertmann, U., 1984. The influence of aluminum on iron oxides: properties of Al substituted goethites. Clay Min., 19, 521-539.

Schwertman, U., Cornell, R.M., 1991. Iron oxide in the laboratory: Preparation and characterization. 1st Ed. Wiley-VCH, Wernheim.

Schwertmann, U. Cornell, R.M., 2000. Iron oxides in the laboratory: Preparation and characterisation. (Wiley-VCH: Weinham 2nd edition).

Schwertmann, U., 1979. The influence of aluminium on iron oxides: Five clay minerals as sources of aluminium. Soil Sci., 128, 195-200.

Schwertmann, U., 1987. Some properties of soil and synthetic iron oxides. In: Stucki, J.W., Goodman, B.A., Schwertmann, U., (Eds.). Iron in soils and clay minerals (1st ed., pp. 203-250). Dordrecht, Holland: Reidel, D., publishing.

Schwertmann, U., Cambier, P., Murad, E., 1985. Properties of goethites of varying crystallinity. Clay Miner., 33(5), 369-378.

Schwertmann, U., Schulze, D.G, Murad, E., 1982. Identification of ferrihydrite in soils by dissolution kinetics, differential X-ray diffraction and Mossbauer spectroscopy, Soil Sci. Soc. Amer. J., 46, 869-875.

Scott, J.D., Donyina, D.K.A, Mouland, J.E., 1986. Iron-the good with the bad – Kidd Creek zinc plant experience In: Dutrizac, J.E., Monhemius, A.J. (Eds.), Iron control in hydrometallurgy. Ellis Horwood Ltd., Chichester, U.K 657-675.

Shang, Y., van Weert, G., 1993. Iron control in nitrate hydrometallurgy by autoclave hydrolysis of iron (III) nitrate. Hydrometallurgy, 33, 273-290

Shwertmann, U., Fischer, W.R., 1973. Natural amorphous ferric hydroxide. Geoderma, 10, 237-247.

Singhania, S., Wang, Q., Filippou,D., Demopoulos, G.P., 2006. Acidity, valency and third-ion effects on the precipitation of scorodite from mixed sulfate solutions under atmospheric-pressure conditions. Metallurgical and Materials Transactions B., 37B, 189-197.

Spiro, T.G., Allerton, S.E., Renner, J., Terzis, A., Bils, R., Saltman, P., 1966. The hydrolytic polymerization of iron (III). J. Am. Chem. Soc., 88, 2721-2726.

Steel, A., Hawboldt, K., Khan, F., 2010. Assessment of minerals and iron-bearing phases present in hydrometallurgical residues from a nickel sulfide concentrate and availability of residue associated metals. Hydrometallurgy, 101, 126-134.

Sugimoto, T., Wang, Y., 2001. Mechanism of the shape and structure control of monodispersed α-Fe_2O_3 particles by sulfate ions. J. Colloid Interface Sci., 207, 137-149.

Suresh, G., Ramasamy, V., Ponnusamy, V., 2011. Mineralogical and thermoluminescence characterizations of the river sediments from Tamilnadu, India. Natural Resources Research, 20, 389-399.

Swamy, Y.V., Kar, B.B., Mohanty, J.K., 2003. Physico-chemical characterization and sulphatization roasting of low-grade nickeliferous laterites. Hydrometallurgy, 69, 89-98.

Söhnel, O., Garside, J., 1992. Precipitation: Basic principles and industrial applications. Butterworth Heinemann, Oxford, U.K.

Tang, M., Liu, Q., 2012. The acidity of caustic digested starch and its role in starch adsorption on mineral surfaces. Intl. J. of Mineral Processing, 112, 94–100

Taylor, R.M., 1959. Amorphous iron oxides in soils. J. Soil Sci., 10, 309-315.

Tessier, A., Campbell, P.G.C., Bisson, M., 1979. Sequential extraction procedure for speciation of particulate trace metals. Analytical Chemistry, 51, 844-851.

Thomas, A., 2009. Improved process for chalcopyrite leaching. http://www.ibridgenetwork.org/ucb/improve_process for chalcopyrite.

Timmons, R.J., Goertz, H.M., 1994. Processes for the preparation of sulfur coated fertilizers and products produced thereby. https://www.google.com/patents/US5405426.

Tombácz, E., Libor, Z., Illés, E., Majzik, A., Klumpp, E., 2004. The role of reactive surface sites and complexation by humic acids in the interaction of clay mineral and iron oxide particles. Org. Geochem., 35, 257-267.

Towe, K.M., Bradley, W.F., 1967. Mineralogical constitution of colloidal "hydrous ferric oxides". J. Colloid and Interface Sci., 24, 384-392.

Tozawa, K., Sasaki, K., 1986. Effect of co-existing sulphates on precipitation of ferric oxide from ferric sulphate solutions at elevated temperatures. In: Dutrizac, J.E., Monhemius, A.J., (Eds.). Iron control in hydrometallurgy. Ellis Horwood Ltd., Chichester, U.K. 454-476.

Umetsu, Y., Tozawa, K., Sasaki, K., 1977. The hydrolysis of ferric sulphate solutions at elevated temperatures. Canadian Metallurgical Quarterly, 16, 111-117.

Van Niekerk, C.J., Begley, C.C., 1991. Zinc in South Africa. J. S. Afr. Inst. Min. Metall., 91, 233-248.

Van Weert, G., Shang, Y., 1993. Iron control in nitrate hydrometallurgy by auto decomposition of iron (II) nitrate. Hydrometallurgy, 33, 255-271.

Vempati, R.K. Loeppert, R.H., 1989. Influence of structural and adsorbed Si on the transformation of synthetic ferrihydrite. Clay Miner., 37, 273-279.

Vignes, A., 2013. Extractive metallurgy 2: Metallurgical reaction processes, ISTE. Wiley.

Vöigt, B., Gobler, A., 1986. Formation of pure hematite by hydrolysis of iron (III) salt solutions under hydrothermal conditions. Cryst. Res. Technol., 21, 1177-1183.

Walter, B., Buxbaum, G., Laqua, W., 2001. The mechanism of the thermal transformation from goethite to hematite. Journal of Thermal Analysis and Calorimetry, 63, 733-748.

Wang, K., Li, J. McDonald, R.G. Browner, R.E., 2011. The effect of iron precipitation upon nickel losses from synthetic atmospheric nickel laterite leach solutions: Statistical analysis and modelling. Hydrometallurgy, 109, 140-152.

Ward, T., 2015, Metal recovery from medium temperature pressure leach residues. Master thesis, Dept. of materials engineering, University of British Columbia, Canada.

Welham, N.J., Malatt, K.A., Vukcevic, S., 2000. The effect of solution speciation on iron sulphur–arsenic–chloride systems at 298 K. Hydrometallurgy, 57, 209-223.

Wolska, E., 1981. The structure of hydrohematite. Zeitschrift für Kristallographie, 154, 1-2, 69-75.

Xu, W., Hausner, D.B., Harrington, R., Lee, P.L., Strongin, D.R., Parise, J.B., 2011. Structural water in ferrihydrite and constraints this provide on possible structural models. American Mineralogist, 96, 513-520.

Yue, G., Zhao, L., Olvera, O.G., Asselin, E., 2014. Speciation of the H_2SO_4–$Fe_2(SO_4)_3$–$FeSO_4$–H_2O system and development of an expression to predict the redox potential of the Fe^{3+}/Fe^{2+} couple up to 150 °C. Hydrometallurgy, 147-148, 196-209.

Žic, M., Ristić, M., Musić, S., 2011. Monitoring the hydrothermal precipitation of α-Fe_2O_3 from concentrated $Fe(NO_3)_3$ solutions partially neutralized with NaOH. J. Molecular Structure, 993,115-119.

Zinck, J.M., 1993. An investigation into the hydrolytic precipitation of iron (III) from sulphate-bearing effluents, Master Thesis, Dept. of mining and metallurgical engineering, McGill University, Montreal, Canada.

Appendices

Appendix A. Rietveld refinement

In Rietveld phase analysis method it is considered that:

$$\sum x_i = 100\ \% \qquad (1a)$$

where x_i is the weight percent of phase i as obtained by Rietveld method.

When a certain percent of a material is leached from the sample, the weight percent of the remaining phases increases therefore it should be normalized to take into account the leached materials, as follows:

$$\sum X_i = (100 - \mathrm{a})\% \qquad (2a)$$

where X_i is the renormalized weight percent of i, and a is the phase leached; thus the new weight percent can be written as:

$$X_i = \frac{x_i(100 - a)}{100} \qquad (3a)$$

Appendix B. Transformation applied to % Fe precipitated in Figure 7.1

Often power transformations from the family $y^* = y^\lambda$ are used where λ is parameter of the transformation to be determined (e.g., λ= -1/2 means use the inverse square root of the original response). This procedure uses the method of maximum likelihood. Various values of λ are selected and a standard analysis of variance is performed on:

$$y^{(\lambda)} = \frac{y^{\lambda-1}}{\lambda \dot{y}^{\lambda-1}}, \qquad y^{(0)} = \dot{y} ln y \qquad (1b)$$

The value of $\lambda = 0$ corresponds to the log transformation and it can be shown that $y^{(0)} = \dot{y} ln y$. The quantity $\dot{y}$ is the geometric mean of the response data. The maximum likelihood value for λ, for the fitted model, is the lowest point in the graph of residual sum of squares (RSS) versus λ (Box *et al*., 1978). For the % Fe precipitated used in this study, values of ($lnRSS$) for various values of λ are plotted in Figure 1B below. The values ($lnRSS$) are used because the range of values for (RSS) is quite large. An approximate 95 % confidence interval for (λ) may also be obtained from the graph by calculating the critical sum of squares(SS^*):

$$SS^* = RSS\left[1 + \frac{t_\nu^2(0.025)}{\nu}\right] \qquad (2b)$$

Where, ν is the number of degree of freedom. A line is plotted parallel to λ-axis at a height SS^* on the graph of $(lnRSS)$ versus λ. By locating the points on λ-axis where the SS^* cuts the curve $(lnRSS)$, we can read the 95 % confidence interval limits on λ directly from the graph. The values of low and high confidence interval in this study are -0.3 and 0.91, respectively. The optimum value of λ in this case is 0.18 which is the lowest point in the $(lnRSS)$ versus λ graph. As the minimum value of λ and zero both fall within the 95 % confidence limit, therefore the transformation procedure is good enough to process the % Fe precipitation data in Figure 7.1.

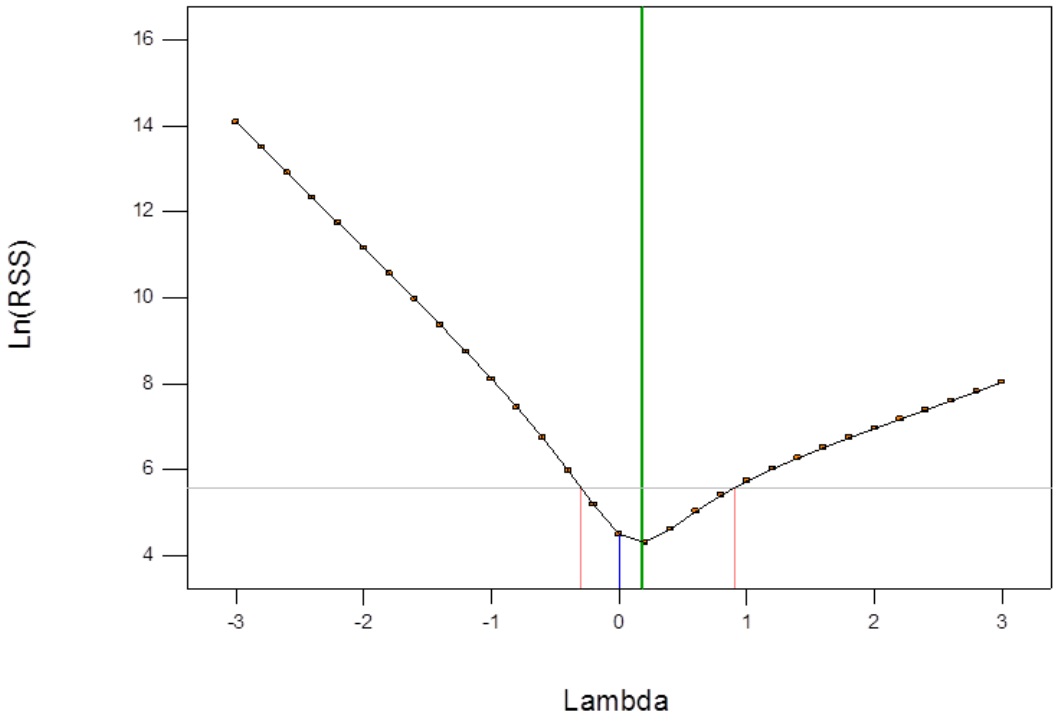

Figure 1B Box-Cox plot for the power transformation applied to % Fe precipitation.

Appendix C. Box–Behnken design

The Box–Behnken design (Myers and Montgomery, 2002) is an independent quadratic design to navigate response surfaces. It does not contain an embedded fractional factorial design. The treatment combinations are at the midpoints of edges of the process space and at the center. These designs are rotatable (or near rotatable) and require 3 levels of each factor. The no. of experiments in this design are: $N = 2k(k-1) + C_0$. Where k is the no. of factors and and C_0 is the no. of central points. The experimental data is normally fitted to a quadratic model given below:

$$Y = \beta_0 + \sum_{i=1}^{k} \beta_i x_i + \sum_{i=1}^{k} \sum_{j=1}^{k} \beta_{ij} x_{ij} + \sum_{i=1}^{k} \beta_{ii} x_{ii}^2 + \varepsilon \qquad (1c)$$

where Y is the response variable β_0 is regression coefficient and β_i, β_{ij}, β_{ii} are coefficients of the linear, interaction and quadratic terms respectively. The trem $'\varepsilon'$ represents the random errors. The error terms, in general, are normally distributed. The relationship between the coded and actual factors can be written as:

$$x_i = \frac{X_i - X_0}{\Delta X} \qquad (2c)$$

where X_i is the actual value of the variable, x_i is the coded value, X_0 is the actual value of the variable at the central point and ΔX corresponds to the unit variation of the value.

Appendix D. Assays and experimental data

Iron precipitation and copper loss data provided in Chapter 6, Chapter 7 and Chapter 8 is extracted from Tables: D-1, D-2 and D-3 respectively.

Table D-1. Assay results and experimental data used in Chapter 6.

Initial Fe (g/L)	Precipitates Cu, Fe and S contents			Precipitates mass (g)	% Fe precipitation	Mass (Cu out/Cu in) x 100	Precipitates (%Cu/%Fe) x 100
	Cu %	Fe %	S %				
1.5	0.75	59.4	2.23	1.36	53.86	0.03	1.26
3.0	0.65	58.9	2.52	2.68	52.61	0.06	1.26
4.5	0.55	58.8	2.62	3.91	51.09	0.07	1.10
6.0	0.44	58.6	2.49	4.5	43.95	0.07	0.94
7.5	0.43	57.7	2.90	4.6	35.39	0.07	0.75
9.0	0.39	57.1	3.13	5.49	34.83	0.07	0.75
10.5	0.39	56.6	3.21	5.3	28.57	0.06	0.68
15.0	0.25	52.6	4.25	4.81	16.87	0.04	0.69
20.0	0.10	39.6	10.3	3.89	7.70	0.01	0.48
30.0	0.05	35.6	11.8	3.19	3.78	0.01	0.25
Initial acid (g/L)	Cu %	Fe %	S %	Precipitates mass (g)	% Fe precipitation	Mass (Cu out/Cu in) x 100	Precipitates (%Cu/%Fe) x 100
0	1.13	56.5	1.74	9.3	87.57	0.35	2.00
5	0.82	55.6	1.91	7.92	73.39	0.22	1.47
10	0.92	55.1	2.26	6.58	60.43	0.20	1.67
12.5	0.58	55.2	2.87	5.03	48.28	0.10	1.05
15	0.51	55.5	2.39	4.7	42.48	0.08	0.92
20	0.35	54.1	1.87	0.47	14.24	0.07	0.81
25	0.33	53.5	1.85	0.1	0.89	0.01	0.65
30	0.30	52.5	1.75	0.01	0.10	0.01	0.62
Initial chloride (g/L)	Cu %	Fe %	S %	Precipitates mass (g)	% Fe precipitation	Mass (Cu out/Cu in) x 100	Precipitates (%Cu/%Fe) x 100
0	0.52	53.0	3.15	3.65	32.24	0.06	0.98
3	0.56	53.2	3.09	3.95	35.02	0.07	1.05
6	0.47	54.2	2.88	4.5	40.65	0.07	0.87
9	0.52	54.4	2.76	4.8	43.52	0.08	0.96
12	0.49	54.6	2.63	5.1	46.41	0.08	0.90
15	0.46	54.7	2.56	5.4	49.23	0.08	0.84
20	0.59	53.4	3.07	5.7	50.73	0.11	1.10
25	0.54	56.0	2.38	5.9	55.07	0.11	0.96
30	0.47	55.8	2.25	6.3	58.59	0.10	0.84

Retention time (hr) no seed	Cu %	Fe %	S %	Precipitates mass (g)	% Fe precipitation	Mass (Cu out/Cu in) x 100	Precipitates (%Cu/%Fe) x 100
0	0.63	54.9	2.90	0.36	3.33	0.01	1.15
1	0.44	58.6	2.49	4.18	40.83	0.07	0.75
2	0.44	57.9	2.01	5.18	50	0.09	0.76
4	0.38	59.5	1.76	5.71	56.67	0.08	0.64
6	0.36	59.5	1.69	6.13	60.83	0.08	0.61
8	0.31	60.1	1.80	6.16	61.67	0.07	0.52
12	0.27	61.1	1.47	6.38	65.0	0.06	0.44
Retention time (hr) 15 g/L seed	Cu %	Fe %	S %	Precipitates mass (g)	% Fe precipitation	Mass (Cu out/Cu in) x 100	Precipitates (%Cu/%Fe) x 100
0	0.10	62.7	0.82	2.8	29.26	0.01	0.16
1	0.10	63.7	0.82	5.34	56.67	0.01	0.16
2	0.10	64.7	0.82	6.03	65.0	0.02	0.15
4	0.12	65	0.8	6.28	68.0	0.02	0.18
6	0.15	65.2	0.76	6.32	68.70	0.03	0.23
Temperature (°C)	Cu %	Fe %	S %	Precipitates mass (g)	% Fe precipitation	Mass (Cu out/Cu in) x 100	Precipitates (%Cu/%Fe) x 100
150	0.5	57.3	2.64	4.5	42.97	0.08	0.87
180	0.40	61.3	1.45	7.71	78.77	0.10	0.65
200	0.45	63.2	1.08	7.87	83.0	0.11	0.71
220	0.49	65.6	0.77	7.95	87.0	0.12	0.75
Initial Cu (g/L)	Cu %	Fe %	S %	Precipitates mass (g)	% Fe precipitation	Mass (Cu out/Cu in) x 100	Precipitates (%Cu/%Fe) x 100
0	0.0	54.0	3.28	0.40	3.60	0.0	0.0
10	0.16	54.5	3.22	1.33	12.08	0.02	0.29
20	0.37	55.2	3.10	3.8	34.96	0.07	0.67
30	0.44	58.6	2.49	5.03	49.13	0.07	0.75
40	0.58	56.9	2.62	5.8	55.01	0.08	1.02
50	0.65	57.9	2.50	5.9	56.94	0.08	1.12
60	0.80	57.1	2.46	6.0	57.10	0.08	1.40

Table D-2. Assay results and experimental data used in Chapter 7.

Exp. No	Precipitates Cu, Fe, S content (%)			Precipitates mass (g)	% Fe precipitated	Mass (Cu out/Cu in) x 100	Precipitates (%Cu/%Fe) x 100
	Cu	Fe	S				
F-1	0.157	62.3	1.33	13.7	57.03	0.072	0.252
F-2	0.194	59.7	2.57	18.4	73.36	0.119	0.325
F-3	0.094	47.8	5.72	3.2	10.20	0.01	0.197
F-4	0.084	64.0	1.09	11.3	48.30	0.032	0.131
F-5	0.045	56.2	2.47	1.6	14.99	0.002	0.080
F-6	0.046	61.6	1.58	8.4	86.65	0.013	0.075
F-7	0.035	64.5	0.91	8.8	94.60	0.01	0.054
F-8	0.074	66.2	0.62	7.2	79.99	0.018	0.112
G-1	0.031	64.6	0.89	5.7	60.72	0.006	0.048
G-2	0.132	63.4	1.36	8.5	34.24	0.036	0.208
G-3	0.252	58.5	1.18	7.5	72.54	0.062	0.431
G-4	0.051	61.2	1.23	5.7	22.85	0.01	0.083
G-5	0.497	48.0	4.04	16.9	44.24	0.262	1.183
G-6	0.288	53.4	2.87	2.1	10.00	0.019	0.539
G-7	0.522	51.8	2.91	8.1	39.14	0.138	1.008
G-8	0.865	54.8	1.98	8.4	75.81	0.239	1.578
G-9	0.532	60.4	0.86	8.9	86.57	0.153	0.881
G-10	0.152	62.6	1.00	11.2	65.58	0.056	0.243
G-11	0.067	63.3	0.95	8.7	56.00	0.021	0.106
G-12	0.164	59.5	1.20	14.8	52.00	0.072	0.276
G-13	0.121	60.5	1.37	9.4	54.00	0.038	0.200
G-14	0.151	60.9	1.39	9.7	53.00	0.046	0.248
G-15	0.141	60.7	1.38	9.5	55.00	0.045	0.232

Table D-3. Assay results and experimental data used in Chapter 8.

Impurity	Cu	Fe	S	As	Precipitates mass	% Fe precipitated
As (mg/L)	%	%	%	%	(g)	%
0	0.44	58.6	2.49	0	4.3	44.0
60	0.22	31.7	2.20	0.65	0.2	1.05
120	0.31	31.5	1.80	2.23	0.17	0.89
250	1.32	30.5	1.75	10.2	0.18	0.88
500	1.37	26.5	1.50	12.7	0.2	0.90
1000	1.66	26.0	1.34	21.0	2.04	8.84
2000	1.72	24.7	1.26	22.1	5.5	22.64
Na (g/L)	Cu %	Fe %	S %	Na %	Precipitates mass (g)	% Fe precipitated
0	0.44	58.6	2.49	0	4.3	44.0
0.25	0.34	47.2	7.22	0.53	5.9	46.41

Impurity	Cu	Fe	S	As	Precipitates mass	% Fe precipitated
Na (mg/L)	%	%	%	%	(g)	%
0.5	0.19	38.5	10.4	1.62	9	57.75
1	0.28	38.7	10.3	1.93	10.6	68.37
2	0.51	37.1	10.7	2.78	13.02	80.51
5	1.14	36.4	10.8	3.19	15.3	92.82
Al (g/L)	Cu %	Fe %	S %	Al %	Precipitates mass (g)	% Fe precipitated
0	0.44	58.6	2.49	0	4.3	44.0
1	0.33	52.4	1.72	0.32	2.82	24.628
3	0.42	51.8	1.93	0.23	1.77	15.281
6	0.51	53.0	2.24	0.15	0.45	3.975
Mg (g/L)	Cu %	Fe %	S %	Mg %	Precipitates mass (g)	% Fe precipitated
0	0.44	58.6	2.49	0	4.3	44.0
1	0.60	51.6	2.39	0.073	4.8	41.28
3	0.58	51.6	2.23	0.074	5.15	44.29
6	0.77	51.9	2.23	0.084	5.82	50.343